INVESTIGATION OF THE AGGREGATION OF NANOPARTICLES IN AQUEOUS MEDIUM AND THEIR PHYSICOCHEMICAL INTERACTIONS AT THE NANO-BIO INTERFACE

A Thesis
Presented to
The Academic Faculty

by

Kungang Li

In Partial Fulfillment
of the Requirements for the Degree
Doctor of Philosophy in Environmental Engineering in the
School of Civil and Environmental Engineering

Georgia Institute of Technology
May, 2014

INVESTIGATION OF THE AGGREGATION OF NANOPARTICLES IN AQUEOUS MEDIUM AND THEIR PHYSICOCHEMICAL INTERACTIONS AT THE NANO-BIO INTERFACE

Approved by:

Dr. Yongsheng Chen, Advisor
School of Civil and Environmental Engineering
Georgia Institute of Technology

Dr. Sotira Yiacoumi
School of Civil and Environmental Engineering
Georgia Institute of Technology

Dr. John Crittenden
School of Civil and Environmental Engineering
Georgia Institute of Technology

Dr. Lin Jiang
School of Biology
Georgia Institute of Technology

Dr. Ching-Hua Huang
School of Civil and Environmental Engineering
Georgia Institute of Technology

Date Approved: [March 05, 2014]

To my wife, Xixi Lin, and my parents

ACKNOWLEDGEMENTS

This dissertation would not have been possible without the generous help from several individuals, and therefore I would like to express my gratitude to all of them. First and foremost, I would like to express my deepest gratitude to my thesis advisor, Dr. Yongsheng Chen, for his tremendous support, advice and guidance for my study, research, personal matters, and career development. He has taught me everything essential to a PhD student and a researcher, and trained me to become a scientist without any reservation. He has provided me with many opportunities to get involved in various academic activities. He has also helped, supported and advised me whenever I have difficulties, troubles and confusions in research, personal life and careers. He is a great person, advisor and mentor. There are too many things that I will always remember in my life. I have been fortune to be his student.

Secondly, I would like to say thank you to my committee members: Dr. John Crittenden, Dr. Ching-Hua Huang, Dr. Sotira Yiacoumi and Dr. Lin Jiang for their invaluable advice and comments on my research.

To every member in Chen group. I have had pleasant experience to work with them. I would like to thank Wen Zhang and Ying Yao for their tremendous help on my research particularly during the early stage of my PhD life. Visiting scholars, Dr. Ying Huang and Dr. Chungang Yuan, are greatly appreciated for their experimental help and insightful discussion. Special thanks go to Dr. Songyan Du. She is such a great friend and collaborator. Without her, I cannot accomplish my study on nano-DNA interaction. And

Jin Gi Hong, my good friend and officemate, is appreciated for the great atmosphere in office and our discussion on research.

I would also like to appreciate Dr. Guangxuan Zhu for his help and guidance on lab management and maintenance of various analytical instruments.

I appreciate the help from several friends in School of Biology at Georgia Tech. Dr. Xiaonan Zhao helps me a lot on nano-DNA interaction research. Zhichao Pu teaches and helps me on *paramecium* study. Their generous help are greatly appreciated.

There are several friends coming to Georgia Tech and joining the Environmental Engineering program at the same time with me. We took the same class, helped each other both in and out of class, spent a lot of leisure time together, and shared great memories. I would like to thank them to make the long way (to become a doctor) a pleasure journey.

Finally, my biggest thanks and love go to my wife and my parents. I have been in a relationship with my wife, Xixi Lin, for almost 8 years. And we are married for over 4 years. I will never forget her unconditional support and love particularly during the down days of my life. I always remember when I spent the whole night doing experiment in the lab, she was there with me. Whenever I confront difficulties, she is always with me. I also would like to thank my parents for their endless support and love, always.

TABLE OF CONTENTS

LIST OF TABLES

LIST OF FIGURES

Page

LIST OF ABBREVIATIONS

AAC	Acoustic alternating current
AFM	Atomic force microscopy
DI water	Deionized water
DLS	Dynamic light scattering
DLVO	Derjaguin–Landau–Verwey–Overbeek
E. coli	*Escherichia coli*
EDL	Electrostatic double layer
EDLVO	Extended DLVO
EDTA	Ethylenediaminetetraacetic acid
EPM	Electrophoretic mobility
FTIR	Fourier transform infrared spectroscopy
HA	Humic acid
HR-TEM	High-resolution transmission electron microscopy
ICP-MS	Inductively coupled plasma-mass spectrometry
NOM	Natural organic matter
NP	Nanoparticle
PCR	Polymerase chain reaction
PDDA	Polydiallydimethylammonium chloride
PDI	Polydispersivity index
PEG	Poly (ethylene glycol)
P. multimicronucleatum	*Paramecium multimicronucleatum*

QD	Quantum dot
RNAP	RNA polymerase
ROS	Reactive oxygen species
SEI	Surface element integration
TEM	Transmission electron microscopy
vdW	Van der Waals

SUMMARY

Owing to their unique physical, chemical, and mechanical properties, nanoparticles (NPs) have been used, or are being evaluated for use, in many fields (*e.g.*, personal care and cosmetics, pharmaceutical, energy, electronics, food and textile). However, concerns regarding the environmental and biological implications of NPs are raised alongside the booming nanotechnology industry. Numerous studies on the biological effect of NPs have been done in the last decade, and many mechanisms have been proposed. In brief, mechanisms underlying the adverse biological effect caused by NPs can be summarized as: (i) indirect adverse effect induced by reactive oxygen species (ROS) generated by NPs, (ii) indirect adverse effect induced by released toxic ions, and (iii) adverse effect induced by direct interactions of NPs with biological systems. Up to now, most efforts have been focused on the first two mechanisms. In contrast, adverse biological effects induced by direct nano-bio interactions are the least researched. This is largely because of the complexity and lack of suitable techniques for characterizing the nano-bio interface.

This dissertation aims at advancing our understanding of the nano-bio interactions leading to the adverse biological effect of NPs. Specifically, it is comprised of three parts. Firstly, because the aggregation of NPs alters particle size and other physicochemical properties of NPs, the property of NPs reaching and interacting with biological cells is very likely different from that of what we feed initially. Consequently, as the first step and an essential prerequisite for understanding the biological effect of NPs, NP aggregation is investigated and models are developed for predicting the stability and the extent of aggregation of NPs. Secondly, interactions between NPs and cell membrane are studied with *paramecium* as the model cell. Due to the lack of cell wall, the susceptible cell membrane of *paramecium* is directly exposed to NPs in the medium. The extent and

strength of direct nano-cell membrane interaction is evaluated and quantified by calculating the interfacial force/interaction between NPs and cell membrane. A correlation is further established between the nano-cell membrane interaction and the lethal acute toxicity of NPs. We find NPs that have strong association or interaction with the cell membrane tend to induce strong lethal effects. Lastly, we demonstrate systematic experimental approaches based on atomic force microscope (AFM), which allows us to characterize nano-bio interfaces on the single NP and single-molecular level, coupled with modeling approaches to probe the nano-DNA interaction. Using quantum dots (QDs) as a model NP, we have examined, with the novel application of AFM, the NP-to-DNA binding characteristics including binding mechanism, binding kinetics, binding isotherm, and binding specificity. We have further assessed the binding affinity of NPs for DNA by calculating their interaction energy on the basis of the DLVO models. The modeling results of binding affinity are validated by the NP-to-DNA binding images acquired by AFM. The investigation of the relationship between the binding affinity of twelve NPs for DNA with their inhibition effects on DNA replication suggests that strong nano-DNA interactions result in strong adverse genetic effects of NPs.

In summary, this dissertation has furthered our understanding of direct nano-bio interactions and their role in the biological effect of NPs. Furthermore, the models developed in this dissertation lay the basis for building an “ultimate” predictive model of biological effects of NPs that takes into account multiple mechanisms and their interactions, which would save a lot of testing costs and time in evaluating the risk of NPs.

CHAPTER 1

INTRODUCTION

1.1. Background of nanotechnology

Nanotechnology is defined by National Nanotechnology Initiative (NNI) as the "understanding and control of matter at dimensions between approximately 1 and 100 nanometers, where unique phenomena enable novel applications" [1]. NPs (NPs) are defined as primary particles with at least one dimension less than 100 nanometers [2, 3]. Due to the size-endowed unique physicochemical properties of NPs compared to their bulk counterparts, NPs have sparked interests and found applications in numerous scientific and industrial areas such as pharmaceuticals, electronics, cosmetics, health care, energy, agriculture, environment, and many more others [4-9]. According to the Project on Emerging Nanotechnologies, which has been tracking the number of consumer products containing engineered NPs since March 2006, the number increased 668% from 212 to 1628 in just 7 years [10]. In addition, the National Science Foundation projects that by 2020, the field of nanotechnology will employ some 6 million workers, 2 million of whom are expected to be in the United States [11, 12]. A more shocking projection is that nanotechnology will impact more than over $2.5 trillion worth of manufactured goods by 2015 according to Lux Research, although many of these goods may contain only minute amounts of intentionally engineered NPs [13, 14].

It is necessary to outline several of the many applications of NPs in order to broaden understanding of the importance that NPs have and will play in our future. The established applications and applications currently entering widespread use of NPs include but not limited to electronics [15-19], transportation [20, 21], microscopy [22, 23], biomedical fields [24-29], environmental remediation [30-33], cosmetics [34], coatings [35-38],

textiles [39-42], and paints [43-45]. Some of the most widely used NPs and their applications were listed in Table 1.1.

Table 1.1. Current applications of NPs in consumer goods

NPs	**Number of Consumer Products[10]**	**Applications**
Silver	408	Textiles, clothing, shoes, supplements, personal care and cosmetics, food storage containers, home cleaning, filtration
TiO_2	184	Colored pigments, personal care, cosmetics and sunscreen, toothpaste, food additives, nutritional supplements, paints, UV protection
ZnO	38	Personal care and sunscreens, paints, clothing (*e.g.*, antibacterial & deodorant shoes), coatings
Silicon	38	Computer hardware (*e.g.*, memory and processors), personal care and cosmetics, supplements, sporting goods
SiO_2	29	Paint and coatings, sporting goods, construction materials, computer hardware, home cleaning, supplements
Gold	21	Personal care and cosmetics, supplements, automotive catalysts
CeO_2	2	Automotive catalysts, coatings
Polystyrene latex bead	Not Available	Electron microscopy, diagnostics, and biological carriers

1.2. Literature review of biological effects of NPs

Environmental and public exposure to engineered NPs will increase dramatically in the near future due to the ubiquity of NPs in many consumer products and applications [4]. Engineered NPs probably will be released into the environment through manufacturing processes, waste disposal or product uses [46], which lead to the exposure of many organisms to NPs in the environment. People could also get exposed to commercially available NPs in many settings, including silver (Ag) NPs in sheets and clothing, titanium dioxide (TiO_2) NPs in cosmetics, sunscreens, and food, carbon NPs in bikes, and even clay NPs in beer bottles [10, 47]. It is thus of paramount importance to thoroughly understand the biological effect and risk of NPs before their massive production and widespread consumer applications.

Because of their very small size and other unique physicochemical properties, NPs have been identified as a distinct category from conventional chemicals and particulates [9, 48-50]. Not only the chemical composition has an effect on the biological effect of NPs, but also size, surface properties, shape, crystal structure and other properties of NPs influence their biological effects [51-53]. To deal with this unique class of toxicant, during the last decade, there are numerous studies investigating potential toxic impacts of NPs on biological and ecological systems with an emphasis on establishing a relationship between the physicochemical properties of the NPs and the toxicological responses [47, 48]. The classical toxicity paradigm that was initially developed for the evaluation of chemical substances is often inadequate for the assessment of biological effects of NPs [48]. Although numerous studies on biological effects of NPs have been published in the last decade, to date, there are still many unknowns about the underlying mechanisms, which can prohibit the development of nanotechnology [8, 54-57].

1.2.1. Environmental and ecological risks of NPs

It is projected that the global production of NPs will grow to over half a million tons by 2020 [58, 59]. The increasing use of engineered NPs in industrial and commercial applications will very likely lead to the release of such materials into the environment, deliberately or accidentally. The NPs released to the environment will disperse in the environment including soil, water, and air, where they can persist for a long time or be uptaken by organisms, which may subsequently induce environmental and ecological risks [6, 8]. Particularly, NPs have been shown to bioaccumulate in the body of environmental organisms and then transfer through the food chain or food web, reaching organisms in each level and finally being taken up by humans [60-64] (Figure 1.1).

There are a variety of entry routes for engineered NPs into the environment, such as direct application in environmental remediation, wastewater treatment plant effluent and sludge, exhaust emission of NPs acting as fuel additives or catalysts, and spills from production, transport, and disposal of NPs or consumer products [6, 65-67]. A number of environmental risk assessment studies have been done to model the predicted environmental concentrations (PEC) of NPs [65, 66, 68-75]. For example, PECs of TiO_2 NPs in surface water, wastewater treatment plant (WWTP) effluent, and WWTP sludge respectively ranged from 0.021 to 10 μg/L, 1 to 100 μg/L, and 13.6 to 64.7 mg/kg [6, 66, 68-71, 74-76]. PECs of Ag NPs in surface water, wastewater treatment plant (WWTP) effluent, and WWTP sludge respectively ranged from 0.000088 to 10 μg/L, 0.0164 to 17 μg/L, and 1.29 to 39 mg/kg [6, 66, 72, 75, 76].

Numerous studies have been published on the biological effect of NPs towards environmental organisms including bacteria, algae, plants, plankton, protozoa, fish, mussel, earthworm, and many others [76-83]. These ecotoxicological studies show that many NPs such as Ag, fullerene, metal oxides are toxic to environmental organisms. Moreover, as mentioned above, a few studies found that NPs have the potential to accumulate in the

body of organisms and then transfer to organisms of higher tropical level through food chains, suggesting NPs may disrupt the whole ecosystem. Ecosystem processes [84] and environmental services [76] are potentially at risk as NPs enter the environments [85]. Besides the ecotoxicity of NPs on the individual and population levels [85], they also have community level impacts, such as altered competition and predator-prey interactions, loss of biodiversity [86] or community function, symbiosis interferences [87], host community or disease pattern changes, and food web alterations [85].

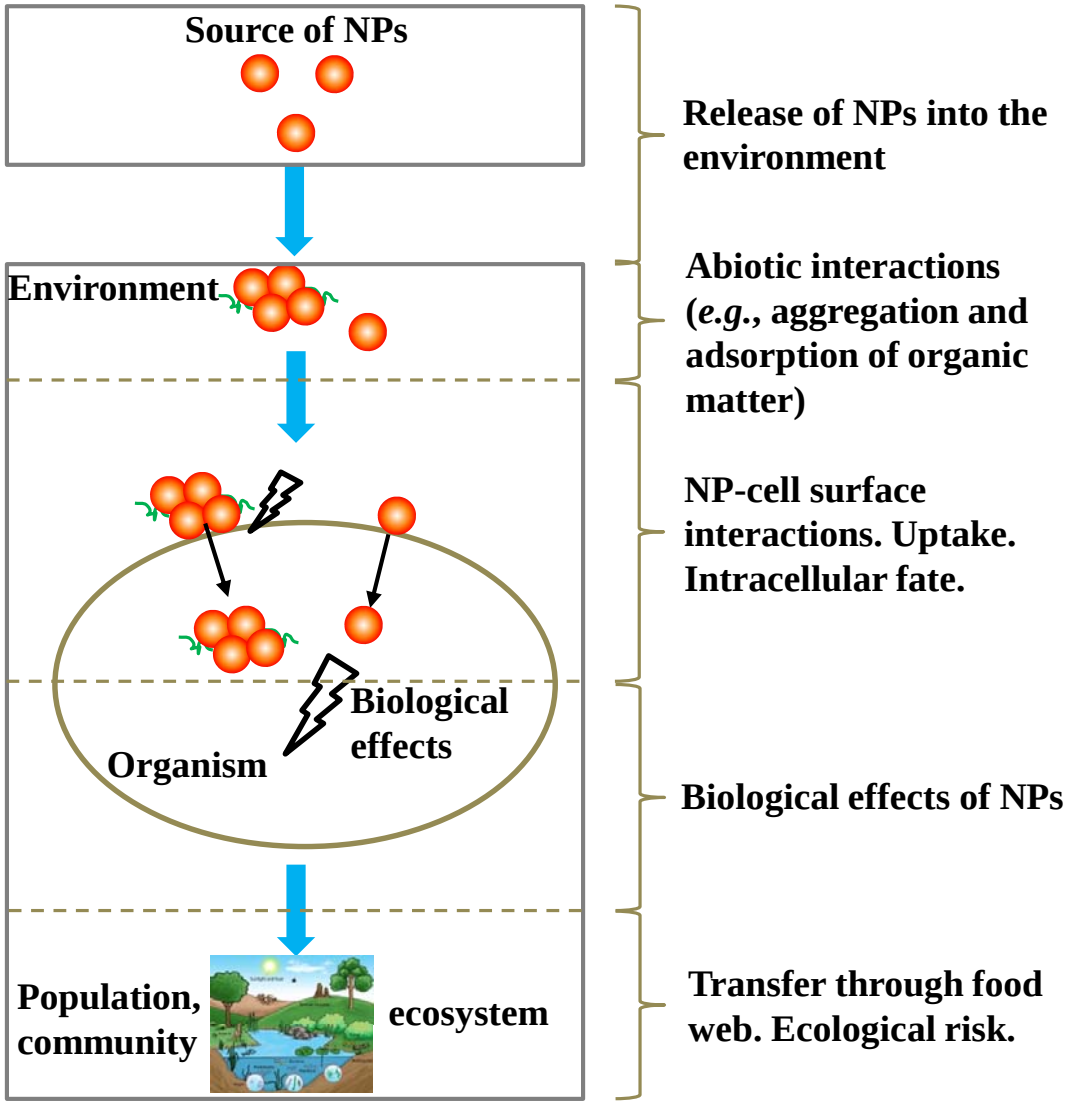

Figure 1.1. The logical chain of event accounting for the environmental and ecological risk of NPs.

1.2.2. Mechanisms of adverse biological effects induced by NPs

Currently, there are nine primary mechanisms leading to adverse biological effects of NPs including the generation of reactive oxygen species (ROS) and oxidative stress [88-90], membrane disruption/leakage [91-94], protein binding/unfolding response [95-98], DNA damage and adverse genetic effects [99-102], mitochondrial damage (e-transfer/ATP/PTP opening/apoptosis) [103-106], lysosomal damage (proton pump activity/lysis/frustrated phagocytosis) [107-111], inflammation (signaling cascades/cytokines/chemokines/adhesion) [88, 112-115], fibrogenesis and tissue remodeling [116-119], and blood clotting [5, 120-123]. These multiple mechanisms are not independent, rather, they interact among each other [120], which further entangles the biological effect study of NPs. For instance, NPs may indirectly damage DNA and biological membranes *via* generated ROS [124-126].

The generation of ROS and oxidative stress is considered to be of major importance in the toxicological profile of NPs [90, 127]. Up to now, this mechanism has been extensively studied on a wide range of NPs [105, 128-132]. ROS can be generated by several mechanisms, including (i) direct generation of ROS by chemical reactions of the coatings, reactive surface groups or ions leached from the surface of NPs in the acidic environment of endo- or lysosomes, (ii) interference with redox active proteins such as NADPH oxidase, (iii) interactions with oxidative organelles such as the mitochondria, and (iv) interactions with cell surface receptors and the activation of intracellular signaling pathways [50, 127, 133, 134]. However, not all NPs induce ROS. For example, CeO_2 NPs were found not to induce ROS but on the contrary showed a protective effect against ROS damage [135, 136].

NPs contacting cell membrane can induce physical and chemical damages to the membrane, which may result in death of the cell [137]. Because NPs possess numerous edges, defects, and other reactive sites [138], they may directly inflict physical damage to cell membranes. In addition, localization of NPs on the cell surface could result in ROS

accumulation and subsequent cellular damage [139]; ROS formed close to the cell surface would have a greater toxic effect [139]. Moreover, NPs may generate transient holes in the cell membrane during the uptake process and then induce a loss of membrane polarization and/or the leakage of cell contents, which can result in cell death [91, 92, 140]. The NPs can also lead to the formation of "pits" in cell surface, which subsequently causes a significant increases in permeability and result in cell death [137]. NPs also likely perturb membrane potential and result in increased intracellular Ca^{2+} concentration, which in turn modulates cellular signaling pathways [141].

When NPs enter biological fluids, they are almost invariably coated with proteins, form the so called "protein corona", with consequent structural and functional perturbations of the surface-bound proteins [97, 98, 142, 143]. The large surface-to-volume ratio of NPs and the potentially high concentration of proteins adsorbed at the particle surface may lead to faster clustering of proteins or even radically new protein clusters [97]. NPs can also influence protein self-assembly reactions, leading to perturbations of important biological processes [144]. Additionally, disceases involving protein misfolding and assembly could be enhanced in the presence of NPs. For instance, amyloidosis, involving self-assembly of soluble proteins into large insoluble fibrils, could be promoted through the interaction with the particle surface of NPs [145, 146].

Genetic effects of NPs may be produced by direct interactions of NPs with the genetic material (e.g., DNA and mRNA), or by indirect damage from ROS generated by NPs, or by toxic ions released from soluble NPs [147, 148]. Secondary genetic effects can be induced by oxidative DNA attack by ROS via activated phagocytes (neutrophils, macrophages) during NP-elicited inflammation [149]. NPs that were uptaken by the cell could reach the nucleus through diffusion across the nuclear membrane or transportation through the nuclear pore complexes, and subsequently directly interact with DNA molecules [127, 150]. Particularly, NPs of small size could reach the nucleus through nuclear pores (~ 10 nm in diameter) [150, 151]. Large NPs may also have access to

the DNA molecules in dividing cells during mitosis when the nuclear membrane dissolves [152, 153]. Furthermore, NPs can also alter gene expression via interactions with signal transduction pathways or the transcriptional or translational machinery through perinuclear localization [152, 154]. In detail, NPs can induce adverse genetic effects through the following mechanisms: (a) ROS generated by NPs can directly induce DNA point mutations or single or double strand breaks in DNA [152]. (b) The perinuclear localization of the NPs may hinder the cellular transcription and translation machinery and hereby affect global protein synthesis [154]. (c) Metal ions released from lysosomal located NPs can transfer to the cell cytoplasm where they can then alter protein or gene expressions [155]. (d) Interaction of NPs with cell surface located receptors may result in receptor activation and triggering of intracellular signaling cascades [156]. (e) NP-mediated ROS induction may indirectly affect gene expression patterns by activation of stress response or repair genes [157]. (f) NPs (such as gold NPs) may penetrate the nucleus and bind to and interact with DNA directly [127].

Mitochondria play a key role in energy metabolism; they produce energy via the citric acid cycle and are critically dependent on redox reactions from the respiration chain [158]. They are responsive to even small stresses in multiple ways [159]. NPs have been found to be in direct contact with and to produce damage within mitochondria [103-106]. When cells are exposed to NPs, which can lead to the generation of ROS, mitochondria are among the first and most sensitive organelles affected [160]. For instance, in quantum dots injured cells, the reduction of mitochondrial membrane potential and swelling of mitochondria have been detected [161, 162]. NP-induced mitochondrial perturbation has important biological effects, including the initiation of apoptosis (which is a form of cell death) and decreased ATP production [163, 164].

Lysosomes are organelles commonly associated with cell death. They play a key role in the engulfment and digestion of dead cells and in cellular autolysis during necrosis [158]. After taken up by cells via endocytosis, spherical NPs such as quantum dots, gold

NPs, and TiO_2 NPs appear to be stored in lysosomes and they can accumulate there [165-167]. NPs were shown to damage lysosomes through the generation of ROS [89]. Significant dilatation of the lysosomal system and reduced activity of lysosomal sulfatases were found after exposure to polystyrene NPs [168]. The lysosomal membrane can potentially be disrupted by ROS generated by NPs internalized by endocytosis, which can result in the release of lethal hydrolyses from lysosomes and cause cell death [160].

1.2.3. Relate physicochemical properties of NPs to their biological effects

The physicochemical properties of NPs such as the size, surface properties, shape, chemical composition, dissolution, and crystal structure (Figure 1.1), influence the biological interaction of NPs and hence determine their biological effects [5, 169-171].

Effect of size. Particle size is probably the most crucial material characteristic from the toxicological perspective because this is what differentiate NPs from their bulk counterparts and endows NPs with many unique properties [5]. It is well known that the pathway through which NPs enter biological cells, such as direct penetration, endocytosis or phagocytosis, depends on particle size [167, 170, 172]. The internalization efficiency of NPs is also influenced by particle size [173, 174]. Hence, particle size determines how many intracellular NPs can be found and can interact with organelles at a certain time of cellular exposure to NPs. Counterintuitively, it is not true that the smaller the particle, the higher the uptake efficiency. In general, the highest uptake efficiency with regard to particle size occurs at approximately 50 nm, which could be explained by different entry pathway of particles of different size into cell [167]. The biological effect of NPs is also size-dependent [175], and generally, the smaller the particle, the higher its toxicity [50]. This effect may originate from an increasing reactive surface area of smaller particles. As the particle size decreases, its surface area-to-volume ratio increases and allows a greater proportion of its atoms to be exposed to the exterior. Additionally, the number of

structural defects may increase as the particle size shrinks due to discontinuous crystal planes created by small size, which also increases surface reactivity of NPs [169].

Effect of surface charge. Surface charge plays an important role in the biological effect of NPs [176, 177]. It is a major determinant of colloidal stability; it determines the aggregation or agglomeration of NPs, and thus may change the size and shape of NPs [178]. Additionally, surface charge regulates interaction of NPs with the biological environments, such as the adsorption of ions and biomolecules that may change cellular responses to particles, or it may change the protein conformation and incorporation of NPs by cells such as the uptake rate and pathway of internalization [169]. In general, cationic particles are believed to be more toxic to cells than their anionic or neutral counterparts [140]. This may be due to the affinity of cationic particles to the cellular lipid bilayer, which carries a net negative charge, and thus cationic particles are easier to be internalized. Moreover, the strong interaction of cationic particles with the cell membrane leads to hole formation, membrane thinning and/or erosion, damage to the acidifying endosomal compartments by the proton sponge effect, followed by mitochondrial injury, increase of intracellular Ca^{2+} concentration, or membrane depolarization [92, 94, 141].

Effect of particle shape. Particle shape and aspect ratios are also key factors that determine the biological effect of NPs [5]. NPs have different shapes including spheres, rods, tubes, rings, and planes. Shape can influence the membrane warping process during endocytosis or phagocytosis and thus the internalization of NPs [140]. For instance, the endocytosis of spherical particles is found to be faster than rod-shaped NPs [179]. This is because rod-shaped NPs have a larger contact area with the cell membrane receptors than spherical particles when the longitudinal axis of the rods interacts with the receptors. Hence, the ends with high curvature at the half-cup stage of endocytosis are very likely to cause a higher membrane surface energy, resulting in a large distorting force that exceeds the maximum force provided by the actin polymerization [5]. Shape can also influence

biological effects of NPs [169, 180]. Silver NPs, for instance, were found to be more toxic as plates than spheres and wires [181].

Effect of surface coatings. By the incorporation of surface coatings, the toxic effects of NPs may be mitigated or eliminated [5]. For instance, a recent study compared toxic effects of uncoated and PVP- and citrate-coated silver NPs in macrophage and epithelial cells. They found that uncoated silver NPs are more toxic than coated NPs. Also, the toxicity mechanisms are coating-dependent; while coated silver NPs induce toxic effects through up-regulation of cytokines, uncoated NPs enhance oxidative stress in test cells [182]. Proper surface coatings can stabilize particles and avoid agglomeration. Coating is also an effective means of preventing the release of toxic ions [183]. However, coating-dependent biological effects of NPs are entangled. The steric hindrance of coatings can inhibit the cellular internalization of NPs, but some coatings can facilitate NP endocytosis [5]. Coatings modify the surface properties of NPs and subsequently impact intracellular distribution and the generation of ROS. Lastly, many coating materials are environmentally degradable and after exposure to acidic environments, they may shed or degrade and expose the core NP [5].

Effect of particle aggregation propensity or stability. Arguably, NP stability or aggregation is the crucial physicochemical property of NPs, as it influences most of the other properties, and thus has a great effect on biological effects of NPs [169, 184]. Obviously, aggregation increases the size of NPs. Also the surface charge of NPs are strongly affected by aggregation [185]. Aggregation also alters the shape and angle of curvature, and porosity and surface roughness of NPs. Additionally, the NP aggregation reduces the number concentration (a dose metric) of NPs to which the biological systems are exposed. Therefore, it is obvious that the aggregation of NPs plays a key role on their effects on biological systems.

NP aggregation is in turn determined by some physicochemical properties of NPs such as the particle size, shape, and surface charge. For instance, smaller particles

typically aggregate more than their large counterparts, and nanorods and fibres have been shown to aggregate more easily than spheres [186, 187]. The characteristic of medium including ionic strength, pH, temperature, and the presence of organic molecules also influences NP aggregation [188-190]. Aggregation is believed to be inevitable for the majority of the NPs in biological fluids [190]. Hence, it is crucial to examine the aggregation of nanomaterals when evaluating their biological effects.

The NP aggregation influences cellular uptake of NPs. However, the impact of aggregation is not very straightforward; compared to the uptake of primary particles, the aggregates show either enhanced or inhibited uptake [186, 187, 191]. This is consistent with the effect of particle size on the uptake. As discussed earlier, the effect of particle size on cellular uptake of NPs is complicated. Smaller particles do not necessarily lead to more efficient cellular uptake. This could be explained by different entry pathway of particles of different size into cell. Similarly, large aggregates do not enter the cell via the same mechanism as primary particles or small aggregates [191]. Moreover, the uptake pattern of aggregates and primary particles is cell-type dependent. For example, Albanese and Chan found that there was a 25% decrease in uptake of aggregates with HeLa and A549 cells in comparison to single NPs. However, there was a 2-fold increase in MDA-MB 435 cell uptake for the largest aggregates [190]. From available data, it cannot be concluded whether aggregates or primary particles are uptaken in a more efficient way. The extent of aggregation, the size of the aggregates, and the cellular uptake mechanism collectively determine the uptake rate of NPs. Obviously, the aggregation of NPs may influence the biological effect of NPs by altering the uptake behavior of NPs.

Similarly, the role of NPs' aggregation in their biological effects is not straightforward. For example, Taniguchi et al. shows that large TiO_2 aggregates had a greater toxic effect on cell viability and gene expression compared to small aggregates [192]. In contrast, other studies show reduced cytotoxicity for aggregates. Cui et al shows that large gold aggregates were nontoxic to HeLa and *E. coli* cells while small gold

aggregates and single NPs were toxic [193]. There is hence a huge need for understanding the aggregation propensity of NPs and the role of aggregation in their biological effects.

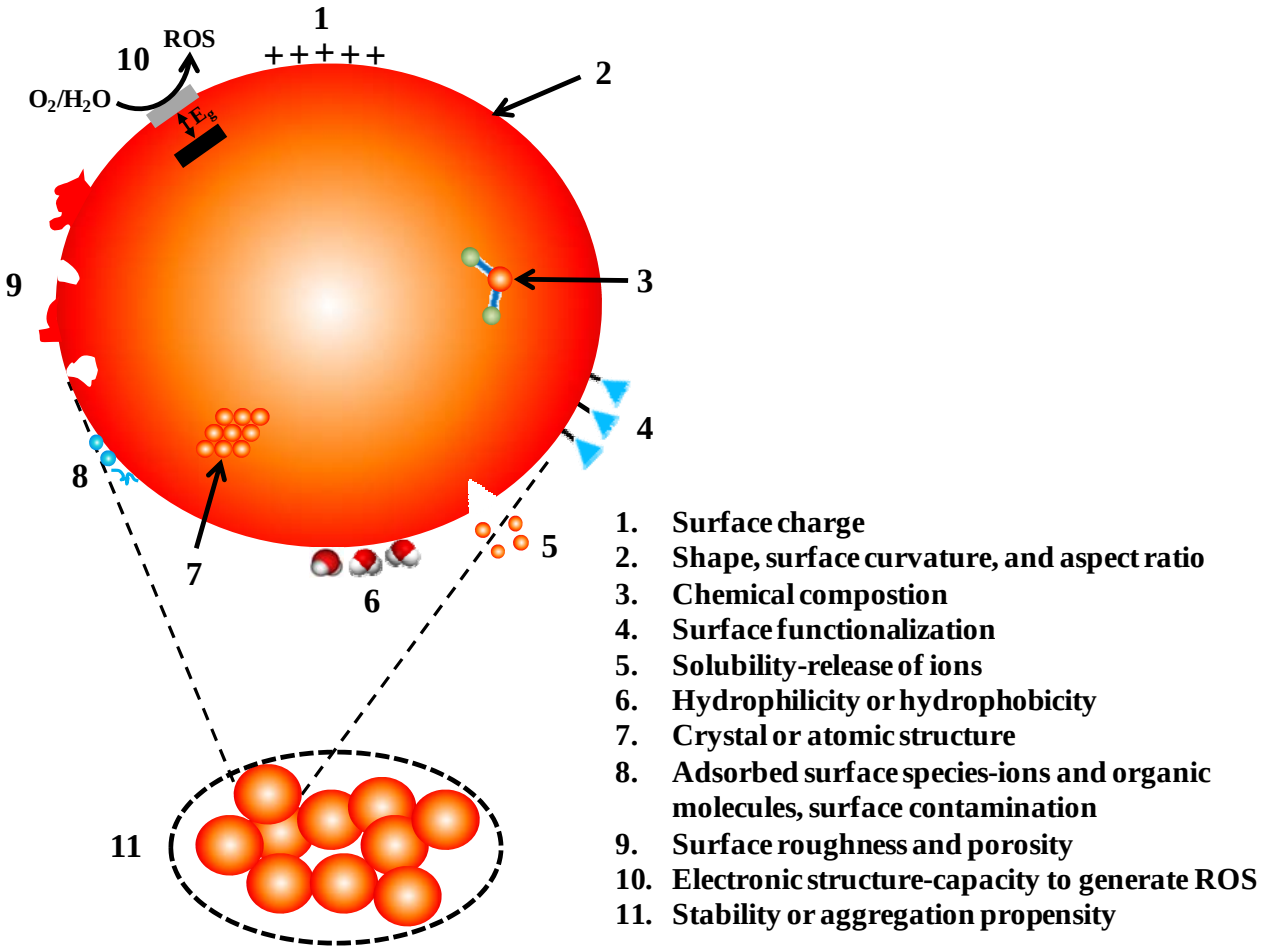

Figure 1.2. Physicochemical properties of NPs related to the biological effect of NPs

1.3. Why predictive models are important in evaluating the biological effect of NPs?

Toxicological tests of NPs are time consuming and expensive. A complete set of toxicological assays for a single chemical, including assessment of carcinogenicity, chronic, reproduction and developmental effects could involve hundreds of animals and costs in the range of $1–3 million per test [120, 194]. In the United States, it has been

estimated that the cost for testing existing NPs in 2009 ranges from $249 million to $1.18 billion and requires 34-53 years to complete the toxicological testing [195]. Obviously, these values will continue to increase as new NPs are introduced.

By using a predictive toxicology approach, it is possible to significantly reduce the cost and time required for evaluating the biological effect and risk of NPs. Scientists are developing models to predict the behavior and effects of NPs in biological systems [120, 194, 196-204], which would allow researchers to streamline the toxicological testing of NPs by prioritizing NPs that are most likely to be harmful. The predictive approach not only can supplement or replace some expensive and time-consuming assays, but also help and guide chemists and material scientists to design and manufacture safe NPs.

Quantitative structure–activity relationships, abbreviated as QSARs, are theoretical models that can be used to predict the physicochemical and biological properties of molecules [198, 204-207]. According to the QSAR paradigm, it is possible to interpolate the activity of chemical compounds from the molecular descriptors using a statistical model built on the experimental data on the activity of other compounds in the same group [207]. In recent years, the concept of "nano-QSAR" was proposed and raised many interests [198, 201, 204]. It is easy to conceive that nano-QSAR is the QSAR approach applied to NPs, i.e., using structural/physicochemical properties of NPs to predict their biological effects. For example, Puzyn et al. applied nano-QSAR to predict the toxicity of 17 different metal oxides NPs to *E. coli* cells. Their theoretical model along with experimental data was able to describe the relationship between NP structure and toxic effect to *E. coli* cells [198]. Sayes et al. used the QSAR method to develop mathematical models to predict cellular membrane damage resulting from several NP physicochemical features [199]. They found that the size, concentration and zeta potential of particles in ultra-pure aqueous medium are among the most influential factors on cytoplasm leaking [199].

However, nano-QSARs have some intrinsic or challenging limitations [202, 204]: (i) QSAR methodology was developed for small organic compounds with diverse structural

types while the size of NPs are large and structurally limited in diversity, (ii) experimental data accumulated for NPs are far from sufficient for fully assessing their biological effects and many data are even contradictory, and (iii) classical QSAR descriptors that are applicable for small organic compounds are generally not suitable for NPs. Essentially, nano-QSAR is an approach built on data mining techniques; it, however, does not take into account the underlying mechanisms leading to the biological effect of NPs.

We proposed an alternative "reductionism" approach for predictive modeling of the biological effect of NPs. Firstly, we identify the major mechanisms for the biological effects induced by NPs. Secondly, we develop predictive models for each mechanism. For instance, it is well known that NPs can induce gentoxicity by directly bind to DNA [127]. Towards this identified mechanism that results in toxic effects of NPs towards organisms, we can develop a model to predict the binding activity of NPs to DNA and further predict the genetic effects of NPs based on the physicochemical properties of NPs. Similarly, we can also develop predictive models for the other mechanisms such as the generation of ROS and membrane damage [208]. Lastly, we link and combine those discrete models into one "ultimate" model that takes into account multiple mechanisms and their interactions for predicting the biological effect of NPs.

1.4. Physicochemical interactions at nano-bio interfaces

The mechanisms for NPs to induce adverse biological effects can be briefly summarized as: (i) indirect adverse effects induced by ROS generated by NPs, (ii) indirect adverse effects induced by released toxic ions, and (iii) direct interactions with biological systems. Because this thesis will focus on the last mechanism, this section will discuss in depth the physicochemical interactions that occur at nano-bio interfaces, which ultimately lead to the adverse biological effects of NPs.

The nano-bio interface comprises the dynamic physicochemical interactions and kinetic and thermodynamic exchanges between the surface of NPs and the surface of biological components (*e.g.* membrane, DNA, protein, and organelles) [209, 210]. It is probably one of the most complex and the least understood interfacial systems. The characteristic and behavior of this interface depends on physicochemical properties of the NPs, the biological components, the surrounding medium, and most importantly any changes that occur because of mutual effects within the interfacial zone. In a given medium, the NP characteristics which predominantly determine the surface interactions include the material's chemical composition, surface charge, size and state of aggregation, shape and surface curvature, porosity and surface crystallinity, heterogeneity and roughness, hydrophobicity or hydrophilicity, and surface functionalization with charged groups or ligands [209, 210]. The most important properties of the biological components that govern the nano-bio interfacial interactions vary depending on the biomolecular moieties and their sequence, conformation, molecular charge distribution, molecular weight, and the configuration of the macromolecule and membranes or cells comprising them. Many of these properties are in turn determined by the characteristics of the suspending medium, including the pH, temperature, ionic strength, polarity, and the presence of large organic molecules. These media characteristics also govern important interfacial processes such as the adsorption of ions and organic molecules as well as the aggregation and dissolution of NPs. Indeed, it is the combined effect of the properties of NPs and biological components in the surrounding medium that shape the nano-bio interface [210].

The interactions at nano-bio interfaces are mediated and governed by large numbers of forces and molecular interactions [210]. This suggests that in order to predict the nanotxicity induced by the direct interactions of NPs with biological systems, we may develop models bricked with these forces and interactions. The forces comprise of van der Waals force, electrostatic interactions, steric interaction, polymer bridging

interactions, and depletion and hydration interactions [211]. Van der Waals force originates from the quantum mechanical dance of the electrons, the fluctuations of which produce dipoles in the object and then induce a dipole moment in the atoms of interacting objects (e.g. NPs and biological components) and cause an attractive force [212, 213]. Electrostatic interactions arise between charged surfaces across liquids. An electrical double layer develops near the charged surfaces in aqueous solutions. When two charged surfaces approach one another, the double layer overlaps and a repulsive force develops [212, 213]. Solvent interactions, including hydration and hydrophobic interactions, arise from the affinity of interacting surfaces for water molecules [211]. Steric interactions are caused by polymeric groups or ligands on the surface of NPs and/or biological components, which give rise to spring-like repulsive interactions at nano-bio interactions [211]. Polymer bridging interactions are also induced by surface polymeric groups or ligands, but they are attractive forces between oppositely charged moieties on two interacting surfaces [210]. Lastly, the hydrodynamic interactions are very long-ranged, originating from the convective drag, shear, lift forces in the fluid and Brownian diffusion [210]. The possible impacts of each force on the nano-bio interface are summarized in Table 1.2. By computing each force at the nano-bio interface and under the rule of additivity [210, 214], we can obtain a thorough depiction of the interface and may build predictive models for the toxic effects of NPs.

This dissertation will primarily focus on the characterization of direct nano-bio interactions and the assessment of subsequent biological implications. Considering the crucial role that NP aggregation plays in altering the physicochemical properties of NPs and determining the biological effect of NPs, this dissertation will firstly investigate the aggregation of NPs using both predictive modeling and experimental approaches. Then the nano-bio interactions leading to the adverse biological effects of NPs will be addressed. Chapter 2 will discuss in detail the objective and organization of this dissertation.

Table 1.2. Forces at nano-bio interfaces and their possible impact on the interface

Force	**Possible impact on the interface**
van der Waals (vdW) intractions	Universally attractive in aqueous media
Electrostatic interactions	Overlapping double layers are generally repulsive as most materials acquire negative charge in aqueous media, but can be attractive for oppositely charged materials
Solvent Interactions (Hydration and hydrophobic interactions)	Hydrophilic materials are thermodynamically stable in water and do not aggregate; Hydrophobic materials are spontaneously expelled from the bulk of the water and forced to aggregate
Steric interactions	Generally increase stability of individual particles but can interfere in cellular uptake, especially when surface polymers are highly water-soluble
Polymer bridging interactions	Generally promote aggregation or deposition, particularly when charge functionality is carboxylic acid and dispersed in aqueous media containing calcium ions
Hydrodynamic interactions	Increase the frequency of collisions between NPs and other surfaces responsible for transport

CHAPTER 2

RESEARCH OBJECTIVES

2.1. Research objectives

Among the mechanisms leading to the adverse biological effects of NPs discussed in Chapter 1, up to now, most efforts have been made and focused on the generation of ROS and oxidative stress, and toxic ion releases. In contrast, biological effects of NPs caused by direct nano-bio interactions is the least researched. This is largely because of the complexity and lack of suitable techniques for characterizing the nano-bio interface.

The overall goal of this dissertation is to gain better understanding of the nano-bio interactions leading to the adverse biological effect of NPs. Specifically, because the aggregation alters particle size and other physicochemical properties of NPs, the property of NPs reaching and interacting with cells is very likely different from that of what we feed initially. Consequently, as the first step, NP aggregation was investigated and models were developed for predicting the stability and the extent of aggregation of NPs. Then, nano-bio interactions including nano-cell membrane and nano-DNA interactions were investigated using novel modeling and experimental approaches particularly with the novel application of atomic force microscopy (AFM) in characterizing the nano-bio interface.

2.2. Organization of this dissertation

Chapter 1 briefly introduced the background of nanotechnology and why there are great needs for the understanding of biological effects of NPs. The mechanisms underlying the biological effect induced by NPs and the role of their physicochemical properties were reviewed. Due to the crucial role that NP aggregation plays in the biological effect of NPs, I specifically reviewed in detail the effect of aggregation on the

biological effect of NPs. Then I discussed the need of predictive models in the assessment of biological effects of NPs. I further discussed a possible approach for building predictive models of the biological effect induced by direct nano-bio interactions on the basis of physicochemical principles governing the nano-bio interface. Chapter 2 outlined the research objective, organization of the dissertation, and important contributions.

Chapter 3 investigated the aggregation of NPs (with CeO_2 as a model NP) in monovalent and divalent solutions. By combining extended Derjaguin–Landau–Verwey–Overbeek (EDLVO) with von Smoluchowski's population balance equation, I developed a novel NP aggregation kinetics model. The model gave much better predictions than conventional models based on DLVO theory.

Chapter 4 investigated the effect of natural organic matter (NOM) on the aggregation of CeO_2 NPs. The introduction of NOM complicates the aggregation system by bringing in additional interaction forces for depicting the aggregation of NPs. I incorporated the new forces including steric interaction and polymer bridging interaction forces into the EDLVO framework developed in Chapter 3 and built the first quantitative model for predicting the aggregation of NPs in the presence of NOM.

Chapter 5 studied the temperature effect on aggregation of CeO_2 NPs. Temperature was an important yet previously neglected factor that influences NP aggregation; this chapter filled the knowledge gap. The EDLVO theory was used to interpret the fundamentals of the temperature effect on NP aggregation. Furthermore, the kinetic model developed in Chapter 3 was used to predict the aggregation kinetics of CeO_2 NPs under different temperatures.

After characterizing and modeling the aggregation behavior of NPs, Chapter 6 investigated the direct nano-cell membrane interactions with seven different types of engineered metal oxide NPs as the model NPs and *Paramecium* as the model cell. The interaction energies between NPs and cell membrane were calculated according to the

DLVO theory, and a further correlation was established between the nano-cell membrane interaction and the toxicity of NPs.

Chapters 7-9 demonstrated systematic experimental approaches based on the single-molecular imaging technique, atomic force microscope (AFM), coupled with modeling computation to probe the nano-DNA interaction. Using quantum dots (QDs) as a model NP, I examined the binding mechanism, binding kinetics, binding isotherm, and binding specificity of QDs to DNA with the novel application of AFM. I further assessed the binding affinity of NPs for DNA by calculating their interaction energy on the basis of the DLVO models. The modeling results of binding affinity were validated by the NP/DNA binding images experimentally derived by AFM. The investigation of the relationship between the binding affinity of twelve NPs for DNA with their inhibition effects on DNA replication indicated that strong nano-DNA interactions lead to adverse genetic effects of NPs.

Chapter 10 summarized findings in the dissertation and recommended future research direction to advance the understanding of nano-bio interactions. In brief, future work to advance the understanding of nano-bio interactions may include the following crucial issues: (a) Identify the real nano-induced effects. (b) Investigate the internalization amount and pathway of NPs into cell. (c) Development of predictive models for other toxicity mechanisms of NPs. (d) Investigate the long term ecological and evolutionary consequences of NPs.

2.3. Originality and merit of research

The findings of this dissertation are original and aimed at achieving better understandings of nano-bio interactions. The most important message to deliver from this dissertation is to underscore the important role of direct nano-bio interactions in the biological effects of NPs, which is somewhat neglected by previous studies. Specifically,

the knowledge gained from this dissertation is dedicated to the advancement of NP implication research from the following four major aspects:

(1) Aggregation of NPs under various medium conditions;

(2) Nano-cell membrane interactions and resulting cytotoxicity;

(3) Development of novel approaches based on single-molecule imaging technique, AFM, to study nano-DNA interactions;

(4) Predictive modeling of the binding affinity of NPs for DNA and correlation with the genetic effect of NPs

CHAPTER 3

EFFECT OF MONOVALENT AND DIVALENT SALTS ON THE AGGREGATION OF NANOPARTICLES

3.1. Abstract

Aggregation of NPs is one of the most important processes that influence the environmental behavior and biological effects of NPs. This chapter investigates the effect of monovalent and divalent salts (KCl and $CaCl_2$) on the aggregation kinetics of NPs using time-resolved dynamic light scattering (TR-DLS). CeO_2 NPs were used as a model NP because of their extensive commercial applications. The initial hydrodynamic radius of CeO_2 NPs measured by DLS was approximately 95 nm. Attachment efficiencies were derived both from aggregation data and predictions based on the DLVO theory. The deviations of the DLVO predictions were corrected by employing the extended DLVO (EDLVO) theory. The critical coagulation concentration (CCC) of CeO_2 NPs at pH = 5.6 is approximately 34 mM for KCl and 9.5 mM for $CaCl_2$. Furthermore, based on the EDLVO theory and the von Smoluchowski's population balance equation, a model accounting for diffusion-limited aggregation (DLA) kinetics was established. For the reaction-limited aggregation (RLA) kinetics, a model that takes fractal geometry into account was established. The models fitted the experimental data well and proved to be useful for predicting the stability and the aggregation kinetics of CeO_2 NPs.

3.2. Introduction

The booming nanoscience and nanotechnology during recent years has demonstrated that nanotechnology will play a significant role in advancing the technologies of the 21st century in many sectors (e.g., pharmaceutical, energy, electronic

and textile) [215]. Engineered NPs probably will be released into the aquatic environment through manufacturing processes, waste disposal or product uses; however, insufficient research has examined the environmental behavior of NPs [46]. There are only limited data available on aggregation and deposition of NPs. Especially, theoretical analysis and quantitative models are insufficiently developed to quantify the environmental transport and fate of NPs [216].

Given the unique properties of NPs, they could constitute a new class of nonbiodegradable pollutants that aquatic organisms may uptake and food webs may transfer, and thus they could affect ecosystems and human health. It is imperative to evaluate the biological effect and risks of NPs to avoid repeating past environmental tragedies. Aggregation of NPs is arguably the most crucial process, as it influences most of the physicochemical properties of NPs, and thus has a great effect on the environmental behavior and toxicity of NPs [169, 184]. However, current understandings of the aggregation of NPs are still limited [217, 218].

In aquatic environments, solution chemistry strongly influences the aggregation process. Studies have shown that electrolytes promote the aggregation of NPs [219-222], which is widely interpreted by the Derjaguin-Landau-Verwey-Overbeek (DLVO) theory [212, 213]. As electrolyte concentrations increase, the repulsive electrostatic double layer interaction between particles becomes weaker, and the attractive van der Waals force prevails. However, much evidence indicates that DLVO theory is limited to describing particle aggregation qualitatively; a sizable discrepancy exists between theoretical predictions and experimental observations [223-226]. The EDLVO theory, which considers Lewis acid-base interactions in the total interaction energy, is gaining popularity due to its good agreement with experimental data [227-231].

Although the EDLVO theory can quantitatively predict the aggregation of NPs, it is not extensively employed in aggregation modeling studies, whereas the DLVO theory is still widely used. Specifically, particle collision efficiency, an important parameter in

von Smoluchowski's population balance equation, commonly is calculated by the DLVO theory [232-234]. Furthermore, two limiting regimes are distinguished in the aggregation process, the reaction-limited aggregation (RLA) and the diffusion-limited aggregation (DLA) regimes [235, 236]. DLA occurs when the collision efficiency between particles is close to unity, whereas RLA dominates at very low collision efficiencies [237]. The aggregation behavior in these two regimes is fundamentally different in both kinetics and aggregate structures, and thus they require different models.

The objective of this study is to investigate and model the aggregation kinetics of NPs in the presence of monovalent (KCl) and divalent ($CaCl_2$) electrolytes using time-resolved dynamic light scattering (TR-DLS). CeO_2 was used as a model NP due to their extensive commercial applications. For instance, they are used as a fuel additive to enhance combustion efficiency [238], a constituent of catalytic converters [239, 240], and an oxygen conductor in solid oxide fuel cells (SOFCs) [241-243]. The increasing applications will inevitably lead to CeO_2 release into the environment, which will impose risks on humans and ecosystems. Therefore, the Organization for Economic Co-operation and Development (OECD) has listed CeO_2 NPs as priority NPs for immediate testing [244252254254254254253] (List of Manufactured NPs and List of Endpoints for Phase One of the Sponsorship Programme for the Testing of Manufactured NPs: Revision. 2010).

The attachment efficiencies calculated from experimental data of the aggregation of CeO_2 NPs were compared with the DLVO and EDLVO theoretical predictions. In addition, we established aggregation models for DLA and RLA regimes to predict the aggregation kinetics on the basis of von Smoluchowski's population balance equation and EDLVO theory or of fractal geometry, respectively. Overall, this work enhances our knowledge of aggregation mechanisms of NPs in electrolyte solutions.

3.3. Modeling of NP aggregation

Von Smoluchowski's population balance equation describes the irreversible aggregation kinetics of particles [245] and is expressed as

$$\frac{dn_k}{dt} = \frac{1}{2}\sum_{i+j=k}\alpha\left(r_i,r_j\right)\beta\left(r_i,r_j\right)n_i n_j - n_k\sum_{i=1}\alpha\left(r_i,r_k\right)\beta\left(r_i,r_k\right)n_i \qquad (1)$$

where n_k (or n_i and n_j) is the number concentration of aggregates comprised of k (or i and j) primary particles (also called k-class or k-fold particles or aggregates), $\alpha\,(r_i,r_j)$ and $\beta\,(r_i,r_j)$ are the collision efficiency function and collision frequency function for class i and j particles, and r_i and r_j are the radii of class i and j particles.

For the same class of particles, $\beta\,(i,i)$ is equal to $8kT/3\mu$, where k is Boltzmann's constant (1.38×10^{-23} J/K), T is the absolute temperature (298 K), and μ is the viscosity of the solution (1×10^{-3} Pa·s). Taking into account the van der Waals forces and hydrodynamic interactions, the collision frequency rate is then expressed as [246, 247]:

$$\beta\left(i,i\right) = \frac{8kT}{3\mu}\left[2\int_0^\infty \lambda\left(u\right)\frac{\exp\left(V_A\left(h\right)/kT\right)}{\left(2+u\right)^2}du\right]^{-1} \qquad (2)$$

where $V_A\,(h)$ is the van der Waals attraction energy (kT); h is the surface-to-surface separation distance between two particles (nm); r is the particle radius (nm); $u=h/r$; and $\lambda\,(u)$ is the correction factor for the diffusion coefficient, which is related to the separation distance by the equation [248]:

$$\lambda\left(u\right) = \frac{6\left(u\right)^2+13\left(u\right)+2}{6\left(u\right)^2+4\left(u\right)} \qquad (3)$$

The collision efficiency α is the reciprocal of the stability ratio, which is defined as [220, 249]:

$$\alpha\left(i,i\right) = \left[\int_0^\infty \lambda\left(u\right)\frac{\exp\left(V_A\left(h\right)/kT\right)}{\left(2+u\right)^2}du\right]\times\left[\int_0^\infty \lambda\left(u\right)\frac{\exp\left(V_T\left(h\right)/kT\right)}{\left(2+u\right)^2}du\right]^{-1} \qquad (4)$$

where $V_T(h)$ is the total interaction energy between particles separated with a distance h. In classical DLVO theory, $V_T(h)$ is the sum of the van der Waals attraction energy $V_A(h)$ and the electrical repulsion energy $V_R(h)$. However, as discussed above, DLVO may not quantitatively explain experimental observations. The EDLVO theory adopted includes an additional term, Lewis acid-base interaction energy $V_{AB}(h)$, such that $V_T(h) = V_A(h) + V_R(h) + V_{AB}(h)$.

The interaction energies between two identical particles in a 1-1 electrolyte solution are expressed using Eq. (5a-e) [228, 232, 250, 251]:

$$V_A = -\frac{Aa}{12h\left(1+11.12h/\lambda_c\right)} \quad (5a)$$

$$V_R(h) = \frac{128\pi k_B T n \gamma_1 \gamma_2}{\kappa^2} \times \frac{r^2}{2r+h} \exp\left(-\kappa h\right) \quad (5b)$$

$$\gamma_i = \tanh\left(\frac{z_i e \psi_{Si}}{4kT}\right) \quad (5c)$$

$$\kappa^{-1} = \sqrt{\frac{\varepsilon\varepsilon_0 k_B T}{2N_A I e^2}} \quad (5d)$$

$$V_{AB}(h) = \pi r \lambda \Delta G_{h_0}^{AB} \exp\left(\frac{h_0 - h}{\lambda}\right) \quad (5e)$$

where A is the Hamaker constant and for CeO_2 a value of A of 5.57×10^{-20} J was obtained from [252]. a is the particle radius. h is the separation distance between the interacting surfaces. λ_c is the "characteristic wavelength" of the interaction, often assumed to be 100 nm [250]. n is the concentration of electrolytes. k_B is the Boltzmann constant, 1.38×10^{-23} J/K; T is absolute temperature, 298 K. z_i is the valency of the i^{th} ion. e is unit charge, 1.602×10^{-19} C. ψ_{Si} is the intrinsic constant surface potential (V) of the interacting particles in an aqueous medium. κ^{-1} is the Debye length (nm). ε_0 is the dielectric permittivity of a vacuum, 8.854×10^{-12} $CV^{-1}m^{-1}$. ε is the relative dielectric constant of water, 78.5; N_A is Avogadro's number, 6.02×10^{-23} mol^{-1}. I is the ionic strength (M), $I=0.5\cdot\Sigma c_i Z_i^2$, where c_i is

the molar concentration of one species of ions (*i*). λ is the correlation length, or decay length, of the molecules of the liquid medium (for pure water, this value is estimated to be 1 nm [228]); ΔG_{h0}^{AB} is the polar or acid-base free energy of interaction between particles at the distance h_0 [253], which is the minimum equilibrium distance due to Born repulsion, 0.157 nm [228].

In 2-1 electrolyte solutions, Eqs. (5b) and (5c) are replaced by Eqs. (5f) and (5g), respectively [224, 254]:

$$V_R(h) = \frac{384\pi k_B T n \gamma_1 \gamma_2}{\kappa^2} \times \frac{r^2}{2r+h} \exp(-\kappa h) \qquad (5f)$$

$$\gamma_i = \frac{3}{2} \frac{\left[2\exp\left(\frac{e\psi_{Si}}{kT}\right)/3 + 1/3\right]^{1/2} - 1}{\left[2\exp\left(\frac{e\psi_{Si}}{kT}\right)/3 + 1/3\right]^{1/2} + 1} \qquad (5g)$$

Going back to Eq. (1), we can write the change rate of number concentrations of each class of particles.

$$\begin{aligned}
\frac{dn_1}{dt} &= -\alpha_{11}\beta_{11}n_1^2 - \alpha_{12}\beta_{12}n_1n_2 - \alpha_{13}\beta_{13}n_1n_3 - \cdots \\
\frac{dn_2}{dt} &= \frac{1}{2}\alpha_{11}\beta_{11}n_1^2 - \alpha_{12}\beta_{12}n_1n_2 - \alpha_{22}\beta_{22}n_2^2 - \alpha_{23}\beta_{23}n_2n_3 - \cdots \\
\frac{dn_3}{dt} &= \alpha_{12}\beta_{12}n_1n_2 - \alpha_{13}\beta_{13}n_1n_3 - \alpha_{23}\beta_{23}n_2n_3 - \alpha_{33}\beta_{33}n_3^2 - \cdots \\
\frac{dn_4}{dt} &= \frac{1}{2}\alpha_{22}\beta_{22}n_2^2 + \alpha_{13}\beta_{13}n_1n_3 - \alpha_{14}\beta_{14}n_1n_4 - \alpha_{24}\beta_{24}n_2n_4 - \alpha_{34}\beta_{34}n_3n_4 - \cdots \\
&\vdots
\end{aligned} \qquad (6)$$

where α_{ij} and β_{ij} stand for $\alpha\,(i,j)$ and $\beta\,(i,j)$, respectively.

If the particle size distribution is not broad, e.g., the NP sizes differs by a factor of approximately two or less, it is safe to assume β_{ij} to be constant (β_{ii}) [246]. In the collision efficiency function α_{ij} approximation, the collision efficiency between two primary

particles (α_{11}) is used as a substitute under the assumption that only the two involved primary particles determine the interaction energy between aggregates (see Figure 3.1 for more illustrations) [232].

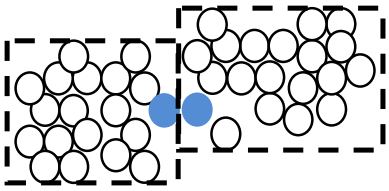

Figure 3.1. Two primary particles (blue) determine the interaction energy between the two large aggregates (marked by black dashed boxes).

Under above approximations, we summed the terms in Eq. (6) and obtained a simple Eq. (7), which showed the rate of change of the total particle concentration.

$$\frac{dn_{tot}}{dt} = -\frac{1}{2}\alpha_{11}\beta_{ii}{n_{tot}}^2 \qquad (7)$$

Replacing β_{ii} and α_{11} with Eqs. (2) and (4), respectively, we obtained the equation (8).

$$\frac{dn_{tot}}{dt} = -\frac{4kT}{3\mu}\left[2\int_0^\infty \lambda(u)\frac{\exp\left(V_T(h)/kT\right)}{(2+u)^2}du\right]^{-1}{n_{tot}}^2 \qquad (8)$$

We used a symbol "*w*" to represent the complex integration equation, and it is actually the classical expression of inverse stability ratio:

$$w = \left[2\int_0^\infty \lambda(u)\frac{\exp\left(V_T(h)/kT\right)}{(2+u)^2}du\right]^{-1} \qquad (9)$$

$$\frac{dn_{tot}}{dt} = -\frac{4kTw}{3\mu}{n_{tot}}^2 \qquad (10)$$

Solving Eq. (10) yields:

$$n_{tot} = \frac{n_0}{1+4kTwn_0t/3\mu} \qquad (11)$$

where n_{tot} is the total number concentration of various classes of particles, and n_0 is the initial number concentration of primary particles.

The structures of aggregates have been recognized to be fractal and can be described as $n \propto r^{-dF}$ or $n = c \cdot r^{-dF}$, where n is the number of aggregates, r is the radius of aggregates, d_F is the fractal dimension [235, 236] and c is a constant. Thus, Eq. (11) can be rewritten as Eqs. (12a-e):

$$c \cdot r^{-d_F} = \frac{c \cdot a^{-d_F}}{1 + 4kTwn_0 t / 3\mu} \qquad (12a)$$

$$r^{-d_F} = \frac{a^{-d_F}}{1 + 4kTwn_0 t / 3\mu} \qquad (12b)$$

$$\log r^{-d_F} = \log a^{-d_F} - \log\left(1 + 4kTwn_0 t / 3\mu\right) \qquad (12c)$$

$$-d_F \log r = -d_F \log a - \log\left(1 + 4kTwn_0 t / 3\mu\right) \qquad (12d)$$

$$\log r = \frac{1}{d_F} \log\left(1 + \frac{4kT}{3\mu} wn_0 t\right) + \log a \qquad (12e)$$

where a is the radius of the primary particles. The k, T, n_0, μ, and a are constants; and w can be calculated using EDLVO theory.

The aggregation kinetics in Eq. (12e) can be used to describe the growth of the aggregate radius over time. However, this equation can be applied only in regimes where the collision efficiency is relatively high or close to unity (i.e., in the DLA regime). In the RLA regime and at other conditions with very low collision efficiencies, a rigorous expression does not exist because the collision efficiency is determined by the aggregate structure in addition to the interaction forces [237, 255]. In such regimes, a large number of collisions are required to achieve a successful aggregation, and the aggregates explore many possible mutual configurations before they stick together firmly. The aggregation rate coefficient in RLA (K_{RLA}) is then directly proportional to the volume of the phase space V_c, over which the center of one aggregate can be positioned to reach a bondable

contact with another aggregate [255]. For two solid spheres with similar radii ($r_1 \approx r_2$ and both are equal to *r), V_c is* proportional to r^2. V_c is expected to be larger for fractal aggregates with similar radii than for solid spheres because the surfaces of the former are rough. In the RLA regime, it is proposed that $V_c \propto r^{dF}$ [255].

Therefore, for two fractal aggregates with similar radii, the aggregation rate coefficient is given by $K_{RLA} \propto V_c \propto r^{dF}$. Combining this expression with $n_{tot} \propto r^{-dF}$ yields Eq. (13):

$$K_{RLA}=k_{RLA}n_{tot}^{-1} \qquad (13)$$

where k_{RLA} is the rate constant.

Eq. (13) is then substituted into the reduced von Smoluchowski's population balance, Eq. (7), which yields

$$\frac{dn_{tot}}{dt} = -k_{RLA}n_{tot} \qquad (14)$$

Thus, the aggregation kinetics equation for RLA (r vs. t) is as follows:

$$n_{tot} = n_0 \exp\left(-k_{RLA}t\right) \qquad (15)$$

$$\log r = \frac{2.303k_{RLA}}{d_F}t + \log a \qquad (16)$$

3.4. Materials and Methods

3.4.1. Materials

CeO_2 NP suspension was purchased from Sigma Aldrich. The pH of the stock suspension was 4.5 as measured by pH meter (Accumet model 15, Fisher Scientific). The concentration of the stock suspension was 50 g/L, and for the aggregation experiments, 10 mg/L dilutions were made with 18 MΩ deionized (DI) water unless otherwise indicated.

3.4.2. Characterization of CeO_2 NPs

The morphology, particle size distribution (PSD), and zeta potential of CeO_2 NPs were determined. Morphology was examined in liquid by atomic force microscopy (AFM). In each experiment, 10 μL of the liquid suspension was left on a clean silicon wafer for 15 min, and the silicon substrate was thoroughly rinsed with deionized water to remove weakly sorbed particles. The substrate was subsequently fixed on the AFM sample plate, and a liquid cell (Agilent, Santa Clara, CA) enabled the imaging in deionized water. Silicon nitride probes coated with gold/chromium (SiNi, BudgetSensors, Bulgaria) were used. The sample was analyzed on an Agilent 5500 Molecular Imaging AFM in acoustic alternating current (AAC) mode with a scanning speed of 2 μm/s, an AC frequency of 56.72 kHz, and a setpoint amplitude of 3.17 V.

PSD was determined on a Zetasizer Nano ZS instrument (Malvern Instruments) using 1.5 mL CeO_2 solution in a clean vial. The light scattering detector was positioned at a scattering angle of 173° from the incident laser beam, and the autocorrelation function automatically accumulated for at least 10 runs for each sample.

Zeta potentials were measured for a range of pH and salt concentrations with the Zetasizer Nano ZS instrument. Acid/base and salt solutions were added immediately prior to zeta-potential measurements. At least four measurements were made for each condition.

3.4.3. Aggregation kinetics

The aggregation kinetics of CeO_2 NPs was investigated using TR-DLS experiments. For each measurement, 1.5 mL of the dilution was added to a new vial, which was placed in the DLS instrument. A premeasured amount of electrolytes was added into the vial, and DLS measurements started immediately. The measurements were performed for at least 1 h for each sample, and hydrodynamic radius was monitored and recorded.

3.5. Results and Discussion

3.5.1. Characteristics of CeO_2 NPs

AFM imaging of the CeO_2 NPs (the inset in Figure 3.2) shows that most of them were close to spherical in shape. The hydrodynamic radius of a single CeO_2 NP was within the range of 40 to 100 nm. The PSD diagram of CeO_2 NPs (Figure 3.1) shows that the size distribution was narrow with a low polydispersivity index (PDI) value. The mean initial hydrodynamic radius of CeO_2 NPs was approximately 95 nm, which was in the range that determined by AFM in-liquid imaging.

The zeta potentials of CeO_2 NPs as a function of pH and salt concentrations are presented in Figure 3.2b-c. As the solution shifted from acidic to basic, zeta potentials changed from positive to negative. The pH at the zero point of charge (pH_{ZPC}) was approximately 7.6, at which CeO_2 NPs were nearly neutral and highly unstable. In the aggregation experiments, pH was approximately 5.6, and thus CeO_2 NPs were positively charged and were supposed to be resistant to aggregation due to electrostatic repulsion. Increasing the monovalent and divalent electrolyte concentrations screened the electrostatic double layer and promoted aggregation.

The dashed lines and corresponding equations in Figure 3.2c show that the zeta potentials of CeO_2 NPs vary linearly with the logarithm electrolyte concentration (ζ vs. log C). This is commonly observed and consistent with previous studies [256-258]. The linear relation between ζ and log C can be used to estimate zeta potentials in an appropriate range of electrolyte concentrations.

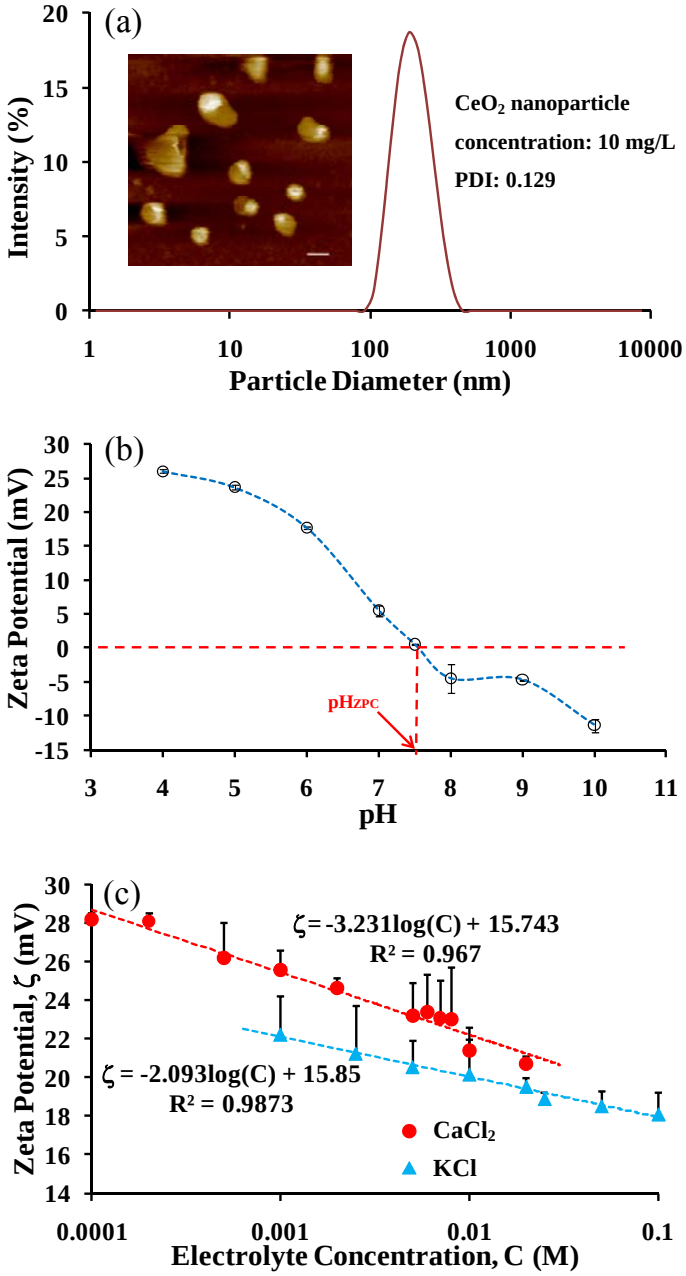

Figure 3.2. Characterization of CeO_2 NPs. (a) Particle size distribution of 10 mg/L CeO_2 NPs in DI water. The inset in (a) is an AFM image of CeO_2 NPs. The white bar is equal to 100 nm. (b) The zeta potential of CeO_2 NPs varies with pH in 0.001M KCl solution. (c) Zeta potential of CeO_2 NPs in monovalent and divalent electrolytes (pH 5.6). The dashed lines and corresponding equations in (c) show the linear fit to the experimental data points for zeta potential vs. log C.

3.5.2. Aggregation kinetics and analysis with DLVO and EDLVO theories

The aggregation kinetics of CeO_2 NPs was investigated with addition of KCl at concentrations of 0.001-0.25M and $CaCl_2$ at concentrations of 0.003-0.05M. Figure 3.3 present the aggregation curves. Distinct DLA and RLA regimes were observed in both monovalent and divalent electrolytes, and CeO_2 NPs exhibited different aggregation kinetics in the two regimes.

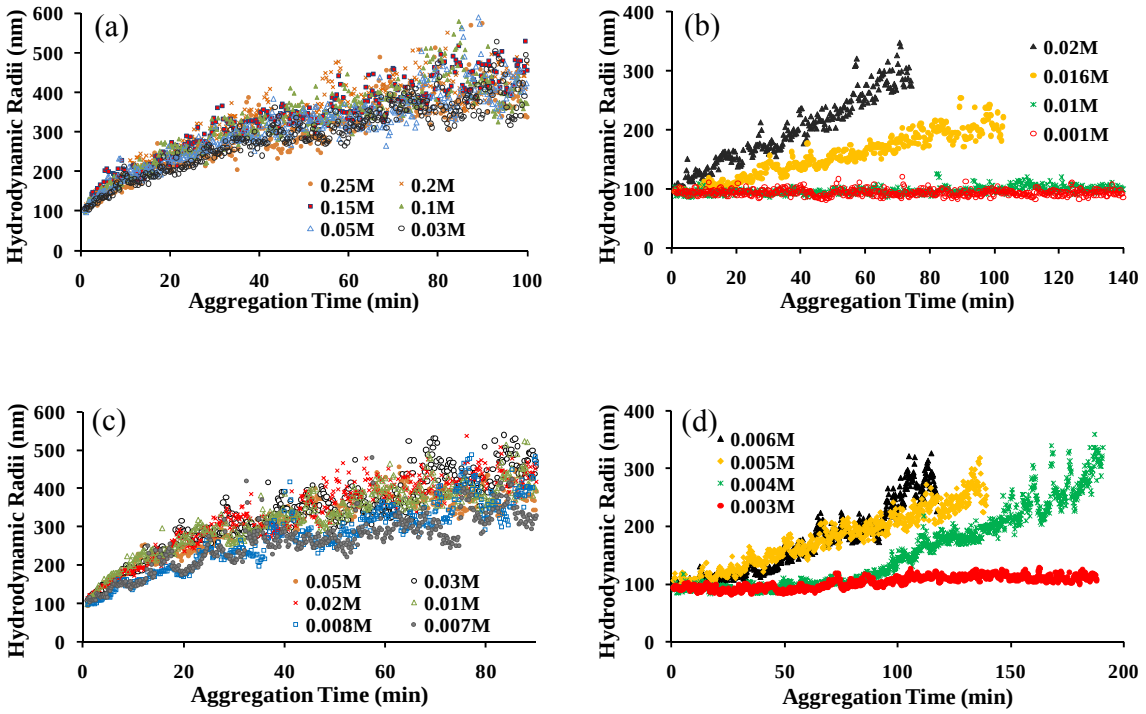

Figure 3.3. Aggregation kinetics of CeO_2 NPs in monovalent electrolyte (KCl) solution in the (a) DLA regime and (b) RLA regime, and in divalent electrolyte ($CaCl_2$) solution in the (c) DLA and intermediate regimes and (d) RLA regime.

The initial slopes of the aggregation curves were taken from the starting point (primary radius, a) to the point at which the hydrodynamic radius reaches 1.3 fold of a [219, 259]. The attachment efficiencies (α), or inverse stability ratios ($1/W$), were calculated by normalizing the slopes with those obtained in the DLA regime. Figure 3.4 shows that attachment efficiencies vary with KCl and $CaCl_2$ concentrations. According to DLVO

and EDLVO theories, as the salt concentration increases, the electrostatic energy barrier is reduced (see Figure 3.5), which promotes aggregation so that the attachment efficiency gradually increases. as the salt concentration reaches the critical coagulation concentration (CCC), the energy barrier is completely eliminated, and the attachment efficiency is close to unity, from which the aggregation falls into in the DLA regime.

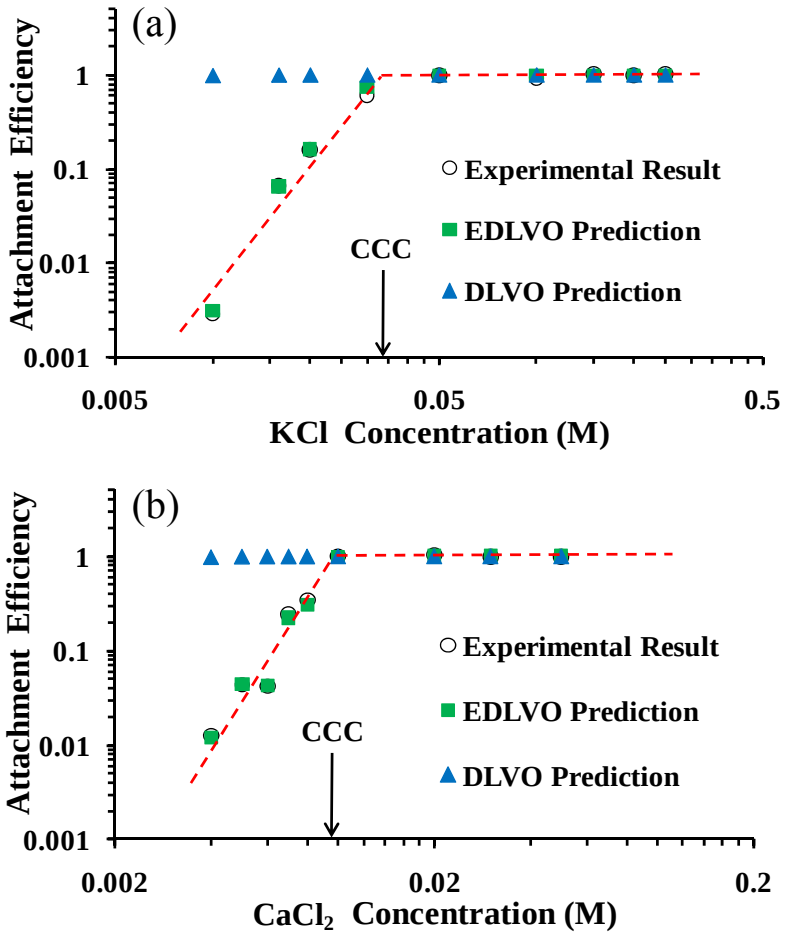

Figure 3.4. Attachment efficiencies (or inverse stability ratios) derived from experimental data and DLVO and EDLVO theories, as a function of (a) KCl concentration at pH 5.6 and (b) $CaCl_2$ concentration at pH 5.6. The CCCs based on the experimental data are approximately 34 mM KCl and 9.5 mM $CaCl_2$. The dashed lines are a guide to the eye.

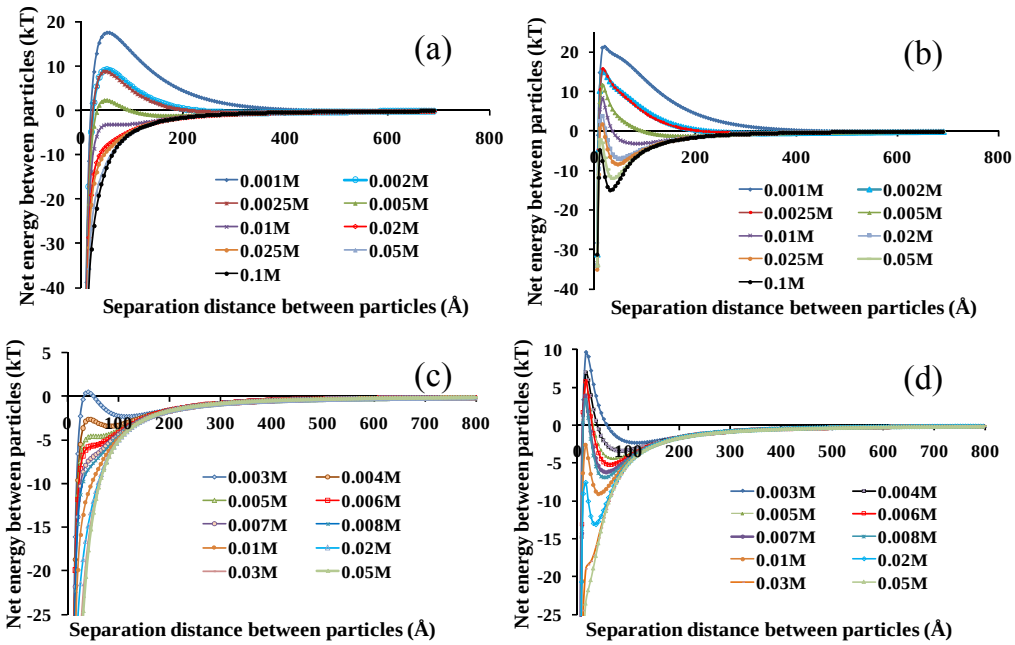

Figure 3.5. Interaction energy between CeO_2 NPs under different KCl concentrations as calculated from (a) DLVO and (b) EDLVO theory, and under different $CaCl_2$ concentrations as calculated from (c) DLVO and (d) EDLVO theory.

The CCC, at which the energy barrier is just eliminated, can be obtained from the intersection of the lines extrapolated from the experimentally derived aggregation regimes. For CeO_2 NPs, the CCC was approximately 34 mM for KCl and 9.5 mM for $CaCl_2$. At pH 5.6, the CeO_2 NPs were positively charged, and the Cl^- ions were counterions, but the CCC for KCl was more than twice that for $CaCl_2$. Because Ca^{2+} cations are unlikely to be adsorbed to the particle's positive surface and unlikely to act as bridges between particles, the effect of valence on Debye length could be the explanation [260]. As valence increases, the inverse of the Debye length increases, which results in lower repulsive electrostatic energy that likely promotes aggregation.

The attachment efficiency can also be determined theoretically with DLVO. The Hamaker constant of 5.57×10^{-20} J for CeO_2 was employed in the DLVO calculation [252]. Using Eqs. (3-5), the attachment efficiencies in various electrolyte solutions were calculated and then compared with those derived from experimental data (Figure 3.4).

The predicted attachment efficiency reached 1 at lower salt concentrations than did the attachment efficiency obtained from experiments, which was once observed in previous aggregation studies [220, 223]. This could be caused by inherent limitations of the DLVO theory (i.e., lack of consideration of non-DLVO interactions). Because CeO_2 NPs have hydrophilic surfaces, the AB interactions produce hydration repulsion [261] such that the adsorbed water clusters around particle surfaces repulse approaching particles [230]. The total repulsive effects then arise from both electrostatic and AB interactions, and the repulsive energy barrier is higher than that caused by electrostatic repulsion alone. Higher electrolyte concentrations are thus required to eliminate the energy barrier. Therefore, we also employed EDLVO to determine the attachment efficiencies. Because no literature value for ΔG_{h0}^{AB} could be found, we fit the experimental data with ΔG_{h0}^{AB} as the only fitting parameter. The EDLVO theory predictions yielded an excellent fit to the experimental data (Figure 3.4). For KCl, the fitted value of ΔG_{h0}^{AB} was 1.9 mJ/m^2, and for $CaCl_2$, ΔG_{h0}^{AB} was 1.5 mJ/m^2. The two values are similar and compare well with those of other metal oxides [262, 263]. The ΔG_{h0}^{AB} value for $CaCl_2$ is slightly smaller than that for KCl, probably because the same characteristic decay length (λ = 1 nm) was assumed when calculating the AB force under these two electrolytes. Actually, electrolytes may affect the decay length [264-267]; nevertheless, precise values for decay lengths are too difficult to identify [266], and therefore we used the same value, i.e., 1 nm as suggested previously [230].

3.5.3. Aggregation model

Eq. (12e) was used to model the aggregation kinetics of CeO_2 NPs in the DLA regime. The fractal dimension d_F was the only fitting parameter. A plot of *log r* vs. $log\ (1+4kTwn_0t/3\mu)$ is shown in Figure 3.6a-b, and the experimental data points were fitted with the linear least squares method. The inset table of Figure 3.6a-b contains the fitting parameters. In the model, the d_F values were the inverses of the slopes and were

calculated to be approximately 1.8 in both KCl and $CaCl_2$ solutions. This is congruent with the commonly acknowledged d_F value for the DLA regime [235, 236, 268, 269], which apparently validated our model.

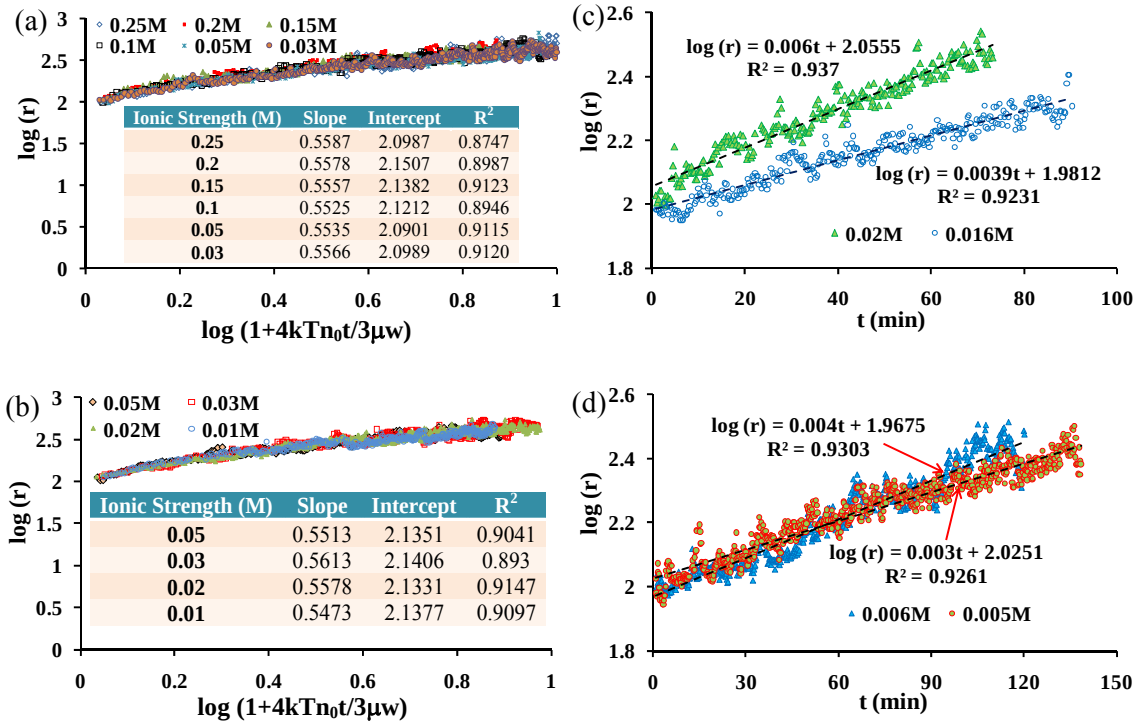

Figure 3.6. Aggregation kinetics models (referring to Eqs. (1) and (3)) fitting the aggregation data of CeO_2 NPs in the DLA regime in (a) KCl solution and (b) $CaCl_2$ solution, and in the RLA regime in (c) KCl solution and (d) $CaCl_2$ solution. The insets in (a) and (b) show the linear fit parameters for the experimental data (log r vs. log ($1+4kTwn_0t/3\mu$)). The dashed lines and corresponding equations in (c) and (d) show the linear fit to the experimental data points.

An intermediate aggregation regime exists between the DLA and RLA regimes (Figure 3.3c); specifically, the aggregation of CeO_2 in 0.008 M and 0.007 M $CaCl_2$ solutions resulted in attachment efficiencies between 0.2 and 0.4. Aggregation kinetics in these solutions could not be described well with either the DLA or RLA model

established in this paper. However, the power-law growth of hydrodynamic radii (i.e., the linear relationship of *log r* vs. *log (1+4kTwn$_0$t/3μ)*) remains valid for the intermediate aggregation regime (as shown in Figure 3.7), which is consistent with previous studies [268]. A correction factor (*f*), which accounts for the aggregate structure effect, is thus needed to model the aggregation kinetics in the intermediate regime, and Eq. (12e) is rewritten as follows:

$$\log r = \frac{f}{d_F}\log\left(1+\frac{4kT}{3\mu}wn_0t\right)+\log a \qquad (4)$$

In our case, the *f* value was approximately 1.6 to yield the best fit to the experimental data.

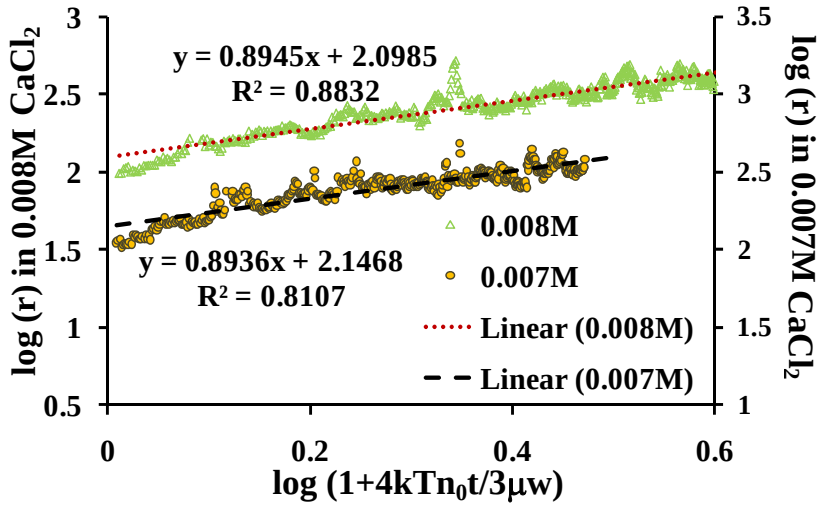

Figure 3.7. Aggregation kinetics model fitting the aggregation data for CeO_2 NPs in the intermediate aggregation regime in 0.008M and 0.007M $CaCl_2$ solution. The dashed lines and corresponding equations show linear fits to the experimental data points.

Eq. (16) was employed to simulate the aggregation kinetics of CeO_2 NPs in the RLA regime. The plot of *log r* vs. *t* was fitted with the linear least squares method (presented in Figure 3.6c-d). The correlation coefficients (R^2) that were 0.8~0.9 indicating that the model could explain at least 80% of the variance of the experimental data. For both KCl and $CaCl_2$ solutions, the aggregation rate constant k_{RLA} was larger in

high concentration solutions. The fractal dimension d_F, which is generally known to be 2.1 in RLA, could not be determined in our model, because k_{RLA} was also unknown, which is dependent on ion species, ionic strength, NP properties, etc. However, by means of AFM, CeO_2 aggregates formed in the DLA and RLA regimes were imaged and presented in Figure 3.8. The aggregates in the RLA regime had a more compact structure [268, 270], indicating a larger fractal dimension value. Assuming that d_F is equal to 2.1, k_{RLA} can be obtained for each case and ranges from 0.0027 to 0.0055.

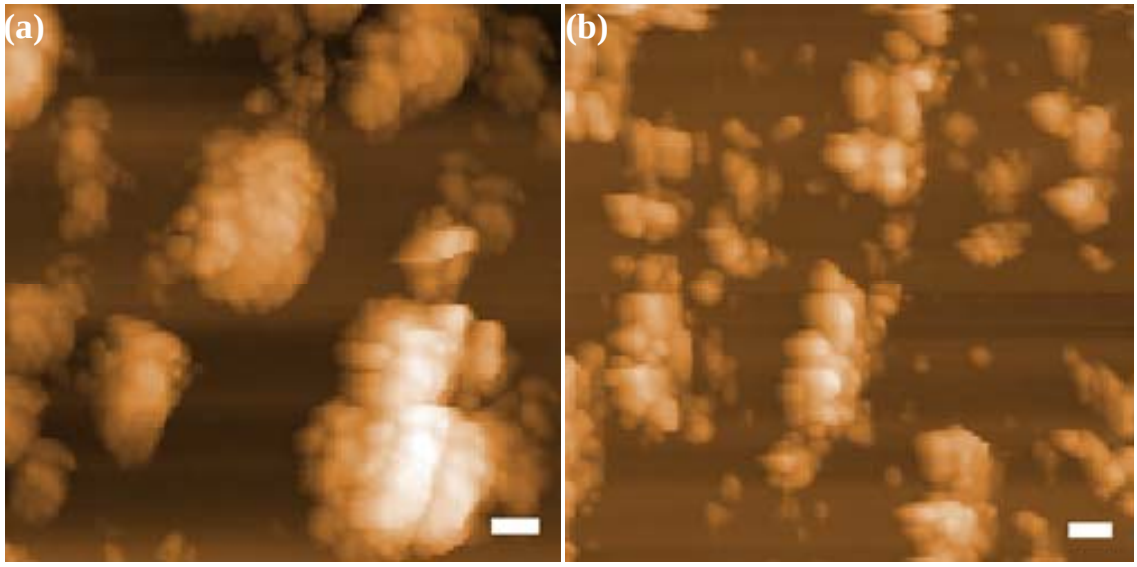

Figure 3.8. AFM images of CeO_2 aggregates formed in the (a) RLA and (b) DLA regimes. White scale bars are equal to 50 nm. The aggregates in RLA have a more compact structure than those in DLA, indicating that the fractal dimension of CeO_2 aggregates is larger in the RLA regime.

The models were then used to predict the aggregation kinetics of CeO_2 NPs in the DLA and RLA regimes in both KCl and $CaCl_2$ solutions. As discussed above, k_{RLA} values in the RLA regime were unknown, so we assumed that they are proportional to the salt concentration. The model predictions and experimental data were in good agreement (presented in Figure 3.7).

3.6. Conclusions

- The EDLVO theory overcame the discrepancy existing between the DLVO theoretical prediction and experimental observations of NP aggregation.
- At pH 5.6, the critical coagulation concentration (CCC) of CeO_2 NPs was approximately 34 mM for KCl and 9.5 mM for $CaCl_2$.
- The ELDVO-based DLA model agreed with the experimental data well in the diffusion limited aggregation regime. The RLA model, which considered fractal geometry of aggregates, also yielded good fitting results.
- More efforts are required to improve the models especially in the RLA and intermediate aggregation regimes. In particular, we need to determine accurate f and k_{RLA} values to obtain better predictions.

CHAPTER 4

EFFECT OF NATURAL ORGANIC MATTER ON THE AGGREGATION OF NANOPARTICLES

4.1. Abstract

This chapter investigates the effect of natural organic matter (NOM) on the aggregation kinetics of NPs using time-resolved dynamic light scattering. CeO_2 was used as a model NP and humic acid (HA) was used as a model NOM. In KCl solutions, regardless of their concentration, HA drastically reduces the aggregation kinetics of CeO_2 NPs. However, the effect of HA was more complicated in $CaCl_2$ solutions. At low $CaCl_2$ concentrations, HA inhibited NP aggregation, whereas at high $CaCl_2$ concentrations, HA promoted aggregation. The critical coagulation concentration (CCC) in KCl in the absence of HA is approximately 36.5 mM. In presence of both 1 ppm and 10 ppm HA in KCl solutions, extremely low aggregation kinetics were observed even at very high KCl concentrations (500 mM), implying KCl-CCCs in presence of HA were larger than 500 mM. The CCCs under conditions of no HA, 1 ppm HA and 10 ppm HA in $CaCl_2$ solutions are approximately 9.5, 8.0 and 12.0 mM, respectively. These observations were analyzed in the framework of extended Derjaguin-Landau-Verwey-Overbeek (EDLVO) theory. Moreover, a kinetic model was used to predict the aggregation kinetics of CeO_2 NPs. The model predictions are in close agreement with experimental observations. To the best of our knowledge, this work is the first to model quantitatively the aggregation of NPs in the presence of natural organic matter.

4.2. Introduction

NOM such as humic acid (HA) and fulvic acids is ubiquitous in natural environments, and a more realistic investigation of NP aggregation may need to involve the NOM in the system. In solutions containing monovalent electrolytes (e.g., KCl and NaCl), HA probably increases the stability of NPs regardless of the ionic strength [221]. However, aggregation becomes remarkably complicated in the presence of Ca^{2+} [219, 221], which is the predominant ion in groundwater and river water samples [271]. For example, HA stabilized C_{60} NPs at low $CaCl_2$ concentrations, whereas it enhanced C_{60} aggregation at high $CaCl_2$ concentrations [221]. NOM is expected to adsorb onto the NP surface, which alters the physicochemical properties of NPs and thus the interfacial forces/energies between them. It has been suggested that NOM might introduce a steric force [211] and a bridging force [272, 273] as well as perturb vdW attraction, EL repulsion and AB interaction [273]. Consequently, non-DLVO forces must be incorporated in a precise theoretical analysis of NP interaction and a quantitative description of the aggregation process. This analysis is known as the extended DLVO theory (EDLVO or XDLVO) approach [230], which provides a more solid theoretical basis. However, to the best of our knowledge, few published studies employ the EDLVO approach to model the aggregation of NPs theoretically.

CeO_2 NP was used as a model NP in this study because it has many commercial applications [76, 239, 241] and thus is very likely to be released into the environment. The Organization for Economic Co-operation and Development (OECD) has listed CeO_2 NPs as one of priority NPs for immediate testing [244]. We investigated the effect of Suwannee River HA on the aggregation of CeO_2 NPs in KCl and $CaCl_2$ using time-resolved dynamic light scattering (TR-DLS). The aggregation tendency or attachment efficiency was derived from experimental results. Moreover, a kinetic model combining EDLVO theory and von Smoluchowski's population balance equation was used to predict the aggregation kinetics of CeO_2 NPs, which were then compared with experimental data. To

the best of our knowledge, this study is the first to model quantitatively the aggregation kinetics of NPs in the presence of NOM.

4.3. Materials and methods

4.3.1. Materials

CeO_2 NP suspension with a nominal size of 25 nm was purchased from Sigma Aldrich. The atomic compositions of the sample were verified by X-ray diffraction technique (data not shown here). The pH of the stock suspension was 4.5 as measured by pH meter (Accumet model 15, Fisher Scientific). The concentration of the stock suspension was 109.5 g/L, and for the aggregation experiments, 10 mg/L dilutions were made with 18 MΩ deionized (DI) water unless otherwise indicated. KCl and $CaCl_2$ stock solutions were prepared using ACS reagent-grade chemicals and were filtered through 0.02-μm filters before use. The Suwannee River Humic Acid (SRHA or HA) (standard II, 2S101H, International Humic Substances Society) solution was prepared by dissolving 100 mg SRHA standard II in 250 mL DI water; the solution was then filtered through 0.4-μm membrane filters that were pre-dried at 60°C in an oven overnight. The membrane filters were dried under the same conditions after use. The final HA concentration was determined by the filter weight difference. The HA solution was stored in the dark at 4°C. Primary properties of SRHA, such as the molecular weight (range of 1–5 kDa) and composition, have been reported elsewhere [274].

4.3.2. Characterization of CeO_2 NPs

The morphology of CeO_2 NPs was determined by transmission electron microscopy (TEM). Samples were prepared by depositing 5 μL of CeO_2 NP suspension on a copper grid (400-mesh size) coated with carbon film (Ted Pella, Redding, CA). A Philips EM420 model TEM was operated at an accelerating voltage of 210 kV to acquire images. Particle size distribution (PSD) was obtained using DLS on a Zetasizer Nano ZS

instrument (Malvern Instruments). In brief, 1.5 mL of CeO_2 NP suspension was injected into a clean cuvette, and the DLS instrument was then operated with a scattering angle of 173° from the incident laser beam, and the autocorrelation function automatically accumulated at least 10 runs for each sample. The electrophoretic mobilities (EPMs) of CeO_2 NPs were measured for a range of K^+ and Ca^{2+} concentrations in the presence and absence of HA using the Zetasizer Nano ZS instrument. At least four parallel measurements were made for each condition. To minimize the interference of aggregation, measurements began immediately after the desired conditions were achieved.

4.3.3. Aggregation kinetics

The aggregation kinetics experiments were carried out at pH 5.7, at which the CeO_2 NPs are stable for at least 24 h. The pH values of the CeO_2 NP, KCl, $CaCl_2$ and HA solutions were pre-adjusted to 5.7 to ensure that each measurement could start immediately after addition of K^+, Ca^{2+} and HA. For the aggregation experiments in the absence of HA, a premeasured amount of KCl or $CaCl_2$ was added to 1 mL of CeO_2 NP suspension in a cuvette. The NP suspension was then shaken slightly and placed in the Zetasizer. For the experiment in the presence of HA, a premeasured amount of HA stock solution was added to the NP suspension along with the KCl or $CaCl_2$. The effect of HA concentration was investigated with two concentrations, 1 ppm and 10 ppm.

4.3.4. Modeling the aggregation kinetics

The adsorption of HA alters the physicochemical properties of the CeO_2 NP surface by introducing steric and bridging forces as well as by perturbing vdW attraction, EL repulsion and AB interaction [273]. The vdW attraction is affected because HA adsorption alters the particle size and the Hamaker constant [266]. The HA layer also alters the surface charge density, or surface potential, of NPs, which further affects the EL repulsion [254]. In addition, HA adsorption alters the surface electron-acceptor or electron-

donor properties, which changes the AB interaction [230]. The total interaction energy (V_T) between HA-coated particles is computed by assuming that each force acts individually and is thus additive: $V_T = V_{vdW} + V_{EL} + V_{HA} + V_{AB}$. Detailed computation methods for each interaction energy are presented below.

The vdW attractive energy (V_{vdW}) between two identical spherical particles can be computed using Eq. (1), which incorporates the retardation effect [275]:

$$V_{VdW}(h) = -\frac{Ar}{12h(1+11.12h/\lambda_c)} \qquad (1)$$

where A is the Hamaker constant for CeO_2 in water; a value of 5.57×10^{-20} J is obtained from ref [252]. r is the particle radius. h is the separation distance between the interacting surfaces. λ_c is the "characteristic wavelength" of the interaction, which is often assumed to be 100 nm [250]. For HA-coated NPs, the Hamaker constant is calculated to be 6.6×10^{-21} J as below, which is approximately eight times lower than that between bare particles.

For particles 1 in a medium consisting of material 2, the Hamaker constant is denoted as A_{121}. A_{11} and A_{22} are used to denote the Hamaker constants of materials 1 and 2 in a vacuum. Eq. (2) has been proposed as an approximation of A_{121} [276, 277]. The Hamaker constant for water in vacuum (A_{22}) is 3.7×10^{-20} J [266, 278]. However, the Hamaker constant for HA (A_{11}) cannot be found in the literature, and an estimate must be made. Because most reported Hamaker constants for soft polymers are within the range of 4×10^{-20}–11×10^{-20} J [276, 279], we estimated A_{11} to be 7.5×10^{-20} J. Consequently, A_{121} is calculated to be 6.6×10^{-21} J.

$$A_{121} \approx \left(\sqrt{A_{11}} - \sqrt{A_{12}}\right)^2 \qquad (2)$$

The EL repulsive energy (V_{EL}) between two identical spheres of radii r in 1-1 electrolyte solutions (e.g., KCl) is given by Eqs. (3a-c). However, in 2-1 electrolyte solutions (e.g., $CaCl_2$), Eqs. (3a) and (3b) are replaced by Eqs. (3d) and (3e), respectively [224, 254, 280]:

$$V_{EL}(h) = \frac{128\pi k_B T n \gamma_1 \gamma_2}{\kappa^2} \times \frac{r^2}{2r+h} \exp(-\kappa h) \quad (3a)$$

$$\gamma_i = \tanh\left(\frac{z_i e \psi_{Si}}{4kT}\right) \quad (3b)$$

$$\kappa^{-1} = \sqrt{\frac{\varepsilon \varepsilon_0 k_B T}{2 N_A I e^2}} \quad (3c)$$

$$V_{EL}(h) = \frac{384\pi k_B T n \gamma_1 \gamma_2}{\kappa^2} \times \frac{r^2}{2r+h} \exp(-\kappa h) \quad (3d)$$

$$\gamma_i = \frac{3}{2} \frac{\left[2\exp\left(\frac{e\psi_{Si}}{kT}\right)/3 + 1/3\right]^{1/2} - 1}{\left[2\exp\left(\frac{e\psi_{Si}}{kT}\right)/3 + 1/3\right]^{1/2} + 1} \quad (3e)$$

where n is the concentration of electrolytes; k_B is the Boltzmann constant, 1.38×10^{-23} J/K; T is absolute temperature, 298 K; z_i is the valency of the i^{th} ion; e is unit charge, 1.602×10^{-19} C; ψ_{Si} is the surface potential (V) of the interacting particles in an aqueous medium; κ^{-1} is the Debye length (nm); ε_0 is the vacuum permittivity, 8.854×10^{-12} $CV^{-1}m^{-1}$; ε is the relative permittivity of water, 78.5; N_A is Avogadro's number, 6.02×10^{23} mol^{-1}; and I is the ionic strength (M), $I=0.5\cdot\Sigma c_i Z_i^2$, where c_i is the molar concentration of one species of ions (i).

The adsorption of negatively charged HA molecules onto CeO_2 NPs will shift the positive surface potential of the NPs toward the negative domain. The surface potentials are calculated from the measured zeta potentials (ζ) of NPs under various water chemistries: $\psi_{Si} = \zeta(1+z/r)\exp(\kappa z)$, where z is assumed to be 0.5 nm.

The forces contributed by the adsorbed HA layer can be computed with scaling theory [273, 281, 282], which is based on minimizing the surface free energy under the constraint that total amount of adsorbed HA is fixed in the region between two interacting surfaces. The interaction energy due to the HA layers (V_{HA}) can be computed with Eq. (4):

$$V_{HA}(h) = \pi r\left(\frac{\alpha_{Sc}K_BT}{a_m^3}\right)\Phi_{s0}^{9/4}D_{Sc}\left\{-\frac{16\Gamma D_{Sc}}{\Gamma_0}\times\ln\left(\frac{2\delta}{h}\right)\right.$$
$$\left.+\frac{4D_{Sc}^{5/4}}{2^{5/4}}\left(\frac{8\Gamma}{\Gamma_0}\right)^{9/4}\left[\frac{1}{h^{1/4}}-\frac{1}{(2\delta)^{1/4}}\right]\right\} \quad (4)$$

where δ is thickness of the adsorbed-HA layer, α_{Sc} is a numerical constant, a_m is the effective monomer size, Φ_{so} is polymer concentration at a single saturated surface, D_{Sc} is the scaling length, Γ is total amount of HA adsorbed on a single surface, and Γ_0 is the adsorbed amount at saturation. The first and the second terms within the brace in equation S3 represent bridging attraction and steric repulsion, respectively.

Finally, the acid-base energy (V_{AB}) between two identical spheres is expressed in Eq. (5):

$$V_{AB}(h) = \pi r\lambda\Delta G_{h_0}^{AB}\exp\left(\frac{h_0-h}{\lambda}\right) \quad (5)$$

where λ is the correlation length or decay length of the molecules of the liquid medium (for pure water, this value is estimated to be 1 nm [228]), and ΔG_{h0}^{AB} is the polar or acid-base free energy of interaction between particles at the distance h_0 [253], which is the minimum equilibrium distance due to Born repulsion, 0.157 nm [228]. The value of ΔG_{h0}^{AB} is subject to change upon HA adsorption onto the NP surface.

Upon computing the total interaction energy (V_T), the aggregation kinetics of CeO_2 NPs can be obtained on the basis of Eq. (6) [283]:

$$r = a\cdot\left\{1+\frac{4k_BTn_0}{3\mu W}t\right\}^{1/d_F} \quad (6)$$

where a is the primary particle radius, k_B is the Boltzmann constant, T is the absolute temperature, μ is the viscosity of the solution (8.90×10^{-4} Pa·s), n_0 is the initial number concentration of primary particles, d_F is the fractal dimension of aggregates, and t is the time. W is the stability ratio, which can be expressed as [220, 249]:

$$W = \left[\int_0^\infty \lambda(u) \frac{\exp\left(V_T(u)/kT\right)}{(2+u)^2} du \right] \cdot \left[\int_0^\infty \lambda(u) \frac{\exp\left(V_A(u)/kT\right)}{(2+u)^2} du \right]^{-1} \quad (7)$$

where u is the normalized surface-to-surface separation distance (h) between two particles ($u=h/a$). $V_A(u)$ is the attractive energy. vdW energy is the only contributing term to $V_A(u)$ for bare particles. However, for particles coated with HA, the bridging attraction contributes as well. $\lambda(u)$ is the correction factor for the diffusion coefficient, which is related to the separation distance by Eq. (8) [248]:

$$\lambda(u) = \frac{6(u)^2 + 13(u) + 2}{6(u)^2 + 4(u)} \quad (8)$$

Eq. (6) was derived to describe the diffusion-limited aggregation. In this study, we attempted to apply it in the initial radius-growth stage of reaction-limited aggregation as well. This is because the aggregate structure might not greatly influence the particle collision efficiency in the early stage of reaction-limited aggregation; moreover, a rigorous expression does not exist for describing the reaction-limited aggregation [237, 283]. However, as aggregation proceeds, the aggregate structure indeed affects particle collision efficiency, which implies that Eq. (6) may be invalid in modeling reaction-limited aggregation beyond the early stage.

The number concentration of CeO_2 NPs is determined from the mass concentration. The lattice parameter (a_l) of CeO_2 unit cells is 5.4087 Å [284], and each unit cell contains four Ce atoms and eight O atoms. The number of Ce atoms (N) per CeO_2 NP with radius r can be calculated using Eq. (9).

$$N = 4 \times \frac{4}{3} \pi r^3 / a_l^3 = \frac{16}{3} \pi \left(r / a_l \right)^3 \quad (9)$$

The mass of a single CeO_2 NP is then obtained, and the number concentration of NPs can be computed.

4.4. Results and discussion

4.4.1. Characterization of CeO_2 NPs

A TEM image of CeO_2 NPs is presented in Figure 4.1. The NPs are close to spherical in shape and have a relatively uniform size distribution. The inset in Figure 4.1 shows the PSD diagrams of CeO_2 NPs in the absence and presence of HA; these diagrams are obtained from DLS measurements. The NP size measured with DLS is greater than that determined with TEM, which is consistent with previous studies [217, 285]. This is probably caused by some minor particle aggregation or the thickness of the adsorbed water layer on the NP surfaces. The average hydrodynamic radii of CeO_2 NPs in the absence of HA and in the presence of 1 ppm and 10 ppm HA are 50.7, 52.5, and 55.0 nm, respectively. The polydispersivity indices (PDI) are quite small (~0.1), indicating that CeO_2 NPs are highly monodispersed.

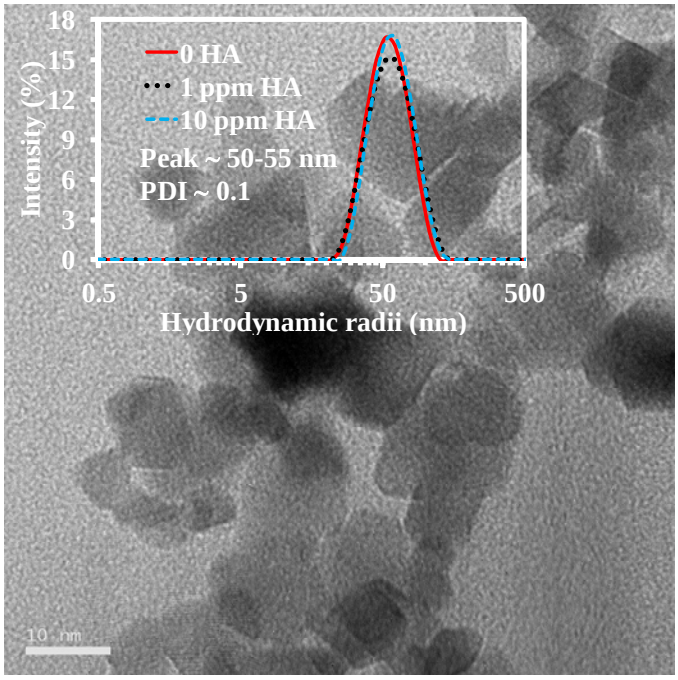

Figure 4.1. TEM image of CeO_2 NPs. The inset is the particle size distribution of 10 mg/L CeO_2 NPs in the absence and presence of HA. The size peak increases slightly in the presence of HA, which indicates that the HA forms a coating around CeO_2 NPs. The

narrow particle size distribution and small PDI value in the presence of HA imply that the coating is almost uniform.

Figure 4.2 shows the EPMs of CeO_2 NPs under different HA concentrations in KCl and $CaCl_2$ solutions. In the absence of HA, the CeO_2 NPs are positively charged at pH 5.7. However, with HA present, the surface charge (potential) of CeO_2 NPs shifts to the negative domain, which indicates HA adsorption onto the CeO_2 NPs. Because the HA was introduced into the NP suspension just before the EPM measurements, this verified that HA adsorption occurred almost immediately. The EPMs under all conditions tended to become less positive (no HA) or less negative (1 and 10 ppm HA) as ionic strength increased, which was caused by the compressed electrical double layer and by cation binding to the carboxylic functional groups of HA adsorbed on the NPs [221, 286]. Although the magnitude of the EPMs is expected to decrease continuously with increasing ionic strength owing to compression of the electrical double layer and neutralization of surface charge, Figure 4.2 reveals that the general shape of the mobility curves exhibits an extremum at moderate ionic strength. Similar trends have been reported elsewhere [287, 288] and might be explained by the preferential adsorption of co-ions onto the NP surface, which results in a decrease in the electrokinetic potential [288, 289]. Figure 4.2 also reveals that the divalent ions (Ca^{2+}) are more effective in screening the NP surface charge than monovalent ions (K^+). The EPMs were further converted to zeta potential via the Henry equation [290]. Although the presence of HA changed the sign of the particle surface charge, in $CaCl_2$ solution the absolute values of the EPMs/zeta potentials changed only slightly, which means that the EL repulsion force did not change greatly in the presence of HA. However, the impact of HA on CeO_2 NP stability was significant (see next section). This observation suggested that non-DLVO forces played an important role in the system.

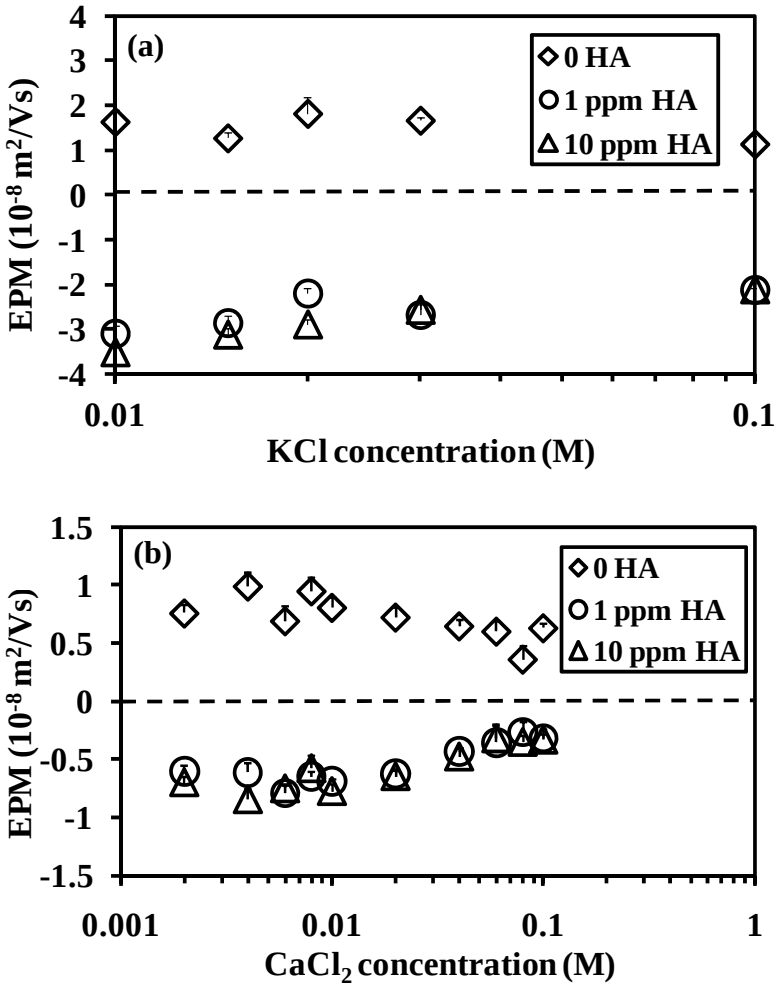

Figure 4.2. Electrophoretic mobilities (EPMs) of CeO_2 NPs under different HA concentrations in (a) KCl and (b) $CaCl_2$. The small marks in the symbols of Figure 4.2 are error bars.

4.4.2. Influence of HA on the aggregation of CeO_2 NPs in KCl and $CaCl_2$

Figure 4.3 shows representative aggregation kinetics profiles of CeO_2 NPs in KCl and $CaCl_2$ solutions in the absence and presence of HA as obtained from TR- DLS measurements. The initial number concentration of CeO_2 NPs is approximately 2.35×10^{15} particles/m^3 in all aggregation experiments. HA stabilizes CeO_2 NPs at all KCl concentrations. In the presence of a relatively low concentration of HA (1 ppm), the CeO_2 NPs were stabilized, and no aggregation was observed even at a high KCl concentration

(0.1 M) (Figure 4.3a). When a higher HA concentration was applied (10 ppm), the aggregation of CeO_2 NPs further decreased, and no aggregation was observed even when the KCl concentration increased to 0.5 M. This stabilizing effect of NOM also has been reported in other studies [221, 291]. However, in $CaCl_2$ solutions, the behavior of the NPs was more complicated. At low Ca^{2+} concentration (0.004 M), the aggregation rate of CeO_2 NPs is inhibited in the presence of HA, possibly because of steric repulsion due to the adsorption of HA molecules onto NPs, which greatly stabilizes the system. However, at high $CaCl_2$ concentration (0.08 M), HA enhanced the aggregation of CeO_2 NPs, probably owing to the bridging attraction between CeO_2 NPs, which is induced by the HA aggregates formed through intermolecular bridging via Ca^{2+} complexation [221, 292].

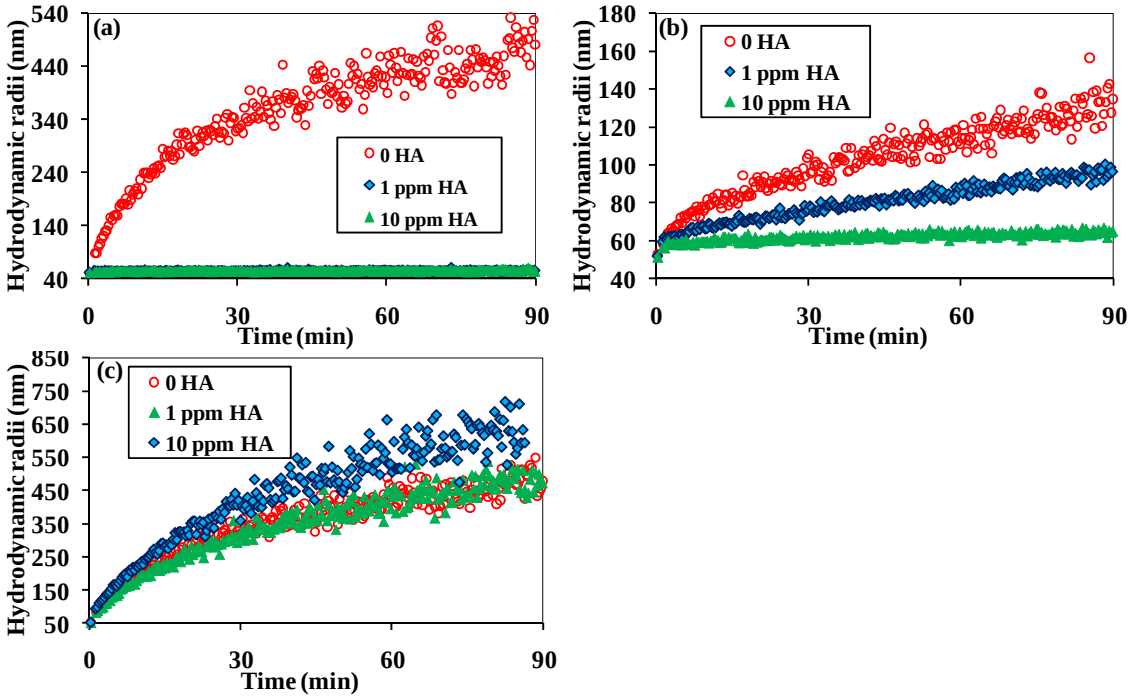

Figure 4.3. Aggregation kinetics of CeO_2 NPs in the absence and presence of HA under (a) 0.1 M KCl, (b) 0.004 M $CaCl_2$ and (c) 0.08 M $CaCl_2$.

The attachment efficiencies (α), or inverse stability ratios ($1/W$), were calculated by normalizing the initial slopes of the aggregation curves with those obtained in the diffusion-limited aggregation regime (presented in Figure 4.4). Since extremely low

aggregation kinetics were observed even at high KCl concentrations in the presence of HA, the attachment efficiency profiles were not produced with KCl in the presence of HA. Two distinct aggregation regimes, diffusion limited and reaction limited, are observed in the absence of HA. The CCCs were determined by the intersection of two lines extrapolated through the reaction-limited and diffusion-limited regimes (not shown here owing to the crowding). In the absence of HA, the CCCs were approximately 36.5 mM in KCl and 9.5 mM in $CaCl_2$ solutions. In the presence of HA, diffusion-limited and reaction-limited regimes were also observed in $CaCl_2$ solution, which was consistent with other studies [293]. Moreover, in $CaCl_2$ solution, the attachment efficiency was smaller in the presence of HA than in its absence in the reaction-limited regime but larger in the diffusion-limited regime. However, the enhancement of the aggregation rate by HA in high concentrations of $CaCl_2$ was not as great as that in other NP systems, such as silicon and fullerene [221, 293]. The CCCs under no HA, 1 ppm HA and 10 ppm HA conditions are approximately 9.5, 8.0 and 12.0 mM, respectively, which indicates that the HA concentration has an influence on the CCC.

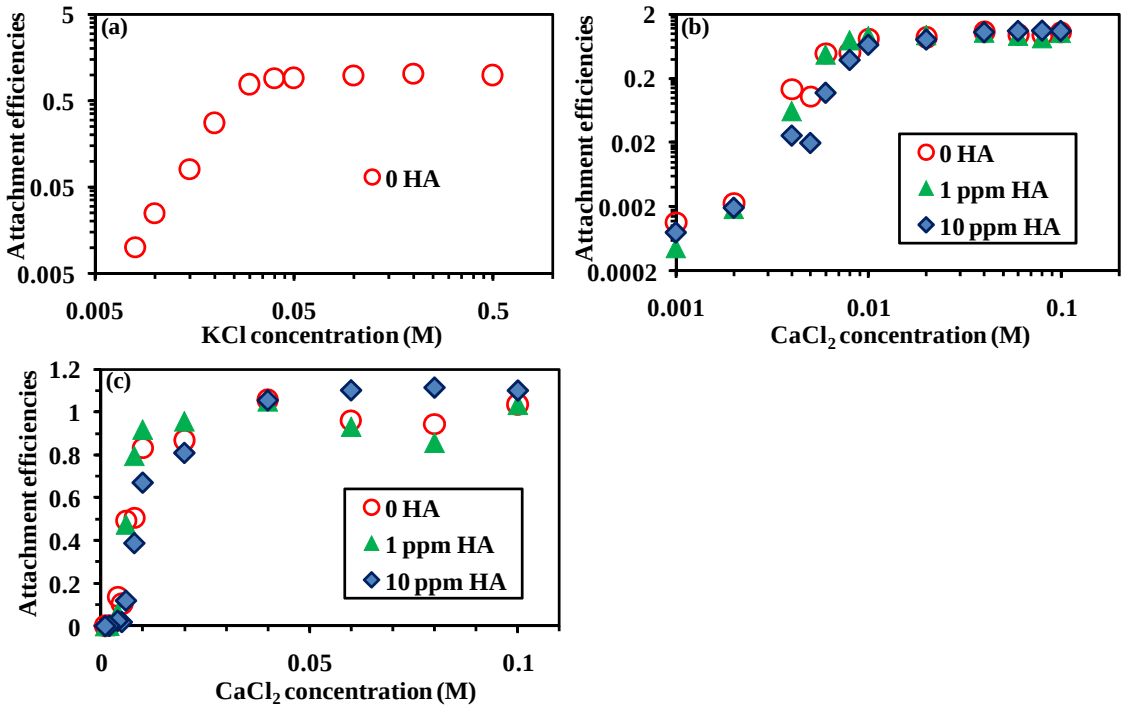

Figure 4.4. Attachment efficiencies (or inverse stability ratios) of CeO_2 NPs derived from experimental data in the absence and presence of HA in (a) KCl, (b) $CaCl_2$ solutions. To give a clear differentiation of data points in the high concentration regime of $CaCl_2$ solutions, the attachment efficiency profiles in normal scale instead of logarithmic scale was shown in (c).

4.4.3. Model parameter determination and interaction energy analysis

Because the aggregation process is fundamentally controlled by the interaction forces/energies between NPs, computing the interaction energy enables us to better understand the effect of HA on aggregation. Eqs. (1-4) were employed to compute each interaction energy term (V_{vdW}, V_{EL}, V_{HA} and V_{AB}) and the total interaction energy (V_T). Those equations involve many parameters that could be measured experimentally or computed theoretically. However, some measurements and calculations are extremely challenging, and thus, inevitably, some parameters must be estimated. For example, ΔG_{h0}^{AB} for bulk materials might be determined by contact angle measurements. However, for nanoscale materials, whose physiochemical properties greatly differ from their bulk counterparts, the contact angle measurement is not applicable. Although parameter estimation could have been achieved by "artificial" optimization, this can result in physically unrealistic values. In this study, most parameters were determined through experiments or obtained from the literature. In brief, the surface potentials (ψ_S) of CeO_2 NPs under different solution chemistries were calculated from the EPMs. The adsorbed HA-layer thicknesses (δ) were measured by DLS rather than calculated from Ohshima's soft particle theory [294, 295] because the primary NPs are highly monodispersed in the system. The δ values obtained in this study are consistent with those reported earlier [296]. Consistent with another study [273], a value of 0.5 was assigned to the fractional HA surface coverage (Γ/Γ_0) in the presence of 10 ppm HA; in the presence of 1 ppm HA, Γ/Γ_0 values were determined from adsorption experiments. The Hamaker constant of bare

CeO_2 NPs, the term $\alpha S_c k_B T/a_m^3$, the scaling length (D_{Sc}), and the HA volume fraction at the NP surface (Φ_{S0}) were obtained or estimated from the literature [252, 273, 297-299]. The calculation of the Hamaker constant of HA-coated NPs is presented in section 4.3.4. The only remaining parameter, ΔG_{h0}^{AB}, was adjusted to make the theoretically calculated attachment efficiencies match the experimentally derived ones. The attachment efficiencies, or the inverse stability ratios ($1/W$), were then computed according to Eq. (7).

$V_T(u)$, the total interaction energy between NPs separated by a normalized distance u, can be computed as discussed above. $V_A(u)$ is the attractive energy. For bare particles, vdW energy is the only contributing term for $V_A(u)$. However, for particles coated with HA, the bridging attraction should be incorporated as well. For the primary parameters used in the computation of attachment efficiencies, refer to Table 4.1.

Table 4.1. Model parameters

Parameter	**Value**
Boltzmann constant	1.381×10^{-23} J/K
Avogadro's number	6.022×10^{23}
Elementary charge, e	1.6×10^{-19} C
Hamaker constant for bare CeO_2 NPs	5.57×10^{-20} J
Hamaker constant for HA-coated CeO_2 NPs	6.6×10^{-21} J
Dielectric constant of a vacuum	8.85×10^{-9} C/mV
Viscosity of water (298 K)	8.90×10^{-4} Pa·s
Scaling length, D_{Sc}	1 nm
$\alpha S_c k_B T/a_m^3$	3×10^5 N/m^2
Fractional HA surface coverage (Γ/Γ_0)	0.5 under 10 ppm HA;

Adsorbed HA layer thickness, δ	0.08–0.19 under 1 ppm HA* 1.73 nm for 1 ppm HA; 4.23 nm for 10ppm HA
HA volume fraction at a single saturated surface, Φ_{S0}	0.3
ΔG_{h0}^{AB}	2.0–2.6 mJ/m^2 in absence of HA in KCl; 2.7–3.0 mJ/m^2 in absence of HA in $CaCl_2$; 0.15–0.7 mJ/m^2 in presence of HA in $CaCl_2$

* The surface coverage under 1 ppm HA was determined from adsorption experiments by assuming that it was proportional to the amount of HA adsorbed under the same ionic strength.

The ΔG_{h0}^{AB} values fell into the narrow ranges of 2.0–2.6 mJ/m^2 for bare CeO_2 NPs in KCl, 2.7–3.0 mJ/m^2 for bare CeO_2 NPs in $CaCl_2$, and 0.15–0.7 mJ/m^2 for HA-coated CeO_2 NPs in $CaCl_2$, which have the same order of magnitude as the values for other metal oxides [258, 262]. Although ΔG_{h0}^{AB} is expected to be constant in the same type of electrolyte, it exhibits narrow distributions. This might be caused by error in EPM measurements, i.e., the EPMs we obtained were not 100% accurate owing to the instrument deviations. Moreover, converting EPMs to zeta potentials and then to surface potentials using approximation equations introduces deviations. Errors in the size measurements and adsorption experiments, the approximation equations in the EDLVO analysis, and the numerical integration used in Matlab also lead to the ΔG_{h0}^{AB} value distributions. The ΔG_{h0}^{AB} value for the bare CeO_2 NPs used in this study is slightly larger than that for another type of bare CeO_2 NPs that are larger, as discussed in our previous study [283]; this is reasonable because the hydrophilicity of metal oxide NPs is size dependent, and larger size might lead to smaller hydrophilicity and thus a smaller ΔG_{h0}^{AB} value [300].

It is difficult to quantify the magnitude of each interaction energy term for cases in the presence of HA in KCl solution because almost no aggregation was observed under those conditions. Moreover, theoretical calculations showed that, regardless of the steric force, the increased EL force and decreased vdW force owing to the introduction of HA results in marked repulsion among CeO_2 NPs and then stabilizes the system. Consequently, V_{HA}, V_{AB}, and relevant parameters cannot be determined in the presence of HA in KCl solution.

On the basis of the parameters listed in Table 4.1, the interaction energy profiles for CeO_2 NPs under representative solution chemistries are computed and presented in Figure 4.5. The energy barrier reflects the aggregation tendency. In the absence of HA in 0.1-M KCl solution, no energy barrier is observed, which indicates that the aggregation of CeO_2 NPs is within the diffusion-limited regime. However, a high barrier (approximately 50 kT) arose with the introduction of HA into the system, and correspondingly, the aggregation of NPs did not occur under those conditions. In 0.004-M $CaCl_2$, the magnitude of the energy barrier decreases in the order 10 ppm HA, 1 ppm HA, and no HA, which implies that the aggregation rate increases in the same order. The experimental data shown in Figure 4.3b prove this. Moreover, in 0.08-M $CaCl_2$ solution, no energy barrier is observed under all conditions; however, Figure 4.3c shows that the aggregation rate under 10 ppm HA is higher than that under the other two conditions. This indicates that the energy barrier cannot be used as a quantitative index. Therefore, a more complicated, but quantitative, index involving integration, as shown in Eq. (7), was used to compute the aggregation efficiency.

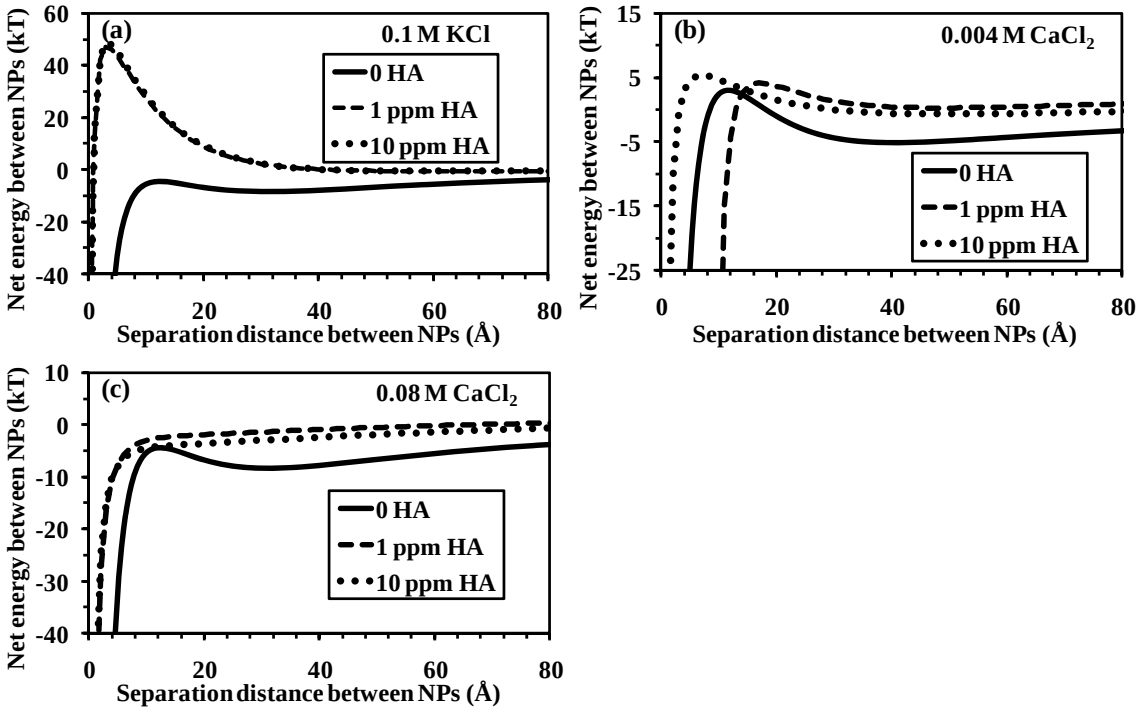

Figure 4.5. Interaction energy profiles of CeO_2 NPs in the absence and presence of HA under (a) 0.1 M KCl, (b) 0.004 M $CaCl_2$ and (c) 0.08 M $CaCl_2$. The continuous, dashed and dotted lines are model simulations corresponding to 0, 1 ppm and 10 ppm HA, respectively.

To better understand the contribution of each interaction energy term, the representative profiles were plotted and are presented in Figure 4.6a. Steric repulsion clearly contributes greatly, whereas EL repulsion does not, which implies that screening surface charges by counter-ions may not be crucial for the aggregation. Figure 4.6b compares each energy term in the absence and presence of 10 ppm HA in 0.002 M $CaCl_2$ solution. The vdW attractive force decreased in the presence of HA, mainly because of the smaller Hamaker constant. EL repulsion remains almost constant because, although HA adsorption changed the sign of the NP surface charge, the absolute values are similar. In addition, owing to smaller ΔG_{h0}^{AB} value for HA-coated NPs, the AB force decreased with HA present in the solution. The total energy barrier increased in the presence of HA,

which means that HA stabilized CeO_2 NPs in the solution. In some other cases, the energy barrier decreased in the presence of HA, and thus HA destabilized NPs.

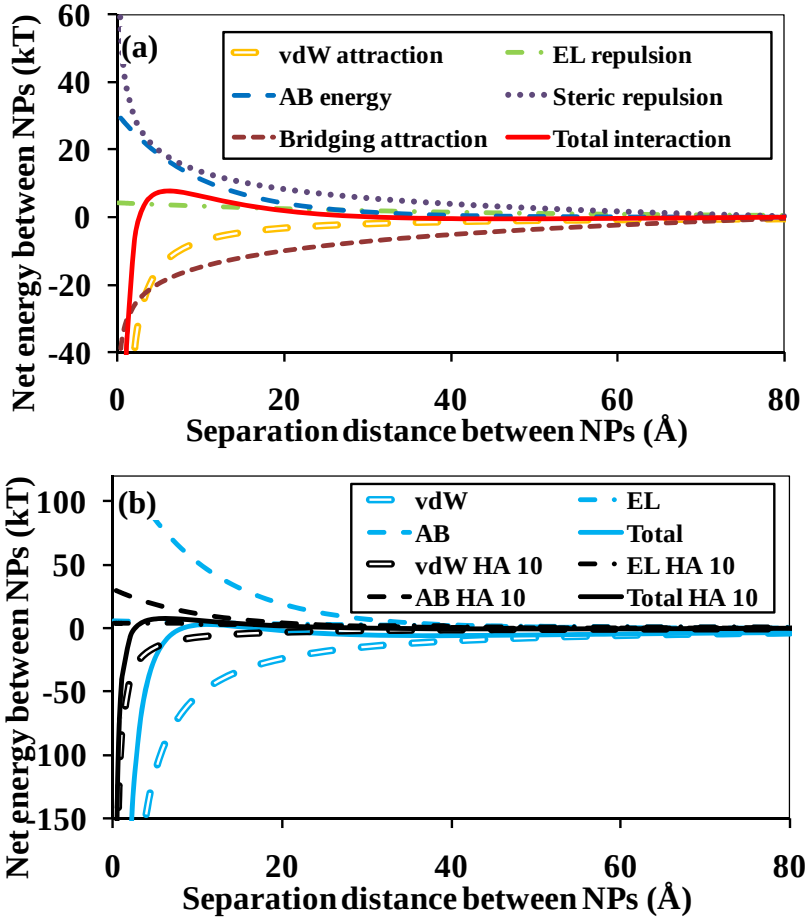

Figure 4.6. (a) Representative profiles of total interaction energy and contributing energy terms (under 0.002 M $CaCl_2$ and 10 ppm HA). (b) Comparison of interaction energy profiles in the absence and presence of HA.

4.4.4. Modeling the aggregation kinetics of CeO_2 NPs

Eq. (6) was used to model the aggregation kinetics of CeO_2 NPs. The fractal dimension d_F is widely acknowledged to be ~1.8 for diffusion-limited aggregation and ~2.1 for reaction-limited aggregation [235, 236, 268, 269] (see Table 4.2). V_T and n_0 were computed as discussed earlier, and other parameters are located in Table 4.1.

Table 4.2. Fractal dimension (d_F) values used in the modeling

Ionic strength (M)		d_F		
		no HA	1 ppm HA	10 ppm HA
$CaCl_2$	0.1	1.8	1.8	1.8
	0.08	1.8	1.8	1.8
	0.06	1.8	1.8	1.8
	0.04	1.8	1.8	1.8
	0.02	1.8	1.8	1.8
	0.01	1.8	1.8	1.8
	0.008	1.8	1.8	1.8
	0.006	1.8	1.8	2.1
	0.004	2.1	2.1	2.1
	0.002	2.1	2.1	2.1
KCl	0.1	1.8	N/A	
	0.03	1.8		
	0.02	1.8		
	0.015	2.1		
	0.01	2.1		

Representative computed results are compared with experimental data in Figures 4.7 and 4.8. Model predictions and experimental observations closely agreed under various solution chemistries. The model predictions could be further improved to match the experimental observations by optimizing the d_F values. However, we did not do that in order to avoid introducing any physically unrealistic values from the blind optimization. It is worth noted that Eq. (6) was derived for diffusion-limited aggregation. However, the close agreements shown in this study indicate that the equation also could be applicable to the initial aggregation stage (< 1.5 h) in the reaction-limited aggregation regime. The discrepancies between model predictions and experimental data can be attributed to several causes. First, it is difficult to accurately determine the surface potential of NPs, particularly in the presence of HA. Second, the primary NPs were assumed to be uniform in size, which is reasonable given the small PDI, but a narrow particle size distribution does exist. Third, HA adsorption was assumed to occur uniformly on all NPs, whereas in reality, non-uniform adsorption and disproportionate surface coverage occurred. Finally, to simplify the computation, HA adsorption was

assumed to reach equilibrium before the NPs aggregated, which is reasonable because the adsorption is fast and the preliminary experiments showed that a rough equilibrium is attained within minutes. However, the adsorption kinetics should be incorporated into a more accurate model.

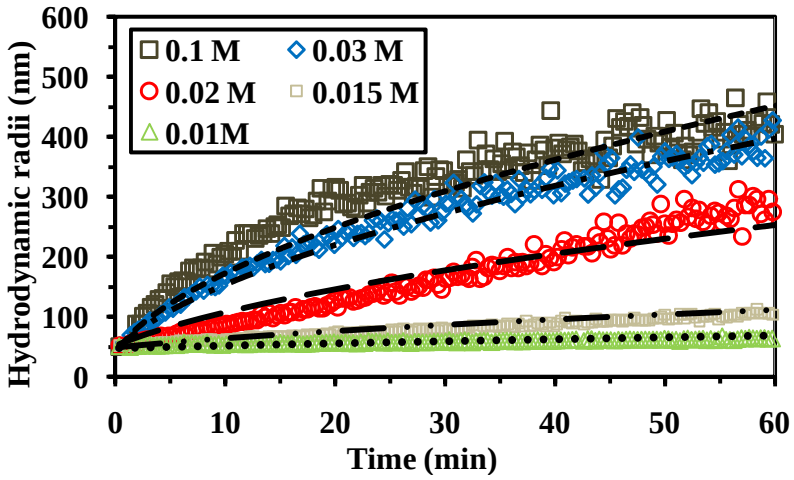

Figure 4.7. Comparison of the simulated and experimental time evolution of the hydrodynamic radii of CeO_2 NPs in the absence of HA in KCl solutions. The lines are model simulations.

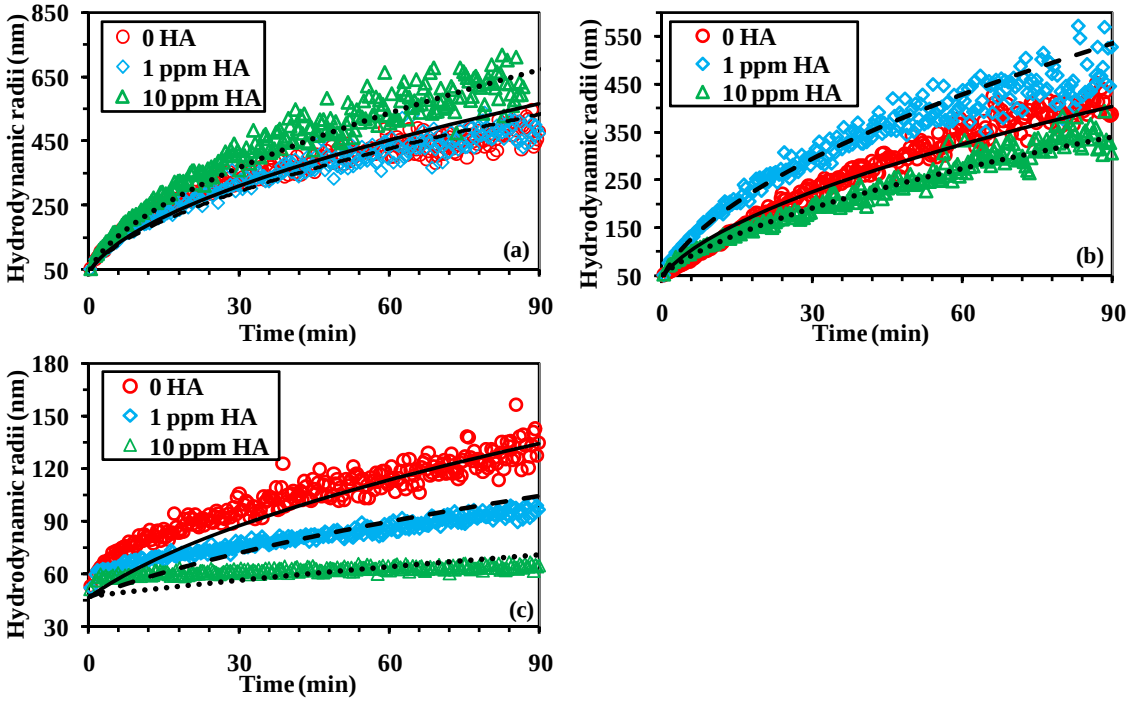

Figure 4.8. Comparison of the simulated and experimental time evolution of the hydrodynamic radii of CeO_2 NPs under (a) 0.08 M, (b) 0.008 M and (c) 0.004 M $CaCl_2$ solutions. The continuous, dashed and dotted lines are model simulations corresponding to the conditions of 0, 1 ppm and 10 ppm HA, respectively.

4.4.5. Application of the aggregation kinetics model to other NP systems

The aggregation kinetics model was tested via application to other NP systems in the presence and absence of NOM. We compared our model computations with the experimental data of Chen et al. [221] and Saleh et al. [219, 291]. In Chen et al. [221], the early-stage aggregation kinetics of fullerene (C_{60}) NPs in the absence and presence of HA was investigated, and the attachment efficiencies and representative aggregation profiles were presented. Because the study did not provide EPMs and HA adsorption data, we cannot calculate the particle interaction energy (V_T) theoretically using equation 1. Instead, we obtained the value of the W in equation 1 from the attachment efficiency profile. The initial fullerene NP concentration, n_0, is 1.6×10^{14} particles/m^3. We calculated the aggregation kinetics according to equation 1 and compared it with the experimental data (presented in Figure 4.9). The fractal dimension d_F was 1.8 and 2.2 for the conditions of no HA and 1 ppm HA, respectively; this is reasonable because in the presence of HA, the aggregates formed are in a loose structure and therefore have a higher d_F value. It is worth noted that although HA may interact with Fullerene and CeO2 with π-π interactions and chemical bonding in the particle-HA intersurface, respectively, in our case the focus was the interaction between NPs coated with HA, which are analogous between Fullerene and CeO_2. HA molecules were found to adsorb onto both types of NPs, thus both NPs would become HA-coated particles and the interaction between two such particles were analogous.

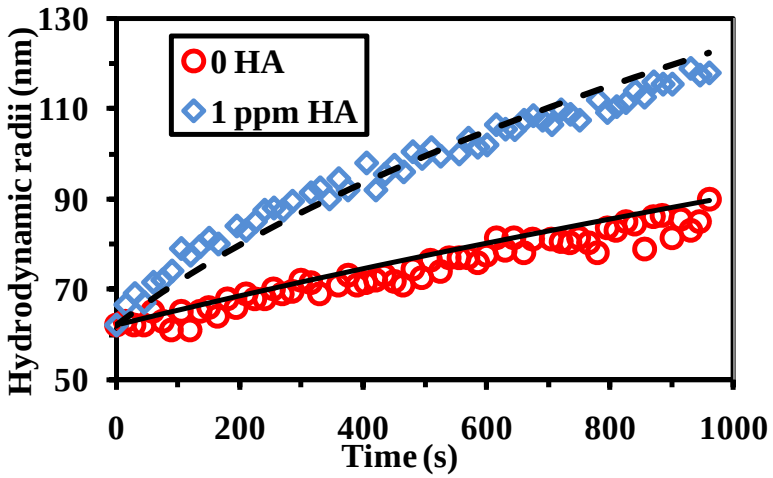

Figure 4.9. Comparisons of the simulated and experimental time evolution of the hydrodynamic radii of fullerene NPs in the absence and presence of HA (1 mg/L total organic carbon (TOC)) under solution conditions of 40 mM $CaCl_2$. The continuous and dashed lines are model simulations corresponding to the conditions of 0 and 1 ppm HA, respectively. Good agreements were reached under those two conditions. The experimental data were obtained from Chen et al. [221].

4.5. Conclusion

In summary, NP aggregation is governed by the interaction force/energy; through computation of this, we are able to determine the aggregation tendency and aggregation kinetics of NPs in different solutions. This work attempted to model the aggregation kinetics of CeO_2 NPs by integrating surface force theories in the presence of HA. The model predictions were compared with experimental data and agreed well. To the best of our knowledge, this is the first attempt to quantitatively model the NP aggregation process in the presence of NOM, and the reported results indicate that the model could be applied in both monovalent and divalent ionic solutions. All of the parameters in the model are physically meaningful and were obtained, as far as possible, from experimental studies rather than blind optimization or fitting. Moreover, the computation is relatively less demanding than computer simulations, and thus the model is suitable for pre-

evaluation of the aggregation tendency of NPs under different conditions. This theoretical analysis and modeling lays the groundwork for prediction of the aggregation process of NPs in complex media, which greatly influences their behavior and toxic effects as reported by a number of previous studies [140, 143, 210, 216, 301]. Therefore, this work would contribute to the risk assessment of NPs.

CHAPTER 5

TEMPERATURE EFFECT ON THE AGGREGATION OF NANOPARTICLES

5.1. Abstract

This chapter investigated the temperature effect on the aggregation kinetics of CeO_2 NPs in KCl and $CaCl_2$ solutions using time-resolved dynamic light scattering. The results show that in KCl and $CaCl_2$, the aggregation rate became faster as the temperature increased. The critical coagulation concentration (CCC) of CeO_2 NPs went down from approximately 100 to 10 mM in KCl and from approximately 10 to 2 mM in $CaCl_2$ solutions when the temperature increased from 4 to 37°C. The observations were analyzed in the framework of extended Derjaguin-Landau-Verwey-Overbeek (EDLVO) theory in order to find out the mechanisms underlying the temperature effect. Moreover, a theoretical model developed on the basis of EDLVO theory and von Smoluchowski's population balance equation was used to predict the aggregation kinetics of CeO_2 NPs under different temperature. The model predictions agreed well with experimental data, suggesting that the model could be employed to predict the size change of NPs in solution. Overall, this work provides insights into NP aggregation using experimental and modeling approaches, and allows people to better understand and theoretically predict the environmental behavior and risk of NPs.

5.2. Introduction

On the basis of EDLVO theory, our previous studies have addressed the effects of ionic strength and natural organic matter on NP aggregation with modeling approaches [302, 303]. It is well known that temperature also greatly influences the aggregation of NPs.

Understanding the temperature effect is important for environmental and health risk assessments of NPs, as both natural water and human body fluids can be at temperatures that are remarkably different from the typically used room temperature. For example, river waters in some cold areas may be only 4°C, whereas the temperature of blood in the human body is as high as 37°C. NPs in these solutions would undergo different aggregation processes. The temperature effect, however, has not gained much attention in NP aggregation studies.

In this study, we investigated the temperature effect on the aggregation of NPs in KCl and $CaCl_2$ solutions using time-resolved dynamic light scattering (TR-DLS). We selected CeO_2 NP as a model NP owing to its wide range of commercial applications [76, 239, 241]. We used the EDLVO theory to interpret the fundamentals of the temperature effect on NP aggregation. Furthermore, a kinetic model developed on the basis of EDLVO theory and von Smoluchowski's population balance equation was used to predict the aggregation kinetics of CeO_2 NPs, which were then compared with experimental observations. Our aim was to fundamentally understand the temperature effect on NP aggregation and theoretically predict the aggregation kinetics of NPs under different temperature, which were anticipated to benefit the predictive modeling research of environmental behavior and toxicity assessment of NPs.

5.3. Materials and methods

5.3.1. Materials

CeO_2 NPs with a nominal diameter of 25 nm were purchased from Sigma-Aldrich. The atomic composition of the sample was verified using X-ray diffraction (data not shown). The pH of the stock suspension was measured to be 4.5 by pH meter (Accumet model 15, Fisher Scientific Co., USA). KCl and $CaCl_2$ stock solutions were prepared using ACS reagent-grade chemicals (Fisher Scientific Co., USA) and were filtered through 0.02-μm filters (VWR International, USA) before use.

5.3.2. Characterization of CeO_2 NPs

The morphology and primary particle size of CeO_2 NPs were determined using transmission electron microscopy (TEM). 5 μL of CeO_2 NP suspensions were deposited on a copper grid (400-mesh size) coated with carbon film (Ted Pella, Redding, CA, USA). A Philips EM420 TEM was employed to acquire images. Particle size distribution (PSD) was obtained with DLS on a Zetasizer Nano ZS instrument (Malvern Instruments). Briefly, 1.5 mL of 10 mg/L CeO_2 NP suspension was injected into a clean cuvette; the DLS instrument was then operated with a scattering angle of 173° from the incident laser beam, and the autocorrelation function automatically accumulated at least 10 runs for each sample. The electrophoretic mobilities (EPMs) of 10 mg/L CeO_2 NPs were measured for a range of K^+ and Ca^{2+} concentrations under different temperatures using the Zetasizer Nano ZS instrument. At least four parallel measurements were made for each condition. The measurement began immediately after the desired conditions were achieved to minimize the interference of aggregation.

5.3.3. Aggregation kinetics

The aggregation kinetics experiments were carried out at pH 5.7, at which the CeO_2 NPs are stable for at least 24 h. The pH values of the CeO_2 NP, KCl and $CaCl_2$ solutions were pre-adjusted to 5.7 to ensure that each measurement could start immediately after addition of K^+ and Ca^{2+}. For the aggregation experiment, the sample holder of the Zetasizer Nano ZS instrument was preheated or precooled to the desired temperature. A premeasured amount of KCl or $CaCl_2$ was added to 1 mL of CeO_2 NP suspension in a cuvette. The NP suspension was then shaken slightly and placed in the sample holder.

5.3.4. Modeling the aggregation kinetics

According to the EDLVO theory, the total interfacial force between two metal oxide NPs is comprised of the vdW force, EL force and AB force [230]. The total interfacial

energy (V_T) between NPs is computed by assuming that each force acts individually and is thus additive: $V_T = V_{vdW} + V_{EL} + V_{AB}$.

The vdW attractive energy (V_{vdW}) between two identical spherical particles, which considers the retardation effect, can be computed using Eq. (1) [275]:

$$V_{VdW}(h) = -\frac{A_H r}{12h(1+11.12h/\lambda_c)} \qquad (1)$$

where A_H is the Hamaker constant, which is 5.57×10^{-20} J for CeO_2 in water [252]. r is the particle radius. h is the separation distance between the interacting surfaces. λ_c is the "characteristic wavelength" of the interaction, which is often assumed to be 100 nm [250].

The EL repulsive energy (V_{EL}) between two identical spheres of radii r in 1-1 electrolyte solutions (e.g., KCl) is given by Eqs. (2a-c). In 2-1 electrolyte solutions (e.g., $CaCl_2$), Eqs. (2a) and (2b) are replaced by Eqs. (2d) and (2e), respectively [224, 254, 280]:

$$V_{EL}(h) = \frac{128\pi k_B T n \gamma_1 \gamma_2}{\kappa^2} \times \frac{r^2}{2r+h} \exp(-\kappa h) \qquad (2a)$$

$$\gamma_i = \tanh\left(\frac{z_i e \psi_{Si}}{4kT}\right) \qquad (2b)$$

$$\kappa^{-1} = \sqrt{\frac{\varepsilon\varepsilon_0 k_B T}{2N_A I e^2}} \qquad (2c)$$

$$V_{EL}(h) = \frac{384\pi k_B T n \gamma_1 \gamma_2}{\kappa^2} \times \frac{r^2}{2r+h} \exp(-\kappa h) \qquad (2d)$$

$$\gamma_i = \frac{3}{2} \frac{\left[2\exp\left(\frac{e\psi_{Si}}{kT}\right)/3 + 1/3\right]^{1/2} - 1}{\left[2\exp\left(\frac{e\psi_{Si}}{kT}\right)/3 + 1/3\right]^{1/2} + 1} \qquad (2e)$$

where n is the concentration of electrolytes; k_B is the Boltzmann constant; T is absolute temperature; z_i is the valency of the i^{th} ion; e is unit charge; ψ_{Si} is the surface potential of the interacting particles in an aqueous medium, which can be calculated from the EPMs of NPs (U_E), the solution viscosity (μ) and permittivity ($\varepsilon \cdot \varepsilon_0$) of water by the

Smoluchowski equation: $\psi_{Si} = (U_E \cdot \mu)/(\varepsilon \cdot \varepsilon_0)$ [254]; ε_0 is the vacuum permittivity; ε is the relative permittivity of water; κ^{-1} is the Debye length; N_A is Avogadro's number; and I is the ionic strength (M), $I = 0.5 \cdot \Sigma c_i z_i^2$, where c_i is the molar concentration of the i^{th} ion.

Finally, the AB energy (V_{AB}) between two identical spheres is expressed by Eq. (3):

$$V_{AB}(h) = \pi r \lambda \Delta G_{h_0}^{AB} \exp\left(\frac{h_0 - h}{\lambda}\right) \qquad (3)$$

where λ is the correlation length or decay length of the molecules of the liquid medium, which is estimated to be 1 nm for pure water [228], and ΔG_{h0}^{AB} is the polar or AB free interaction energy between particles at the distance h_0 [253], which is the minimum equilibrium distance due to Born repulsion, 0.157 nm [228].]

Upon computing the total interaction energy (V_T), the aggregation kinetics of CeO_2 NPs can be obtained by Eq. (4), which was developed on the basis of the EDLVO theory and von Smoluchowski's population balance equation [283]:

$$r_t = a \cdot \left\{1 + \frac{4 k_B T n_0}{3 \mu W} t\right\}^{1/d_F} \qquad (4)$$

where r_t is the particle radius at time t, a is the primary particle radius, n_0 is the initial number concentration of primary particles, μ is the solution viscosity, and d_F is the fractal dimension of aggregates. W is the stability ratio, which can be expressed by Eq. (5) [220, 249]:

$$W = \left[\int_0^\infty \lambda(u) \frac{\exp\left(V_T(u)/kT\right)}{(2+u)^2} du\right] \cdot \left[\int_0^\infty \lambda(u) \frac{\exp\left(V_A(u)/kT\right)}{(2+u)^2} du\right]^{-1} \qquad (5)$$

where u is the normalized surface-to-surface separation distance (h) between two particles ($u = h/a$) and $V_A(u)$ is the attractive energy. Here, vdW energy is the only contributing term to $V_A(u)$ and thus $V_A = V_{vdW}$. $\lambda(u)$ is the correction factor for the diffusion coefficient, which is related to the separation distance by Eq. (6) [248]:

$$\lambda(u) = \frac{6(u)^2 + 13(u) + 2}{6(u)^2 + 4(u)} \qquad (6)$$

The number concentration of CeO_2 NPs is determined from the mass concentration. The lattice parameter (a_l) of CeO_2 unit cells is 5.4087 Å [284], and each unit cell contains four Ce atoms and eight O atoms. The number of Ce atoms (N) per CeO_2 NP with radius r can be calculated by $N = 16\pi (r/a_l)^3/3$. The mass of a single CeO_2 NP is then obtained, and the number concentration of NPs can be computed.

5.4. Results and discussion

5.4.1. Characterization of CeO_2 NPs

A TEM image of CeO_2 NPs is presented in Figure 5.1a. The NPs have a relatively uniform size distribution. The inset in Figure 5.1a shows the PSD diagram of CeO_2 NPs, which was measured by DLS. Consistent with previous studies, the DLS-measured NP size is larger than that determined by TEM [217, 285]. This is probably owing to particle aggregation and the water layer surrounding the NP surface. The polydispersivity index (PDI) is quite small (~0.1), indicating that CeO_2 NPs are relatively monodispersed in solution. Figure 5.1b shows the zeta potentials of CeO_2 NPs under different temperatures in KCl and $CaCl_2$ solutions. The CeO_2 NPs are positively charged under all tested conditions. The divalent ion (Ca^{2+}) is more effective than the monovalent ion (K^+) in screening the surface charge of NPs. As ionic strength increased, the zeta potential became smaller due to the compression of the electrical double layer surrounding the NP. The temperature effect is apparent; as the temperature increased, the zeta potential became less positive, which was consistent with previous studies [304, 305]. The reason could be that increasing temperature favors proton desorption from the particle surface [304]. At higher temperature, the lower zeta potential of CeO_2 NPs implies that the electrostatic

repulsion force between particles is weaker, and this probably promotes the particle aggregation.

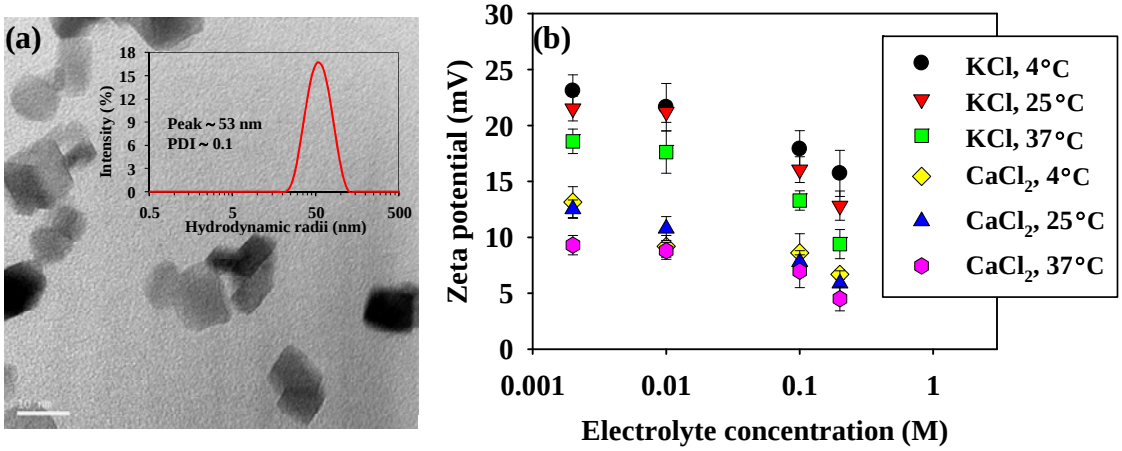

Figure 5.1. Characterizations of CeO_2 NPs. (a) TEM image of CeO_2 NPs. The inset is the particle size distribution of 10 mg/L CeO_2 NPs. The narrow particle size distribution and small PDI value imply that the NPs are relatively monodispersed. (b) Zeta potentials of CeO_2 NPs under different temperatures in KCl and $CaCl_2$ solutions.

5.4.2. Effect of temperature on the aggregation of CeO_2 NPs in KCl and $CaCl_2$

The representative aggregation kinetics profile of CeO_2 NPs in KCl and $CaCl_2$ solutions under different temperatures were presented in Figure 5.2. As the temperature increased, the NP aggregation became faster. The attachment efficiency (α), or inverse stability ratio ($1/W$), was calculated by normalizing the initial slopes of aggregation kinetics curves with the slopes obtained in the diffusion-limited aggregation regime (shown in Figure 5.3). The critical coagulation concentration (CCC) for CeO_2 NPs in KCl was *ca.* 100, 40 and 10 mM at 4, 25 and 37°C, respectively. In $CaCl_2$, CCCs were *ca.* 10, 10 and 2 mM at 4, 25 and 37°C, respectively. The substantially lower CCCs for CeO_2 NPs in Ca^{2+} solutions than those in K^+ solutions is because divalent ions more effectively screen the surface charge of NPs and subsequently enhance the aggregation. Higher temperature leads to a smaller CCC and thus promotes NP aggregation.

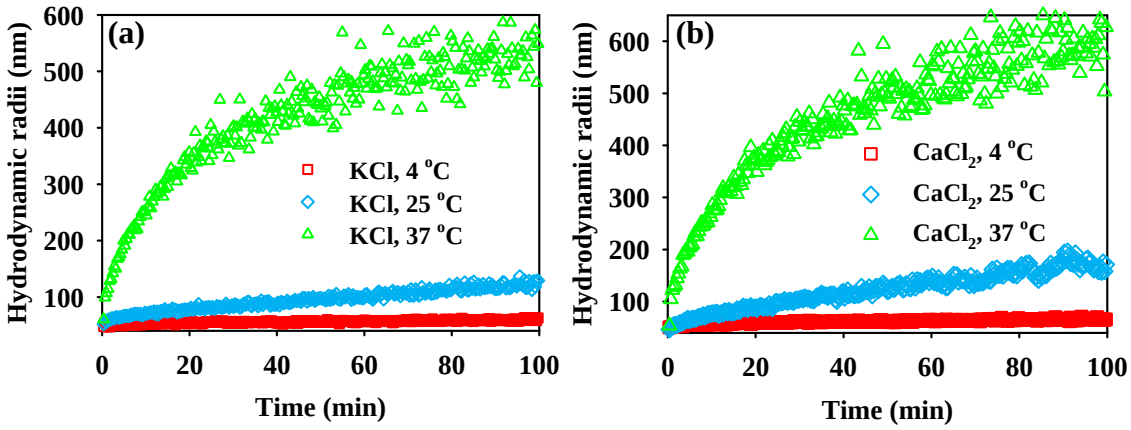

Figure 5.2. Aggregation kinetics profiles of CeO_2 NPs under different temperatures in 0.01 M KCl (a) and 0.002 M $CaCl_2$ (b).

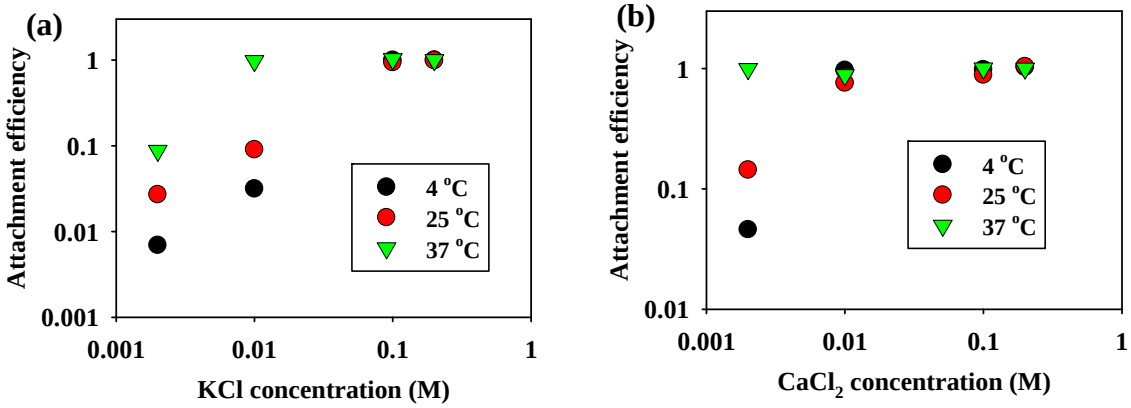

Figure 5.3. Attachment efficiencies (or inverse stability ratios) of CeO_2 NPs derived from experimental data under different temperatures in KCl (a) and $CaCl_2$ (b) solutions.

Higher temperature promotes NP aggregation for two reasons. First, the solution viscosity μ was smaller at higher temperature; according to Eq. (4), the particle aggregation was thus enhanced. Second, the interaction energy between NPs also changes as the temperature increases. The total interfacial energy V_T can be calculated using Eqs. (1)-(3). Parameters involved in these equations could be either measured or computed. Surface potentials (ψ_S) of CeO_2 NPs under different temperatures were calculated from

the EPMs with the Smoluchowski equation [254]. The other major parameters are listed in Table 5.1.

Table 5.1. Model parameters

Parameter	**Value**
Boltzmann constant, k_B	1.381×10^{-23} J/K
Avogadro's number, N_A	6.022×10^{23}
Elementary charge, e	1.6×10^{-19} C
Hamaker constant, A_H	5.57×10^{-20} J
Characteristic wavelength, λ_c	100 nm
Vacuum permittivity, ε_0	8.85×10^{-12} C/V/m
Relative permittivity of water, ε	86.7 for 4°C, 78.5 for 25°C, 75.7 for 25°C
Viscosity of water, μ	1.47×10^{-3} Pa·s for 4°C, 8.90×10^{-4} Pa·s for 25°C, 8.59×10^{-4} Pa·s for 37°C
Decay length, λ	1 nm
ΔG_{h0}^{AB}	2.2 mJ/m^2 in KCl, 2.8 mJ/m^2 in $CaCl_2$

The interaction energies for CeO_2 NPs under different temperatures were computed and are presented in Figure 5.4, which shows that the interaction energy between NPs is lower at a higher temperature in both KCl and $CaCl_2$ solutions. The energy barrier reflects the aggregation tendency. The energy barrier diminished as the temperature increased. When the temperature increased from 4 to 37°C, the magnitude of the energy barrier decreased from 11 to 4 k_BT and from 7 to 1 k_BT in 0.01 M of KCl and 0.002 M $CaCl_2$, respectively. This suggests that NPs more easily overcome the energy barrier and aggregate at high temperatures. Moreover, according to Eqs. (1)-(3), the EL force is the only force that is influenced by the change in temperature (shown in Figure 5.5). Parameters in Eq. (3), such as the surface potential of NPs, solution permittivity and

Debye length, are affected by temperature. The temperature has no impact on vdW and AB forces.

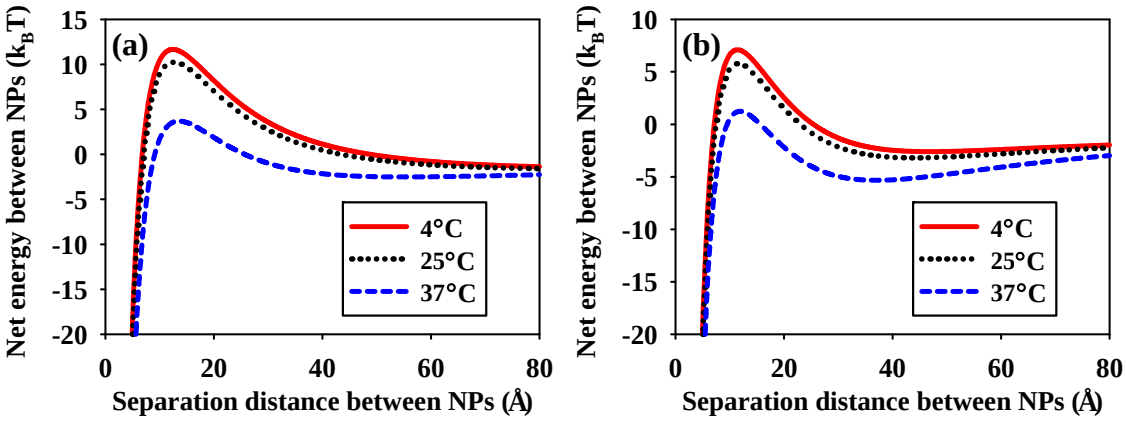

Figure 5.4. Interaction energy profiles of CeO_2 NPs in 0.01 M KCl (a) and 0.002 M $CaCl_2$ (b). The solid, dotted and dashed lines correspond to 4, 25 and 37°C, respectively.

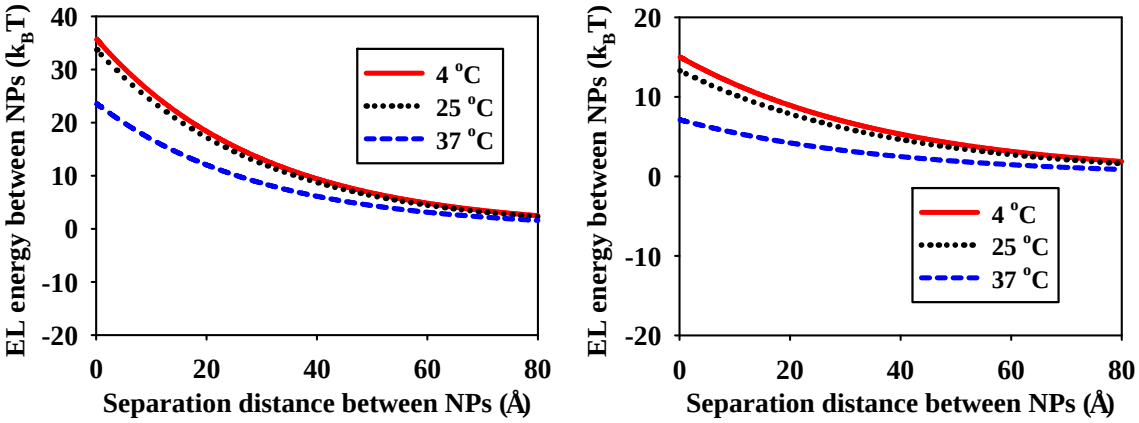

Figure 5.5. EL energy profiles of CeO_2 NPs in 0.01 M KCl (a) and 0.002 M $CaCl_2$ (b). The solid, dotted and dashed lines correspond to 4, 25 and 37°C, respectively.

For a better understanding of the contribution of each energy term to the total interaction, the representative energy profiles are presented in Figure 5.6. Apparently, the AB repulsion energy contributes more relative to EL repulsion energy. This indicates that, compared with EDLVO theory, the conventional DLVO theory, which considers

only EL and vdW energy, provides a less accurate description of the interfacial energy between CeO_2 NPs.

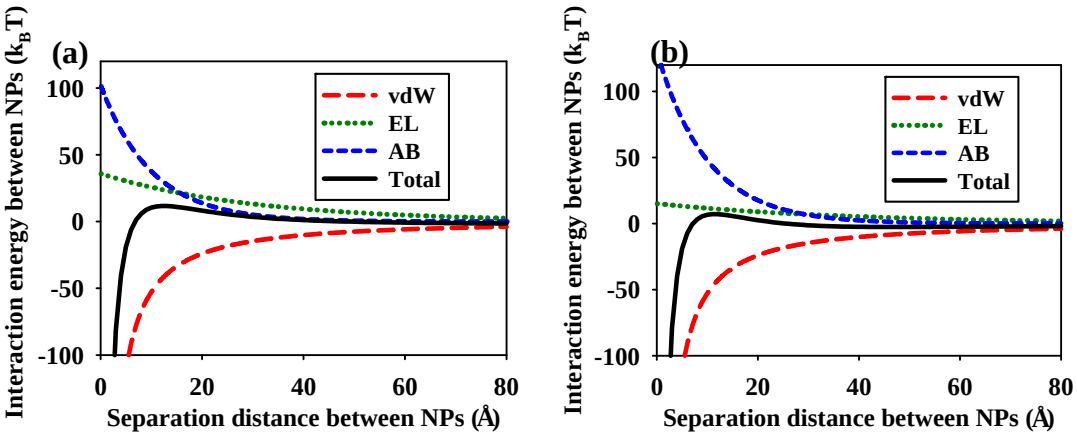

Figure 5.6. Representative profiles of each energy term in 0.01 M KCl (a) and 0.002 M $CaCl_2$ (b) at 4°C.

5.4.3. Modeling the aggregation kinetics of CeO_2 NPs

Eq. (4) was used to model the aggregation kinetics of CeO_2 NPs. The initial number concentration of CeO_2 NPs is approximately 2.35×10^{15} particles/m^3 in all aggregation experiments. The fractal dimension d_F was reported to be *ca.* 1.8 [235, 236, 268, 269]. The total interaction energy V_T was computed according to Eqs. (1)-(3). The attractive energy, V_A, equals the vdW energy (V_{vdW}). The AB free interaction energy between particles at the distance h_0, ΔG_{h0}^{AB}, was consistent with our previous studies. Other parameters are listed in Table 5.1. The modeling results were further compared with experimental observations, and representative comparisons are presented in Fig. 5.7. At all temperatures, model predictions agreed well with experimental data. Some minor discrepancies between model predictions and experimental observations may be attributed to deviations in the surface potential of NPs and the size distribution of particles.

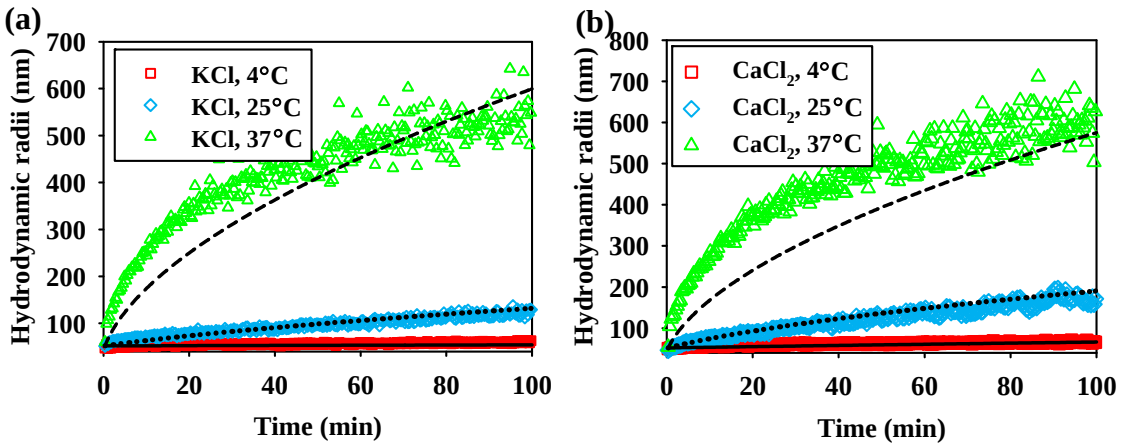

Figure 5.7. Comparison of the simulated and experimental time evolution of the hydrodynamic radii of CeO_2 NPs in 0.01 M KCl (a) and 0.002 M $CaCl_2$ (b) solutions. The solid, dotted and dashed lines are model simulations corresponding to the conditions of 4, 25 and 37°C, respectively.

In conclusion, this work investigated the temperature effect on the aggregation of CeO_2 NPs with both experimental and modeling approaches. As the temperature increased from 4°C to 37°C, the CCCs for CeO_2 NPs decreased from *ca.* 100 to 10 mM in KCl and from *ca.* 10 to 2 mM in $CaCl_2$. The promotive effect of temperature on NP aggregation is ascribed to the smaller solution viscosity and lower interfacial energy barrier at higher temperature. For instance, the energy barrier height decreased from 11 to 4 k_BT in 0.01 M KCl and from 7 to 1 k_BT in 0.002 M $CaCl_2$, which resulted from the smaller repulsive EL energy at a higher temperature. The aggregation model based on the EDLVO theory gave fairly good predictions of NP aggregation under different temperatures. To the best of our knowledge, this is the first study to investigate the temperature effect on NP aggregation with modeling approaches, which is expected to benefit the theoretical predictions of the environmental behavior and biological effects of NPs and to further contribute to the environmental and biological risk assessment of NPs.

CHAPTER 6

INTERACTIONS OF METAL OXIDE NANOPARTICLES WITH CELL MEMBRANE AND CORRELATION WITH THEIR ACUTE CYTOTOXICITY

6.1. Abstract

To better understand the role of cell membrane-nano interactions in the toxicity of NPs, we investigated the acute toxicity of seven different types of engineered metal oxide NPs against *Paramecium multimicronucleatum*, a ciliated protozoan, using the 48-h LC_{50} (Lethal Concentration, 50%) test. Our results showed that the 48-h LC_{50} values of these NPs to *Paramecium* ranged from 0.81 mg/L (Fe_2O_3 NPs) to 9269 mg/L (Al_2O_3 NPs); their toxicity to *Paramecium* increased as follows: Al_2O_3 < TiO_2 < CeO_2 < ZnO < SiO_2 < CuO < Fe_2O_3 NPs. On the basis of the Derjaguin-Landau-Verwey-Overbeek (DLVO) theory, interfacial interactions between NPs and cell membrane were evaluated and the magnitude of interaction energy barrier correlated well with the 48-h LC_{50} data of NPs to *Paramecium*; this implies that metal oxide NPs with strong association with the cell surface might induce more severe cytotoxicity in unicellular organisms.

6.2. Introduction

Recently, engineered NPs (NPs) have received enormous attention for their wide applications in cosmetics, sunscreens, toothpastes, food products, textiles and water treatment [306]. Large-scale discharges of these NPs into the aquatic environment could potentially threaten human and environmental health [2].

Once in the environment, aquatic organisms would likely interact with and uptake those NPs [82, 307]. Thereafter, the NPs might have toxic effects on the organisms [308].

Moreover, NPs probably bioaccumulate in higher-trophic-level organisms [309], which may affect the entire food chain and impose risks for human beings. The common model systems used in the research of the environmental toxicity of NPs include bacteria, algae, *Daphnia*, and zebrafish [310-315]. However, a variety of other organisms in the aquatic environment are important to maintain the balance of ecological systems, and the toxicity of NPs against these organisms has not been extensively investigated yet. Of special note are aquatic protozoa, which differ from multicellular organisms (e.g., *Daphnia*) because they are composed of a single cell, but unlike single-celled algae, they do not possess a protective cell wall. Thus, NPs could enter protozoan cells more easily than bacterial and algal cells and then interact directly with the cellular structures and organelles. Species in the genus *Paramecium* are ciliated unicellular protozoa that are widely distributed in freshwater. *Paramecium* can absorb solid food particles using its cell membrane in a process called phagocytosis [316]. *Paramecium* primarily feed on bacteria and algae and fall prey to multicellular animals such as copepods and larger protists such as dinoflagellates. Therefore, *Paramecium* and other ciliates represent a major link between microbial organisms and multicellular animals.

Various studies have explored the cytotoxicity mechanism of metal oxide NPs [88, 139, 317-320]. Although the exact toxicity mechanism is still unclear, it is recognized that the toxicity of metal oxide NPs to unicellular organisms (e.g. bacteria and ciliates) is ascribed, at least in part, to interactions between the NPs and the cell surface.[139] Many studies reported that direct spatial contact between NPs and cell surface is necessary for manifestation of the cytotoxicity [139, 317, 319, 321], and their interaction is central to the cytotoxicity of NPs [139, 322, 323]. An apparent mechanism relies on direct damages, either physical (e.g. pitting [137]) or chemical (e.g. oxidative stress [139]), of NPs to cell surface (cell wall or cell membrane), which can result in death of the cell [137]. Prolonged contact between the cell and NPs likely alters the cellular surface properties or integrity [324, 325], and triggers the internalization of NPs through endocytosis [210] or direct penetration [326].

The internalized NPs may further exert adverse effects on organelles (e.g., lysosomes and mitochondria) [94, 210] as well as on DNA and other biomacromolecules [98, 327, 328].

The contact of NPs with bacterial cell surface is strongly dependent on the interfacial forces between them [317, 329]. Prior work has revealed that NPs with positive charge induced more toxic effects than their counterparts with negative charge, which might be attributed to the attractive or repulsive interaction between the positively or negatively charged NPs and negatively charged cell surface [141, 322, 323, 330]. Feris et al. [139] modeled the interactions between ZnO NPs and four types of bacterial strains that carried different charge on outer cell surface, and found that the interfacial interactions greatly contributed to the cytotoxicity of NPs. Those previous studies compared NPs of the same type but of different surface charges or sizes, and suggested that the NPs with strong interaction with cell surface likely possessed higher cytotoxicity. However, to the best of our knowledge, there were no studies to compare and address the effect of the interfacial interaction on the cytotoxicity of different types of NPs. It is thus interesting to explore whether or not interfacial interactions between different types of NPs and cell surface correlate with the cytotoxicity of the NPs.

In this study, the acute toxicities of seven engineered metal oxide NPs to *Paramecium* were investigated, and the 48-h LC_{50} was determined for each NP. Furthermore, the interfacial interaction between each NP and the cell membrane was evaluated on the basis of the Derjaguin-Landau-Verwey-Overbeek (DLVO) theory, and a further correlation was established between the interaction energy and NP toxicity. Finally, we analyzed the underlying mechanisms of this correlation.

6.3. Materials and methods

6.3.1. Materials

Nano-sized ZnO (nZnO), TiO_2 (nTiO_2, anatase), SiO_2 (nSiO_2), CeO_2 (nCeO_2), CuO (nCuO) and Fe_2O_3 (nFe_2O_3) were purchased from Sigma-Aldrich (St. Louis, MO,

USA). Nano-sized Al_2O_3 (nAl_2O_3, α-form) was purchased from Nanostructured & Amorphous Materials, Inc (Houston, TX, USA).

The ciliated protozoan *Paramecium multimicronucleatum* (*P. multimicronucleatum*) was obtained from the American Type Culture Collection (Manassas, VA, USA). The culture medium was prepared using a formula of 0.55 g of protozoan pellet (Carolina Biological Supply Co., Burlington, NC, USA) per 1 L deionized (DI) water, and after autoclaving, the medium was inoculated with three bacterial species: *Serratia marcescens, Bacillus cereus, and Bacillus subtilis*, which were also obtained from Carolina Biological Supply Co.. The *P. multimicronucleatum* culture was contained in 250-mL glass bottles, which had been autoclaved and contained 100 mL of culture medium plus two wheat seeds, which slowly released nutrients into the medium [331]. In the experiment, *ca.* 100 individuals of *P. multimicronucleatum* were used as a starting density. The culture was maintained at 22°C in 12:12-h light:dark cycle. A stereoscopic microscope (Olympus SZX12, Center Valley, PA, USA) was used to count the number of *P. multimicronucleatum* in the solution.

The Dryl's solution was prepared and autoclaved; it contained 1 mM NaH_2PO_4-monobasic (Fisher Biotech, Pittsburgh, PA, USA), 1 mM Na_2HPO_4-dibasic (Fisher Chemical, Pittsburgh, PA, USA), 2 mM trisodium citrate dihydrate (Fisher Scientific, Pittsburgh, PA, USA), and 1.5 mM $CaCl_2$ (Fisher Scientific, Pittsburgh, PA, USA) per 1 L of DI water. The $CaCl_2$ solution was autoclaved separately.

6.3.2. Characterization of metal oxide NPs

The primary particle size and morphology of metal oxide NPs were determined by transmission electron microscopy (TEM). 5 μL of NP suspension was deposited on a copper grid (400-mesh size) coated with carbon film (Ted Pella, Redding, CA, USA). A Philips EM420 TEM was operated to acquire images.

Number-averaged hydrodynamic radii of NPs were obtained using dynamic light scattering (DLS) on a Zetasizer Nano ZS instrument (Malvern Instruments, UK). In brief, 1.5 mL of NP suspensions of 10 mg/L in the Dryl's solution was injected into a clean cuvette, and the DLS was then operated with a scattering angle of 173° from the incident laser beam. The autocorrelation function automatically accumulated at least 10 runs for each sample. The electrophoretic mobilities (EPMs) of NPs of 10 mg/L in the Dryl's solution were measured using the Zetasizer Nano ZS instrument. At least four parallel samples were measured for each condition in the NP size and EPM measurements. It is noted here that metal oxide NPs aggregation might occur in the aqueous solution, but in our preliminary experiments, the aggregation reached a plateau stage within 48 h after sample preparation (representative results shown in Figure 6.1), at which further aggregation was not observed. The measurement of NP size and EPM was thus conducted at the plateau stage.

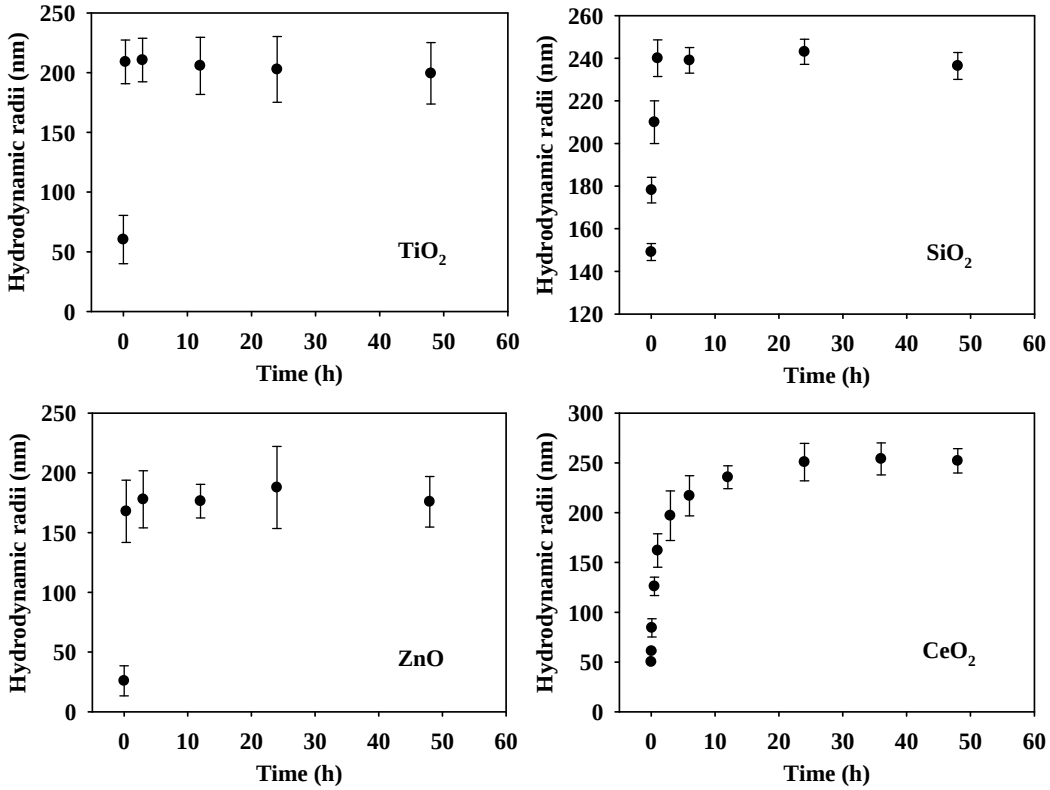

Figure 6.1. Representative aggregation kinetics profiles of NPs in the Dryl's solution.

The ion releases from NPs were measured by inductively coupled plasma mass spectrometry (ICP-MS, Elan DRC II, PerkinElmer, USA) [332, 333]. Since it might take up to 48 h for the ion release from freshly prepared NPs suspensions to reach equilibrium according to preliminary results, we measured the ion release after 48 h. 4 mL of NP suspensions of 10 mg/L in the Dryl's solution were sampled from plastic centrifugation tubes (Fisher Scientific, Pittsburgh, PA, USA), and the released ions were separated from the NPs using Amicon Ultra-4 centrifugal filter units with pore diameters of 1–2 nm (Amicon Ultracel 3K, Millipore, USA). After centrifugation for 30 min at 7000 × g (5430R, Eppendorf, Germany), 3 mL of the filtrates were collected and mixed with 2 mL of 67% nitric acid for ICP-MS analysis.

6.3.3. Acute toxicity tests

Acute (48-h) toxicity tests were conducted against *P. multimicronucleatum* by the static method, following Organisation for Economic Co-operation and Development (OECD) guidelines on aquatic toxicity testing of chemicals [334]. *P. multimicronucleatum* individuals were removed from the stock culture with a micropipette, washed in Dryl's solution, and inoculated into fresh Dryl's solution containing different NPs at different concentrations in a clean petri dish. The concentration gradients of NPs were summarized in Table 6.1. Consistent with the size and EPM measurements, NPs in the aggregation-plateau stage were used in the acute toxicity tests. For each test concentration, three replicates with 12 cells each were used. Simultaneously, control experiments were performed without NPs. *P. multimicronucleatum* was not fed with bacteria for both control and test groups during the tests. The sample solutions were mixed every three hours with a pipette, as some NPs might settle out of the suspension. The mortality was checked 48 h after inoculation under a stereomicroscope (Olympus, Center Valley, PA, USA) at low magnification. We counted swimming *P. multimicronucleatum* as the live cells, and accordingly, cells that were ruptured or could not be found were considered

dead. The median lethal concentrations (48-h LC_{50}) were determined using probit analysis performed in the statistical program SPSS 13.0 (IBM Corporation, USA).

Table 6.1. Concentration gradients of NPs in acute toxicity tests

Tested NPs	**Concentration gradient (mg/L)**										
nFe_2O_3	0.1	0.5	0.8	1	5	10	50				
nCuO	0.1	0.5	1	5	10	50	100				
$nSiO_2$	1	10	100	300	500	1000	2000	2500	3000	5000	10000
nZnO	0.1	1	5	10	50	100	500	1000	1500	2000	5000
$nCeO_2$	1	10	100	300	500	1000	1300	1500	1800	2000	2500
$nTiO_2$	0.1	1	10	50	100	500	1000	1500	2000	3000	10000
nAl_2O_3	1	10	50	100	500	1000	1500	2000	3000	5000	30000

6.4. Results and discussion

6.4.1. Characterization of metal oxide NPs

TEM images of tested metal oxide NPs are presented in Figure 6.2, which showed that although NP aggregation happened, the primary particle sizes were at the nanoscale. By examining forty randomly selected particles of each type of NPs from TEM images, we obtained the average radius of each NP, and the statistical results were tabulated in Table 6.2. The primary particle radius of all NPs except nAl_2O_3 is < 15 nm. Number-based hydrodynamic radii of NPs in Dryl's solution, as measured by DLS, were also presented in Table 1. Consistent with previous studies [302, 303], the NP radius measured with DLS is remarkably larger than that determined with TEM. This is probably caused by particle aggregation and the water layer surrounding NP surface. The representative particle size distribution histograms were presented in Figure 6.3, which indicated that the aggregated NPs were dominant in the total number of NPs. Table 6.2 also listed EPMs of metal oxide NPs and *P. multimicronucleatum* in Dryl's solution. All of these

NPs and *P. multimicronucleatum* were negatively charged. Thus, an electrostatic repulsion force would arise between NPs and the cell surface.

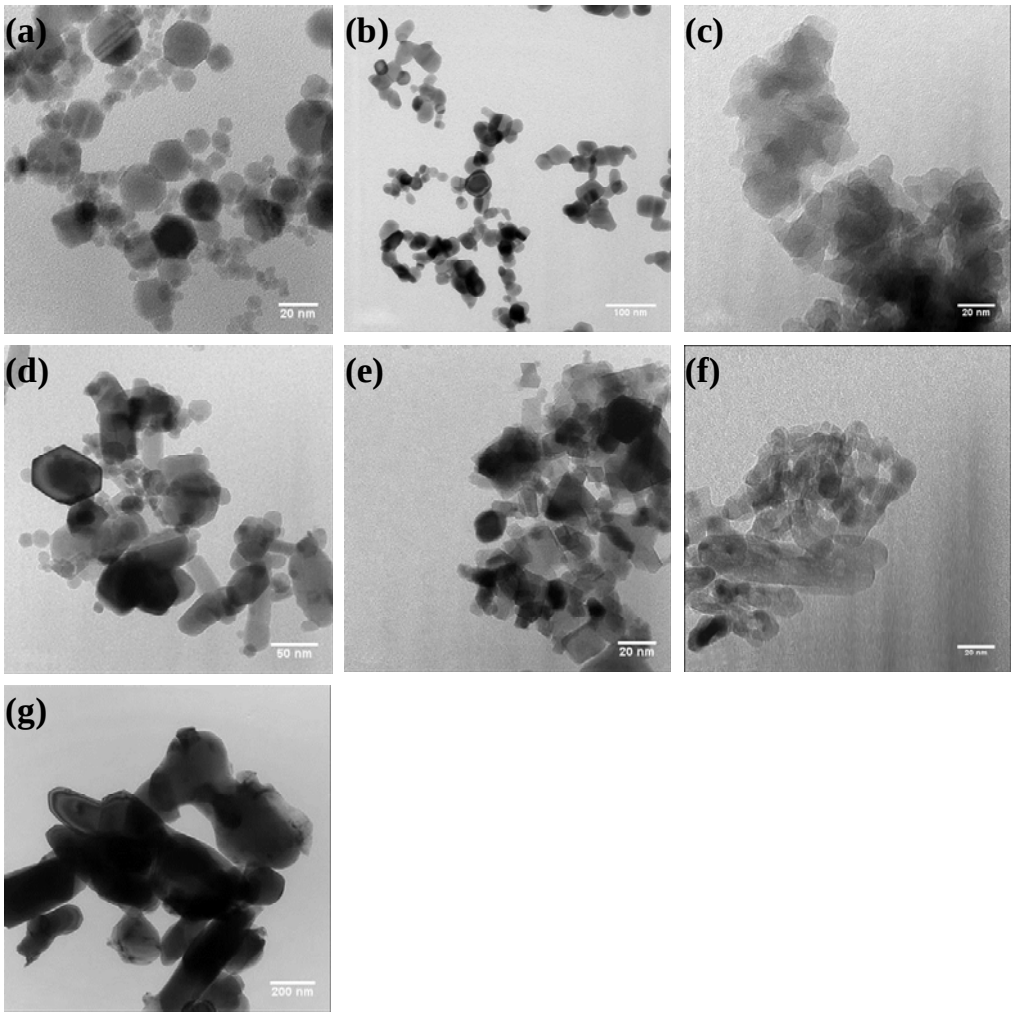

Figure 6.2. TEM images of (a) nFe_2O_3, (b) nCuO, (c) $nSiO_2$, (d) nZnO, (e) $nCeO_2$, (f) $nTiO_2$, and (g) nAl_2O_3.

Table 6.2. Characterizations of tested metal oxide NPs in Dryl's solution, including primary particle radii measured with TEM, hydrodynamic radii (number-based) of metal oxide NPs measured with DLS, and EPMs.

NPs	**TEM radius (nm)**	**DLS radius (nm)**	**EPM (10^{-8} m^2/Vs)**
nFe_2O_3	4.7±1.8	74.5±21.5	-2.57±0.02
nCuO	13.3±3.9	133.4±4.1	-2.01±0.11

$nSiO_2$	8.2±1.7	236.4±6.3	-1.66±0.19
nZnO	9.8±5.0	175.8±21.2	-1.75±0.16
$nCeO_2$	5.5±1.6	252.1±12.3	-2.19±0.04
$nTiO_2$	5.1±1.4	199.4±25.7	-2.04±0.09
nAl_2O_3	83.5±21.4	508.8±38.5	-2.74±0.10
P. multimicronucleatum	N.A.[a]	N.A.	-0.99±0.17

[a]N.A. means not applicable

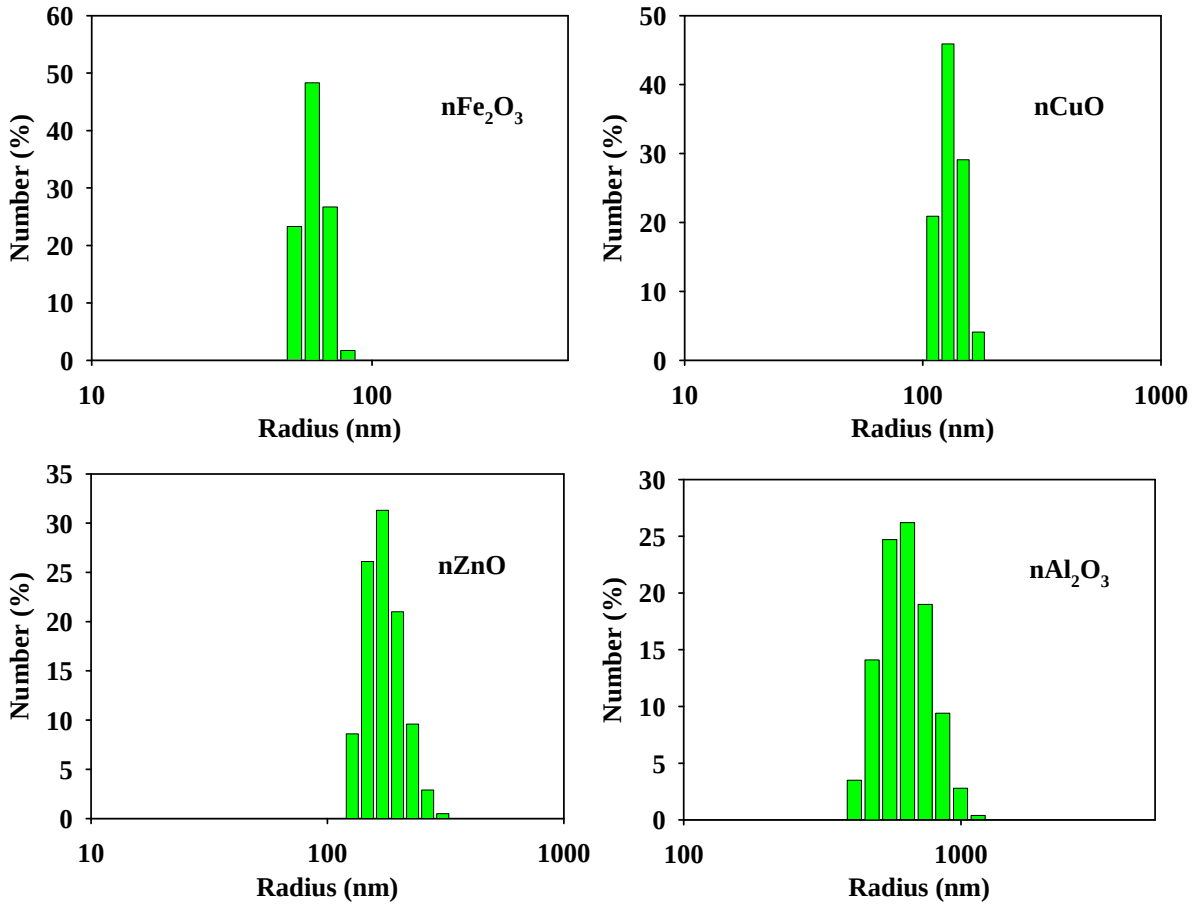

Figure 6.3. Representative particle size distribution histograms of metal oxide NPs, as measured using DLS.

6.4.2. Acute toxicity of metal oxide NPs to *P. multimicronucleatum*

The acute toxicities of all tested metal oxide NPs to *P. multimicronucleatum* were found to increase as particle concentration increased, indicating a dose dependency (Figure 6.4). The 48-h LC_{50} values for these NPs are listed in Table 6.3. These NPs, except nFe_2O_3 and nCuO, are not highly toxic to *P. multimicronucleatum*; the large LC_{50} values (>1000 mg/L) for some NPs are consistent with a prior study, which investigated the toxicity of metal oxide NPs to *E. coli* [335]. The acute toxicity ranking of the tested NPs to *P. multimicronucleatum* has the order nFe_2O_3 > nCuO > $nSiO_2$ > nZnO > $nCeO_2$ > $nTiO_2$ > nAl_2O_3. The order of nZnO > $nTiO_2$ > nAl_2O_3 compares well with a previous study on the toxicity of six NPs to *Daphnia magna* (*D. magna*) [308]. $nTiO_2$ and nAl_2O_3 had the lowest toxicity (if any) among the tested metal oxide NPs, whereas nFe_2O_3 and nCuO were the two most toxic NPs. A previous study also found that nCuO was highly toxic to *D. magna* with the 48-h LC_{50} 3.2 ± 1.6 mg/L [336], which was somewhat more toxic than that to *P. multimicronucleatum* in the current study. To our knowledge, the toxicity of nFe_2O_3 to aquatic organisms has not been reported previously in the literature. However, nFe_2O_3 was acutely toxic to rats [337, 338] and mouse hepatocytes [339]. The extremely low toxicity of nAl_2O_3 was also reported on human lung cells [340]. The acute toxicity of $nTiO_2$ was also quite low, consistent with a previous study on the toxicity of $nTiO_2$ to *D. magna* which showed that even at the highest tested concentration of 500 mg/L, only 9% mortality of *D. magna* was observed [341]. Although the confidence interval for nAl_2O_3 and $nTiO_2$ was broad, it did not impact our analysis on their toxicity owing to the extremely high 48-h LC_{50} of nAl_2O_3 and $nTiO_2$ to *P. multimicronucleatum*. $nSiO_2$ was more toxic than $nTiO_2$, which was also reported previously [342]. $nCeO_2$ was less toxic than $nSiO_2$ but more toxic than $nTiO_2$. A prior study showed that the 48-h LC_{50} of $nCeO_2$ to *D. magna* was greater than 1000 mg/L [310], which agrees well with the present study. The toxicity of nZnO to *P. multimicronucleatum* was close to that of $nSiO_2$.

The ion release from NPs was measured with ICP-MS, and the results were presented in Table 6.4. Only nZnO and nCuO released detectable metal ions. Zn^{2+} and Cu^{2+} are thus possible sources for the toxicity of nZnO and nCuO, respectively. However, at the concentration of 48-h LC_{50} point, nZnO and nCuO released 108.5 ± 23.6 mg/L of Zn^{2+} and 3.2 ± 0.5 μg/L of Cu^{2+}, respectively; the concentrations of released ions were less than the 48-h LC_{50} values for Zn^{2+} (175.2 mg/L) and Cu^{2+} (19.5 μg/L), which were measured in the current study using $ZnCl_2$ and $CuCl_2$. This suggested that the toxicity of nZnO and nCuO to *P. multimicronucleatum* might partially be attributed to particles. The other five types of metal oxide NPs did not release metal ions, implying that particles instead of released ions governed the toxicity of these NPs.

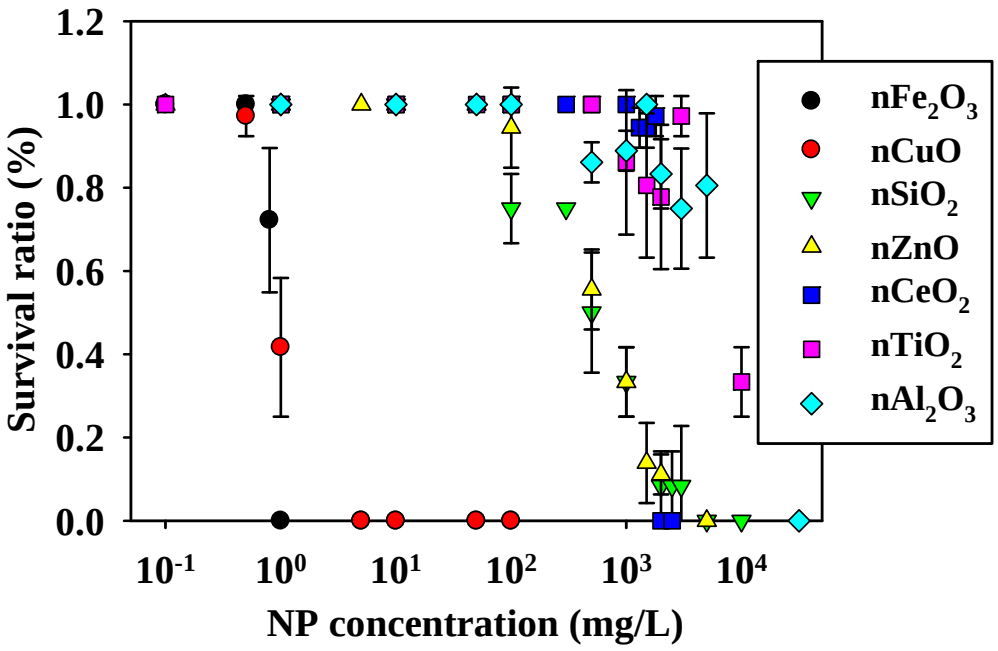

Figure 6.4. Mean survival ratios (± s.d.) of *P. multimicronucleatum* after 48-h exposure to NPs with varying concentrations.

Table 6.3. The 48-h LC_{50} of tested metal oxide NPs to *P. multimicronucleatum*, the magnitude of interaction energy barrier between NPs and cell surface, and the adsorption rate constants of NPs onto the cell membrane.

NPs	48-h LC_{50} (mg/L)	95% confidence intervals (mg/L)	Energy barrier (kT^a)	Adsorption rate constant (m/s)
nFe_2O_3	0.81	0.60–1.09	1.36	3.05×10^{-5}
nCuO	0.98	0.84–1.25	1.61	9.26×10^{-6}
$nSiO_2$	442.6	337.0–559.8	10.9	2.75×10^{-10}
nZnO	573.8	448.6–707.9	5.71	5.46×10^{-8}
$nCeO_2$	1832.5	1739.9–1925.1	7.81	5.15×10^{-9}
$nTiO_2$	7215.2	3730.1–38142.7	31.8	1.45×10^{-19}
nAl_2O_3	9269.2	4783.1–35409.6	33.9	6.62×10^{-21}

[a]kT is an energy unit. k–Boltzmann constant (1.38×10^{-23} JK^{-1}); T–Absolute temperature

Table 6.4. The ion release ratios of tested NPs suspended in Dryl's solution, as measured with ICP-MS.

Tested NPs	Ion release ratio (%)
nAl_2O_3	0
$nCeO_2$	0
$nSiO_2$	0
nZnO	23.56 ± 0.12
nCuO	0.41 ± 0.04
nFe_2O_3	0
$nTiO_2$	0

6.4.3. Calculation of interfacial interactions between NPs and cell membrane

Ion release and reactive oxygen species (ROS) production were recognized as two important mechanisms for the cytotoxicity of NPs in addition to interactions between NPs and cell surface [82, 343]. We investigated the generation of three types of ROS ($^1O_2$, •OH,

and $O_2^{\bullet-}$) by metal oxide NPs using indicator method. The results showed that under room light, even TiO_2 NPs did not produce any of the three types of ROS that could be detected using the indicator method. This is probably owing to the antioxidant effect of citrate ions in the Dryl's solution [344, 345]. In addition, *Paramecium* species are relatively tolerant to oxidative stress [346]. Therefore, in the current study, ROS may play a very minor role in the toxicity of tested metal oxide NPs to *P. multimicronucleatum.* Ion release, as discussed earlier, only occurred on nCuO and nZnO; also, released Cu^{2+} and Zn^{2+} ions were not the sole factor that contributed to the toxicity of nCuO and nZnO. Hence we proposed that in this study, the interaction between NP and cell membrane was an important mechanism for NP toxicity to *P. multimicronucleatum*. It is thus worth exploring whether or not the interfacial interactions correlate with the toxicity of NPs.

The interfacial interaction between two charged surfaces is widely described by the famous DLVO theory [213, 347], which characterizes the total interaction as the combination of van der Waals (vdW) and electrostatic double layer (EDL) interactions. Because the vdW interaction is always attractive while the EDL interaction can be repulsive in some cases, an energy barrier may arise in the total interaction energy profile. The energy barrier denotes the maximum height of the total interaction profile and has to be surmounted by the interacting objects to approach one another and adhere together. A low energy barrier between NPs and cell surface implies that the NPs would more easily approach the cell surface and subsequently result in a strong association. Hence the energy barrier is potentially used for evaluating the strength of interfacial interactions between NPs and cell surface.

Because *P. multimicronucleatum* is remarkably larger than NPs, their interaction can be approximated as a sphere-flat plate interaction. The vdW attractive energy (V_{vdW}) of NP-cell membrane interaction, as a function of separation distance h, can thus be computed using Eq. (1) [262]:

$$V_{VdW}(h) = -\frac{A_H r}{6h} \qquad (1)$$

where A_H is the NP-cell Hamaker constant in water; the computation of A_H is given below. r is the radius of NPs, which in computation is replaced with the hydrodynamic radius as measured from DLS.

For materials 1 and 3 in a medium consisting of material 2, the Hamaker constant is denoted as A_{121} and A_{323}, respectively. A_{11}, A_{22}, and A_{33} are used to denote the Hamaker constants of materials 1, 2 and 3, respectively, in a vacuum. Eq. (2) was proposed to obtain an approximate value of A_{123} [266].

$$A_{123} \approx \left(\sqrt{A_{11}} - \sqrt{A_{22}}\right)\left(\sqrt{A_{33}} - \sqrt{A_{22}}\right) \qquad (2)$$

The Hamaker constant for water in vacuum (A_{22}) is 5.0×10^{-20} J.[348] The Hamaker constant for *P. multimicronucleatum* (A_{33}) has not been reported in the literature, and thus an estimate must be made. The Hamaker constants for other unicellular microbial organisms were reported to range from 4.13×10^{-20} to 8.04×10^{-20} J,[349] with a mean value of 6.8×10^{-20} J, which was used in our study.

Table 6.5. The Hamaker constants for the particle-particle interaction in water (A_{121}) and for the particle-cell interaction in water (A_{123})

Tested materials	A_{121} **($\times10^{-20}$ J)**	A_{123} **($\times10^{-21}$ J)**
nAl_2O_3	3.67 [a]	7.12
nCeO_2	5.57 [b]	8.77
nSiO_2	1.02 [a]	3.75
nZnO	1.89 [a]	5.11
nCuO	3.5 *	6.95
nFe_2O_3	5.4 [c]	8.64
nTiO_2	0.35 [d]	2.20

* The Hamaker constant for CuO was not found in the literature. Because most reported A_{121} values for metal oxides fell into the range of $1–6\times10^{-20}$ J, we used the mean value 3.5×10^{-20} J as the A_{121} for CuO.

References: [a]Bergström, 1997;[350] [b]Karimian and Babaluo, 2007;[252] [c]Amal, 1990;[351] [d]Gómez-Merino et al., 2007;[352] [e]Ma, 2010.[353]

The EDL repulsive energy (V_{EDL}) of NP-cell membrane interaction is given by Eqs. (3a-c) [251].

$$V_{EDL}(h) = \frac{128\pi kTn\gamma_1\gamma_2 r}{\kappa^2}\exp(-\kappa h) \qquad (3a)$$

$$\gamma_i = \tanh\left(\frac{z_i e\psi_{Si}}{4kT}\right) \qquad (3b)$$

$$\kappa^{-1} = \sqrt{\frac{\varepsilon\varepsilon_0 kT}{2N_A Ie^2}} \qquad (3c)$$

where n is the concentration of electrolytes; k is the Boltzmann constant; T is absolute temperature; z_i is the valency of the i^{th} ion; e is unit charge; ε_0 is the vacuum permittivity; ε is the relative permittivity of water; N_A is Avogadro's number; ψ_{Si} is the surface potential of NPs and cell in an aqueous medium, which can be calculated from EPMs of NPs (U_E), the solution viscosity (η) and permittivity ($\varepsilon\cdot\varepsilon_0$) of water by the Smoluchowski's equation: $\psi_{Si}=(U_E\cdot\eta)/(\varepsilon\cdot\varepsilon_0)$;[254] κ^{-1} is the Debye length; I is the ionic strength (M), $I=0.5\cdot\Sigma c_i Z_i^2$, where c_i is the molar concentration of one species of ions (i). Different EDL energy expressions exist for different types of electrolytes [254]. However, Dryl's solution is a complex mixture composed of 1-1, 1-2, 2-1, and 1-3 electrolytes, and thus an exact analytical expression was not obtained. We instead simplified the system and used Eqs. (3a-c), which was derived for a 1-1 electrolyte, to calculate the V_{EDL}. Using different energy expressions might change the absolute values of the results, but the relative magnitude of the EDL energy among different NP systems would not change.

The NP-cell membrane interaction energy was calculated according to Eqs. (1) and (3), and the net interaction energy profiles were plotted in Figure 6.5. Physicochemical properties of NPs, such as particle size, surface charge, and the Hamaker constant, govern the interaction energy of NPs with cell surface. The magnitude of energy barrier, obtained from Figure 6.5, was then tabulated in Table 6.3. The

magnitude of energy barrier of each NP with cell membrane increases as follows: nCuO < nFe_2O_3 < $nCeO_2$ < nZnO < $nSiO_2$ < $nTiO_2$ < nAl_2O_3.

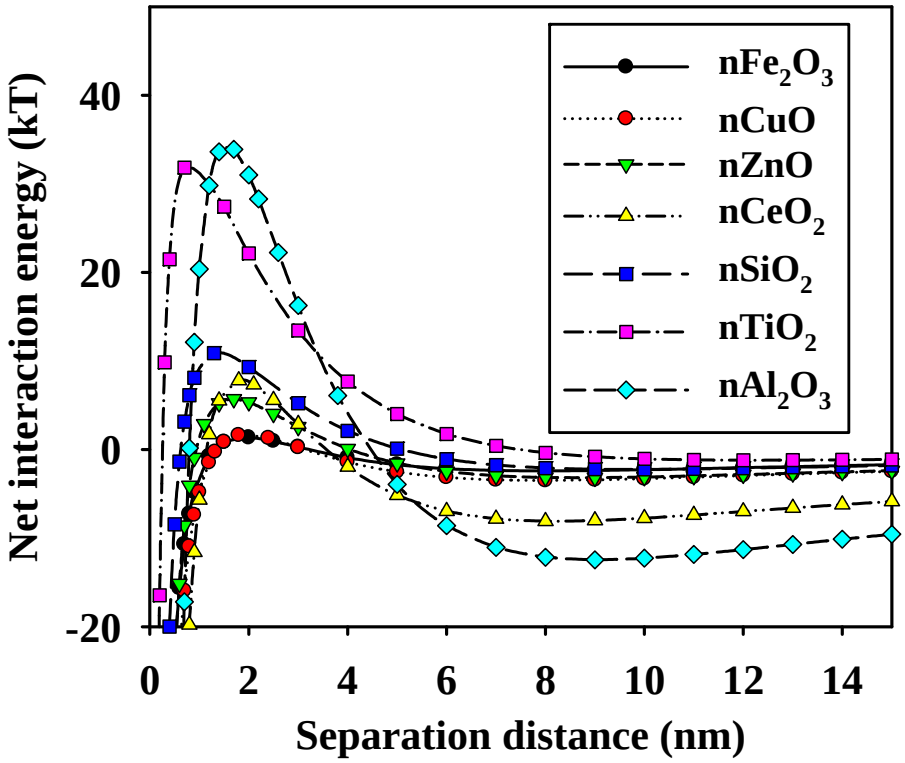

Figure 6.5. Net interaction energy profiles between NPs and *P. multimicronucleatum.*

6.4.4. Correlation between the interaction energy and NP toxicity and underlying mechanisms

We compared the relationship between the magnitude of energy barrier and the 48-h LC_{50} in Figure 6.6, which shows that the 48-h LC_{50} increased linearly (note the log-scale of the Y axis) with increasing energy barrier magnitude, as fitted with the least squares regression method. Depending on the magnitude of energy barrier, three zones can be distinctly divided in our case. The first zone, in which the magnitude of energy barrier is close to 0 and 48-h LC_{50} values were smaller than 1 mg/L, included nFe_2O_3 and nCuO. The second zone, which included $nCeO_2$, nZnO, and $nSiO_2$, had 48-h LC_{50} values

larger than 100 mg/L but smaller than 2000 mg/L. The magnitude of energy barrier was *ca.* 10 kT. The third zone, which included $nTiO_2$ and nAl_2O_3, had 48-h LC_{50} values larger than 5000 mg/L, and the magnitude of energy barrier was larger than 20 kT. With atomic force microscopy (AFM), we examined three or more NP-treated *P. multimicronucleatum* cell surfaces for nCuO, $nSiO_2$ and $nTiO_2$, which respectively belonged to zones 1, 2 and 3. Representative images of NP-treated *P. multimicronucleatum* cells are shown in Figure 6.7. Clearly, many particles or aggregates were observed on *P. multimicronucleatum* after exposure to nCuO. However, on the surface of $nSiO_2$–treated *P. multimicronucleatum,* less particles were observed, while there was almost no particles observed on the surface of $nTiO_2$–treated cells. Since weakly associated-NPs were very likely washed away during the four-times washing cycles with DI water, these AFM results suggested that nCuO particles were more strongly associated with the cell surface relative to the other two NPs, which was consistent with the theoretical analysis on interaction energy barrier. In addition, we noticed that a number of previous studies have compared the toxicity of the same type of NPs in different sizes or with different surface charges [139, 141, 317, 322, 323, 325, 330, 354-356]. The reported results were consistent with the finding of the current study, namely, NPs with lower interaction energy barrier with the cell surface probably induced more severe cytotoxicity. We are investigating the toxicity of same type of NPs with different sizes and surface charges to *Paramecium*, which will make up an interesting follow-up analysis.

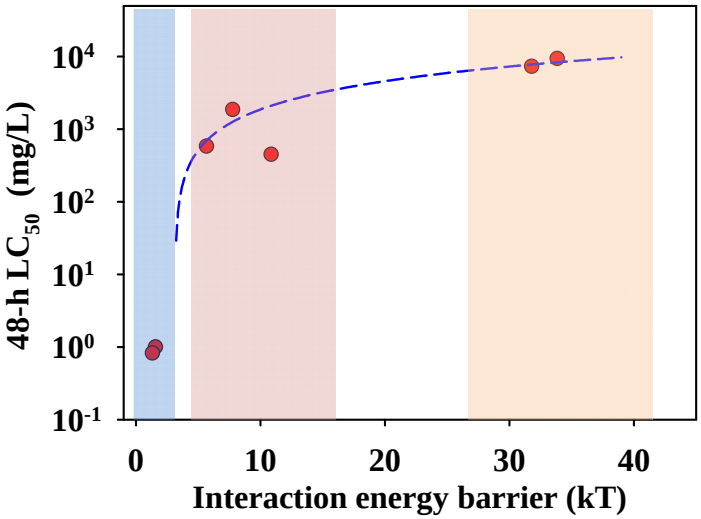

Figure 6.6. Relationship of the magnitude of energy barrier and the 48-h LC_{50} of metal oxide NPs to *P. multimicronucleatum*. The dashed line represents the linear regression (y = 271.1x-843.4, R^2=0.9470).

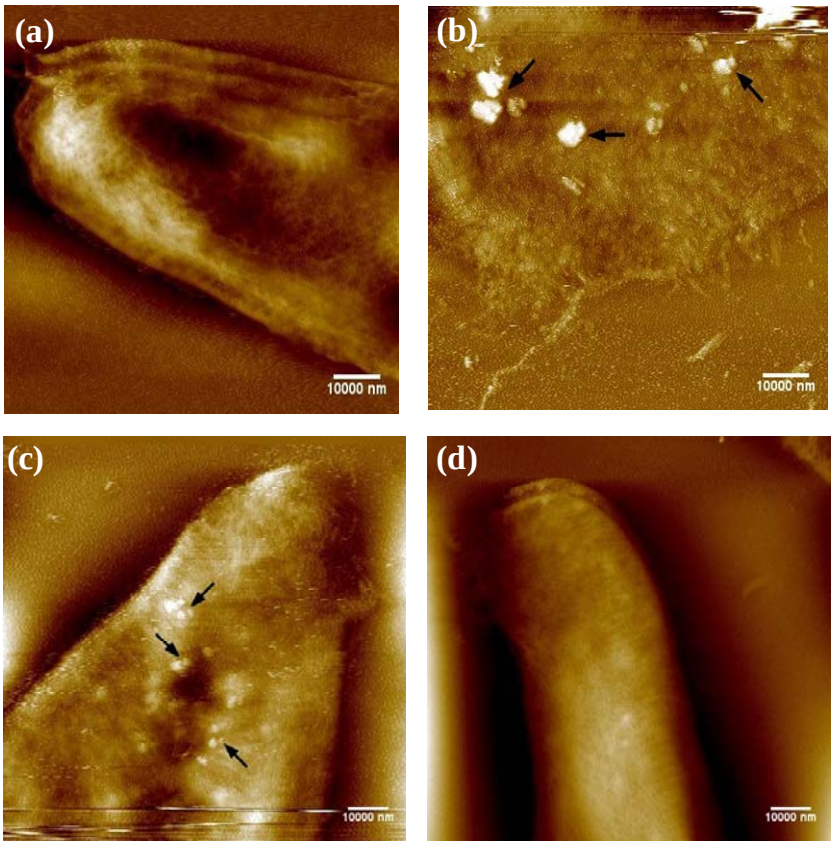

Figure 6.7. AFM images of *P. multimicronucleatum*. (a) Untreated P. multimicronucleatum; (b) P. multimicronucleatum treated with nCuO of 0.5 mg/L; (c) *P. multimicronucleatum* treated with $nSiO_2$ of 100 mg/L; (d) *P. multimicronucleatum* treated with $nTiO_2$ of 100 mg/L. Black arrows indicate the location of NPs on the cell surface.

Although the magnitude of energy barrier is suitable for evaluating the strength of interfacial interactions between NPs and cell surface, it does not give a direct measure of the extent of NP's contact or association with the cell surface. Does a lower energy barrier imply that more NPs will associate with the cell surface? To answer this question, we evaluated the adsorption of NPs onto *P. multimicronucleatum* membrane on the basis of the DLVO and interfacial force boundary layer (IFBL) theories [354]. Given in Eqs. (4) and (5), the adsorption rate can be calculated with the model:

$$\frac{d\Gamma}{dt} = k_a C_w \qquad (4)$$

$$k_a = \frac{D_\infty}{\int_{h=h_0}^{h=\delta_{IFBL}} \left[\left(1 + R_H / h\right)\exp\left(V^{TOT}\left(h\right)/kT\right) - 1\right] dh} \qquad (5)$$

where in Eq. (4) $d\Gamma/dt$ is the rate of NPs' adsorption onto the cell surface in adsorbed number per unit surface area per time. C_w, the effective wall concentration of NPs, is the average local particle concentration within the IFBL. k_a is the adsorption rate constant, which is expressed as in Eq. (5). D_∞ is the diffusion coefficient of bulk NPs, δ_{IFBL} is the thickness of the interfacial force boundary layer, R_H is the hydrodynamic radius of NPs, h is the separation distance between the interacting surfaces, k is the Boltzmann constant, T is the absolute temperature, and the V^{TOT} is the total interaction energy determined from DLVO theory. The calculation of V^{TOT} follows the same equations as that in the calculation of interaction energy barrier.

The experimental determination of C_w is extremely difficult [354]. Since C_w is much less than C_b, with the same bulk concentration, the greater adsorption rate constant correspond to higher adsorption rate. Thus, we directly compared the adsorption rate constant with the magnitude of energy barrier, which was plotted in Figure 6.8. A significant inversely exponential relationship is observed, indicating that a lower energy barrier results in faster adsorption of NPs to cell membrane and thus more NPs contacting the cell surface.

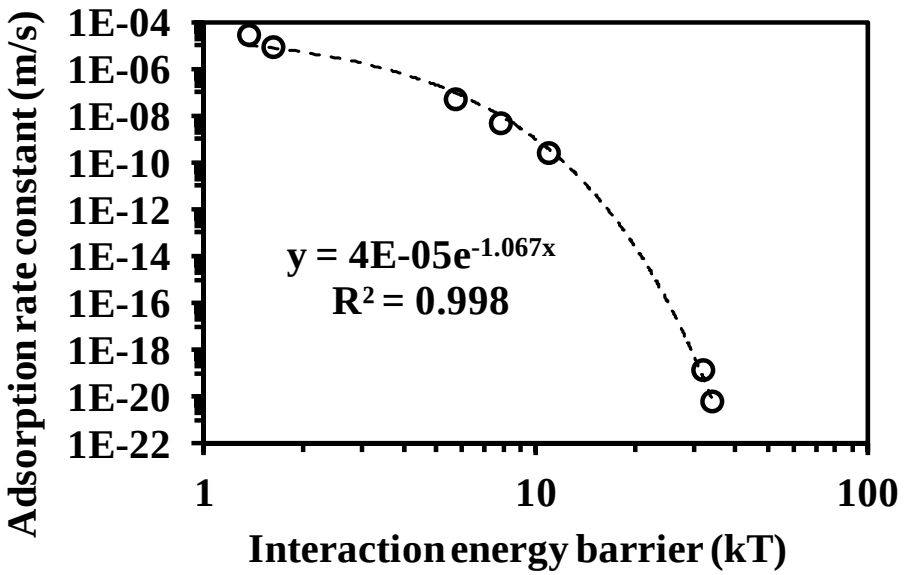

Figure 6.8. The adsorption rate constant of NPs onto *Paramecium* had an inverse exponential relation with the magnitude of interaction energy barrier.

NPs on the cell surface (cell wall or cell membrane) can induce physical and chemical damages to the cell, which may result in death of the cell [137]. Because NPs possess numerous edges, defects, and other reactive sites [138], they may directly inflict physical damage to cell membranes. In addition, for the NPs that released ions, their adsorption on cell surface probably increased local ion concentrations and resulted in toxic effects. Moreover, NPs may generate transient holes in the cell membrane during the uptake process and then induce a loss of membrane polarization and/or the leakage of

cell contents, which can result in cell death [91, 92, 137, 140]. NPs also likely perturb membrane potential and result in increased intracellular Ca^{2+} concentration, which in turn modulates cellular signaling pathways [141]. The optical microscope was used to observe the morphology of the *P. multimicronucleatum* cells treated with NPs. Membrane disruption of *P. multimicronucleatum* was observed after treatment with nCuO and $nSiO_2$ (shown in Figure 6.9).

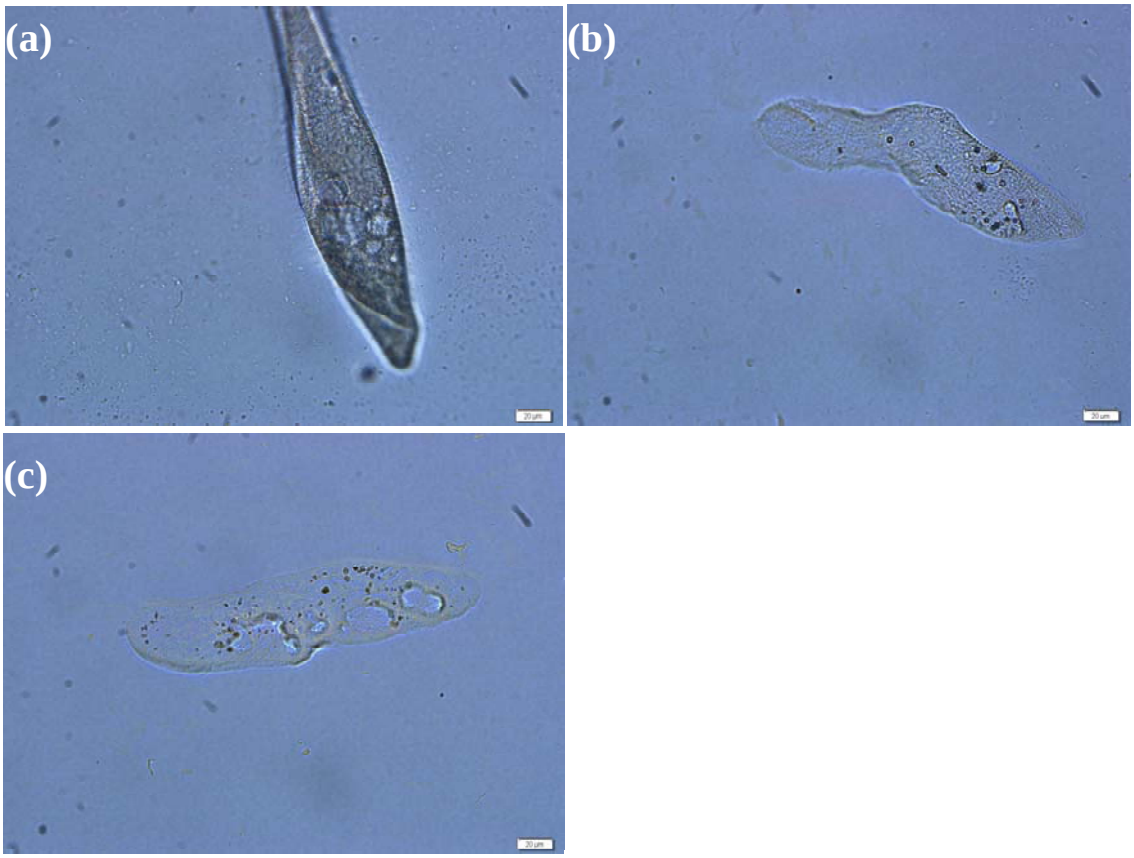

Figure 6.9. Images of *P. multimicronucleatum* under optical microscope. (a) Untreated normal *P. multimicronucleatum*; (b) *P. multimicronucleatum* treated with nCuO of 1 mg/L for 24 h; (c) *P. multimicronucleatum* cells treated with $nSiO_2$ of 500 mg/L for 24 h.

6.5. Conclusion

This study has investigated the toxicity of seven metal oxide NPs to *Paramecium*, which filled in a gap in determining the NP toxicity using this important aquatic organism. Although many mechanisms may contribute to the toxicity of NPs, the importance of interfacial interactions of these NPs with cell surface was stressed in this study. The results presented here showed that metal oxide NPs with strong association with the cell surface tended to induce more severe cytotoxicity. The evaluation of the interfacial interaction between metal oxide NPs and the cell surface is thus of significance in the exploration of NP toxicity mechanisms. It is also implied that the modification of the physicochemical properties of NPs (e.g. surface charge and size) would be an effective approach for regulating the cytotoxicity of metal oxide NPs. Finally, although the current study was conducted on metal oxide NPs and unicellular organisms, there might be a possibility to extend the findings to other NPs and multicellular organisms, which is under further investigation in our lab.

CHAPTER 7

BINDING MECHANISMS OF QUANTUM DOTS WITH DNA: A SINGLE-MOLECULE IMAGING STUDY

7.1. Abstract

The interaction between NPs and DNA is of significance for the toxicological implication research of NPs. In this study, a single-molecule imaging technique based on atomic force microscopy (AFM) was employed to probe the NPs-DNA interactions with quantum dots (QDs) as model NPs. Reproducible high-quality images of single DNA molecules in the air and in liquids were acquired on mica by optimizing sample preparation conditions. Furthermore, the binding of QDs to DNA was explored using AFM. DNA concentration was found to be a key factor influencing AFM imaging quality. The optimal DNA concentration for imaging DNA molecules in the air and in liquids was approximately 2.5 and 0.25 μg/mL, respectively. For imaging DNA binding with QDs in the air and in liquids, the optimal DNA concentration was respectively 0.5 and 0.25 μg/mL. In the presence of QDs, DNA conformation was altered with the formation of DNA condensates. Finally, the fine conformation of QDs-DNA binding sites was examined for analyzing the binding mechanisms. This work is anticipated to advance the understanding of NP-DNA interactions and benefit the toxicity study of NPs induced by the direct NP-DNA interaction.

7.2. Introduction

In the past decade, nanotechnology has achieved tremendous progress in biomedical areas through exploiting unique properties of NPs (NPs) [238]. Of particular interest are small NPs (e.g. quantum dots and gold NPs) in the size range of 1-10 nm,

owing to their size-dependent properties and similar dimensions with biological macromolecules [238]. The similarity stimulates interests for the applications of NPs in medical diagnostics, bio-labeling and bio-imaging, therapy and drug delivery by combining nanotechnology with biology and medicine [238]. These NPs were often conjugated with DNA and other biomolecules for acquiring biocompatibility, molecular recognition capability and other new functions [357, 358]. Understanding the structure of those bioconjugates is important for understanding their stability and functions [359-361].

On the other hand, concerns regarding the toxicity of those small NPs have been raised in view of their unique properties and potential routine applications [362, 363]. The extraordinarily small size of those NPs favors their entry into cells and may subsequently result in adverse effects for intracellular structures [355, 364]. A likely cytotoxicity mechanism of NPs is through their interactions with DNA molecules, which possibly causes DNA deformation and adversely affects the stability and biological functions of DNA [365-369]. It is thus of significance to probe the interaction of NPs and DNA for both understanding the structure of NPs-DNA bioconjugates and evaluating the genetic effect of NPs. To this end, a single-molecule method based on atomic force microscopy (AFM) is employed for direct imaging of NPs-DNA interactions.

AFM has been widely used to image DNA molecules and study DNA-protein interactions [370-373]. Besides three-dimensional visualization, an apparent advantage of AFM over many other high-resolution imaging microscopes (e.g., electron microscopes) is the possibility of observing samples in liquid, which makes it exceptionally suitable for biological molecules imaging [374]. Mica is the commonly used substrate for DNA studies in solutions because DNA can retain its native-like conformation on mica [375]. Since both DNA and mica surfaces carry negative charges under physiological conditions, the binding of DNA onto mica was facilitated either with the aid of divalent ions (e.g. Mg^{2+} and Ni^{2+}) [376] or by modifying mica surface (e.g. 3-aminopropyltriethoxysilane (APTES) modified mica) [377]. Many studies have explored the interaction of proteins and DNA

using AFM [371, 378, 379], but very few attempted to address that between NPs and DNA [380, 381]; to our knowledge, no studies have been done for probing the interaction of NPs and DNA in liquids with AFM.

In this study, we employed semiconductor NPs, also known as quantum dots (QDs), as model small NP, because QDs have unique photophysical properties and thus are especially promising in biological sensing, imaging and detection [359, 382-384]. We firstly acquired reproducible high-quality DNA images in the air and in liquids with AFM, by thoroughly examining different sample preparation methods. Thereafter, we explored the binding of QDs to DNA in the air and in liquids using AFM. The current study is anticipated to benefit the future investigation of the structure of NPs-DNA bioconjugates, and the interaction of NPs and DNA and thus the genetic effect of NPs.

7.3. Materials and methods

7.3.1. Quantum dots

Water-soluble CdSe/ZnS core/shell QDs coated with polydiallydimethylammonium chloride (PDDA) were purchased from Ocean NanoTech, LLC. Size and morphology of QDs were characterized using dynamic light scattering (DLS), high-resolution transmission electron microscopy (HR-TEM) and AFM.

7.3.2. DNA

A SacI-linearized plasmid DNA pGEMEX-1 of 3993 basepairs (Promega Corporation, Madison, WI) was diluted to 5 μg/mL with sterile TE buffer (10 mM Tris(hydroxymethyl)aminomethane hydrochloride (Tris-HCl), pH 7.4, 1 mM ethylenediaminetetraacetic acid (EDTA)) (Fisher Scientific Co., USA) and with 10 mM 4-(2-hydroxyethyl)-1-piperazineethanesulfonic acid (HEPES) buffer (Fisher Scientific Co., USA) for imaging in the air and in liquids, respectively. DNA dilutions were stored in a 4°C refrigerator for no longer than two months to maintain the intact structure.

7.3.3. Substrate

Unmodified mica (Highest grade V1, Ted Pella, Redding, CA) was glued to steel discs (Ted Pella, Redding, CA) with epoxy resin (Loctite, Rocky Hill, CT) and cleaved with adhesive tape immediately before use. APTES (TCI America, Portland, OR)-modified mica was prepared according to previous studies [385, 386]. Briefly, freshly cleaved mica was left in the APTES atmosphere generated by a small pool of APTES solution at the bottom of a glass desiccator for 2 h. Our preliminary results showed that the mica surface after treatment with APTES might become bumpy if the preparation is not delicately controlled. Hence for the sake of convenience, the unmodified mica with the aid of divalent ions was recommended for imaging DNA with AFM.

7.3.4. Sample preparation

DNA immobilization on mica. For imaging in the air, DNA stock solution was diluted to 2.5 μg/mL with sterile TE buffer. $MgCl_2$ (ACS grade, Fisher Scientific Co., USA) was added to a final concentration of 5 mM. 2.5 μL of the DNA solution was deposited on a freshly cleaved mica substrate that was placed in a small covered Petri dish, and incubated for 30 minutes. The edge of the droplet might dry on the surface, but we only imaged a very small area of the central part of the droplet, which was far away from the edge and not affected by the drying. The mica surface was rinsed thoroughly with MilliQ pure water and then blown dry with ultrapure nitrogen gas. For imaging in the liquid, DNA stock was diluted to 0.25 μg/mL with sterial 10 mM HEPES buffer (pH 7.4). $MgCl_2$ was added to a final concentration of 4 mM. 5 μL of the DNA solution was spotted onto a freshly cleaved mica substrate and incubated for 30 minutes. The sample was then rinsed with 1 mL of DNA imaging buffer (10 mM HEPES pH 7.4, 4 mM $MgCl_2$, 2 mM $NiCl_2$ (ACS grade, Boston Bioproducts, Worcester, MA)). Thereafter, the sample was immediately fixed onto a liquid cell sample plate, which was further filled with 500 μL DNA imaging buffer. These conditions were found to be optimal for

acquiring high-quality DNA images. Optimization involved varying the DNA concentration (0.1-5 μg/mL), incubation time (5-60 min), deposition volume (1-10 μL), $MgCl_2$ concentration (1-10 mM), and $NiCl_2$ concentration (1-10 mM).

Binding of QDs to DNA. DNA of final concentration 0.5 μg/mL and 0.25 μg/mL, respectively for imaging in the air and in liquids, was mixed with QDs at a molar ratio of 1:5 and incubated at 37 °C for 1 h. The buffer solutions were the same as those used in the absence of QDs. 2.5 μL of the mixture was applied to the mica substrates following the same procedures as above-mentioned DNA immobilization methods, except that the incubation time on the substrate was 45 min to achieve an optimal imaging quality.

7.3.5. AFM imaging

Images were collected at room temperature in the air or in the liquid using an Agilent 5500 Molecular Imaging AFM in the acoustic alternating current (AAC) mode. Rectangular silicon cantilevers and triangular silicon nitride cantilevers (BudgetSensors, Bulgaria) were used for imaging in the air and in the liquid, respectively [371]. The silicon cantilevers have a force constant of approximately 2–5 N/m and a tip radius smaller than 10 nm, and the silicon nitride cantilevers have a force constant of approximately 0.27 N/m and a tip radius smaller than 15 nm. For imaging in the liquid, it was helpful for improving image quality by manually engage the tip to sample until the trace and retrace signals are highly correlated. The deflection amplitude was 2.5 V and the scanning speed was 1-2 μm/s. Images were processed by flattening to remove the background slope with the Picoview software.

7.4. Results and discussion

7.4.1. Characterization of QDs

HR-TEM image (Figure 7.1a) showed that QDs were close to spherical in shape and had a relatively uniform size distribution. The diameter of QDs was approximately 3.4 ± 0.5 nm, based on the measurement of randomly selected 30 particles. AFM image,

presented in Figure 7.1b, showed that the diameter of QDs was in a range of 15-35 nm, remarkably larger than TEM-size, which is reasonable due to tip-induced broadening effect [387]. The heights of QDs fell into a range of 3-5 nm (see the inset representative cross-sectional profile), which was close to the TEM-measured size. The particle size distribution of QDs in buffer was measured with DLS, which indicated the number-weighted average hydrodynamic diameter of QDs were approximately 5.4 nm with a relatively uniform size distribution. The isoelectric point of QDs was 10.8. At pH 7.4, as used in the current AFM study, the QDs were positively-charged and stable, and particle aggregation was not observed.

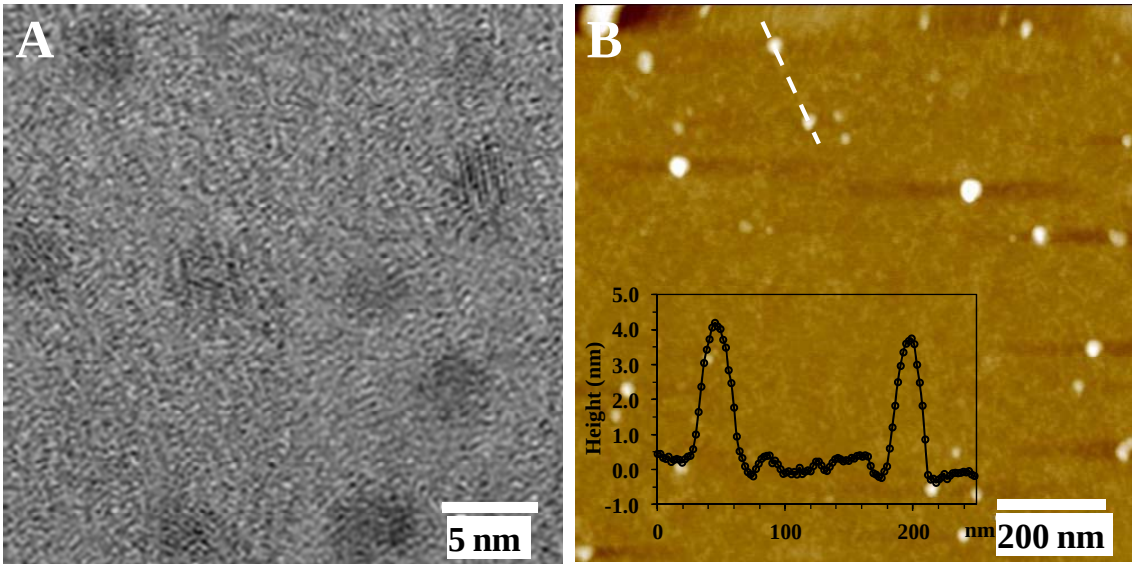

Figure 7.1. (A) HR-TEM image of PDDA-coated QDs. (B) AFM image of PDDA-coated QDs. The inset in (B) is the height profile of the cross-section marked with white dashed line.

7.4.2. Imaging DNA molecules in the air and in liquids with AFM

Figure 7.2a shows a typical AFM topographical image of SacI-linearized pGEMEX-1 DNA molecules immobilized by Mg^{2+} on mica in the air. Single DNA molecules are clearly visualized. The contour length of DNA was determined to be 1414.8 ± 38.9 nm based on the measurement of randomly-selected 50 DNA molecules,

which was quite close to the theoretical length for B-form DNA (3993 kbp and 0.34 nm/basepair). The heights of the DNA molecules were in a range of 0.7–1.2 nm by analyzing the cross-section topographical profiles (shown in Figure 7.2c); the height of DNA is much smaller than the expected value of 2 nm, which may result from the elastic deformation of DNA molecules when the tip tapped on DNA [388]. Similar to other studies [389], the width of DNA molecules was approximately 16–22 nm, which is much greater than 2 nm (theoretical width of double-stranded DNA) probably due to the tip-induced broadening effect.

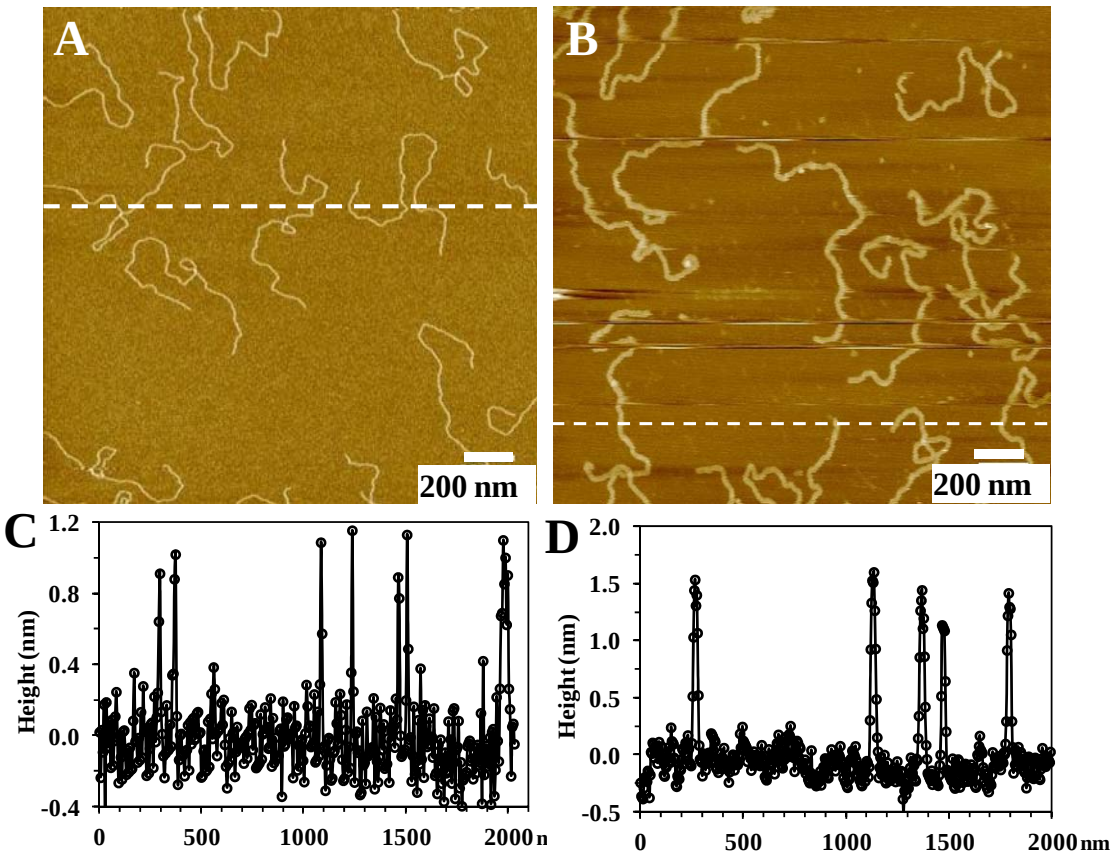

Figure 7.2. AFM topographical images of DNA in the air (A) and in liquids (B). (C, D) Height profiles of cross-sections marked with white dashed lines in (A) and (B), respectively.

One major advantage of AFM is that it can image biological molecules in physiologically relevant buffers, which benefits the direct observation of some in situ biological processes [376, 390-392]. Figure 7.2b showed the AFM images of DNA molecules immobilized by Mg^{2+} and Ni^{2+} on mica in liquids. The height of DNA molecules in liquid was in a range of 1.2–1.8 nm, which was larger than that in the air. The reason was probably that the liquid mitigated the compression of the DNA by the tip [393]. Appropriate DNA concentration (0.25 μg/mL) was of primary significance for imaging DNA in liquids, as high concentration resulted in abnormal DNA conformation.

7.4.3. Imaging the binding of QDs to DNA in the air and in liquids with AFM

AFM images of the binding of QDs to DNA immobilized by Mg^{2+} on mica in the air and immobilized by Mg^{2+} and Ni^{2+} on mica in liquids were shown in Figure 7.3a and 3b, respectively. It is noted here that the binding of QDs onto DNA consists of both specific and non-specific bindings [394, 395]; namely, all of the QDs associated with DNA molecules were counted as bound QDs. It is clearly visualized that many QDs bind onto DNA molecules as indicated by the white dots. The cross-section topographical profiles in Figure 7.3d and 7.3e show that the height of the binding site is approximately 3-4 nm. Phase images were simultaneously acquired along with the topography images. Relying on the phase shift of the cantilever oscillation relative to the driving signal, which is influenced by the material properties, e.g. stiffness, adhesion and other viscoelastic parameters [392, 396], the phase imaging could benefit for differentiating materials in the same image. As we see in Figure 7.3c, QD particles are apparently differentiated from DNA molecules by color. Phase images also likely have a higher signal-to-noise ratio over the topographical images, especially at lower imaging forces and less optimized conditions, e.g. fast scanning rate. As shown in Figure 7.4, the phase image shows better contrast than topography image at a fast scanning rate [397].

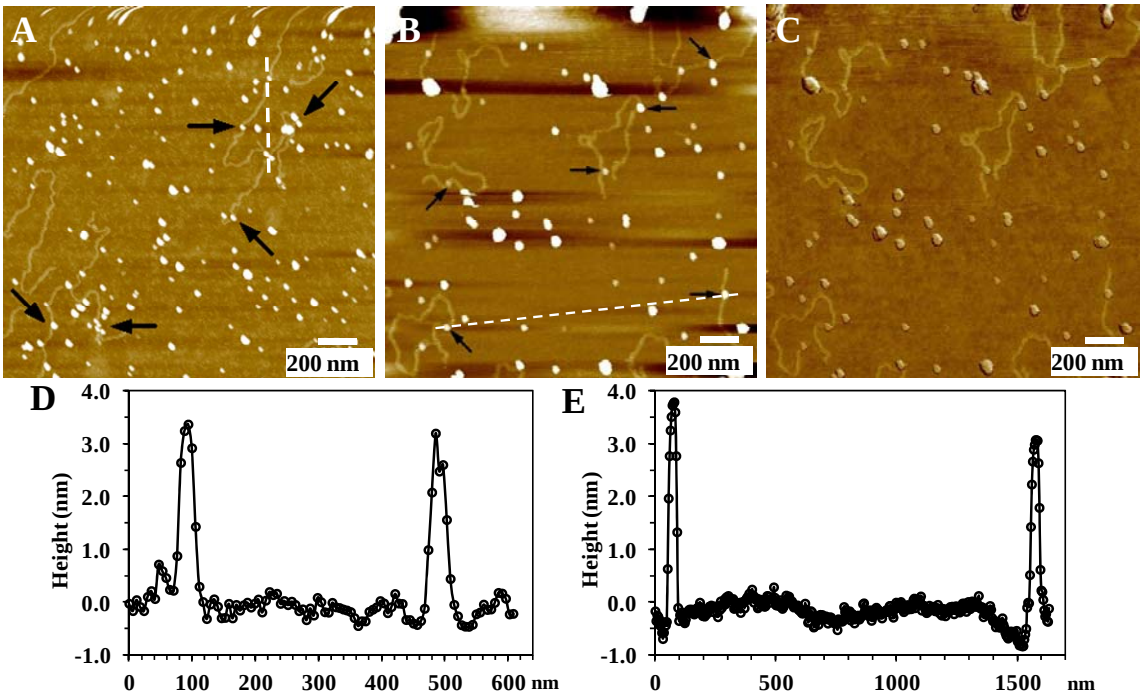

Figure 7.3. (A) AFM topographical image of QDs binding on DNA in air. (B, C) AFM topographical and corresponding phase images of QDs binding on DNA in liquid, respectively. Black arrows indicate representative binding sites of QDs on DNA. (D, E) Height profiles of cross-sections marked with white dashed lines in (A) and (B), respectively.

After interacting with QDs, DNA conformation probably changed; as we see in Figure 7.5, DNA condensations were generated by QDs, which likely further affect the regulation of many cellular processes involving DNA [398-400]. Seeming DNA loops were also observed with QDs bound on the crossing points. It is challenging to determine whether those DNA loops were caused by QDs, because similar "loop-like" DNA conformations were also observed in the absence of QDs (shown in Figure 7.2). Nevertheless, we cannot rule out the possibility that the presence of QDs resulted in some DNA loops, which requires further investigation and validation.

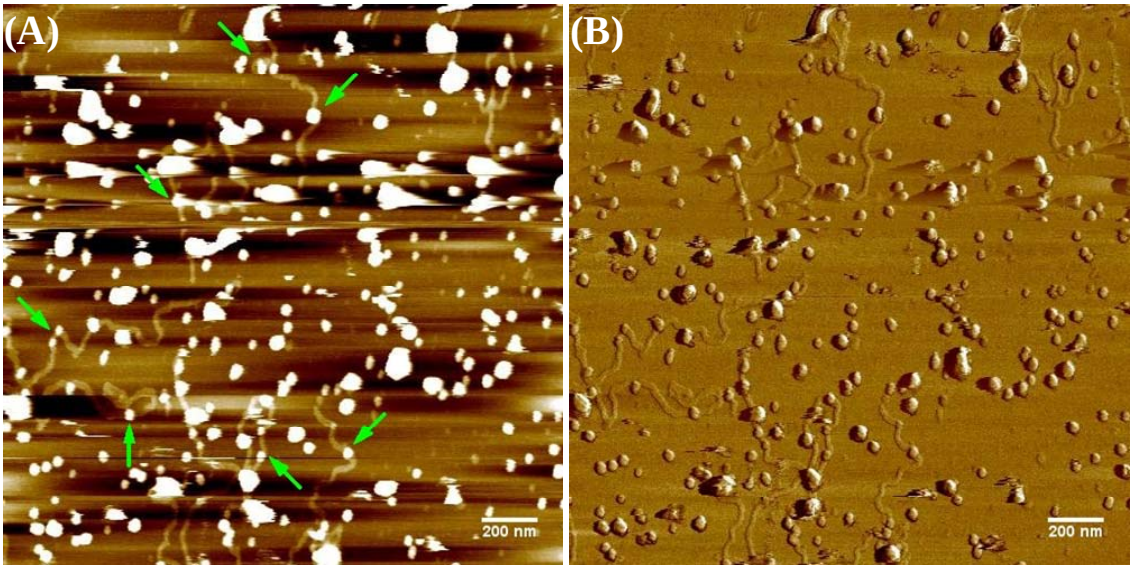

Figure 7.4. (a) and (b) are AFM topographical and corresponding phase images of DNA binding with QDs in the liquid, respectively. Green arrows indicated representative binding sites of QDs on DNA.

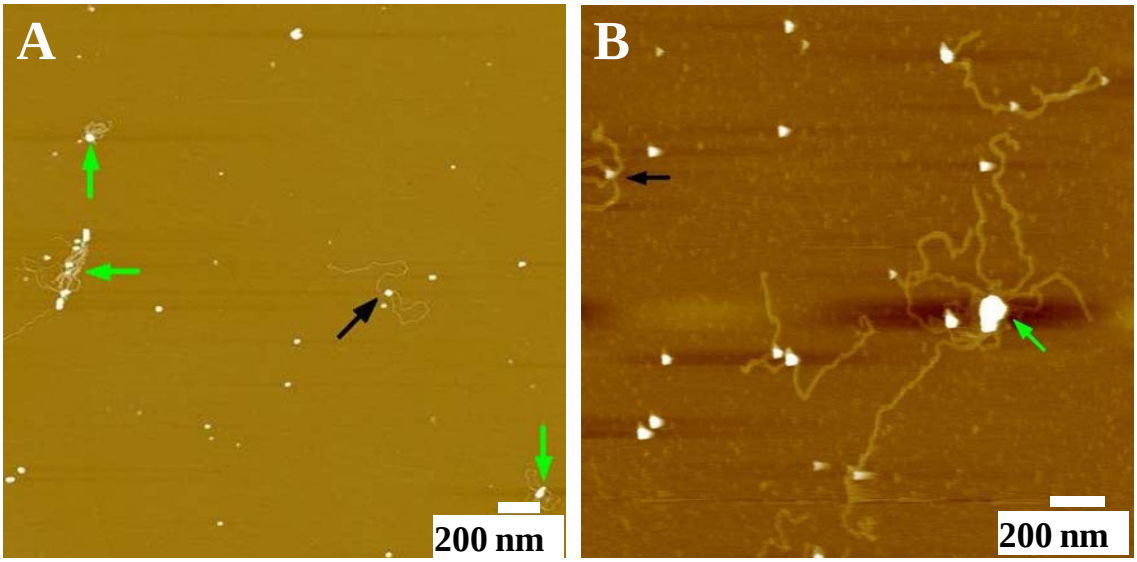

Figure 7.5. AFM topographical images illustrating the change of DNA conformation after binding with QDs in air (A) and liquids (B). DNA condensates and DNA loops were observed after exposure to QDs. Green arrows indicate DNA condensations. Black arrows indicate apparent DNA loops that may be caused by QDs.

7.4.4. Binding mechanisms of QDs to DNA

The high-quality AFM imaging in liquids allows us to examine the fine conformation of QDs-DNA binding sites. From the representative images of binding sites shown in Figure 7.6, we found that QDs may bind onto DNA via four mechanisms: (1) QDs externally bind to DNA backbones; (2) DNA wraps around a QD; (3) QDs seemingly generate DNA loops by simultaneously binding to two different sites on a DNA molecule; (4) QDs form a bridge to connect two or more DNA molecules together. Those binding mechanisms were also observed in a previous study [381]. The binding of QDs onto DNA resulted from the high affinity of QDs to DNA. At pH 7.4, PDDA-coated QDs carry positive charge while DNA molecules bear negative charge due to the phosphate group (PO_4^-) in DNA backbone. Both electrostatic and van der Waals interactions between QDs and DNA are attractive, which favor the attachment of QDs onto DNA.

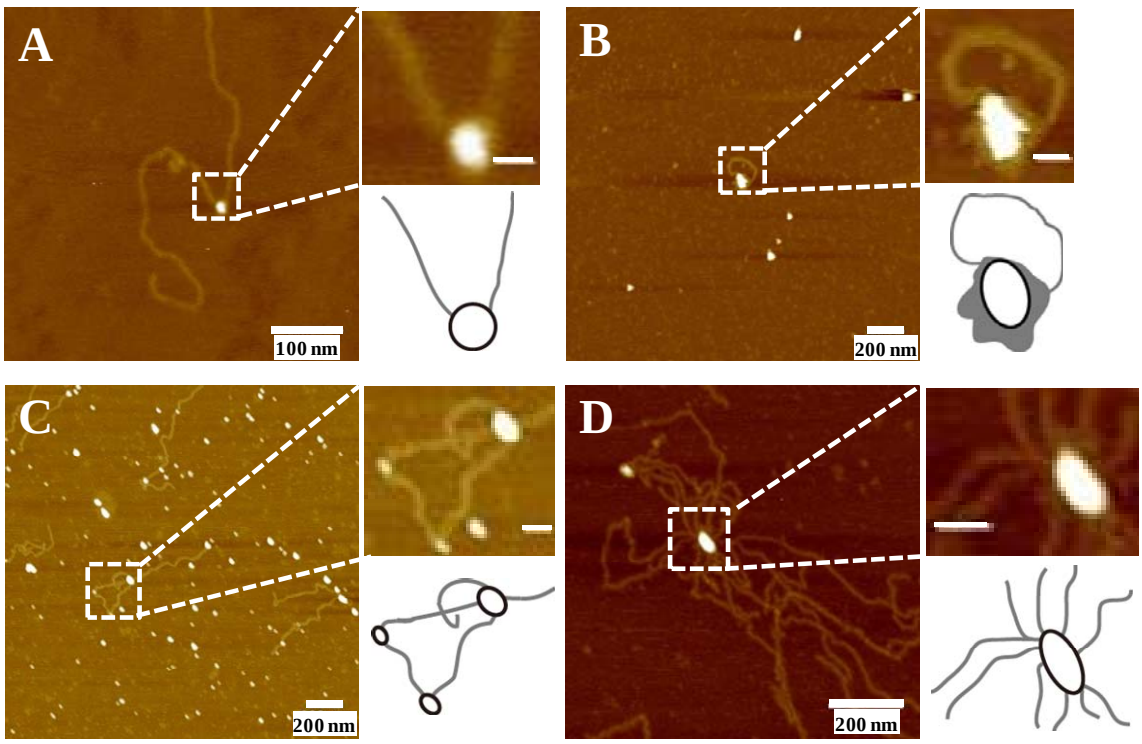

Figure 7.6. Representative images illustrating the binding sites of QDs on DNA. (A) QDs externally bind to the DNA backbone. (B) DNA wraps around a QD. (C) QDs seemingly

induce DNA looping by simultaneously binding to two different sites on a DNA molecule. (D) QDs connect two or more DNA molecules. In each panel, the left image shows the entire DNA molecule, the upper right image shows the "zoomed-in" binding site, and the bottom right figure shows the outline of binding sites.

We statistically examined over 300 DNA molecules to count the frequency of each binding mechanism. As shown in Figure 7.7, approximately 63% of DNA-QDs interactions belong to mechanism (1), namely, QDs directly binding onto the DNA backbone. In addition, approximately 16% of QDs binding to DNA would bridge two or more DNA molecules. The remaining 20% almost equally belong to mechanism (2) and (3).

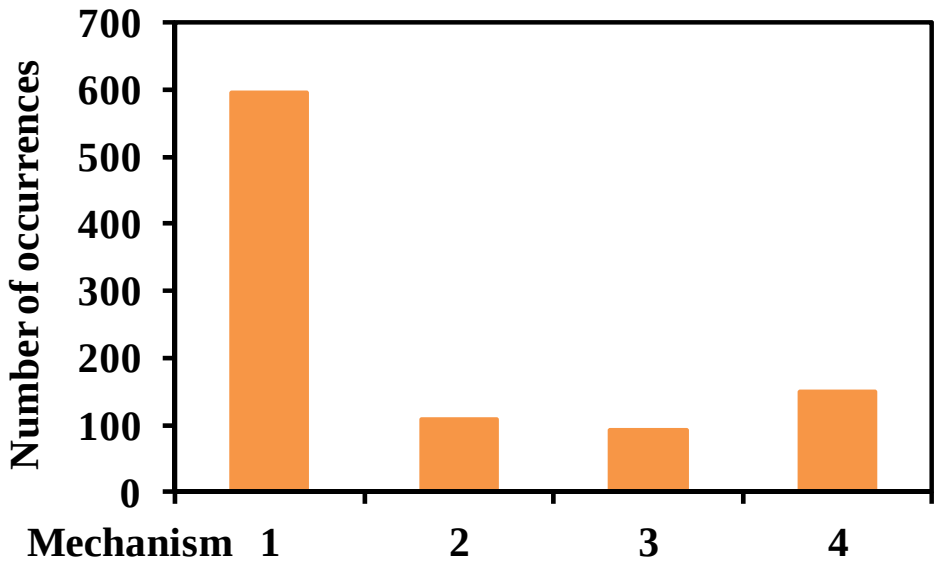

Figure 7.7. Frequency of each binding mechanism.

To explore the underlying fundamentals on the unequal frequency of each binding mechanism, we further computed and analyzed the interaction energy between QDs and DNA molecules. As shown in the net energy profiles (Figure 7.8), no energy barrier exists for the interaction of QDs and DNA, indicating that the binding of QDs to the DNA backbone (i.e. mechanism (1)) was thermodynamically favorable. On the contrary, all of the other three mechanisms involve the approach of one section of DNA to another,

which can be viewed as two negatively charged cylinders approaching each other, as the double-stranded DNA is a rigid polyelectrolyte with a persistent length of approximately 50 nm [401], remarkably larger than the separation distance between neighboring charges (~ 0.17 nm) [402]. The net interaction energy profiles for two parallel and crossed DNA molecules were presented in Figure 7.8, from which we can see that an energy barrier exists between two interacting DNA molecules regardless of their configuration. Hence the QDs-DNA configurations formed by mechanisms (2)-(4) is less energetically favorable than by mechanism (1), which is consistent with the experimental observations that mechanism (1) dominated the QDs-DNA binding mechanisms.

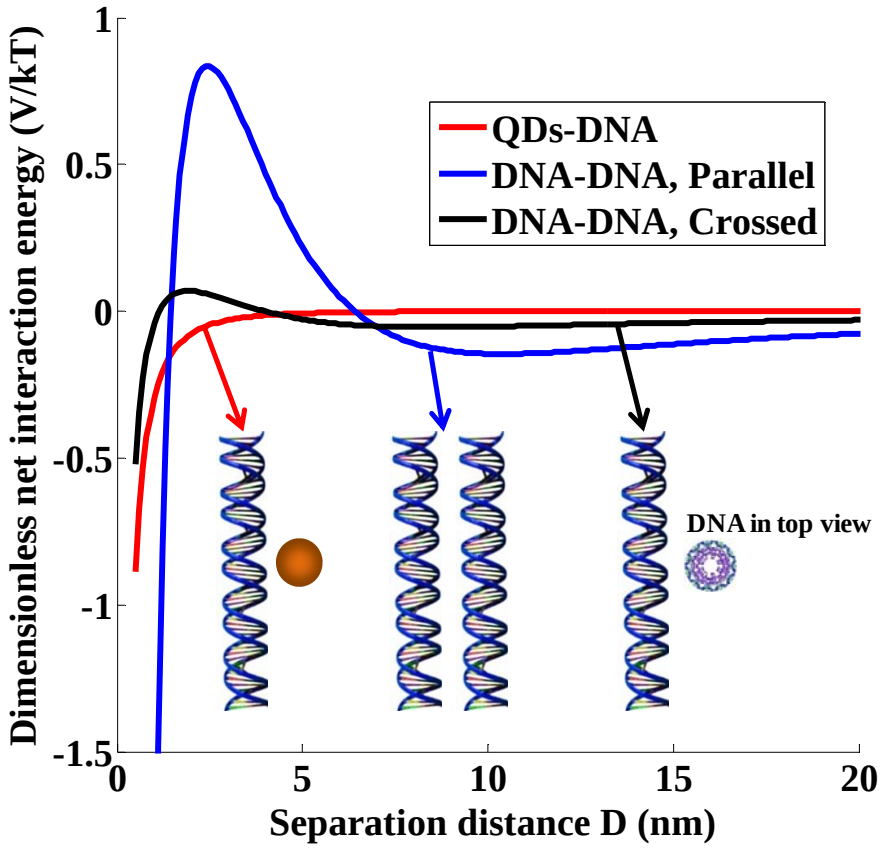

Figure 7.8. Net interaction energy profiles for QDs and DNA, two parallel DNA molecules, and two crossed DNA molecules.

4. Conclusion

This study presented detailed sample preparation methods for acquiring high-quality AFM images of DNA and DNA binding with QDs in the air and in liquids. After interacting with QDs, DNA conformation would change with the formation of DNA condensates. By examining the conformation of QDs-DNA binding sites, four binding mechanisms of QDs with DNA were proposed, which could be helpful for investigating the genetic effect of QDs [381]. This single-molecule imaging technique can be further extended to explore the binding of other NPs on DNA and the structure of NP-DNA bioconjugates, which likely benefit the research on both the implication and application studies of NPs.

CHAPTER 8

PROBING BINDING CHARACTERISTICS OF QUANTUM DOTS WITH DNA: A NOVEL APPROACH USING ATOMIC FORCE MICROSOPY

8.1. Abstract

Understanding the characteristics of NP-to-DNA binding is important for the toxicological assessment of NPs. In this study we employed a single-molecule imaging technique, atomic force microscopy (AFM), to determine the characteristics of NP-to-DNA binding, including the binding kinetics, isotherm, and specificity. We demonstrated the capability of this AFM-based approach using quantum dots (QDs) as a model NP. The binding kinetics and binding isotherm of QDs to DNA were investigated by examining a large number of single DNA molecules after exposure to QDs using AFM; the models that we developed fit the experimental results well. According to the binding kinetics model, the average number of bound QDs per DNA molecule at equilibrium is approximately five, and the binding rate constant is approximately 0.35 s^{-1}. Furthermore, from the binding isotherm the equilibrium binding constant and maximum number of QDs bound to DNA were determined to be approximately 0.23 nM^{-1} and 14, respectively. Finally, by examining the position of QDs on DNA molecules, i.e., the distance from a QD to the nearest DNA terminus, we found that the binding of QDs to DNA is nonspecific.

8.2. Introduction

Owing to their unique physical, chemical, and mechanical properties, NPs (NPs) have been used, or are being evaluated for use, in many fields [403]. In particular, the integration of nanotechnology with biology and medicine means that a diverse array of NPs, such as quantum dots (QDs), gold NPs, and iron oxide NPs, may be used in applications including drug delivery, biolabeling, imaging and tracking, and medical diagnostics [404-410]. However, concerns regarding the toxicity of NPs have been raised in view of their unique properties and potential routine applications [362, 363]. The delivery of NPs into the human body for biomedical uses very likely results in NP entry into cells, which could subsequently cause damage to intracellular structures [411]. One of the primary mechanisms of NP toxicity is through binding to and interaction with DNA molecules, which may induce DNA deformation and adversely affect the normal biological functions of DNA [365-369, 412, 413]. Understanding the binding of NPs to DNA is hence essential for determining the toxicity mechanisms of NPs.

The primary thermodynamic properties used in understanding DNA–NP interactions are binding constants and binding specificities. Several macroscopic methods, such as spectroscopic [414, 415] and electrochemical [416] techniques, have been employed to investigate these properties. Although powerful, these methods cannot determine the binding affinity of NPs for specific sites on DNA and are limited by the assumption that the change in an instrumental signal, such as absorbance, is directly proportional to the extent of binding [395].

To overcome the limitations of these macroscopic methods, we proposed to use atomic force microscopy (AFM) to study the DNA-NP interaction by directly examining single molecules. Using AFM, it is possible to determine the extent of NP binding to DNA as well as binding location on the DNA molecule. The binding characteristics including kinetics, the isotherm, and the specificity can be hence determined. Although this approach has been used in DNA-protein interactions [370-373, 395], to our knowledge,

this study is the first attempt to apply it to the DNA-NP interaction. In this study, we used QDs as a model NP because they have numerous potential applications in biology and medicine as imaging agents [359, 382-384]. We first developed models to describe the binding kinetics and binding isotherm of NPs with DNA. The models were experimentally validated using data acquired from AFM. Essentially, AFM yielded reproducible, high-quality images of the binding of QDs to DNA, and statistical analyses were performed on data from many individual DNA molecules, namely, the number and the position of QDs bound on each DNA molecule under different experimental conditions (*e.g.*, varied incubation time and initial concentration of QDs); in this way we determined the DNA–QD binding constants and specificities for different conditions. The current study is anticipated to benefit future investigations of the interaction of NPs and DNA and thus the toxicological assessment of NPs.

8.3. Theory

8.3.1. Binding kinetics

A DNA molecule may bind with 0, 1, 2, … i, … m NPs; corresponding concentrations of each class of DNA molecules (each class has a particular number of NPs bound to it) are denoted as $[n_0]$, $[n_1]$, $[n_2]$, … $[n_i]$, … $[n_m]$. On the basis of von Smoluchowski's coagulation equation [245], i^{th}-class DNA molecules can be formed from the binding or absorption of $(i–1)^{th}$-class DNA with an NP as well as from the dissociation or desorption of an NP from $(i+1)^{th}$-class DNA; the loss of i^{th}-class DNA stems from the binding or adsorption of an NP onto i^{th}-class DNA as well as from the dissociation or desorption of an NP from i^{th}-class DNA. Using k_a and k_d to represent the adsorption and desorption rate constants, respectively, we can determine the concentration change rate of each class of DNA molecules with the following expressions:

$$\frac{d[n_0]}{dt} = -k_a[NP_{free}][n_0] + k_d[n_1]$$
$$\frac{d[n_1]}{dt} = k_a[NP_{free}][n_0] - k_a[NP_{free}][n_1] + k_d[n_2] - k_d[n_1]$$
$$\frac{d[n_2]}{dt} = k_a[NP_{free}][n_1] - k_a[NP_{free}][n_2] + k_d[n_3] - k_d[n_2] \quad (1)$$
$$\frac{d[n_3]}{dt} = k_a[NP_{free}][n_2] - k_a[NP_{free}][n_3] + k_d[n_4] - k_d[n_3]$$
$$\vdots$$
$$\frac{d[n_m]}{dt} = k_a[NP_{free}][n_{m-1}] - k_d[n_m]$$

where $[NP_{free}]$ represents the concentration of free or unbound NPs. Provided the adsorption and desorption rate constants for all classes of DNA molecules are the same, we can obtain the concentration change rate of the total absorbed/bound NPs on DNA by multiplying the i^{th} term in Eq. (1) (excluding the 1st term) by the corresponding reference number i and then summing those terms:

$$\frac{d}{dt}\left([n_1] + 2[n_2] + 3[n_3] + \cdots\right) = k_a[NP_{free}]\left([n_0] + [n_1] + [n_2] + \cdots\right) - k_d\left([n_1] + [n_2] + [n_3] + \cdots\right) \quad (2)$$

$$\frac{d}{dt}[NP_{bind}] = k_a\left([NP_{tot}] - [NP_{bind}]\right)[DNA] - k_d\left([DNA] - [n_0]\right) \quad (3)$$

where $[NP_{tot}]$, $[NP_{free}]$, and $[NP_{bind}]$ represent the total particle concentration, free particle concentration, and concentration of NPs bound on DNA, respectively. $[DNA]$ represents the total DNA concentration.

The change in the concentration of DNA without any bound NPs ($[n_0]$) is determined in Eq. (4) by solving the system of first-order differential equations in Eq. (1):

$$[n_0] = [DNA]\left(c_0 + c_1 e^{-a_1 t} + c_2 e^{-a_2 t} + c_3 e^{-a_3 t} + \cdots + c_m e^{-a_m t}\right) \quad (4)$$

However, it is a formidable task to obtain the exact expression for all of the constants c_0, c_1, …c_m, a_1, a_2, … a_m. Hence, we directly substituted Eq. (4) into Eq. (3) to obtain Eq. (5):

$$\frac{d}{dt}\left[NP_{bind}\right]+k_a\left[DNA\right]\left[NP_{bind}\right] = k_d\left[DNA\right]\left(c_1e^{-a_1t}+c_2e^{-a_2t}+c_3e^{-a_3t}+\cdots+c_ne^{-a_mt}\right)+k_a\left[NP_{tot}\right]\left[DNA\right]-\left(1-c_0\right)k_d\left[DNA\right] \quad (5)$$

By solving Eq. (5), we can determine $[NP_{bind}]$:

$$\left[NP_{bind}\right]=b_0e^{-k_a[DNA]t}+b_1e^{-a_1t}+b_2e^{-a_2t}+b_3e^{-a_3t}+\cdots+b_me^{-a_mt}+\frac{k_a\left[NP_{tot}\right]-\left(1-c_0\right)k_d}{k_a} \quad (6)$$

where a_1, a_2, … a_m, b_0, b_1, … b_m are constants. Eq. (6) is actually a sum of exponentials; from the standpoint of data fitting, it can be reduced to a sum of two exponential functions, as data conforming to the sum of exponentials are fitted quite well by that type of exponential equation [417].

Furthermore, by dividing the concentration of bound NPs by the concentration of DNA, we can obtain the average number of NPs bound per DNA molecule, which is given by Eq. (7):

$$\frac{\left[NP_{bind}\right]}{\left[DNA\right]}=C_1\left(1-e^{-k_1t}\right)+C_2\left(1-e^{-k_2t}\right) \quad (7)$$

where C_1, C_2, k_1, and k_2 are fitting constants accounting for the roles of adsorption and desorption.

8.3.2. Binding isotherm

A single DNA molecule contains a number of binding sites, S. The "reaction" takes place through this mechanism: $S + NP \leftrightarrow S - NP$. The equilibrium binding constant K is thus given by Eq. (8) [418]:

$$K=\frac{\left[S-NP\right]}{\left[S\right]\left[NP\right]} \quad (8)$$

where $[S]$, $[NP]$, and $[S - NP]$ represent the number of empty sites, the number concentration of NPs, and the number of occupied sites, respectively.

The number of total binding sites $[S_0]$ is the sum of the numbers of empty sites $[S]$ and occupied sites $[S - NP]$:

$$[S_0] = [S] + [S - NP] = \frac{[S - NP]}{K[NP]} + [S - NP] = \frac{1 + K[NP]}{K[NP]}[S - NP] \qquad (9)$$

$$\frac{[S - NP]}{[S_0]} = \frac{K[NP]}{1 + K[NP]} \qquad (10)$$

Because $[S - NP]/[S_0] = N/N_{max}$, where N and N_{max} are the binding number and the maximum number of NPs bound per DNA molecule, respectively, we can obtain Eq. (11), which is actually a Langmuir-type adsorption equation:

$$N = \frac{N_{max} K[NP]}{1 + K[NP]} = \frac{N_{max}[NP]}{1/K + [NP]} \qquad (11)$$

8.4. Materials and methods

8.4.1. DNA and QDs

SacI-linearized plasmid DNA pGEMEX-1 (Promega Corporation, Madison, WI), which has 3993 base pairs, was diluted to 2 nM with sterile 10 mM Tris HCl (pH 7.4) and 1 mM EDTA (TE) buffer (Fisher Scientific Co., USA). AFM images showed that the DNA can be stored in a 4°C refrigerator for two months without loss of structural integrity.

Water-soluble CdSe/ZnS core/shell QDs coated with polydiallydimethylammonium chloride (PDDA) were purchased from Ocean NanoTech, LLC. In our previous studies the QDs were thoroughly characterized using dynamic light scattering (DLS), high-resolution transmission electron microscopy (HR-TEM), Fourier transform infrared spectroscopy (FTIR), and AFM [333, 413].

8.4.2. AFM imaging and analysis

DNA stock solutions were diluted to 0.4 nM with sterile TE buffer. $MgCl_2$ was added to a final concentration of 5 mM. In the binding kinetics study, 0.4 nM DNA samples were incubated with 4 nM of QDs at room temperature for 0.5, 1, 3, 4, 7, 12 and 20 h. In the binding isotherm study, 0.4 nM DNA samples were mixed with QDs at molar

ratios of 1:1, 1:2.5, 1:5, 1:7.5, 1:10, 1:15, and 1:20 and then incubated at room temperature for 12 h. In both binding kinetics and binding isotherm studies, 2.5 μL of the DNA-QD mixture was deposited on a freshly cleaved mica surface and incubated for 45 minutes at room temperature. The mica surface was rinsed thoroughly with MilliQ water and blown dry with ultrapure nitrogen gas, after which the sample was ready for AFM imaging.

Images were collected at room temperature in air using an Agilent 5500 Molecular Imaging AFM in acoustic alternating current (AAC) mode. Rectangular silicon cantilevers (BudgetSensors, Bulgaria) with a force constant of approximately 2–5 N/m were used for imaging.[371] The deflection amplitude was 2.5 V, and the scanning speed was 1–2 μm/s. Images were processed by flattening to remove the background slope with Picoview software.

For the statistical analysis of QDs bound to DNA, we counted only QDs that completely overlapped with the DNA and only DNA whose contour length was within the standard deviation of the DNA length, which was measured with ImageJ software (NIH).[419] The average number of QDs bound per DNA molecule after different incubation times was determined by examining a large number of single molecules from at least three different DNA-QD samples prepared on mica (~150 total under each condition). A single binding isotherm was plotted by examining approximately 150 DNA molecules for each molar ratio of DNA to QDs from samples prepared in triplicate. Moreover, the number of DNA molecules in each class was counted under each experimental condition in both the binding kinetics and binding isotherm studies. These data were used to generate histograms, and the software SigmaPlot 10.0 was used to fit those histograms to a Gaussian distribution. Finally, we used ImageJ software to measure the distance of each bound QD on more than 500 molecules to the nearest DNA terminus to investigate whether QDs have a specific affinity to certain positions on DNA.

8.5. Results and discussion

8.5.1. Binding kinetics of QDs to DNA

Representative AFM images of free DNA and DNA in the presence of QDs are presented in Figure 8.1. Clearly, some QDs are bound to DNA molecules, as indicated by the black arrows. By measuring 50 randomly selected DNA molecules, the contour length of the DNA was determined to be 1414.8 ± 38.9 nm. Thus, QDs might induce DNA condensation.[413] Because it is impossible to measure the distance from the binding site to the DNA terminus in DNA condensates, we ignored such DNA molecules in the statistical measurement of distance. This should not have a significant impact on our statistical results because of the total DNA molecules, less than 10% are condensates.

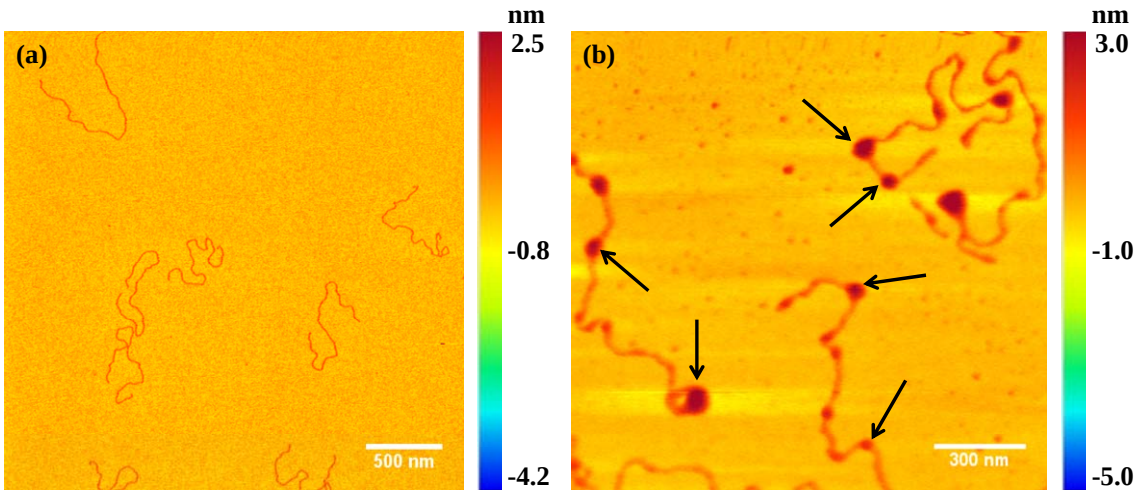

Figure 8.1. Representative AFM topographical images of (a) free DNA molecules and (b) QDs bound to DNA. Black arrows indicate representative sites of QD binding on DNA.

The average number of QDs bound per DNA molecule progressively increased with increasing incubation time until it finally reached a plateau indicating that the adsorption and desorption processes have reached equilibrium (Figure 8.2). The existence of this plateau, at which the concentration of bound QDs is far below that of total QDs, suggests that the adsorption of QDs onto DNA may not be irreversible and that

desorption can also occur. Eq. (7) was used to fit the experimental observations using the least squares method, which resulted in Eq. (12):

$$\frac{[NP]_{bind}}{[DNA]} = 0.42\left(1-e^{-2.95t}\right)+4.77\left(1-e^{-0.35t}\right) \qquad (12)$$

The correlation coefficient (R^2) is 0.9883, indicating a good fit. We further decomposed Eq. (12) to the sum of the first and second exponential terms; the second term ($4.77\left(1-e^{-0.35t}\right)$) is dominant while the first term ($0.42\left(1-e^{-2.95t}\right)$) is nearly constant. Eq. (12) can be hence further approximated by $[NP]_{bind}/[DNA] = 4.77\left(1-e^{-0.35t}\right)+0.42$. Therefore, the average number of bound QDs at equilibrium is approximately five, and the rate constant is approximately 0.35 s^{-1}. This is comparable to a previous binding kinetics study on protein-DNA interactions [420].

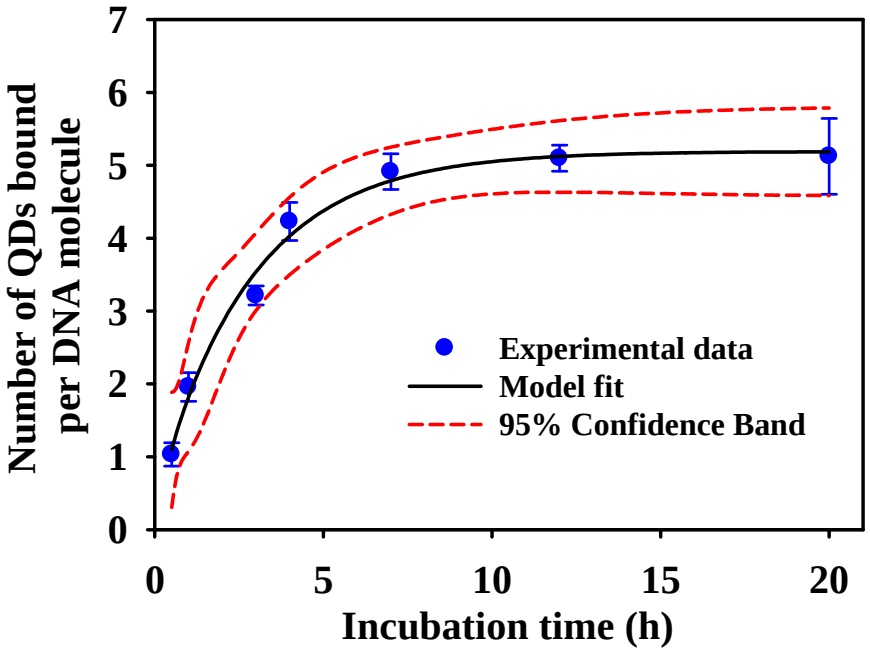

Figure 8.2. Experimental data and model fit for the kinetics of QDs binding to DNA molecules. The molar ratio of DNA to QDs is 1:10. The error bars represent the standard

deviation of the experimental data. The solid line in the figure is the model fit using Eq. (7), and the dashed lines represent the 95% confidence interval for the model prediction.

The number histograms for each class of DNA molecules at four different incubation times are presented in Figure 8.3. The histograms are well described by the Gaussian distribution, and the lines in the figure are the fits. The mean value (or location of the peak in those Gaussian fits) evolved from approximately 1 to 5 as the incubation time elongated from 0.5 h to 20 h, which was consistent with the aforementioned binding kinetics result. Also, the Gaussian distribution becomes broader over time, indicating that DNA molecules become more varied in terms of the number of QDs bound.

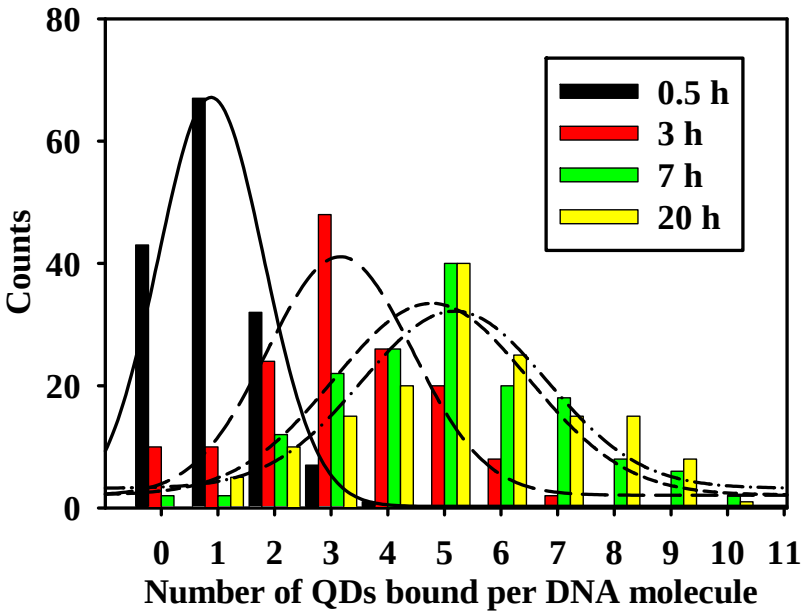

Figure 8.3. Histograms of the number of each class of DNA molecules at four different incubation times. The solid, long dashed, short dashed, and dash-dotted lines are Gaussian distribution fits to the histograms for incubation times of 0.5, 3, 7, and 20 h, respectively.

8.5.2. Binding isotherm for QDs to DNA

The binding of QDs to DNA was further examined using the binding isotherm (Figure 8.4), which characterizes the number of QDs per DNA molecule as a function of the free QD concentration. Based on the binding kinetics study discussed above, for isotherm development we selected the incubation time of 12 h, which was sufficient for the binding process to reach equilibrium. As the initial concentration of QDs increased from 0.4 to 8 nM, which corresponds to the DNA:QD molar ratio increasing from 1:1 to 1:20, the average number of QDs bound to DNA increased from approximately 0.4 to 7. Eq. (11), the Langmuir-type equation, was used to fit the experimental data, resulting in Eq. (13):

$$N = \frac{13.76[NP]}{4.32 + [NP]} \qquad (13)$$

The correlation coefficient (R^2) is 0.9731, indicating a good fit. The maximum QD binding number per DNA molecule is approximately 14. The equilibrium binding constant K is approximately 0.23 nM^{-1}, which is close to previously reported binding constants for the binding of proteins to DNA.[421]

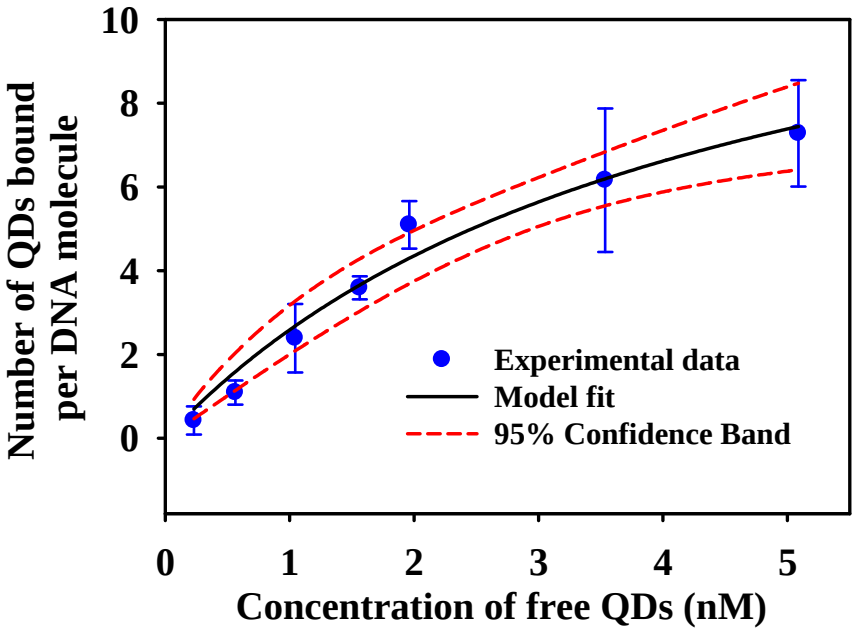

Figure 8.4. Experimental data and model fit of the binding isotherm for QDs to DNA. The error bars represent the standard deviation of the experimental data. The solid line is the Langmuir-type model fit using Eq. (11), and the dashed lines represent the 95% confidence interval for the model prediction.

Figure 8.5 shows the number histograms for various classes of DNA molecules under different QD concentrations. The lines in the histograms are Gaussian distribution fits, which describe the data very well. As the DNA:QD molar ratio changed from 1:1 to 1:20, the peak of the Gaussian distribution shifted from approximately 0 to 7; this is consistent with the average binding number data in Figure 8.4. Based on experimental observations, the maximum binding number for QDs on a single DNA molecule is 14, which agrees well with the theoretical prediction.

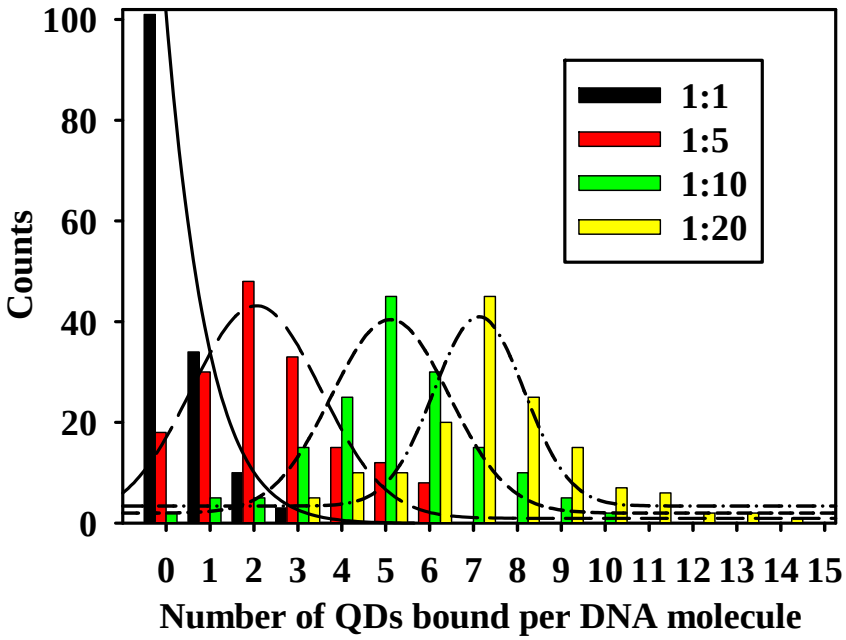

Figure 8.5. Histograms of the number of each class of DNA molecules under different molar ratios of DNA to QDs. The solid, long dashed, short dashed, and dash-dotted lines are Gaussian distribution fits to the histograms for the molar ratios 1:1, 1:5, 1:10, and 1:20, respectively.

8.5.3. Binding specificity of QDs to DNA

We further examined the positions of QDs on DNA to probe whether or not QDs have a specific affinity to certain sites on DNA. We defined the position of a QD as the ratio of the distance from its center to the closest DNA terminus to the contour length of the DNA, as the two DNA ends are indistinguishable in AFM images. After examining a large number of QDs (>500), position histograms were plotted with position ranging from 0 to 0.5 (Figure 8.6). Kolmogorov-Smirnov tests indicated that the position distribution conforms to a uniform distribution (p-value = 0.024) rather than a Gaussian distribution, and thus the binding of QDs to DNA is non-specific. This implies that binding specificity cannot explain the existence of a maximum binding number for QDs on a DNA molecule. We propose that the binding of a QD on DNA prevents another QD from binding to nearby positions owing to the repulsive electrostatic force between two positively charged QDs.

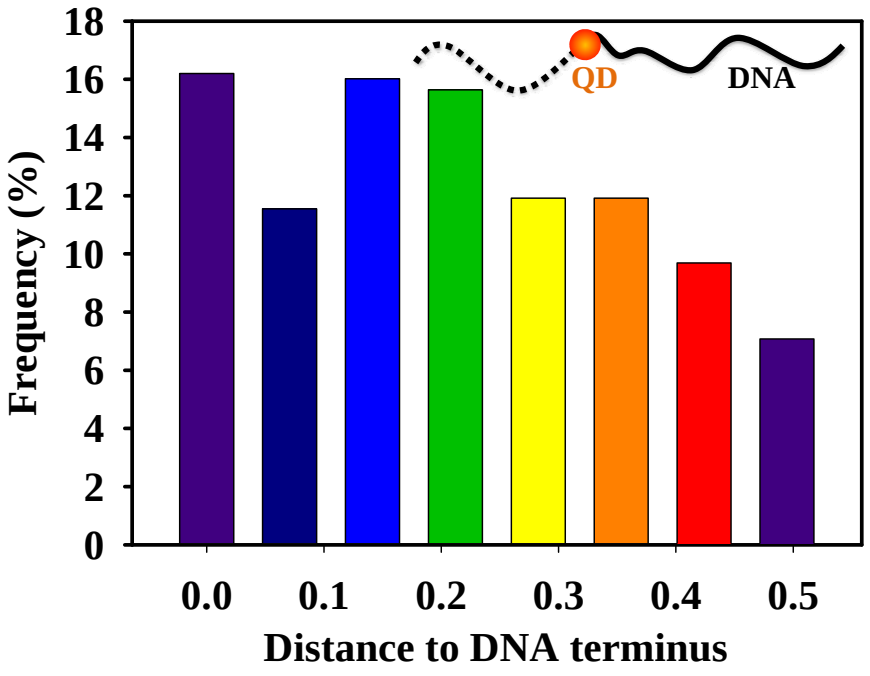

Figure 8.6. Histograms of the position of QDs on DNA. The distance of a bound QD to the DNA terminus is defined as the ratio of its distance to the closer DNA end to the

contour length of the whole DNA. The inset graph provides an example. In this case, the contour length of the DNA segment represented by the dotted line is obviously shorter than the segment of the DNA molecule represented by the solid line. The distance of the QD to DNA terminus is thus the ratio of the contour length of the dotted line to that of the whole line.

8.6. Conclusions

In conclusion, this study proposed a single-molecule imaging approach based on AFM for examining the characteristics of NP binding to DNA that may overcome the intrinsic limitations of the macroscopic techniques used in previous studies on DNA-NP interactions. We investigated the kinetics and isotherm of NP binding to DNA, and further determined the binding constants and specificities, by conducting a statistical analysis on a sufficiently large number of single molecules imaged using AFM. The binding kinetics and isotherm are well described by a double-term exponential-rise type of equation and a Langmuir-type equation, respectively. Also, the binding was found to be nonspecific by determining the distance of bound QDs to the DNA terminus; a QD bound to DNA may prevent the binding of another QD to neighboring sites because of the electrostatic repulsion between the two QDs. This single-molecule technique can be further extended to investigate the binding of other types of NPs to DNA, which will benefit the genetic effect assessment of NPs.

CHAPTER 9

BINDING AFFINITY OF NANOPARTICLES FOR DNA AND CORRELATION WITH GENETIC EFFECTS OF NANOPARTICLES

9.1. Abstract

Predictive models are beneficial tools for researchers to use in prioritizing NPs for toxicological tests; but experimental evaluation can be time-consuming and expensive, and thus priority should be given to tests that identify the NPs most likely to be harmful. For characterization of NPs, the physical binding of NPs to DNA molecules is important to measure, as interference with DNA function may be one cause of toxicity. Here, we determined the interaction energy between twelve types of NPs and DNA based on the Derjaguin-Landau-Verwey-Overbeek (DLVO) model and then predicted the affinity of the NPs for DNA. Using the single-molecule imaging technique known as atomic force microscopy (AFM), we experimentally determined the binding affinity of those NPs for DNA. Theoretical predictions and experimental observations of the binding affinity agreed well. Furthermore, the effect of NPs on DNA replication *in vitro* was investigated with the polymerase chain reaction (PCR) technique. The results showed that NPs with a high affinity for DNA strongly inhibited DNA replication, whereas NPs with low affinity had no or minimal effects on DNA replication. The methodology here is expected to benefit the genotoxicological testing of NPs as well as the design of safe NPs.

9.2. Introduction

Nanotechnology is a new frontier in science and technology in the 21st century that creates the potential for novel materials with unique functions and superior performances. However, concerns regarding the safety and health effects of engineered

NPs arise alongside the booming nanotechnology industry. Numerous toxicological studies on NPs were published in the last decade, but many did not employ real nano-sized materials, mainly because most NPs are subject to slow or fast aggregation in aqueous media [53, 422-426]. The observed toxicity and related mechanisms in those studies are probably associated with the properties of aggregates/agglomerates [171, 427-429]. At the interface between NPs and biological systems, some unaggregated NPs may have unique effects locally and exert different toxicity mechanisms compared with the aggregates; these mechanisms are not well documented yet. To explore the cytotoxic mechanisms of "real" NPs, we are developing systematic experimental approaches based on atomic force microscopy (AFM) to assess the effect of unaggregated NPs on single cells or biomolecules at the nanoscale [381, 430, 431].

Primary or unaggregated NPs are likely to enter into biological cells [432-434] and subsequently exert toxic effects on intracellular structures like DNA [82, 210, 435]. Several mechanisms including oxidative stress and direct binding have been proposed to explain the adverse genetic effect of NPs [50, 127, 210, 436, 437]. Up to now, the mechanism of oxidative stress has been extensively studied on a wide range of NPs [102, 124, 132, 438-445]. In contrast, the significance of direct binding of NPs to DNA is somewhat underestimated and has received less attention. Below we summarized a few studies related to the adverse effects induced by the binding activity of NPs to DNA. Our previous study showed that small quantum dots with a radius of 10 nm could permeate into bacterial cells and bind to DNA [381]. NP binding changed the normal conformation as well as the local electrical properties of DNA molecules [381, 430]. A recent study also found that the binding of gold NPs causes structural changes including local denaturing and compaction to DNA [446]. Such changes may adversely interfere with the genetic functions of DNA, such as transcription, replication, and repair processes, that are crucial to maintain the normal metabolism of a living cell [365-369]. Specifically, NPs that bind to DNA with a high affinity could prohibit the normal functions of some critical DNA-binding proteins, such as RNA polymerase

and DNA polymerase, by occupying protein-binding sites and impeding the movement of protein along the DNA, which could result in competitive inhibition of genetic functions [367-369, 447]. It has been reported that functionalized gold NPs completely inhibited DNA transcription *in vitro* owing to the electrostatic interaction of NPs with DNA [367-369]. A computational simulation study also showed that C_{60} NPs strongly bind to DNA and might adversely impact the conformation and biological functions of DNA [366]. Furthermore, the binding of NPs to DNA might intervene in long-range charge transport through the DNA and thus interfere with signaling processes [448]. Thus, the interaction between NPs and DNA appears to play important roles in the toxicity of NPs and deserves a complete understanding of the underlying principle.

Because toxicological tests of NPs are time-consuming and expensive, scientists are developing models to predict the behavior and effects of NPs in biological systems [196-198], which would allow researchers to streamline the toxicological testing of NPs by prioritizing NPs that are most likely to be harmful. Using theoretical models to describe the interaction between NPs and DNA is an important part of building an "ultimate" biological-effect-predicting model. Recently, several studies attempted to address the interaction of NPs with DNA using computational simulation techniques (mainly molecular dynamics simulations) [366, 446, 449]. Although powerful, the application of these simulation techniques is restricted to ultrasmall NPs (< 5 nm) and short DNA fragments due to the limitations of computational efficiency and capacity [366, 446, 449]. The complexity of these techniques also impedes their widespread use among researchers. Hence, it is necessary to develop some simpler techniques for investigating the NP-DNA interaction. It is well known that in typical colloid physics the interfacial forces or energies fundamentally control the interaction between two objects. The Derjaguin-Landau-Verwey-Overbeek (DLVO) theory, for instance, is widely used to describe such interfacial interactions between charged objects in liquid [213, 347]. According to the DLVO theory, the total interaction is comprised of van der Waals (vdW) and electrical double-

layer (EDL) interactions. The interaction between spherical NPs and DNA can be described with the DLVO theory by treating the NP as a sphere and DNA as a uniformly charged cylinder [450-452] because the dimension of the DNA is significantly larger than the separation distance between its neighboring charges (~0.17 nm) [402]. For example, Sushko and Shluger described DNA/mica interactions using a DLVO model for an interaction between a cylinder and a flat surface [453]. It is reasonable to use the sphere-cylinder DLVO model to describe the NP-DNA interaction.

In this study, we determined the binding affinity of selected NPs [positively and negatively charged quantum dots, gold NPs capped with different surface groups (carrying different surface charge), latex beads, as well as silicon, silver, hematite, CeO_2, ZnO, TiO_2 and SiO_2 NPs] for DNA on the basis of the DLVO model. The binding affinity of NPs to DNA was experimentally evaluated with AFM and then compared with the model prediction. Furthermore, the effect of NPs on DNA replication was investigated using the polymerase chain reaction (PCR) technique and then related to the binding affinity of NPs for DNA. The overall goal of this study is to predict the affinity of NPs for DNA and to provide insights into the prediction of the genetic effect of NPs.

9.3. Materials and methods

9.3.1. Materials

Two types of water-soluble CdSe/ZnS core/shell quantum dots (QDs), respectively coated with polydiallydimethylammonium chloride (PDDA) and poly (ethylene glycol) (PEG) with a carboxylic acid terminal end group, were purchased from Ocean NanoTech, LLC (Springdale, AR). For convenience, we named the former "QDs (+)" and the latter "QDs (-)", as the electrophoresis experiments showed the former carried positive surface charge while the latter carried negative charge. Citrate-stabilized gold NPs were purchased from Sigma-Aldrich (St. Louis, MO). Gold NPs functionalized with COOH surface group were purchase from Ocean NanoTech, LLC (Springdale, AR).

Also for convenience, we named the former "gold NPs (citrate)" and latter "gold NPs (COOH)". Citrate-stabilized silver NPs were purchased from Ted Pella, Inc. (Redding, CA). CeO_2 NPs were purchased from Alfa Aesar (Ward Hill, MA). TiO_2, SiO_2, ZnO NPs and latex beads (30nm) were purchased from Sigma-Aldrich (St. Louis, MO). Silicon NPs were purchased from the US Research NPs, Inc (Houston, TX). Finally, hematite NPs were synthesized in our laboratory using the method of Penners and Koopal [454] with minor modifications [354]. Briefly, 20 mM $FeCl_3$ in 4 mM HCl was incubated at 120°C in a flask coupled with a water-cooled condenser. The size of the hematite NPs was controlled by incubation time. Approximately 20 min were required to produce hematite NPs of size *ca.* 20 nm.

The sizes and morphologies of those NPs were characterized using AFM (shown in Figure 9.1). The other characterizations using transmission electron microscopy, dynamic light scattering, X-ray diffraction and/or fourier transform infrared spectroscopy were published in our previous work [332, 333, 354, 455, 456].

A SacI-linearized plasmid DNA pGEMEX-1 of 3993 base pairs was purchased from Promega Corporation (Madison, WI). The DNA was diluted to 2 nM with sterile TE buffer (10 mM Tris HCl, pH 7.4, 1 mM EDTA) (Fisher Scientific Co., USA). Images acquired by AFM showed that the DNA can be stored in a 4°C refrigerator for two months without loss of structural integrity. Finally, the protein used in this study was T7 RNA polymerase (RNAP) purchased from Promega Corporation (Madison, WI).

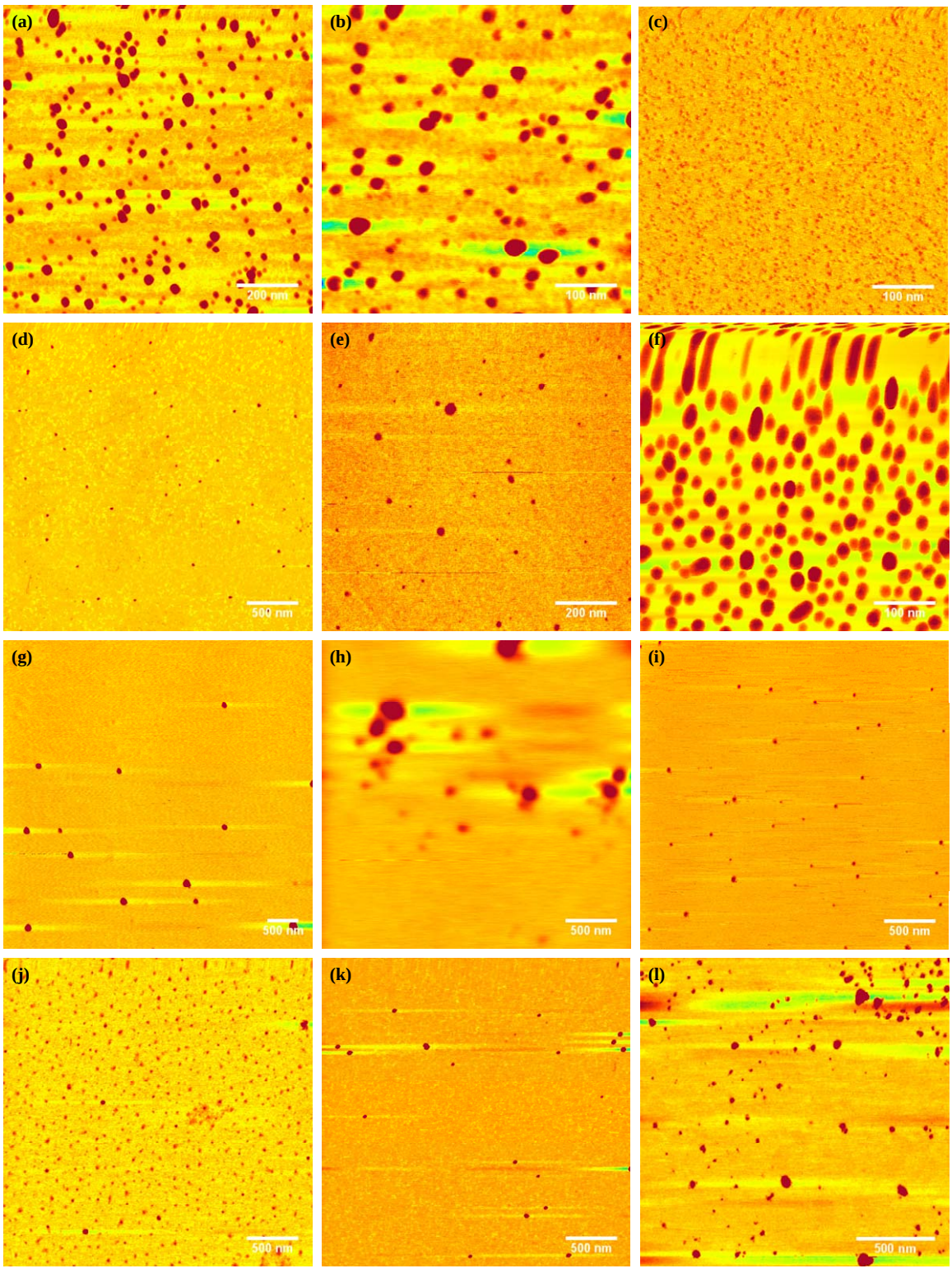
(a)
200 nm
(b)
100 nm
(c)
100 nm
(d)
500 nm
(e)
200 nm
(f)
100 nm
(g)
500 nm
(h)
500 nm
(i)
500 nm
(j)
500 nm
(k)
500 nm
(l)
500 nm

Figure 9.1. Representative AFM topographical images of (a) QDs (+), (b) QDs (-), (c) gold NPs (citrate), (d) gold NPs (COOH), (e) silver NPs, (f) hematite NPs, (g) CeO_2 NPs, (h) ZnO NPs, (i) TiO_2 NPs, (j) SiO_2 NPs, (k) silicon NPs, and (l) latex beads.

9.3.2. Determination of the electrophoretic mobility (EPM) of NPs and protein

The EPM of NPs and protein in the TE buffer containing 4 mM Mg^{2+} was measured using a Malvern Zetasizer Nano ZS instrument. In brief, 1.5 mL of NP or protein suspensions of 10 mg/L in the TE buffer containing 4 mM Mg^{2+} were injected into a clean cuvette, and the instrument was then operated with a scattering angle of 173° from the incident laser beam. The autocorrelation function automatically accumulated at least 10 runs for each sample. At least four parallel measurements were made for each condition.

9.3.3. AFM imaging of the binding of NPs to DNA

DNA stock solution was diluted to 0.2 nM with sterile TE buffer containing 5 mM Mg^{2+}. The DNA was mixed with NPs at a molar ratio of 1:5 and incubated at 37°C for 1 h. Then 2.5 μL of the mixture was deposited on a freshly cleaved mica substrate and incubated for 30 minutes. The mica surface was thoroughly rinsed with MilliQ pure water and then blown dry with ultrapure nitrogen gas.[430] AFM images were collected at room temperature using an Agilent 5500 Molecular Imaging AFM in the acoustic alternating current (AAC) mode. Silicon cantilevers (BudgetSensors, Bulgaria) with a force constant of approximately 2–5 N/m were used. AFM images were processed using the Picoview 1.12 software from Agilent Technologies.

9.3.4. Effects of NPs on DNA replication *in vitro*

The SacI-linearized plasmid DNA pGEMEX-1 was used as template to perform the DNA replication assay. 50 ng of DNA template was used to incubate with serial dilutions of NPs for 5 min on ice. The concentrations of NPs used in PCRs are presented in Figure 3. After the incubation step, PCR amplifications were performed in 25 μL

reaction volumes with DNA-NP mix, 1 U Phusion® High-Fidelity DNA Polymerase (New England Biolabs, MA), 200 μM each dNTP, and 0.5 μM each primer on a Mastercycler pro (Eppendorf). The primers used in the PCR reaction amplify a 180 base pair fragment. The following are the primer sequences:

EP 1: GGGGATCCGGTACCAGCACCAC

EP 2: GGGATGTTCCGGCTGCTGACCGT

PCRs began with a denaturation step at 98°C for 30 s, and 30 cycles of amplification were performed using the following conditions: 30 s at 98°C; 30 s at 58°C; 30 s at 72°C. 15 ul of each amplified product was used for electrophoresis using 1% agarose gel that was stained with ethidium bromide for visualization.

9.4. Results and discussion

9.4.1. Determination of parameters in the DLVO model

The interaction energy between each NP and DNA was computed based on DLVO models for the sphere-cylinder geometry [457] (see Appendix A for details of the model). A number of parameters are required by the model including the size and the surface potential of both NPs and DNA molecules, and the Hamaker constant for NP-DNA interactions.

The sizes of those NPs were measured using AFM (shown in Figure 9.1) by examining at least 100 randomly picked particles. Statistically, the radii of QDs (+), QDs (-), gold NPs (citrate), gold NPs (COOH), silver NPs, hematite NPs, CeO_2 NPs, ZnO NPs, TiO_2 NPs, SiO_2 NPs, silicon NPs, and latex beads are 8.54 ± 2.46, 7.80 ± 2.05, 2.76 ± 0.54, 13.09 ± 4.60, 6.41 ± 3.19, 8.14 ± 1.44, 42.12 ± 15.20, 45.97 ± 17.22, 12.72 ± 3.09, 13.20 ± 4.13, 15.36 ± 4.50, and 15.15 ± 5.54 nm, respectively.

The surface potential (Ψ_o) of DNA was determined from the Grahame equation [458], which, under assumption of low potentials below 25 mV, simplifies to

$$\psi_o = \frac{\sigma}{\varepsilon\varepsilon_0\kappa} \qquad (1)$$

where σ represents the charge density; ε_0 is the vacuum permittivity; ε is the relative permittivity of water; κ represents the inverse Debye length in the buffer solution, which is calculated to be 0.05 $Å^{-1}$ according to the equation below:

$$\kappa = \sqrt{\frac{\sum_i \rho_{\infty i} e^2 z_i^2}{\varepsilon\varepsilon_0 k_B T}} \qquad (2)$$

where k_B is the Boltzmann constant; T is absolute temperature; z_i is the valency of the i^{th} ion; e is unit charge; and $\rho_{\infty i}$ is the number concentration of the i^{th} ion.

For double-stranded DNA molecules, a value of -0.15 $C{\cdot}m^{-2}$ was obtained for σ.[459] Thus, ψ_o for DNA was calculated to be -21.5 mV, which agrees well with a previous study [460].

The surface potentials of NPs were determined from measured electrophoretic mobility (EPM) values *via* the Henry equation [461]:

$$\psi_o = \frac{\mu\eta}{\varepsilon f(\kappa a)} \qquad (3)$$

where μ is EPM; ε is the relative permittivity of water; η is the solution viscosity; and $f(\kappa a)$ is Henry's function, which is reasonably well approximated by [461]

$$f(\kappa a) = \frac{2}{3}\left[1 + \frac{1}{2(1 + 2.5/\kappa a)^3}\right] \qquad (4)$$

where κ is still the inverse Debye length and a is the particle radius [254, 290]. From Eqs. (3) and (4), the average surface potentials of QDs (+), QDs (-), gold NPs (citrate), gold NPs (COOH), silver NPs, hematite NPs, CeO_2 NPs, ZnO NPs, TiO_2 NPs, SiO_2 NPs, silicon NPs, and latex beads were determined to be 4.45 ± 1.90, -40.90 ± 2.85, -29.10 ± 0.60, -63.14 ± 2.83, -21.50 ± 0.75, -13.32 ± 1.15, -9.52 ± 1.52, -10.15 ± 0.86, -12.33 ± 0.99, -17.09 ± 0.40, -28.70 ± 1.31, and -33.85 ± 3.00 mV, respectively.

The Hamaker constant (A_H) for the interaction of NPs and DNA in water was determined with Lifshitz theory. For two media of dielectric constants or permittivity ε_1 and ε_2 interacting in a third medium with dielectric constant ε_3, the Hamaker constant is given by [266]

$$A_H \approx \frac{3}{4}kT\left(\frac{\varepsilon_1-\varepsilon_3}{\varepsilon_1+\varepsilon_3}\right)\left(\frac{\varepsilon_2-\varepsilon_3}{\varepsilon_2+\varepsilon_3}\right)+\frac{3h}{4\pi}\int_{\nu_1}^{\infty}\left(\frac{\varepsilon_1(i\nu)-\varepsilon_3(i\nu)}{\varepsilon_1(i\nu)+\varepsilon_3(i\nu)}\right)\left(\frac{\varepsilon_2(i\nu)-\varepsilon_3(i\nu)}{\varepsilon_2(i\nu)+\varepsilon_3(i\nu)}\right)d\nu \qquad (5)$$

where $\varepsilon(i\nu)$ are the values of ε at imaginary frequencies, and $\nu_1 = 2kT\pi/h = 3.9\times10^{13}$ s^{-1} at 298 K. The first term in the equation represents the zero-frequency energy of the vdW interaction and includes the Keesom and Debye contributions. The second integration term represents the dispersion energy, *i.e.*, the London contribution. The dielectric constant $\varepsilon(i\nu)$ for non-metallic particles is expressed by

$$\varepsilon(i\nu)=1+(n^2-1)/(1+\nu^2/\nu_0^2) \qquad (6)$$

where n represents the refractive index of the medium; ν_0 is the main absorption frequency of the medium. The n values for the DNA molecule, water, hematite, CeO_2 NPs, ZnO NPs, TiO_2 NPs, SiO_2 NPs, silicon NPs, and latex beads are 1.6, 1.33, 3, 2.276, 2.004, 2.488 (anatase), 1.54, 3.5, and 1.59, respectively [462-464]. ν_0 values for DNA molecule and water are 1.15×10^{15} and 3.0×10^{15} s^{-1}, respectively.[266] The QDs, hematite, CeO_2 NPs, ZnO NPs, TiO_2 NPs, SiO_2 NPs, silicon NPs, and latex beads used in this study respectively have maximum absorptions at 530, 190, 310, 190, 260, 230, 470, and 200 nm, corresponding to ν_0 values of 5.66×10^{14}, 1.58×10^{15}, 9.68×10^{14}, 1.58×10^{15}, 1.15×10^{15}, 1.30×10^{15}, 6.38×10^{14}, and 1.50×10^{15} s^{-1}, respectively. The dielectric constant $\varepsilon(i\nu)$ for metallic particles is expressed by

$$\varepsilon(i\nu)=1+\nu_e^2/\nu^2 \qquad (7)$$

where $v_e^2 = n_e e^2/4\pi^2 m_e \varepsilon_0$ is the squared plasma frequency of a free electron gas of number density n_e where m_e is the electron mass. The number densities of gold and silver are 5.90×10^{28} and 5.86×10^{28} m^{-3}, respectively, giving plasma frequencies of $v_e = 2.18 \times 10^{15}$ and 2.17×10^{15} s^{-1}, respectively.

The ε values for the DNA molecule, water, hematite, CeO_2 NPs, ZnO NPs, TiO_2 NPs, SiO_2 NPs, silicon NPs, and latex beads are 2.56, 80, 12, 24.3, 8.34, 114, 3.9, 11.68, and 2.52 respectively [350, 465-467]. The ε values for gold and silver are infinity. For CdSe/ZnS QDs, we take an average of the values of ZnS and CdSe, as to our knowledge no calculation method is available to obtain the n and ε values for nano-heterostructures. The dielectric constants for CdSe and ZnS are 9.75 and 8.9, respectively. The refractive indices for CdSe and ZnS are 2.5 and 2.368, respectively [468]. By taking an average, the dielectric constant and refractive index for CdSe/ZnS were respectively 9.325 and 2.434. By doing numerical integration in Matlab, the Hamaker constants A_H for DNA interacting with QDs, gold NPs, silver NPs, hematite NPs, CeO_2 NPs, ZnO NPs, TiO_2 NPs, SiO_2 NPs, silicon NPs, and latex beads in liquid were calculated to be 4.0, 3.2, 3.2, 3.9, 2.6, 1.6, 1.7, 2.0, 3.6, and 1.8 kT. The Hamaker constant of each type of NPs as well the particle size and surface potential were listed in Table 9.1.

Table 9.1. Particle size, surface potential and Hamaker constants of NPs, and the computed energy barrier between each type of NPs and DNA

NPs	Radius (nm)	Surface potential (mV)	Hamaker constant (kT)	Energy barrier (kT)
QDs (+)	8.54 ± 2.46	4.45 ± 1.90	4.0	0
QDs (-)	7.80 ± 2.05	-40.90 ± 2.85	4.0	0.18
Gold (citrate)	2.76 ± 0.54	-29.10 ± 0.60	3.2	0.06
Gold (COOH)	13.09 ± 4.60	-63.14 ± 2.83	3.2	0.39

Silver	6.41 ± 3.19	-21.50 ± 0.75	3.2	0.08
Hematite	8.14 ± 1.44	-13.32 ± 1.15	3.9	0.02
CeO_2	42.12 ± 15.20	-9.52 ± 1.52	2.6	0.003
ZnO	45.97 ± 17.22	-10.15 ± 0.86	1.6	0.04
TiO_2	12.72 ± 3.09	-12.33 ± 0.99	1.7	0.05
SiO_2	13.20 ± 4.13	-17.09 ± 0.40	2.0	0.10
Silicon	15.36 ± 4.50	-28.70 ± 1.31	3.6	0.16
Latex beads	15.15 ± 5.54	-33.85 ± 3.00	1.8	0.31

9.4.2. Binding affinity of NPs for DNA

The energy barriers between NPs and DNA, as calculated from the DLVO model, are 0.39 kT for gold (COOH)-DNA, 0.31 kT for latex beads-DNA, 0.18 kT for QDs (-)-DNA, 0.16 kT for silicon-DNA, 0.10 kT for SiO_2-DNA, 0.08 kT for silver-DNA, 0.06 kT for gold (citrate)-DNA, 0.05 kT for TiO_2-DNA, 0.04 kT for ZnO-DNA, 0.02 kT for hematite-DNA, 0.003 kT for CeO_2-DNA, and 0 kT for QDs (+)-DNA (Figure 9.2). These theoretical calculation results suggest that gold NPs (COOH), latex beads, QDs (-), silicon NPs, and SiO_2 NPs are more likely not to bind to DNA compared with the other NPs, owing to the high energy barrier between these NPs and DNA.

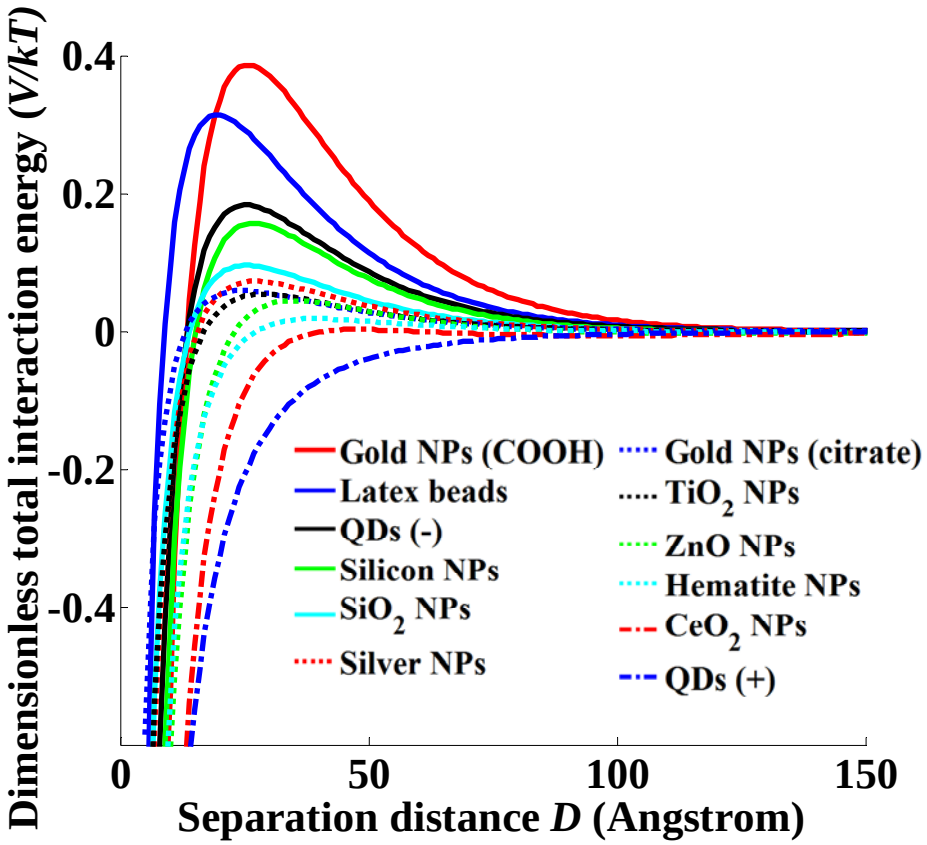

Figure 9.2. The interaction energy profiles between each NP and DNA.

AFM was used to verify the predicted binding affinity of NPs for DNA. DNA molecules looked curved and bent, while the NPs binding to the DNA appeared as large or small dark dots. The AFM results showed that NPs have quite different binding affinities for DNA. On one hand, as shown in Figure 9.3, the QDs (+), silver NPs, hematite NPs, gold NPs (citrate), CeO_2 NPs, ZnO NPs and TiO_2 NPs were observed to bind to DNA, which is consistent with our theoretical analysis. On the other hand, the SiO_2 NPs, silicon NPs, QDs (-), gold NPs (COOH) and latex beads did not bind to DNA molecules, which also agreed well with model predictions. It is worth noting that the majority of NPs tested here for DNA interaction were "real" nano-sized particles, and therefore our models were applicable in the nanoscale.

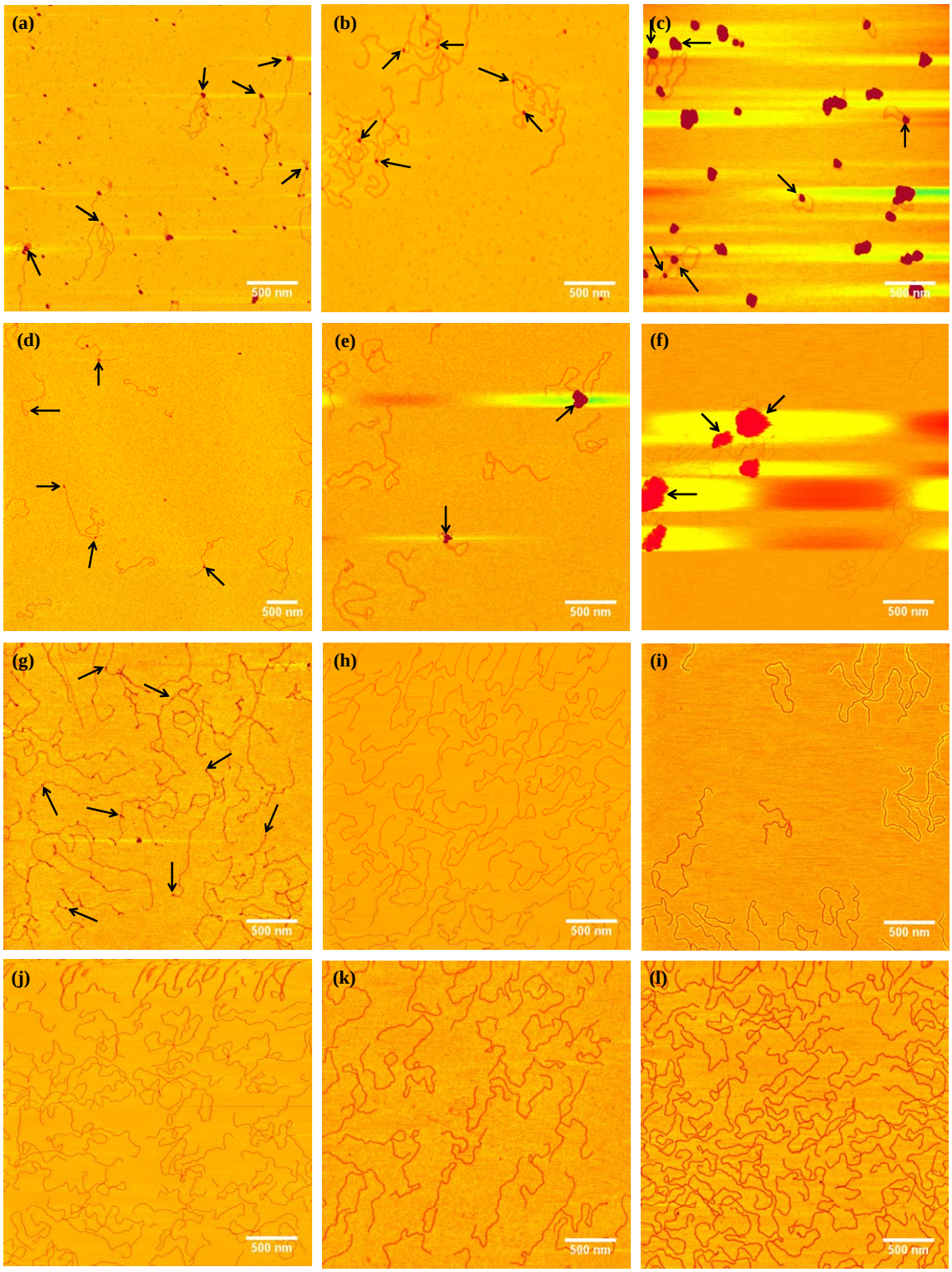

Figure 9.3. AFM topographical images of DNA molecules after exposure to NPs. DNA molecules were observed under AFM after exposure to (a) QDs (+), (b) silver NPs, (c)

hematite NPs, (d) gold NPs (citrate), (e) CeO_2 NPs, (f) ZnO NPs, (g) TiO_2 NPs, (h) SiO_2 NPs, (i) silicon NPs, (j) QDs (-), (k) gold NPs (COOH), and (l) latex beads. The dark dots in (a)-(g), as indicated by black arrows, are NPs, namely, the black arrows indicate representative binding sites of NPs on DNA molecules. SiO_2 NPs, silicon NPs, QDs (-), gold NPs (COOH) and latex beads did not bind to DNA molecules, as observed from (h)-(l).

We noticed from the AFM image that some NPs appeared to induce DNA bending. The subsequent binding activity of NPs to those bent DNA may not be well described by the sphere-cylinder interaction models proposed in the previous section. Instead, we used a section of torus to represent the bent DNA, and computed the interaction energy between NPs and bent DNA using the sphere-torus model (see Appendix B for details of the model). We found that the relative magnitude of the energy barrier between the bent DNA and each NP were the same as that between the straight DNA and each NP, *i.e.*, the energy barrier height increased in the order of QDs (+) < CeO_2 NPs < hematite NPs < ZnO NPs < TiO_2 NPs < gold NPs (citrate) < silver NPs < SiO_2 NPs < silicon NPs < QDs (-) < latex beads < gold NPs (COOH) under both scenarios.

NPs with a high affinity for DNA may interfere with normal DNA functions. The AFM images in Figure 9.3 show that the binding of NPs to DNA has the potential to dramatically change the DNA conformation. We can clearly observe the DNA bending or looping in the presence of QDs (+) and hematite NPs. In addition, when silver and ZnO NPs were present, DNA formed a more compact conformation compared to the native random coil conformation. Two additional AFM images were presented in Figure 9.4 for illustrating the compact DNA conformation induced by silver NPs and QDs (+). These observations were discussed in more details in our previous work [430].

Proteins that are requisite for DNA replication, transcription and repair processes may not function correctly owing to (1) pre-occupation of DNA by NPs in the binding

sites of proteins (*e.g.* DNA polymerase/RNA polymerase and sigma factor); (2) conformational changes in DNA resulting in inhibitory structures that block unwinding of DNA or traversing along DNA. In contrast, DNA molecules incubated with SiO_2 NPs, silicon NPs, QDs (-), gold NPs (COOH) and latex beads did not show conformational changes; it is likely that these DNA molecules still allow for normal functions.

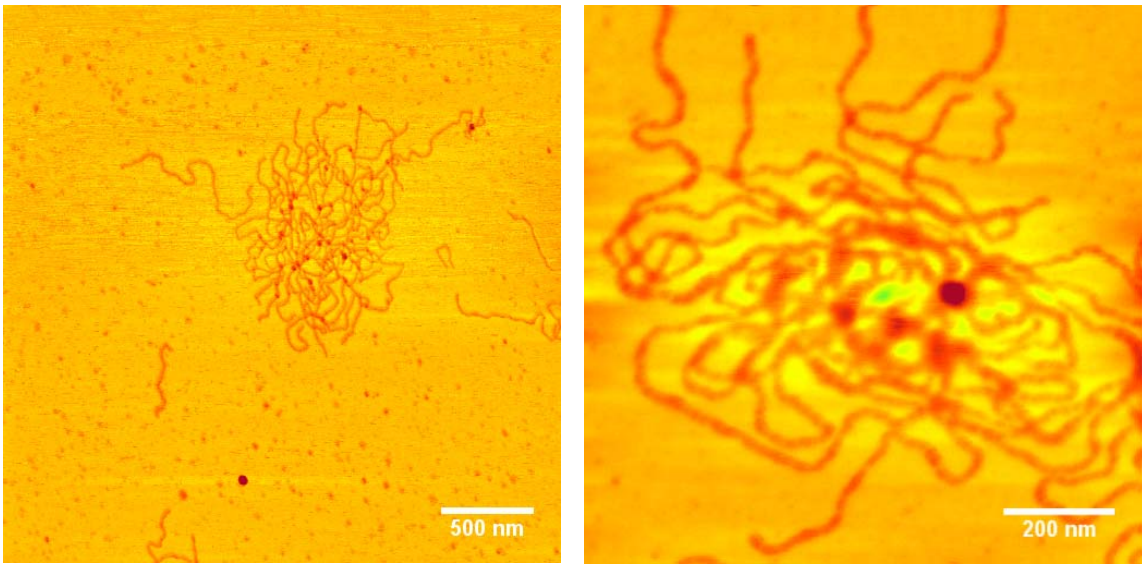

Figure 9.4. Compact DNA conformation induced by silver NPs (left) and QDs (+) (right).

We performed the interaction energy calculation between protein and DNA using T7 RNAP as a model protein. Its surface potential was determined as -9.60 ± 2.80 mV according to Eq. (3). The Hamaker constant (A_H) for protein and DNA interacting in liquid was estimated to be 3 kT.[469] Assuming RNAP has a spherical shape, its radius (nm) was approximated as 3 nm on the basis of its mass M (in Daltons) by the relation $R_S = 0.066M^{1/3}$.[470] The result showed that the energy barrier between protein and DNA is 0.01 kT; the binding affinities of QDs (+), silver, hematite, gold (citrate), CeO_2, ZnO and TiO_2 NPs for DNA are of similar magnitude and may compete for binding to DNA molecules with protein.

9.4.3. Effects of NPs on DNA replication

The PCR method was employed to probe the effect of NPs on DNA replication. The agarose gel electrophoresis results (Figure 9.5) showed how the twelve types of NPs over a range of concentrations affected DNA replication. The quantity of PCR amplified DNA products was reflected by the intensity of each band. QDs (+) completely inhibited DNA replication at the concentration of 0.15 nM, agreeing with a previous study which showed that cationic QDs caused genotoxic effects [471]. The DNA replication was completely inhibited by silver NPs at 0.05 nM. This is consistent with previous studies which showed silver NPs were genotoxic [102, 472, 473]. Hematite NPs showed a complete inhibition at 0.2 nM; hematite NPs also have been found to induce adverse genetic effects [441, 474]. Gold NPs (citrate) affected DNA replication at 0.3 nM and completely impeded the replication process at the concentration of 0.5 nM. This agreed with a previous study showing that gold NPs associated with DNA and subsequently induced DNA bending and strand separation [446]. CeO_2 NPs significantly inhibited DNA replication at 0.05 nM. ZnO suppressed the DNA replication process at 0.2 nM. The latex beads also resulted in the inhibition of DNA replication at a high concentration of 1.5 nM. In contrast, other NPs did not show any signs of inhibition at their highest concentration employed in this study (1.4-1.6 nM). The most interesting result comes from TiO_2 NPs. In the binding affinity experiment, we have observed many TiO_2 NPs binding on DNA (Figure 9.3g), thus we expected that TiO_2 NPs were likely inhibitory to DNA replication. These seemingly contradictory results could be explained by the enhanced thermal conductivity in the PCR. TiO_2 NPs can induce a rapid increase in thermal conductivity sufficient to enhance PCR efficiency,[475] which might offset their inhibitive effects on DNA replication.

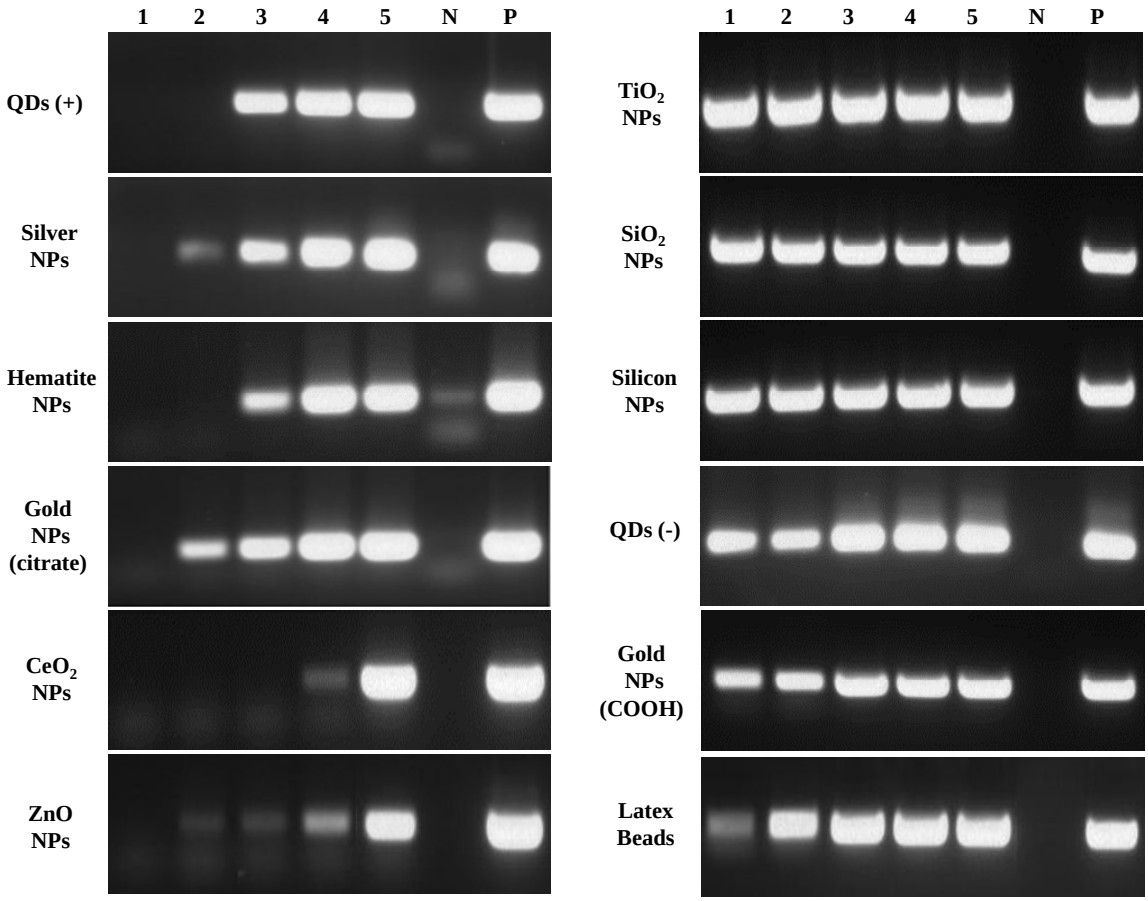

Figure 9.5. Effects of NPs on DNA replication *in vitro* by quantification of PCR products. 50 ng of Linearized pGEMEX-1 was used in each reaction to amplify a 180 bp PCR fragment except for negative control. Each type of NPs was tested under a range of concentrations. From lane 1 to 5, the final concentrations of QDs (+) were 0.2, 0.15, 0.1, 0.05, 0.01 nM, silver NPs were 0.05, 0.03, 0.02, 0.01, 0.002 nM, hematite NPs were 0.5, 0.2, 0.1, 0.05, 0.01 nM, gold NPs (citrate) were 0.5, 0.3, 0.2, 0.1, 0.05 nM, CeO_2 NPs were 0.5, 0.2, 0.1, 0.05, 0.01 nM, ZnO NPs were 2, 0.5, 0.3, 0.2, 0.05 nM, TiO_2, SiO_2 and silicon NPs were all 1.5, 1.0, 0.5, 0.3, 0.2 nM, QDs (-) were 1.6, 0.8, 0.16, 0.08, 0.016 nM, gold NPs (COOH) were 1.4, 1.0, 0.5, 0.3, 0.2 nM, and latex beads were 1.5, 1.0, 0.5, 0.3, 0.2 nM. N and P respectively represent the negative and positive controls for the PCR experiment. N: negative control without DNA template and NPs. P: positive control using 50 ng of DNA template without NPs.

We further investigated the relation between the ability of NPs to inhibit DNA replication and the predicted binding affinity of NPs for DNA. As observed from Figure 9.6, NPs that were predicted to have a high binding affinity (*i.e.*, low energy barrier) for DNA molecules also had a high potential to inhibit DNA replication. This implied that (1) the binding of NPs to DNA is likely an important mechanism for causing the adverse genetic effects of NPs, and (2) the DLVO model may act as a simple and effective tool for predicting the genetic effects of NPs induced by the direct binding activity of NPs with DNA. It is noted that the Ag NPs have a higher inhibition ability compared with the model prediction; this is reasonable, as Ag NPs released Ag ions, which may be also detrimental to the DNA replication [102, 456, 476, 477].

As mentioned earlier in this paper, oxidative stress resulted from reactive oxygen species (ROS) has been reported as an important cause of adverse genetic effects of NPs [120]. Our group has conducted a series of studies on the ROS production by NPs [455, 456]. However, ROS do not appear to explain the effects of NPs observed here. It is well known that among the three primary ROS radicals (*i.e.*, •OH, $^1O_2$ and $O_2^{\bullet-}$), •OH and $^1O_2$ are mainly responsible for DNA damage [478, 479]. Our previous work showed that the ability of NPs to produce •OH and $^1O_2$ increased in the order of QDs (+) / QDs (-) / CeO_2 NPs < hematite NPs < silver NPs < SiO_2 NPs < ZnO NPs < gold NPs (citrate) < silicon NPs < TiO_2 NPs [333, 455, 456]. Apparently, the ROS production does not explain the PCR results, because the genotoxicity of NPs was shown to increase in the order of QDs (-) / TiO_2 / SiO_2 / silicon NPs < gold NPs (citrate) < ZnO NPs < hematite NPs < QDs (+) < CeO_2 / silver NPs. Therefore, we may rule out ROS as the primary cause of adverse genetic effects of NPs in this study; rather, the direct binding activity of NPs to DNA is likely one reasonable genotoxicity mechanism. Overall, the methodology in this study can help researchers screen NPs and prioritize their genotoxicological testing.

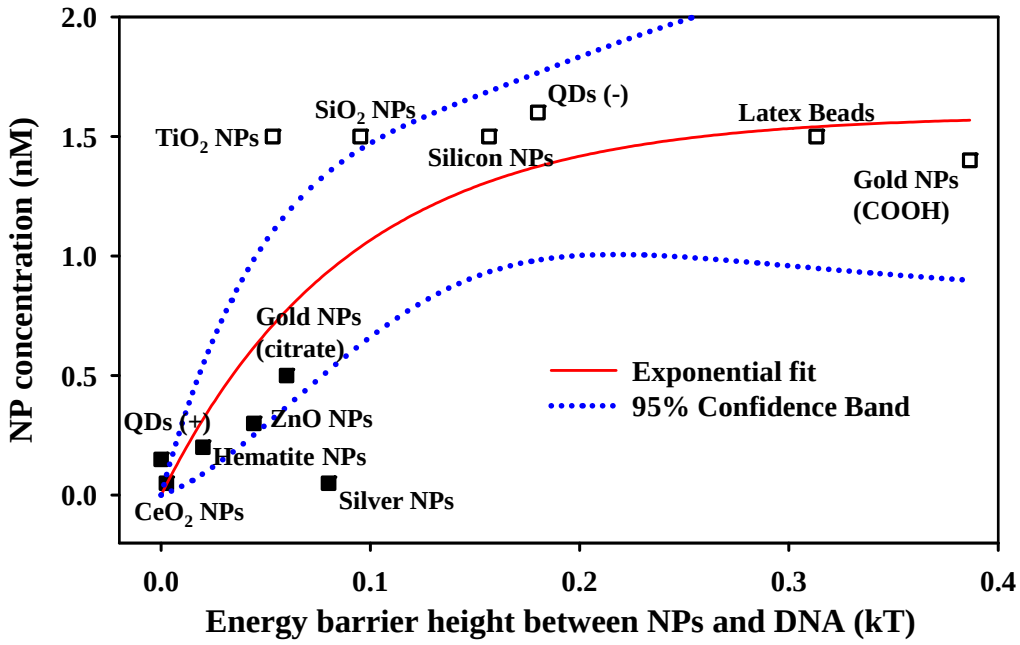

Figure 9.6. Relationship between the tested concentration of NPs significantly inhibiting DNA replication *in vitro* and the determined energy barrier between NPs and DNA. A significant inhibition occurs when the intensity of the gel electrophoresis band in Figure 3 is below 30% of that of the positive control. TiO_2 NPs, SiO_2 NPs, silicon NPs, QDs (-), gold NPs (COOH) and latex beads (open square) did not show a significant inhibition of DNA replication even at the highest concentration employed in this study, still those NPs were included in the figure for comparison with other NPs that have strong inhibition on DNA replication. Data points represent individual replicates. An exponential regression [$y = 1.59(1-\exp(-11.10x))$, $r^2 = 0.62$] was performed.

9.4.4. Two-dimensional diagrams to determine the energy barrier between NPs and DNA

We constructed two-dimensional diagrams (shown in Figure 9.7) to help researchers determine the interaction energy barrier between a certain type of NPs and DNA. Each diagram was produced under a certain NP Hamaker constant (*e.g.*, 1, 3, 4, and 10 kT). Contour lines were also plotted in the diagram to clearly indicate the height of the energy barrier. As the surface potential of the particle shifts from negative to

positive or as the Hamaker constant increases, the energy barrier decreased, indicating that NPs with positive surface potential or a high Hamaker constant have a high affinity for DNA molecules. This is consistent with a previous study [469]. However, the increase in particle size does not always result in an increase in the height of the energy barrier, which can be observed most obviously in the scenario in which the Hamaker constant of the NPs is 10 kT (Figure 9.7d). Provided the size, surface potential, and Hamaker constant of a certain type of NPs are known, we can determine the height of the energy barrier between the NPs and DNA molecules, and subsequently estimate the affinity of the NPs for DNA and further evaluate the potential genetic effects of NPs.

The statement of particle size effect on the energy barrier, *i.e.*, increased particle size does not always result in increased energy barrier, may be less intuitive, but it can be validated by comparing two tested NPs: ZnO and TiO_2 NPs. Their Hamaker constants (1.6 *versus* 1.7 kT) and surface potentials (-10.15 *versus* -12.33 mV) are both quite close, but the particle size of ZnO is much larger than that of TiO_2 NPs. The modeling results showed that ZnO NPs has slightly lower energy barrier with DNA than TiO_2 does (Figure 9.2). The AFM results showed that ZnO as well as TiO_2 NPs were able to bind to DNA (Figure 9.3). This example validated the less intuitive size effect of NPs on their interaction energy with DNA.

It is worth noting that the ionic strength of the solution system used in this study is 0.4 M. If different slovent systems with different ionic strength were used, the computed interaction energy results would vary. Firstly, a different ionic strength would alter the Debye length in the solution and subsequently change the surface potential of NPs and DNA. This was addressed by Eqs. (1)-(4). In addition, particle size may also be altered due to particle aggregation under a high ionic strength. The aggregation kinetics modeling of NPs has been intensively investigated in our group [197, 303, 480]. However, we did not incorporate the aggregation model into the theory in the present study, as particle size that we used as the model input was measured after the aggregation has reached

slow-aggregation stage, namely, the particle size was pseudo-stable. Provided that we determine the physicochemical properties (such as the size and surface potential) of NPs under pseudo-stable states in a new solution, we can still apply the theoretical approach proposed in this study to the new system.

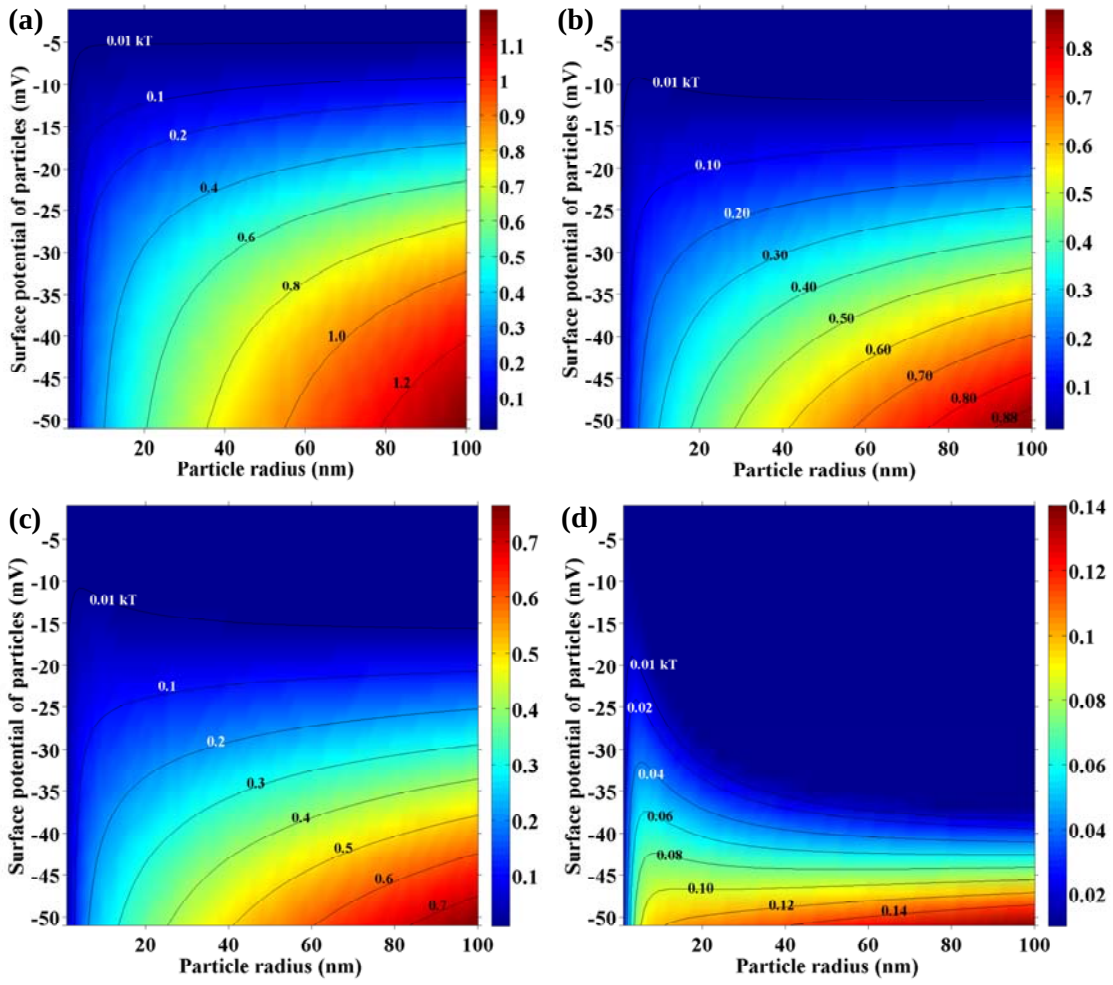

Figure 9.7. Representative two-dimensional diagrams characterizing the effect of NP size and surface potential on the height of the energy barrier between the particle and DNA. The Hamaker constants of the particles in (a)–(d) are 1, 3, 4, and 10 kT, respectively. The lines are contour lines representing the height of the energy barrier (in units of kT) between the particle and DNA. The color indicates the height of the energy barrier of each pixel.

Biological systems are far more complex than the *in vitro* system used in the current study. However, for simplicity, the PCR experiments here employed "naked" DNA (histone-free DNA) similar to that which is present in bacterial cells. This may a less accurate depiction of human DNA, which is complexed with histones, forming nucleosomes, and further packaged into chromosomes. However, the nucleosome is not static and has been reported in dynamic equilibrium between wrapped and unwrapped state [481-483]. Nucleosomes spontaneously undergo a conformational fluctuation process called "DNA site exposure", in which a stretch of DNA transiently unwraps off the histone core.[481] The NPs could gain access to DNA sites in such exposed states. We may reasonably infer that NPs that have a high affinity for naked DNA should also have a high affinity for the nucleosome. The experimental validation of this inference using AFM is very challenging, as the size of a chromosome is much larger than that of NPs (μm *versus* nm) and the chromosome has an irregular surface, which would likely makes it more challenging to locate NPs that bind with a chromosome.

Also, NPs in contact with biological fluids interact with proteins and form a dynamic protein corona, whose composition varies over time and finally reaches equilibrium [98, 484]. The existence of the protein corona would reshape the nature of NPs such as the surface potential and particle size. Understanding the protein corona is crucial in predicting biological effects of NPs in biological systems [485]. The theoretical methodology in the present study could also be applied to the interaction of NP-protein corona complex with DNA, provided that we know the surface potential, size and composition of the complex in equilibrium. The protein corona may introduce additional non-DLVO forces (especially the hydrogen bonding-induced specific interaction force) into the interaction of NPs with DNA, which under additivity assumption [214], can be incorporated into the theoretical interaction model for describing the interaction between NP-protein corona complexes and DNA [486]. Currently, such studies as well as those using AFM as a tool to probe these interactions are under way in our group.

9.5. Conclusion

In conclusion, this study showed that NPs with a high binding affinity for DNA molecules also have a strong inhibitory effect on DNA replication, while NPs with a low binding affinity for DNA do not. The binding affinity can be predicted by calculating the interaction energy between NPs and DNA on the basis of DLVO models. NPs located in the blue-colored region of the two-dimensional diagrams (Figure 9.7) are more likely to result in adverse genetic effects compared with those in the red-colored region. In the future genotoxicological testing of NPs, researchers may be able to prioritize NPs in the blue-colored region, which are predicted to have a high binding affinity for DNA. Also, this study has applications for the rational design of functionalized NPs in DNA labeling, biological imaging and sensing, and drug delivery for medical and therapeutic applications. Finally, although we demonstrate here the effects of direct binding of NPs to DNA, this likely is one of many mechanisms by which NPs can induce adverse genetic effects in living cells. Additional work is required for a comprehensive understanding of the underlying toxicity mechanisms of NPs and to build an “ultimate” predictive model of the biological effect of NPs that takes into account multiple toxicity mechanisms and their interactions.

CHAPTER 10

MAJOR CONCLUSIONS AND FUTURE WORK

10.1. Major conclusions

The key findings and conclusions of this dissertation are briefly summarized below:

(i) Aggregation of NPs in aqueous media is greatly influenced by a variety of media conditions such as salts (or ionic strength), and organic molecules in the media, and temperature. The collective effect of multiple factors on NP aggregation can be very complicated. For instance, when both $CaCl_2$ and natural organic matter are present, depending on the concentration of $CaCl_2$, the NP aggregation can be either enhanced (high $CaCl_2$ concentration) or inhibited (low $CaCl_2$ concentration).

(ii) The aggregation of NPs is in essential governed by the interfacial forces/interactions among NPs. Provided that we can depict these forces, we can predict the aggregation behavior of NPs. The conventional DLVO theory used for describing colloidal stability cannot well describe NP aggregation. Rather, extended DLVO (EDLVO) theory, which incorporated non-DLVO interactions (*e.g.*, Lewis acid-base interactions, steric interactions, and polymer bridging interactions), overcame the discrepancy existing between the DLVO theoretical prediction and experimental observations of NP aggregation. On the basis of the EDLVO theory and the von Smoluchowski's population balance equation, we developed models for predicting the aggregation of NPs, which predicted well the aggregation kinetics of NPs under various conditions including monovalent and divalent salts, natural organic matter, and temperature.

(iii) Interactions between NPs and cell membrane played a crucial role in causing cytotoxicity towards unicellular organisms like *paramecium*. Due to the lack of cell wall, the susceptible cell membrane of *paramecium* is directly exposed to NPs in the medium. The extent and strength of direct nano-cell membrane interaction can be evaluated and quantified by calculating the interfacial force/interaction between NPs and cell membrane. We found NPs that have strong association or interaction with the cell membrane tended to induce more severe cytotoxicity.

(iv) AFM is proved to be a powerful tool for characterizing nano-DNA interactions on the single NP and single-molecular level. With QD as a model NP, the NP-to-DNA binding characteristics including the binding mechanism, binding kinetics, binding isotherm and binding specificity was examined using AFM. Some important kinetic and thermodynamic parameters for QD binding to DNA including binding rate constant, equilibrium constant, and maximum binding number were determined, which are in the similar order of magnitude as protein binding to DNA. The QD-to-DNA binding specificity was determined as non-specific.

(v) The binding of NPs to DNA or the direction nano-DNA interaction is an important mechanism for causing the adverse genetic effects of NPs. NPs with a high binding affinity for DNA molecules also has a strong inhibitory effect on DNA replication, while NPs with a low binding affinity for DNA do not. Moreover, the binding affinity can be predicted by calculating the interaction energy between NPs and DNA on the basis of DLVO models. The good relationship between the calculated energy barrier between NPs and DNA and the adverse genetic effects of NPs suggested that the modeling approach may act as a simple and effective method for predicting the genetic effects of NPs and further evaluating the biological effect of NPs.

10.2. Future work

Based on the current knowledge and challenges, future work to advance the understanding of nano-bio interactions may include the following crucial issues:

(i) Identify the real nano-induced effects. As many NPs undergo aggregation in aqueous media, it is very challenging to differentiate the toxic effect induced by real single NPs from that induced by the aggregates. AFM, as shown in this dissertation, has been demonstrated as a powerful tool for probing the nano-bio interface on the single NP level. It thus has the potential to characterize the effect of single NPs on biological systems such as the change of conformational, mechanical and electrical properties of biological systems.

(ii) Investigate the internalization amount and pathway of NPs into cell. It is difficult to know the exact amount of NPs internalized by the cell, because differentiating intracellular NPs from those adsorbed on cell surface is not easy. Moreover, it is useful to know the entry mechanism (e.g., endocytosis, phagocytosis, or direct penetration) of NPs into cell.

(iii) Development of predictive models for other toxicity mechanisms of NPs. Up to now, we have made remarkable progress in modeling the direct nano-DNA and nano-cell membrane interactions. There are many other mechanisms leading to adverse biological effects of NPs such as protein binding/unfolding response, mitochondrial damage, lysosomal damage, and inflammation. Much more work is required for a comprehensive understanding and predictive modeling of these mechanisms. For instance, protein binding/unfolding induced by NPs is currently a hot research area. Numerous analytical and modeling efforts have been made to unveil the change of protein after binding to NP surface. Our ultimate goal is to

build an “ultimate” predictive model that takes into account multiple toxicity mechanisms and their interactions.

(iv) Investigate the long term ecological and evolutionary consequences of NPs. Specifically, four basic questions need to be answered: (1) do NPs interfere with predator-prey interactions and affect their population dynamics? (2) do NPs influence the competition of multiple species? (3) do NPs restructure ecological community assembly? (4) do NPs affect the evolution of biodiversity?

APPENDIX A

EVALUATION OF DLVO INTERACTION BETWEEN A SPHERE AND A CYLINDER

A.1. Abstract

Van der Waals (vdW) and electrostatic double layer (EDL) interactions between a sphere and a cylinder are determined using the surface element integration (SEI) technique. Compared with Derjaguin approximation, the SEI technique gives more accurate predictions for the EDL interaction between a sphere and a cylinder. However, the SEI technique slightly overestimates the vdW interaction compared with predictions based on Hamaker's approach. The curvature effect is important at small cylinder-to-sphere size ratios, but when the ratio is greater than 10, both EDL and vdW interactions between a sphere and a cylinder can be approximated adequately by that between a sphere and a flat plate. In addition, as Debye length decreases, the EDL interaction energy between a sphere and a cylinder decays more quickly. At small separation distances, a smaller Debye length leads to a stronger EDL interaction between a sphere and a cylinder, whereas at large separation distances, a larger Debye length results in a stronger EDL interaction.

A.2. Introduction

It is important to compute the interaction force or energy between two surfaces to theoretically understand interfacial problems that are frequently encountered in physics, biology, and physical chemistry [266, 487]. The Derjaguin-Landau-Verwey-Overbeek (DLVO) theory is widely used to describe such interfacial interactions between charged surfaces in liquid media [213, 347]. DLVO theory characterizes the total interaction energy as the combination of van der Waals (vdW) and electrostatic double-layer (EDL)

interactions. The evaluation of the DLVO interaction between a sphere and a cylinder is important, as it is widely encountered in practice, e.g., in particle-hollow fiber interaction in membrane filtration, NP-nanotube interaction, and protein-DNA interaction. Hence, it is necessary to derive the expression for the interaction energy between a sphere and a cylinder to facilitate research on relevant systems.

The EDL energy between two macrobodies was derived from the well-known Poisson-Bolztmann equation [246, 254]; however, an exact analytic solution to the equation is limited to the case of two infinite parallel flat plates [488]. In this respect, the Derjaguin approximation technique was conventionally employed to estimate the interaction force or energy between two curved surfaces in terms of the corresponding interaction energy per unit area of two planar surfaces [489]. However, Derjaguin approximation assumes that the range of the interaction energy is remarkably shorter than the radii of curvature of the particles, i.e., its applicability is limited to large particles and other geometries; it may not be a valid approximation in nanoscale studies [490]. The limitation of Derjaguin's approach can be circumvented by employing the surface element integration (SEI) technique [491], which rigorously considers the effects of the curvature and shape of interacting bodies and is thus valid for the interaction of small particles.

The SEI technique also can be employed to calculate vdW energy and other interaction energies [491]. In addition, there are two conventional approaches to the calculation of vdW energy: Lifshitz's quantum electrodynamics approach [492] and Hamaker's microscopic approach [493]. It is a formidable challenge to apply Lifshitz's approach for vdW energy, which generally yields a detailed numerical solution [494]. Hamaker's approach is remarkably simpler, although it involves evaluation of six nested integrals. It assumes that the vdW interaction between two bodies of arbitrary geometry is the sum of the interactions between each molecular/atom pair in the system [493]. Under this pairwise additivity assumption, the vdW energy of a sphere-cylinder interaction was

calculated by integrating the individual interactions between each molecule pair over the two macroscopic bodies [495].

Several previous studies have investigated the interaction of a sphere with a cylinder by calculating either EDL energy [496] or vdW energy [495, 497-499]; the total interaction energy, however, was not evaluated. Moreover, although the SEI technique has been successfully used to derive the interaction energy expression for sphere-sphere [490] and sphere-flat plate geometries [494], it has not been applied to the sphere-cylinder geometry. Therefore, we extended the SEI technique to calculate both EDL and vdW energies between a sphere and a cylinder. To assess the accuracy of this technique, Derjaguin approximation and Hamaker's approach were employed to calculate the EDL and vdW energy, respectively, which were compared with SEI predictions.

A.3. Theory

A.3.1. SEI technique

The SEI technique, developed by Elimelech and Bhattacharjee [491], rigorously considers the curvature effects of interacting macrobodies and provides a remarkably accurate evaluation of interaction energies. In this approach, the surfaces of the interacting macrobodies are projected on two parallel planes, and the interaction energy (V) between two macrobodies with a separation distance D can be calculated by a double integral over the projection plane:

$$\mathrm{V}(D)=\int_A \mathbf{n_2}\cdot\mathbf{k_2}\frac{\mathbf{n_1}\cdot\mathbf{k_1}}{|\mathbf{n_1}\cdot\mathbf{k_1}|}E(r)\,dA \qquad (1)$$

where $\mathbf{n_1}$ and $\mathbf{n_2}$ represent the outward unit vectors normal to the surfaces, $\mathbf{k_1}$ and $\mathbf{k_2}$ represent the unit vectors directed toward the positive z axes of each body-fixed coordinate system which is selected in such a way that the xy planes are parallel while the z axes face each other, $E(r)$ is the interaction energy per unit area between two infinite

flat plates separated by a distance r, and A is the projected area of the macrobody on the xy plane.

A.3.2. EDL energy between a sphere and a cylinder

The SEI technique was utilized to calculate the EDL energy between a sphere and a cylinder, as shown in Figure A.1.

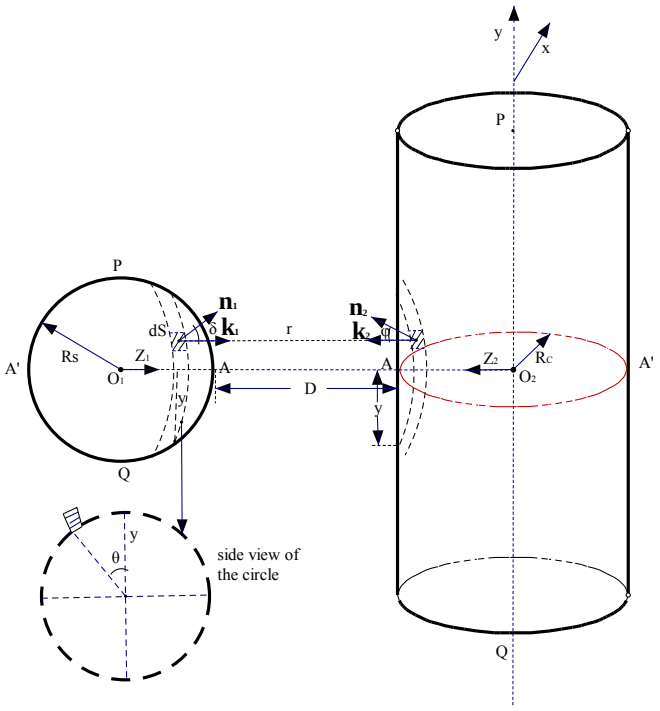

Figure A.1. Schematic illustration of the EDL interaction between a sphere of radius R_S and a cylinder of radius R_C. The sphere is separated from the cylinder by a distance D. $x_1y_1z_1$ and $x_2y_2z_2$ are two body–fixed coordinate systems with the z_1 and z_2 axes directly facing each other and the x_1y_1 and x_2y_2 planes parallel to each other. The surface element in the sphere is denoted as dS, which has a corresponding z_1 axis–projection surface element on the cylinder. The separation distance between the two surface elements is denoted as r. $\mathbf{n_1}$ and $\mathbf{n_2}$ represent the outward unit vectors normal to the surface element. $\mathbf{k_1}$ and $\mathbf{k_2}$ represent the unit vectors directed toward the positive z axes (facing each other). δ and φ are the angles between $\mathbf{n_1}$ and $\mathbf{k_1}$, and $\mathbf{n_2}$ and $\mathbf{k_2}$, respectively. The geometry is conveniently described with coordinates (y, θ). y is the radius of the circle

(parallel to the *xy* plane) on the sphere on which the surface element is positioned. θ is the angle between the reference direction on the circle (i.e., the *y*-axis direction) and the line from the surface element to the center of the circle. The area of the differential surface element in the sphere can be expressed as $yd\theta dy/cos\delta$.

The EDL energy per unit area between two infinite flat plates separated by a distance *r* is given by Eq. (2) [488]:

$$V_{EDL,surface-surface}(r) = \varepsilon_r \varepsilon_0 \kappa \psi_{o1} \psi_{o2} \left[\csc h(\kappa r) + \frac{{\psi_{o1}}^2 + {\psi_{o2}}^2}{2\psi_{o1}\psi_{o2}} (1 - \coth \kappa r) \right] \qquad (2)$$

where ε_r and ε_0 are the relative permittivity of the solution and the permittivity of a vacuum, respectively; κ is the Debye-Hückel parameter of the electrolyte solution; and ψ_{o1} and ψ_{o2} are the unperturbed surface potentials of two interacting macrobodies.

The EDL energy for sphere-cylinder interaction was then derived according to Eq. (1). Because both $\mathbf{n_1 \cdot k_1}/|\mathbf{n_1 \cdot k_1}|$ and $\mathbf{n_2 \cdot k_2}$ will assume a positive or negative value depending on at which semisphere or semicylinder the surface element locates, we determined the total interaction energy between the sphere and the cylinder by calculating the interaction energy between each semisphere and semicylinder. The interaction energies between semisphere *PAQ* and semicylinder *PAQ*, semisphere *PA′Q* and semicylinder *PAQ*, semisphere *PAQ* and semicylinder *PA′Q*, and semisphere *PA′Q* and semicylinder *PA′Q* are positive, negative, negative, and positive, respectively. Therefore, the total interaction energy can be determined using the following equation [490]:

$$V_{TOT} = V_{PAQ-PAQ} - V_{PA'Q-PAQ} - V_{PAQ-PA'Q} + V_{PA'Q-PA'Q} \qquad (3)$$

The distance *r* between two surface elements, one each on the sphere and on the cylinder, is determined by Eq. (4):

$$
\begin{aligned}
r_{PAQ-PAQ} &= D + R_S - \sqrt{R_S{}^2 - y^2} + R_C - \sqrt{R_C{}^2 - y^2 \sin^2\theta} \\
r_{PA'Q-PAQ} &= D + R_S + \sqrt{R_S{}^2 - y^2} + R_C - \sqrt{R_C{}^2 - y^2 \sin^2\theta} \\
r_{PAQ-PA'Q} &= D + R_S - \sqrt{R_S{}^2 - y^2} + R_C + \sqrt{R_C{}^2 - y^2 \sin^2\theta} \\
r_{PA'Q-PA'Q} &= D + R_S + \sqrt{R_S{}^2 - y^2} + R_C + \sqrt{R_C{}^2 - y^2 \sin^2\theta}
\end{aligned}
\tag{4}
$$

In addition, the terms $|\mathbf{n_2}\cdot\mathbf{k_2}|$ and dA are calculated as follows:

$$
\left|\mathbf{n}_2 \cdot \mathbf{k}_2\right| = \cos\varphi = \frac{\sqrt{R_C{}^2 - y^2 \sin^2\theta}}{R_C} \tag{5}
$$

$$
dA = dS \cdot \left|\mathbf{n}_1 \cdot \mathbf{k}_2\right| = dS \cdot \cos\delta = y d\theta dy \tag{6}
$$

By substituting Eqs. (1), (5), and (6) into Eq. (3), we obtain the interaction energy expression between a sphere and a cylinder:

$$
\begin{aligned}
&V_{EDL,sphere-cylinder}^{SEI}\ (D) = 4\int_0^{\frac{\pi}{2}} \int_0^{TBD} \frac{y\sqrt{R_c{}^2 - y^2 \sin^2\theta}}{R_c} \times \\
&\left[E\left(r_{PAQ-PAQ}\right) - E\left(r_{PA'Q-PAQ}\right) - E\left(r_{PAQ-PA'Q}\right) + E\left(r_{PA'Q-PA'Q}\right)\right] dy d\theta
\end{aligned}
\tag{7}
$$

where the upper limit of the integral term dy is to be determined (*TBD*), depending on the relative magnitudes of the sphere radius (R_S) and cylinder radius (R_C). Eq. (7) remains unaltered regardless of the physical origin of the interaction energy, namely, it can be applied to both EDL and vdW energies.

For $R_C \geq R_S$, integration of the term dy in Eq. (7) is conducted over the whole sphere:

$$V_{EDL,sphere-cylinder}^{SEI}(D) = 4\varepsilon_r\varepsilon_0\kappa\psi_{o1}\psi_{o2}\int_0^{\frac{\pi}{2}}\int_0^{R_S}\frac{y\sqrt{R_c{}^2 - y^2\sin^2\theta}}{R_c}\times$$

$$\left\{\begin{array}{l}
\csc h\left[\kappa\left(D + R_S - \sqrt{R_S{}^2 - y^2} + R_c - \sqrt{R_c{}^2 - y^2\sin^2\theta}\right)\right] \\
-\csc h\left[\kappa\left(D + R_S + \sqrt{R_S{}^2 - y^2} + R_c - \sqrt{R_c{}^2 - y^2\sin^2\theta}\right)\right] \\
-\csc h\left[\kappa\left(D + R_S - \sqrt{R_S{}^2 - y^2} + R_c + \sqrt{R_c{}^2 - y^2\sin^2\theta}\right)\right] \\
+\csc h\left[\kappa\left(D + R_S + \sqrt{R_S{}^2 - y^2} + R_c + \sqrt{R_c{}^2 - y^2\sin^2\theta}\right)\right] \\
+\dfrac{\psi_{o1}{}^2 + \psi_{o2}{}^2}{2\psi_{o1}\psi_{o2}}\left[\begin{array}{l}
-\coth\kappa\left(D + R_S - \sqrt{R_S{}^2 - y^2} + R_c - \sqrt{R_c{}^2 - y^2\sin^2\theta}\right) \\
+\coth\kappa\left(D + R_S + \sqrt{R_S{}^2 - y^2} + R_c - \sqrt{R_c{}^2 - y^2\sin^2\theta}\right) \\
+\coth\kappa\left(D + R_S - \sqrt{R_S{}^2 - y^2} + R_c + \sqrt{R_c{}^2 - y^2\sin^2\theta}\right) \\
-\coth\kappa\left(D + R_S + \sqrt{R_S{}^2 - y^2} + R_c + \sqrt{R_c{}^2 - y^2\sin^2\theta}\right)
\end{array}\right]
\end{array}\right\} dyd\theta \qquad (8)$$

However, if $R_C < R_S$, integration of the term *dy* in Eq. (7) is conducted over only the part of the sphere for which the projected area is not beyond the cylinder.

$$V_{EDL,sphere-cylinder}^{SEI}(D)=4\varepsilon_r\varepsilon_0\kappa\psi_{o1}\psi_{o2}\int_0^{\frac{\pi}{2}}\int_0^{R_C}\frac{y\sqrt{R_c^{\,2}-y^2\sin^2\theta}}{R_c}\times$$

$$\left\{\begin{array}{l}\csc h\left[\kappa\left(D+R_S-\sqrt{R_S^{\,2}-y^2}+R_c-\sqrt{R_c^{\,2}-y^2\sin^2\theta}\right)\right]\\ -\csc h\left[\kappa\left(D+R_S+\sqrt{R_S^{\,2}-y^2}+R_c-\sqrt{R_c^{\,2}-y^2\sin^2\theta}\right)\right]\\ -\csc h\left[\kappa\left(D+R_S-\sqrt{R_S^{\,2}-y^2}+R_c+\sqrt{R_c^{\,2}-y^2\sin^2\theta}\right)\right]\\ +\csc h\left[\kappa\left(D+R_S+\sqrt{R_S^{\,2}-y^2}+R_c+\sqrt{R_c^{\,2}-y^2\sin^2\theta}\right)\right]\\ +\dfrac{\psi_{o1}^{\,2}+\psi_{o2}^{\,2}}{2\psi_{o1}\psi_{o2}}\left[\begin{array}{l}-\coth\kappa\left(D+R_S-\sqrt{R_S^{\,2}-y^2}+R_c-\sqrt{R_c^{\,2}-y^2\sin^2\theta}\right)\\ +\coth\kappa\left(D+R_S+\sqrt{R_S^{\,2}-y^2}+R_c-\sqrt{R_c^{\,2}-y^2\sin^2\theta}\right)\\ +\coth\kappa\left(D+R_S-\sqrt{R_S^{\,2}-y^2}+R_c+\sqrt{R_c^{\,2}-y^2\sin^2\theta}\right)\\ -\coth\kappa\left(D+R_S+\sqrt{R_S^{\,2}-y^2}+R_c+\sqrt{R_c^{\,2}-y^2\sin^2\theta}\right)\end{array}\right]\end{array}\right\}dyd\theta$$

$$+4\varepsilon_r\varepsilon_0\kappa\psi_{o1}\psi_{o2}\int_{R_C}^{R_S}\int_0^{\arcsin\left(\frac{R_C}{y}\right)}\frac{y\sqrt{\left(R_s^{\,2}-y^2\right)\left(R_c^{\,2}-y^2\sin^2\theta\right)}}{R_sR_c}\times$$

$$\left\{\begin{array}{l}\csc h\left[\kappa\left(D+R_S-\sqrt{R_S^{\,2}-y^2}+R_c-\sqrt{R_c^{\,2}-y^2\sin^2\theta}\right)\right]\\ -\csc h\left[\kappa\left(D+R_S+\sqrt{R_S^{\,2}-y^2}+R_c-\sqrt{R_c^{\,2}-y^2\sin^2\theta}\right)\right]\\ -\csc h\left[\kappa\left(D+R_S-\sqrt{R_S^{\,2}-y^2}+R_c+\sqrt{R_c^{\,2}-y^2\sin^2\theta}\right)\right]\\ +\csc h\left[\kappa\left(D+R_S+\sqrt{R_S^{\,2}-y^2}+R_c+\sqrt{R_c^{\,2}-y^2\sin^2\theta}\right)\right]\\ +\dfrac{\psi_{o1}^{\,2}+\psi_{o2}^{\,2}}{2\psi_{o1}\psi_{o2}}\left[\begin{array}{l}-\coth\kappa\left(D+R_S-\sqrt{R_S^{\,2}-y^2}+R_c-\sqrt{R_c^{\,2}-y^2\sin^2\theta}\right)\\ +\coth\kappa\left(D+R_S+\sqrt{R_S^{\,2}-y^2}+R_c-\sqrt{R_c^{\,2}-y^2\sin^2\theta}\right)\\ +\coth\kappa\left(D+R_S-\sqrt{R_S^{\,2}-y^2}+R_c+\sqrt{R_c^{\,2}-y^2\sin^2\theta}\right)\\ -\coth\kappa\left(D+R_S+\sqrt{R_S^{\,2}-y^2}+R_c+\sqrt{R_c^{\,2}-y^2\sin^2\theta}\right)\end{array}\right]\end{array}\right\}d\theta dy \quad (9)$$

Moreover, to verify the accuracy of the SEI technique, we also calculated the EDL energy for sphere-cylinder interaction with the Derjaguin approximation approach.

We applied Derjaguin's integration method over the surface area of the semisphere facing the cylinder to calculate the EDL energy between a sphere and a cylinder (illustrated in Figure A.2) [496].

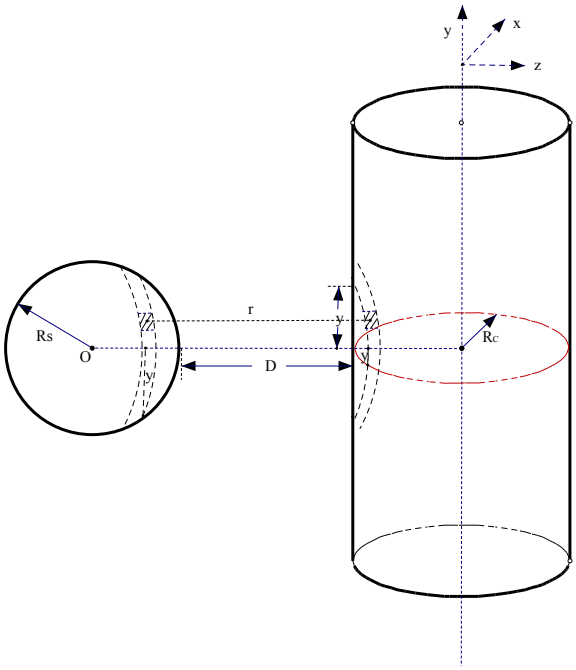

Figure A.2. Schematic representation of the EDL interaction between a sphere of radius R_S and a cylinder of radius R_C, which helps to illustrate the Derjaguin approximation approach. The sphere is separated from the cylinder with a distance D. The surface element in the sphere is denoted as dS, which has a corresponding z-axis–projection surface element on the cylinder. The separation distance between the two surface elements is denoted as r. The geometry is conveniently described with coordinates (y, θ). y is radius of the circle (parallel to the xy plane) on the sphere on which the surface element is positioned. θ is the angle between the reference direction on the circle (i.e., the y-axis direction) and the line from the surface element to the center of the circle.

$$V_{sphere-cylinder}(D) = \iint_{semi-sphere} V(r) y d\theta dy \qquad (10)$$

$$V_{EDL,sphere-cylinder}(D) = 4\int_0^{\frac{\pi}{2}} \left[\int_0^{R_S} V_{surface-surface}(r)\, y dy \right] d\theta \qquad (11)$$

$$r = D + R_S - \sqrt{R_S^{\,2} - y^2} + R_c - \sqrt{R_c^{\,2} - y^2 \sin^2\theta} \qquad (12)$$

For $R_C \geq R_S$, the EDL energy is expressed as Eq. (13):

$$V_{EDL,sphere-cylinder}^{DA-1}(D) = 4\varepsilon_r\varepsilon_0\kappa\psi_{o1}\psi_{o2}\int_0^{\frac{\pi}{2}}\left\{\int_0^{R_C}\left[\begin{array}{l} 1/\sinh\left[\kappa\left(D + R_S - \sqrt{R_S^{\,2} - y^2} + R_c - \sqrt{R_c^{\,2} - y^2\sin^2\theta}\right)\right] \\ + \frac{\psi_{o1}^{\,2} + \psi_{o2}^{\,2}}{2\psi_{o1}\psi_{o2}}\left[1 - \coth\kappa\left(D + R_S - \sqrt{R_S^{\,2} - y^2} + R_c - \sqrt{R_c^{\,2} - y^2\sin^2\theta}\right)\right] \end{array}\right] ydy\right\} d\theta \qquad (13)$$

For $R_C < R_S$, the EDL energy is given by Eq. (14):

$$\begin{aligned} V_{EDL,sphere-cylinder}^{DA-1}(D) = {} & 4\varepsilon_r\varepsilon_0\kappa\psi_{o1}\psi_{o2}\int_0^{\frac{\pi}{2}}\left\{\int_0^{R_C}\left[\begin{array}{l} 1/\sinh\left[\kappa\left(D + R_S - \sqrt{R_S^{\,2} - y^2} + R_c - \sqrt{R_c^{\,2} - y^2\sin^2\theta}\right)\right] \\ + \frac{\psi_{o1}^{\,2} + \psi_{o2}^{\,2}}{2\psi_{o1}\psi_{o2}}\left[1 - \coth\kappa\left(D + R_S - \sqrt{R_S^{\,2} - y^2} + R_c - \sqrt{R_c^{\,2} - y^2\sin^2\theta}\right)\right] \end{array}\right] ydy\right\} d\theta \\ & + 4\varepsilon_r\varepsilon_0\kappa\psi_{o1}\psi_{o2}\int_{R_C}^{R_S}\left\{\int_0^{\arcsin\left(\frac{R_C}{y}\right)}\left[\begin{array}{l} 1/\sinh\left[\kappa\left(D + R_S - \sqrt{R_S^{\,2} - y^2} + R_c - \sqrt{R_c^{\,2} - y^2\sin^2\theta}\right)\right] \\ + \frac{\psi_{o1}^{\,2} + \psi_{o2}^{\,2}}{2\psi_{o1}\psi_{o2}}\left[1 - \coth\kappa\left(D + R_S - \sqrt{R_S^{\,2} - y^2} + R_c - \sqrt{R_c^{\,2} - y^2\sin^2\theta}\right)\right] \end{array}\right] d\theta\right\} ydy \end{aligned} \qquad (14)$$

Derjaguin approximation also can be used to calculate the EDL energy between a sphere and a cylinder by first determining the EDL energy between two parallel cylinders and then integrating the infinitesimal cylinder-cylinder interaction over the sphere, as illustrated in Figure A.3. For convenience, this method is denoted as DA-2; the earlier method is denoted as DA-1.

The EDL energy per unit length between two parallel cylinders with constant surface potential Ψ_{o1} and Ψ_{o2} at separation r is given by Eq. (15) [254, 500]:

$$V_{EDL,cylinder-cylinder}(r) = -2\varepsilon_r\varepsilon_0\sqrt{\kappa}\sqrt{\frac{2\pi R_{C1}R_{C2}}{R_{C1} + R_{C2}}}\left[\left(\frac{\psi_{o1} + \psi_{o2}}{2}\right)^2 Li_{1/2}\left(-e^{-\kappa r}\right) + \left(\frac{\psi_{o1} - \psi_{o2}}{2}\right)^2 Li_{1/2}\left(e^{-\kappa r}\right)\right] \qquad (15)$$

where L_i is the polylogarithm function:

$$Li_s(z) = \sum_{k=1}^{\infty}\frac{z^k}{k^s} \qquad (16)$$

The EDL interaction energy between a sphere and a cylinder with constant surface potential Ψ_{o1} and Ψ_{o2}, respectively, at separation r is given by Eq. (17):

$$V_{EDL,sphere-cylinder}^{DA-2}(D) = -4\varepsilon_r\varepsilon_0\sqrt{2\pi\kappa R_C}\int_0^{Rs} x\sqrt{\frac{x}{(R_S{}^2 - x^2)(R_C + x)}}\left\{\begin{array}{l}\left(\frac{\psi_{o1}+\psi_{o2}}{2}\right)^2 Li_{1/2}\left[-e^{-\kappa(D+R_S-x)}\right] \\ +\left(\frac{\psi_{o1}-\psi_{o2}}{2}\right)^2 Li_{1/2}\left[e^{-\kappa(D+R_S-x)}\right]\end{array}\right\}dx \quad (17)$$

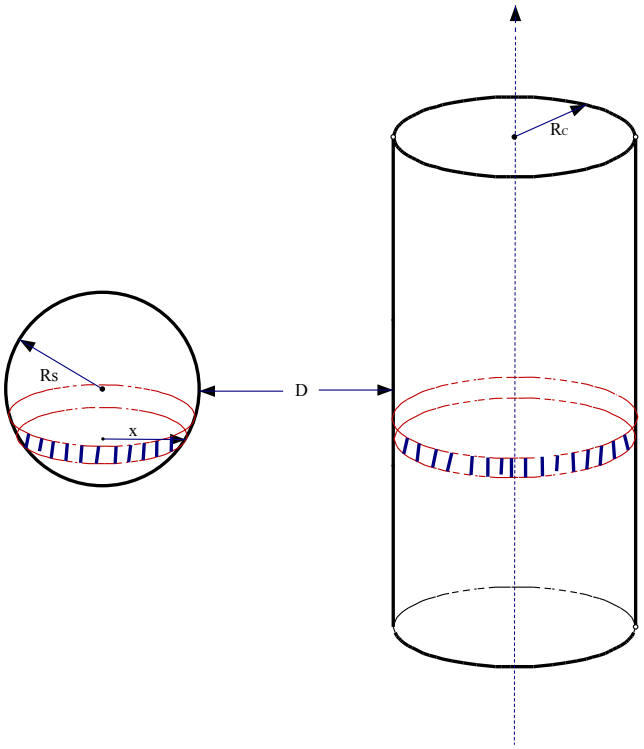

Figure A.3. Schematic representation of the interaction between a sphere of radius R_S and a cylinder of radius R_C. The sphere is separated from the cylinder with a distance D. The EDL interaction between two infinitesimal differential circular rings is approximated by the interaction between two infinitesimal parallel cylinders.

A.3.3. vdW energy between a sphere and a cylinder

Similar to EDL energy, the vdW energy for sphere-cylinder interaction also can be derived with the SEI approach. The non-retarded vdW energy per unit area between two infinite flat plates separated by a distance of r is given by Eq. (18) [493]:

$$E(r) = -\frac{A_H}{12\pi r^2} \quad (18)$$

where A_H is the Hamaker constant of the interacting media.

By substituting Eq. (18) into Eq. (7), we can obtain the SEI expression for the vdW energy between a sphere and a cylinder. Similar to the derivation of EDL energy, if $R_C \geq R_S$, then integration of the term dy is conducted over the whole sphere:

$$V_{vdW,sphere-cylinder}^{SEI}(D) = -\frac{A_H}{3\pi}\int_0^{\frac{\pi}{2}}\int_0^{R_S}\frac{y\sqrt{R_c^2 - y^2\sin^2\theta}}{R_c}\times$$
$$\left\{\begin{array}{l} 1/\left(D + R_S - \sqrt{R_S^2 - y^2} + R_c - \sqrt{R_c^2 - y^2\sin^2\theta}\right)^2 \\ -1/\left(D + R_S + \sqrt{R_S^2 - y^2} + R_c - \sqrt{R_c^2 - y^2\sin^2\theta}\right)^2 \\ -1/\left(D + R_S - \sqrt{R_S^2 - y^2} + R_c + \sqrt{R_c^2 - y^2\sin^2\theta}\right)^2 \\ +1/\left(D + R_S + \sqrt{R_S^2 - y^2} + R_c + \sqrt{R_c^2 - y^2\sin^2\theta}\right)^2 \end{array}\right\} dyd\theta \qquad (19)$$

If $R_C < R_S$, integration of the term dy is conducted over only part of the sphere, and the vdW energy is given by Eq. (20):

$$V_{EDL,sphere-cylinder}^{SEI}(D) = -\frac{A_H}{3\pi}\int_0^{\frac{\pi}{2}}\int_0^{R_C}\frac{y\sqrt{R_c^2 - y^2\sin^2\theta}}{R_c}\times$$
$$\left\{\begin{array}{l} 1/\left(D + R_S - \sqrt{R_S^2 - y^2} + R_c - \sqrt{R_c^2 - y^2\sin^2\theta}\right)^2 \\ -1/\left(D + R_S + \sqrt{R_S^2 - y^2} + R_c - \sqrt{R_c^2 - y^2\sin^2\theta}\right)^2 \\ -1/\left(D + R_S - \sqrt{R_S^2 - y^2} + R_c + \sqrt{R_c^2 - y^2\sin^2\theta}\right)^2 \\ +1/\left(D + R_S + \sqrt{R_S^2 - y^2} + R_c + \sqrt{R_c^2 - y^2\sin^2\theta}\right)^2 \end{array}\right\} dyd\theta \qquad (20)$$
$$-\frac{A_H}{3\pi}\int_{R_C}^{R_S}\int_0^{\arcsin\left(\frac{R_C}{y}\right)}\frac{y\sqrt{R_c^2 - y^2\sin^2\theta}}{R_c}\times$$
$$\left\{\begin{array}{l} 1/\left(D + R_S - \sqrt{R_S^2 - y^2} + R_c - \sqrt{R_c^2 - y^2\sin^2\theta}\right)^2 \\ -1/\left(D + R_S + \sqrt{R_S^2 - y^2} + R_c - \sqrt{R_c^2 - y^2\sin^2\theta}\right)^2 \\ -1/\left(D + R_S - \sqrt{R_S^2 - y^2} + R_c + \sqrt{R_c^2 - y^2\sin^2\theta}\right)^2 \\ +1/\left(D + R_S + \sqrt{R_S^2 - y^2} + R_c + \sqrt{R_c^2 - y^2\sin^2\theta}\right)^2 \end{array}\right\} dyd\theta$$

To verify the accuracy of the SEI technique, the vdW energy between a sphere and a cylinder was also derived with Hamaker's approach. This approach first determines the vdW energy between a point particle and a sphere and then integrates the point particle–sphere interaction over the cylinder, as shown in Figure A.4. The vdW interaction between a point particle and a sphere of radius R_S is given by Eq. (21) [498, 499]:

$$V_{vdW,point-sphere}(r) = -\frac{4A_H}{3\pi}\frac{{R_S}^3}{\left(r^2 - {R_S}^2\right)^3} \qquad (21)$$

where r is the distance between the point particle and the center of the sphere.

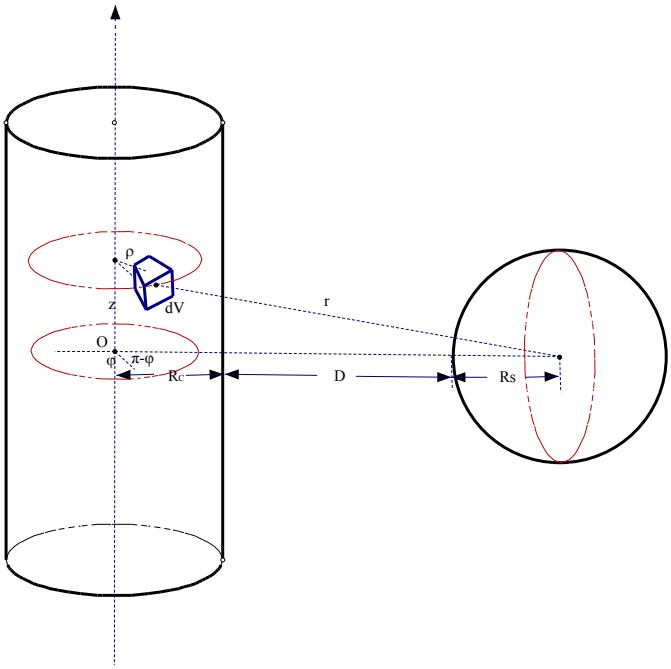

Figure A.4. Schematic representation of the vdW interaction between a sphere of radius R_S and a cylinder of radius R_C. The sphere is separated from the cylinder by a distance D. The volume element in the cylinder is denoted as dV. The separation distance between the volume element and the center of the sphere is denoted as r. The geometry is conveniently described with cylindrical coordinates (ρ, φ, z). The radial distance ρ is the Euclidean distance from the z-axis to the volume element. The azimuth φ is the angle

between the reference direction and the line from the origin to the projection of the volume element on the plane. The height z is the distance from the volume element to the chosen plane.

In cylindrical coordinates, the volume element is $\rho d\varphi d\rho dz$.

$$r^2 = \left(D + R_S + R_C + \rho\cos\varphi\right)^2 + \left(\rho\sin\varphi\right)^2 + z^2 \qquad (22)$$

The vdW energy between a sphere and a cylinder is then given by Eq. (23):

$$\begin{aligned} V_{vdW,sphere-cylinder}^{Hamaker}\left(D\right) &= -\frac{4AR_S^{\,3}}{3\pi}\int_{V_c}\frac{dV_c}{\left(r^2 - R_S^{\,2}\right)^3} \\ &= -\frac{16AR_S^{\,3}}{3\pi}\cdot\int_0^{\pi}d\varphi\int_0^{R_C}\rho d\rho\int_0^{L}\left[\left(D + R_S + R_C + \rho\cos\varphi\right)^2 + \left(\rho\sin\varphi\right)^2 + z^2 - R_S^{\,2}\right]^{-3}dz \end{aligned} \qquad (23)$$

For the interaction of a sphere and an infinite cylinder, the above equation can be further integrated as Eq. (24):

$$\begin{aligned} V_{vdW,sphere-cylinder}^{Hamaker}\left(D\right) &= -\frac{16AR_S^{\,3}}{3\pi}\int_0^{\pi}d\varphi\int_0^{R_C}\frac{3\pi}{16}\left[\left(D + R_S + R_C + \rho\cos\varphi\right)^2 + \left(\rho\sin\varphi\right)^2 - R_S^{\,2}\right]^{-5/2}\rho d\rho \\ &= -AR_S^{\,3}\int_0^{\pi}d\varphi\int_0^{R_C}\left[\rho^2 + 2\rho\left(D + R_S + R_C\right)\cos\varphi + \left(D + R_S + R_C\right)^2 - R_S^{\,2}\right]^{-5/2}\rho d\rho \\ &= \frac{AR_S^{\,3}}{3}\int_0^{\pi}\left\{\frac{\begin{array}{c}\left[\left(D + R_S + R_C\right)\cos\varphi\right]^2\left[6z^2 + \left(D + R_S + R_C\right)^2 - R_S^{\,2}\right] + \left[\left(D + R_S + R_C\right)^2 - R_S^{\,2}\right]^2 + \\ z\left(D + R_S + R_C\right)\cos\varphi\left[2z^2 + 3\left(D + R_S + R_C\right)^2 - 3R_S^{\,2}\right] + 3z\left[\left(D + R_S + R_C\right)\cos\varphi\right]^3\end{array}}{\left[\left(D + R_S + R_C\right)^2\sin^2\varphi - R_S^{\,2}\right]^2\left\{z\left[z + 2\left(D + R_S + R_C\right)\cos\varphi\right] + \left(D + R_S + R_C\right)^2 - R_S^{\,2}\right\}^{3/2}}\right\}_0^{R_C}d\varphi \\ &= \frac{AR_S^{\,3}}{3}\int_0^{\pi}\frac{1}{\left[\left(D + R_S + R_C\right)^2\sin^2\varphi - R_S^{\,2}\right]^2}\left\{-\frac{\left(D + R_S + R_C\right)^2\cos^2\varphi + \left(D + R_S + R_C\right)^2 - R_S^{\,2}}{\left[\left(D + R_S + R_C\right)^2 - R_S^{\,2}\right]^{1/2}}\right. \\ &\left. + \frac{\begin{array}{c}\left(D + 2R_S + R_C\right)\left(D + R_C\right)\left[\left(D + R_S + R_C\right)^2\cos^2\varphi + 3R_C\left(D + R_S + R_C\right)\cos\varphi + \left(D + R_S + R_C\right)^2 - R_S^{\,2}\right] + \\ R_C\left(D + R_S + R_C\right)\cos\varphi\left[2R_C^{\,2} + 6R_C\left(D + R_S + R_C\right)\cos\varphi + 3\left(D + R_S + R_C\right)^2\cos^2\varphi\right]\end{array}}{\left[R_C^{\,2} + 2R_C\left(D + R_S + R_C\right)\cos\varphi + \left(D + R_S + R_C\right)^2 - R_S^{\,2}\right]^{3/2}}\right\}d\varphi \end{aligned} \qquad (24)$$

A.4. Results and discussion

A.4.1. EDL interaction between a sphere and a cylinder

Numerical integrations in this study were performed in Matlab. The surface potentials of both the sphere and the cylinder were assumed to be -25 mV. The curvature effect of the cylinder, as represented by the dimensionless parameter R_C/R_S, on the EDL interaction is shown in Figure A.5. When the cylinder radius R_C is small relative to the sphere radius R_S, a strong effect of curvature is observed on the EDL interaction energy is observed. When R_C is one-tenth of R_S, the EDL energy between the sphere and the cylinder is almost one order of magnitude smaller than that between the sphere and a flat plate. As the cylinder radius increases, the importance of the curvature effect is reduced, and subsequently the EDL interaction between a sphere and a cylinder asymptotically approaches that between a sphere and a flat plate. When R_C is one hundred times larger than R_S, the curvature effect becomes negligible. The EDL interaction between a sphere and a flat plate was calculated from an exact expression specified in Bhattacharjee and Elimelech's study [491], which is a proof that our derivation of the EDL interaction between a sphere and a cylinder is accurate. In fact, by taking R_C in Eq. (8) to infinity, we can obtain the exact same expression for the EDL interaction between a sphere and a flat plate given in the previous study [491].

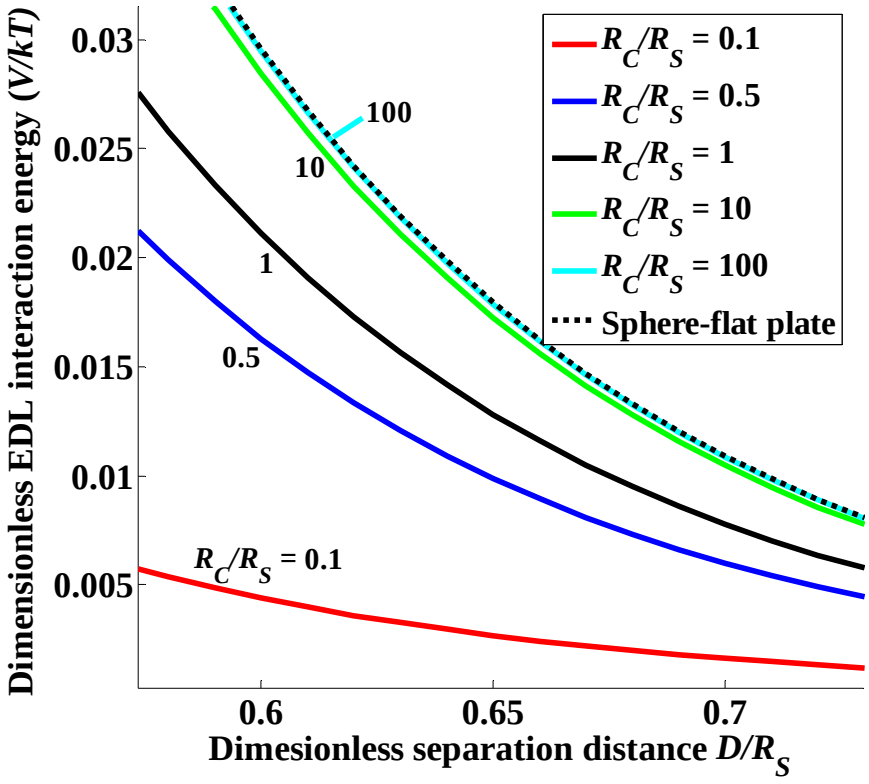

Figure A.5. Effect of cylinder curvature on the EDL interaction energy between a sphere and a cylinder. The sphere radius is fixed at 10 nm. κ is 1 nm^{-1}, which is equivalent to a system of approximately 0.1 M mononvalent electrolyte. When the cylinder radius increases, the EDL interaction energy becomes larger and approaches that between a sphere and a flat plate. With an R_C/R_S ratio of 100, the EDL energy between a sphere and a cylinder was indistinguishable from that between a sphere and a cylinder.

Figure A.6 compares the dimensionless EDL interaction energy for a sphere and a cylinder obtained with the SEI technique and Derjaguin approximation. The EDL energy predictions obtained using the two techniques are markedly different, especially when the curvature of the cylinder is important; with a R_C/R_S ratio of 0.1, Derjaguin's prediction deviates significantly from the SEI prediction. As expected, the SEI predictions are always smaller than Derjaguin's predictions, as Derjaguin's approach overestimates the interaction energy between two surfaces [490]. In the DA-2 method, Derjaguin

approximation was used twice: once for approximation between two parallel cylinders and once for approximation between a sphere and a cylinder; accordingly, the DA-2 method produced predictions that were worse than DA-1.

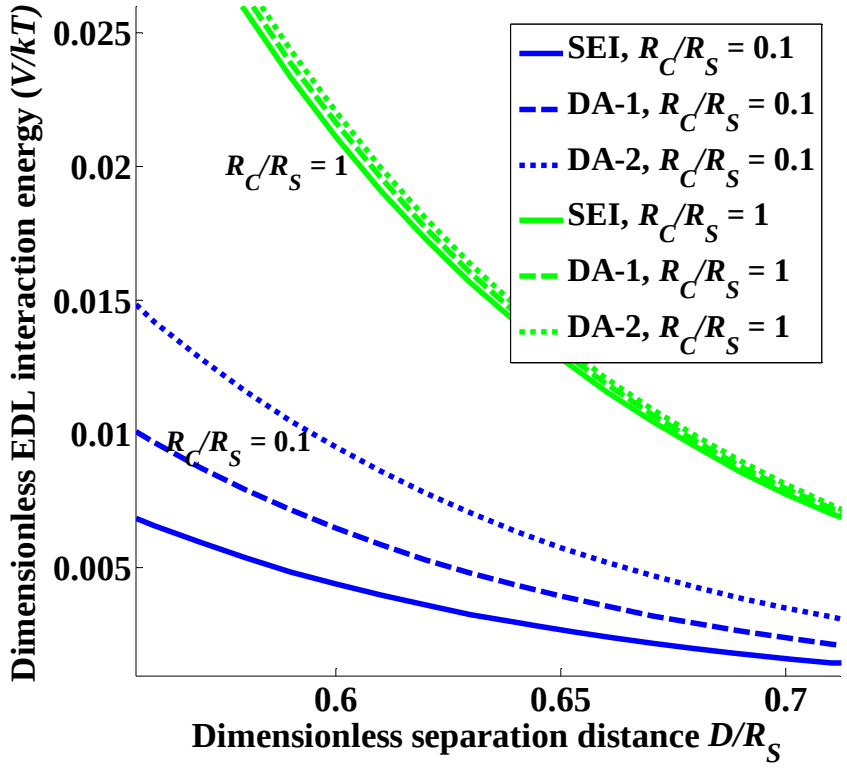

Figure A.6. Comparison of SEI and Derjaguin approximation approaches (DA-1 and DA-2) for calculating the EDL interaction energy between a sphere and a cylinder. κ is 1 nm^{-1}, which is equivalent to a system of approximately 0.1 M ionic strength.

Thereafter, we studied the effect of the ratio of sphere radius to EDL thickness (κR_S) on the EDL interation energy between a sphere and a cylinder. At a constant surface potential, an increase in Debye length (thicker EDL) leads to overlapping EDLs surrounding the sphere and the cylinder, and subsequently results in a longer-range EDL interaction. Figure A.7 shows the EDL interaction for a sphere and a cylinder with κ values of 0.033, 0.1, 0.33, 1 and 3.3 nm^{-1}, which are equivalent to systems with ionic strengths of approximately 10^{-5}, 10^{-4}, 10^{-3}, 10^{-2}, 10^{-1}, and 1 M, respectively. As κ

increases, i.e., as the Debye length decreases, the EDL interaction energy decays faster and approaches zero at a smaller separation distance between the sphere and the cylinder. The relative magnitudes of EDL interactions with various κ values depend on separation distance. At small separation distances, a larger κ (or smaller Debye length) leads to a steeper potential gradient and results in a stronger EDL interaction. However, as the separation distance increases, the EDL interaction with a larger κ may become smaller because EDLs surrounding the sphere and the cylinder are too thin to overlap [496].

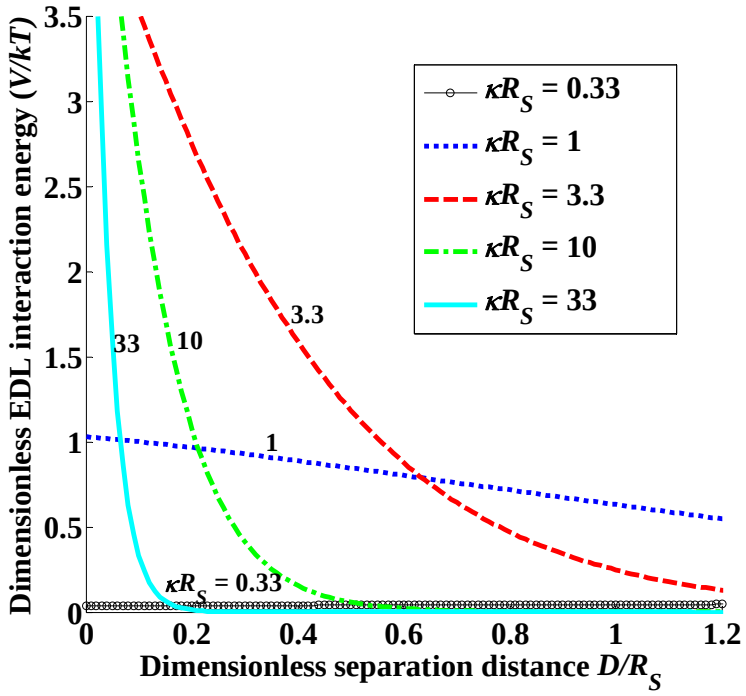

Figure A.7. Effect of the ratio of sphere radius to EDL thickness (κR_S) on the EDL interaction energy between a sphere and a cylinder, each of radius 10 nm.

Investigation of the effect of sphere radius on the EDL interaction between a sphere and a cylinder is also useful, as the size effect is important in many practical problems, such as colloidal fouling in membrane filtration. By fixing the cylinder radius at 10 nm, we investigated how sphere radius influences the EDL interaction. The ionic strength of the system was set at 0.1 M. As shown in Figure A.8, the EDL interaction

between a sphere and a cylinder will increase as the sphere radius increases, i.e., larger spheres have a stronger EDL interactions with cylinders.

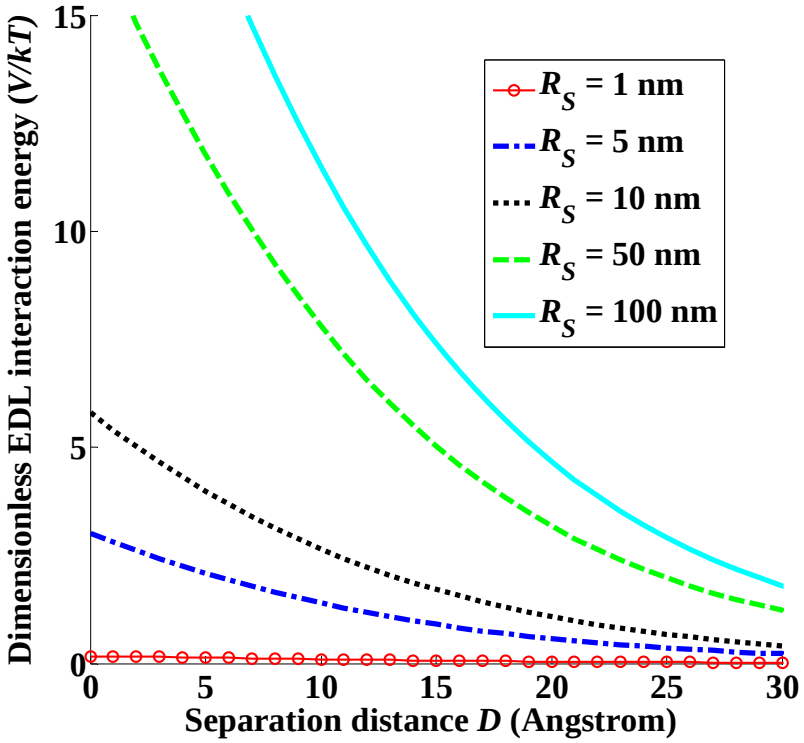

Figure A.8. Effect of sphere radius on the EDL interaction energy between a sphere and a cylinder. The cylinder radius is fixed at 10 nm.. κ is 1 nm^{-1}, which is equivalent to a system of approximately 0.1 M ionic strength.

A.4.2. vdW interaction between a sphere and a cylinder

The effect of curvature of the cylinder on the vdW interaction between a sphere and a cylinder is shown in Figure A.9. The vdW interaction between a sphere and a flat plate was predicted using an exact analytical expression given by Eq. (25) [491, 493]:

$$V^{vdW}_{sphere-flat\ plate}(D) = -\frac{A_H}{6}\left[\frac{R_S}{D} + \frac{R_S}{D+2R_S} + \ln\left(\frac{D}{D+2R_S}\right)\right] \qquad (25)$$

Compared with the vdW interaction for sphere–flat plate, strong curvature effects on the vdW interaction for sphere-cylinder are observed at small cylinder-to-sphere

radius ratios. As the radius ratio increases, the curvature effect becomes weaker, and thus the vdW interaction asymptotically approaches that between a sphere and a flat plate. Calculation of the vdW interaction for sphere–flat plate geometry from an exact expression is a proof that our derivation and numerical integration of the vdW interaction for a sphere-cylinder geometry is accurate. By taking R_C in Eq. (19) to infinity, we can obtain exactly the same expression as Eq. (25).

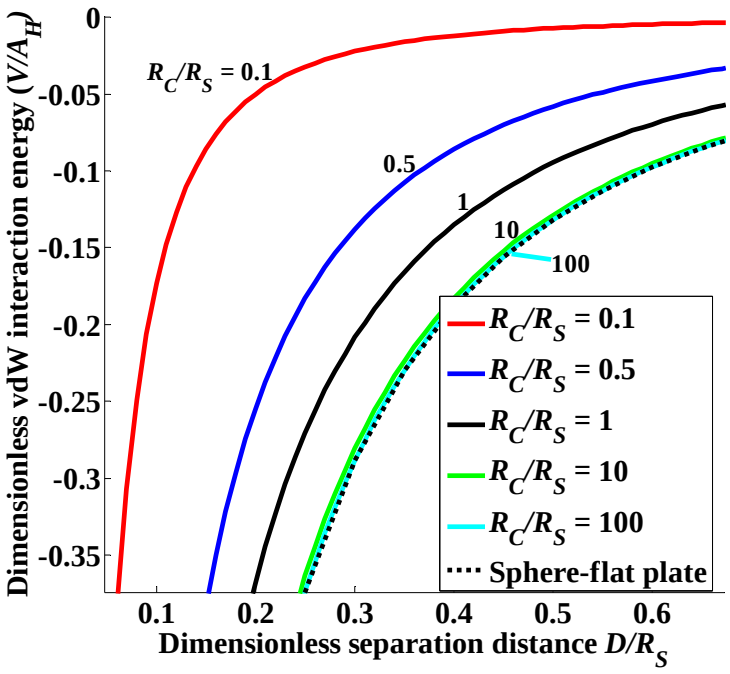

Figure A.9. The effect of cylinder curvature on the dimensionless vdW interaction energy (V/A_H) between a sphere and a cylinder. The sphere radius is fixed at 10 nm. As the cylinder-to-sphere radius ratio increases, the vdW interaction becomes larger. When the radius ratio reaches a large value such as 100, the vdW interaction is indistinguishable from that between a sphere and a flat plate.

By combining the EDL and vdW interaction energies, Figure A.10 shows the effect of cylinder curvature on the total interaction between a sphere and a cylinder. As the cylinder-to-sphere radius ratio increases, that is, the curvature effect becomes strong, the interaction energy barrier of the sphere–cylinder geometry diminishes and deviates

greatly from that of sphere–flat plate geometry. This demonstrates that use of the sphere–flat plate interaction to approximate a sphere–cylinder interaction may greatly overestimate it.

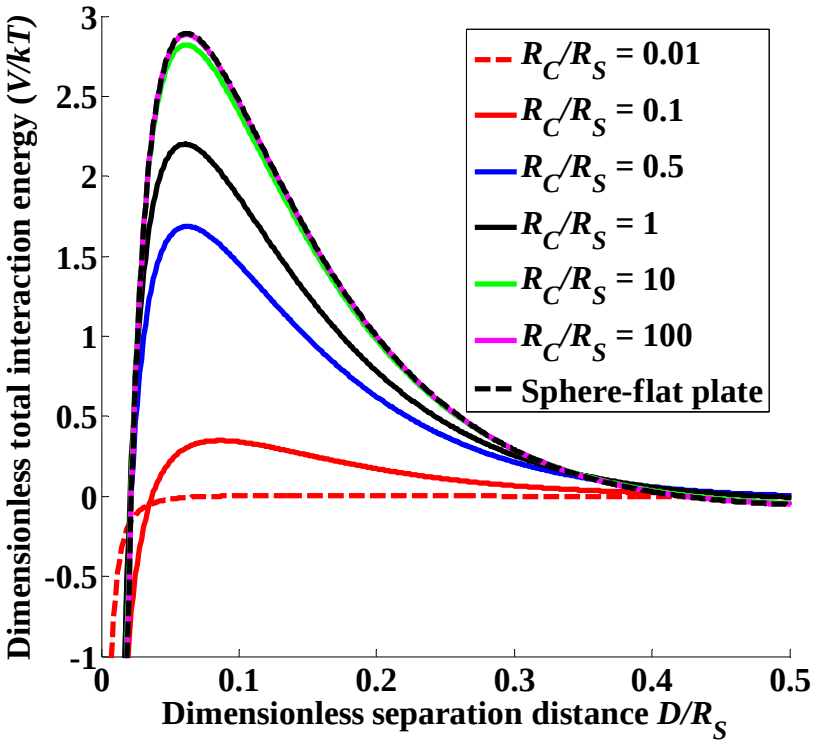

Figure A.10. The effect of cylinder curvature on the dimensionless total interaction energy (V/kT) between a sphere and a cylinder. The sphere radius is fixed at 10 nm. The Hamaker constant of the sphere is set at 1 kT. κ is 1 nm^{-1}. As the cylinder-to-sphere radius ratio decreases, the energy barrier diminishes.

Figure A.11 compares the dimensionless vdW interaction energy, obtained using the SEI technique and Hamaker's approach, for a sphere and a cylinder, each of radius 10 nm. SEI predictions overestimate the interaction energy between two surfaces, owing to the assumption of pairwise interaction between surface elements. Hence, SEI predictions are always larger than Hamaker predictions. The error is small at both small and large

cylinder-to-sphere radius ratios, whereas it is relatively large (up to 20%) at a radius ratio of 1.

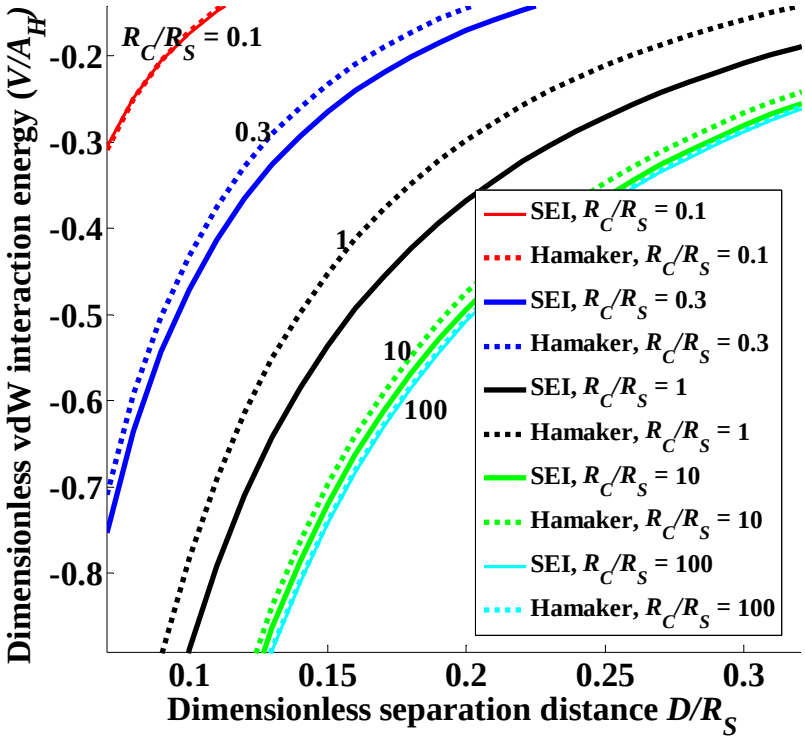

Figure A.11. Comparison of SEI and Hamaker's approach for calculating the vdW interaction energy between a sphere and a cylinder. The sphere radius is fixed at 10 nm.

The effect of sphere radius on the vdW interaction between a sphere and a cylinder is shown in Figure A.12. By fixing the cylinder radius at 10 nm, we investigated how sphere radius influences the vdW interaction. As sphere radius increases, the vdW interaction increases, that is, large spheres have a large vdW interaction with the cylinder. Therefore, both EDL and vdW interactions will become stronger as the sphere radius increases.

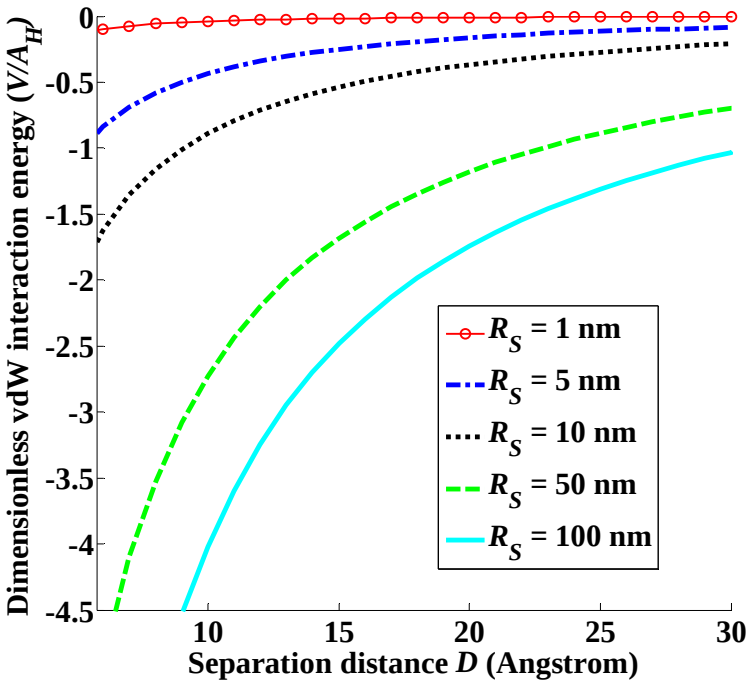

Figure A.12. Effect of sphere radius on the vdW interaction energy between a sphere and a cylinder. The cylinder radius is fixed at 10 nm.

A.5. Conclusion

This study derived expressions for both EDL and vdW interaction energies between a sphere and a cylinder with the SEI technique. The SEI technique better predicts the EDL interaction between a sphere and a cylinder than do Derjaguin approximation, especially when the effect of curvature is important. However, SEI predictions overestimate the vdW interaction for sphere-cylinder geometry as compared with Hamaker's approach. Both EDL and vdW interactions between a sphere and a cylinder asymptotically approach that between a sphere and a flat plate as the cylinder-to-sphere size ratio increases. The model presented in this study can be used to predict the interaction between a sphere and a cylinder, which occurs frequently in natural and engineered systems.

APPENDIX B

EVALUATION OF DLVO INTERACTION BETWEEN A SPHERE AND A SECTION OF TORUS

B.1. EDL energy between a sphere and a section of torus

The SEI technique, developed by Elimelech and Bhattacharjee [491], was utilized to calculate the EDL energy between a sphere and a section of torus. SEI technique considers the curvature effect of interacting bodies and provides accurate calculation of the interaction energy. According to this approach, the interaction energy (V) between two interacting macrobodies with a separation distance D can be calculated by a double integral over the projection plane of surfaces of the macrobodies:

$$\mathrm{V}(D)=\int_A \mathbf{n}_2 \cdot \mathbf{k}_2 \frac{\mathbf{n}_1 \cdot \mathbf{k}_1}{|\mathbf{n}_1 \cdot \mathbf{k}_1|} E(r)\, dA \qquad (1)$$

where xy is the projection plane; $\mathbf{n_1}$ and $\mathbf{n_2}$ represent the outward unit vectors normal to the surfaces; $\mathbf{k_1}$ and $\mathbf{k_2}$ represent the unit vectors directed towards the positive z axes (facing each other) of each body-fixed coordinate system; $E(r)$ is the interaction energy per unit area between two infinite flat plates separated by a distance r; A is the projected area of macrobody on the xy plane.

Figure B.1 schemed the EDL interaction between a sphere and a section of a torus. Utilizing SEI technique expressed by Eq. (1), the EDL energy can be derived. Since both terms $\mathbf{n_1 \cdot k_1} / |\mathbf{n_1 \cdot k_1}|$ and $\mathbf{n_2 \cdot k_2}$ will assume positive and negative values depending on which semi-sphere or semi-torus the surface element locates at, we determined the total interaction energy between the sphere and the torus by calculating the interaction energy between each semi-sphere and semi-torus. The interaction energy between semi-sphere PAQ and semi-torus PAQ, semi-sphere PA'Q and semi-torus PAQ, semisphere PAQ and semi-torus PA'Q, and semi-sphere PA'Q and semi-torus PA'Q are

respectively positive, negative, negative and positive. Therefore, the total interaction energy can be determined by the following equation [490]:

$$V_{TOT} = V_{PAQ-PAQ} - V_{PA'Q-PAQ} - V_{PAQ-PA'Q} + V_{PA'Q-PA'Q} \qquad (2)$$

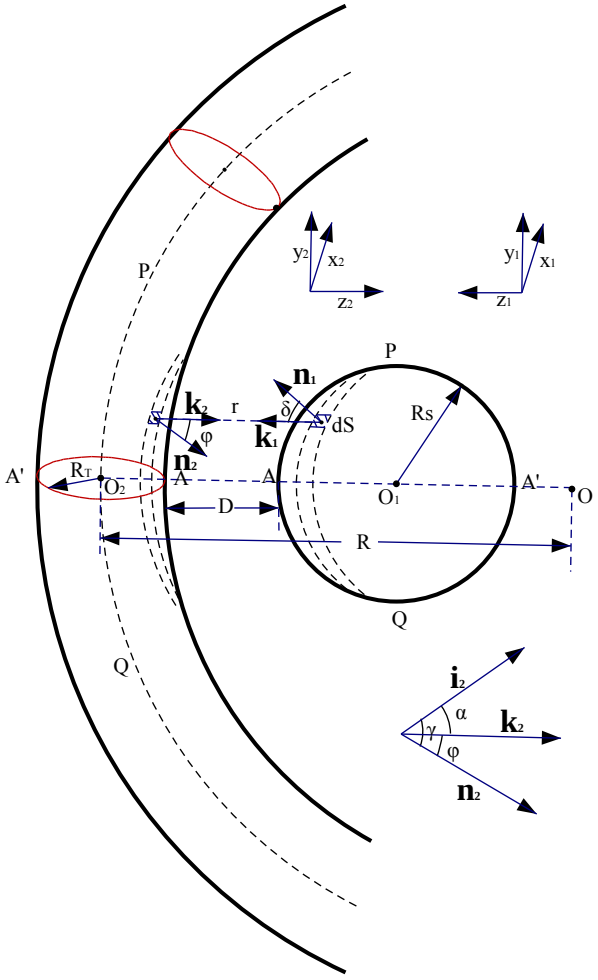

Figure B.1. Schematic illustration of the EDL interaction between a sphere of radius R_S and a section of a torus of major radius R and minor radius R_T. The sphere is separated from the torus with a distance D. $x_1y_1z_1$ and $x_2y_2z_2$ are two body-fixed coordinate systems with z_1 and z_2 axes directly facing each other and x_1y_1 and x_2y_2 planes parallel to each other. The surface element in the sphere is denoted as dS, which has a corresponding z_1 axis-projection surface element on the tours. The separation distance between the two surface elements is denoted as r. $\mathbf{n_1}$ and $\mathbf{n_2}$ represent the outward unit vectors normal to

the surface element. $\mathbf{k_1}$ and $\mathbf{k_2}$ represent the unit vectors directed towards the positive z axes (facing each other). δ and φ are angles between $\mathbf{n_1}$ and $\mathbf{k_1}$, and $\mathbf{n_2}$ and $\mathbf{k_2}$, respectively. The surface element on the sphere is described with coordinates (y, θ). y is radius of the circle (parallel to xy plane) on the sphere where the surface element is positioned. θ is the angle between the reference direction on the circle (i.e. y-axis direction) and the line from the surface element to the center of the circle. The area of differential surface element in the sphere can be expressed as $yd\theta dy/\cos\delta$.

The distance r between two surface elements respectively on sphere and torus was determined by Eq. (3):

$$\begin{aligned}
r_{PAQ-PAQ} &= D + R_S - \sqrt{R_S{}^2 - y^2} + R_T - R + \sqrt{R^2 + R_T{}^2 - y^2 - 2R\sqrt{R_T{}^2 - y^2\sin^2\theta}} \\
r_{PA'Q-PAQ} &= D + R_S + \sqrt{R_S{}^2 - y^2} + R_T - R + \sqrt{R^2 + R_T{}^2 - y^2 - 2R\sqrt{R_T{}^2 - y^2\sin^2\theta}} \\
r_{PAQ-PA'Q} &= D + R_S - \sqrt{R_S{}^2 - y^2} + R_T - R + \sqrt{R^2 + R_T{}^2 - y^2 + 2R\sqrt{R_T{}^2 - y^2\sin^2\theta}} \\
r_{PA'Q-PA'Q} &= D + R_S + \sqrt{R_S{}^2 - y^2} + R_T - R + \sqrt{R^2 + R_T{}^2 - y^2 + 2R\sqrt{R_T{}^2 - y^2\sin^2\theta}}
\end{aligned} \tag{3}$$

Considering that $\mathbf{n_2 i_2}$ plane is normal to $\mathbf{k_2 i_2}$ plane, the term $|\mathbf{n_2 \cdot k_2}|$ was calculated as below.

$$\left|\mathbf{n}_2 \cdot \mathbf{k}_2\right| = \cos\varphi = \cos\alpha \cdot \cos\gamma = \frac{\sqrt{\left(R_T{}^2 - y^2\sin^2\theta\right)\left(R^2 - 2R\sqrt{R_T{}^2 - y^2\sin^2\theta} + R_T{}^2 - y^2\right)}}{R_T\left(R - \sqrt{R_T{}^2 - y^2\sin^2\theta}\right)} \tag{4}$$

And dA was deterimined by:

$$dA = dS \cdot \left|\mathbf{n}_1 \cdot \mathbf{k}_1\right| = dS \cdot \cos\delta = yd\theta dy \tag{5}$$

Substituting Eqs. (1), (4) and (5) in Eq. (2), we obtain the interaction energy expression between a sphere and a section of torus:

$$V_{EDL,sphere-torus}^{SEI}(D) = 4\int_0^{\frac{\pi}{2}}\int_0^{TBD} \frac{y\sqrt{\left(R_T{}^2 - y^2\sin^2\theta\right)\left(R^2 - 2R\sqrt{R_T{}^2 - y^2\sin^2\theta} + R_T{}^2 - y^2\right)}}{R_T\left(R - \sqrt{R_T{}^2 - y^2\sin^2\theta}\right)} \quad (6)$$
$$\times\left[E\left(r_{PAQ-PAQ}\right) - E\left(r_{PA'Q-PAQ}\right) - E\left(r_{PAQ-PA'Q}\right) + E\left(r_{PA'Q-PA'Q}\right)\right]dyd\theta$$

where the upper limit of integral term *dy* is to be determined (*TBD*), depending on the relative magnitude of sphere radius (R_S) and minor radius of the torus (R_T). Equation (6) is unaltered regardless of the physical origin of the interaction energy, namely it can be applied to both EDL and vdW energies.

The EDL energy per unit area between two infinite flat plates separated at a distance of r is given by [488]:

$$V_{EDL,surface-surface}(r) = \varepsilon_r\varepsilon_0\kappa\psi_{o1}\psi_{o2}\left[\operatorname{csc}h(\kappa r) + \frac{\psi_{o1}{}^2 + \psi_{o2}{}^2}{2\psi_{o1}\psi_{o2}}\left(1 - \coth\kappa r\right)\right] \quad (7)$$

where ε_r and ε_0 are the relative permittivity of the solution and the permittivity of a vacuum, respectively. κ is the Debye-Hückel parameter of the electrolyte solution. ψ_{o1} and ψ_{o2} are unperturbed surface potentials of two interacting macrobodies.

Substituting Eq. (7) in Eq. (6), we can obtain the interaction energy equation between a sphere and a section of torus. The upper limit of the integral term *dy* depends on the relative magnitude of sphere radius (R_C) and the minor radius of torus (R_T). If $R_T \geq R_S$, the integration was conducted over the whole sphere:

$$V_{EDL,sphere-torus}^{SEI}(D)=4\varepsilon_r\varepsilon_0\kappa\psi_{o1}\psi_{o2}\int_0^{\frac{\pi}{2}}\int_0^{R_S}\frac{y\sqrt{\left(R_T{}^2-y^2\sin^2\theta\right)\left(R^2-2R\sqrt{R_T{}^2-y^2\sin^2\theta}+R_T{}^2-y^2\right)}}{R_T\left(R-\sqrt{R_T{}^2-y^2\sin^2\theta}\right)}$$

$$\times\left\{\begin{array}{l}\csc h\left[\kappa\left(D+R_S-\sqrt{R_S{}^2-y^2}+R_T-R+\sqrt{R^2+R_T{}^2-y^2-2R\sqrt{R_T{}^2-y^2\sin^2\theta}}\right)\right]\\ -\csc h\left[\kappa\left(D+R_S+\sqrt{R_S{}^2-y^2}+R_T-R+\sqrt{R^2+R_T{}^2-y^2-2R\sqrt{R_T{}^2-y^2\sin^2\theta}}\right)\right]\\ -\csc h\left[\kappa\left(D+R_S-\sqrt{R_S{}^2-y^2}+R_T-R+\sqrt{R^2+R_T{}^2-y^2+2R\sqrt{R_T{}^2-y^2\sin^2\theta}}\right)\right]\\ +\csc h\left[\kappa\left(D+R_S+\sqrt{R_S{}^2-y^2}+R_T-R+\sqrt{R^2+R_T{}^2-y^2+2R\sqrt{R_T{}^2-y^2\sin^2\theta}}\right)\right]\\ +\dfrac{\psi_{o1}{}^2+\psi_{o2}{}^2}{2\psi_{o1}\psi_{o2}}\left[\begin{array}{l}-\coth\kappa\left(D+R_S-\sqrt{R_S{}^2-y^2}+R_T-R+\sqrt{R^2+R_T{}^2-y^2-2R\sqrt{R_T{}^2-y^2\sin^2\theta}}\right)\\ +\coth\kappa\left(D+R_S+\sqrt{R_S{}^2-y^2}+R_T-R+\sqrt{R^2+R_T{}^2-y^2-2R\sqrt{R_T{}^2-y^2\sin^2\theta}}\right)\\ +\coth\kappa\left(D+R_S-\sqrt{R_S{}^2-y^2}+R_T-R+\sqrt{R^2+R_T{}^2-y^2+2R\sqrt{R_T{}^2-y^2\sin^2\theta}}\right)\\ -\coth\kappa\left(D+R_S+\sqrt{R_S{}^2-y^2}+R_T-R+\sqrt{R^2+R_T{}^2-y^2+2R\sqrt{R_T{}^2-y^2\sin^2\theta}}\right)\end{array}\right]\end{array}\right\}dyd\theta \quad (8)$$

If $R_T < R_S$, the integration of *dy* was conducted over only part of the sphere, of which the projection area is not beyond the torus:

$$V_{EDL,sphere-torus}^{SEI}(D)=4\varepsilon_r\varepsilon_0\kappa\psi_{o1}\psi_{o2}\int_0^{\frac{\pi}{2}}\int_0^{R_T}\frac{y\sqrt{\left(R_T{}^2-y^2\sin^2\theta\right)\left(R^2-2R\sqrt{R_T{}^2-y^2\sin^2\theta}+R_T{}^2-y^2\right)}}{R_T\left(R-\sqrt{R_T{}^2-y^2\sin^2\theta}\right)}$$

$$\times\left\{\begin{array}{l}\csc h\left[\kappa\left(D+R_S-\sqrt{R_S{}^2-y^2}+R_T-R+\sqrt{R^2+R_T{}^2-y^2-2R\sqrt{R_T{}^2-y^2\sin^2\theta}}\right)\right]\\-\csc h\left[\kappa\left(D+R_S+\sqrt{R_S{}^2-y^2}+R_T-R+\sqrt{R^2+R_T{}^2-y^2-2R\sqrt{R_T{}^2-y^2\sin^2\theta}}\right)\right]\\-\csc h\left[\kappa\left(D+R_S-\sqrt{R_S{}^2-y^2}+R_T-R+\sqrt{R^2+R_T{}^2-y^2+2R\sqrt{R_T{}^2-y^2\sin^2\theta}}\right)\right]\\+\csc h\left[\kappa\left(D+R_S+\sqrt{R_S{}^2-y^2}+R_T-R+\sqrt{R^2+R_T{}^2-y^2+2R\sqrt{R_T{}^2-y^2\sin^2\theta}}\right)\right]\\+\dfrac{\psi_{o1}{}^2+\psi_{o2}{}^2}{2\psi_{o1}\psi_{o2}}\left[\begin{array}{l}-\coth\kappa\left(D+R_S-\sqrt{R_S{}^2-y^2}+R_T-R+\sqrt{R^2+R_T{}^2-y^2-2R\sqrt{R_T{}^2-y^2\sin^2\theta}}\right)\\+\coth\kappa\left(D+R_S+\sqrt{R_S{}^2-y^2}+R_T-R+\sqrt{R^2+R_T{}^2-y^2-2R\sqrt{R_T{}^2-y^2\sin^2\theta}}\right)\\+\coth\kappa\left(D+R_S-\sqrt{R_S{}^2-y^2}+R_T-R+\sqrt{R^2+R_T{}^2-y^2+2R\sqrt{R_T{}^2-y^2\sin^2\theta}}\right)\\-\coth\kappa\left(D+R_S+\sqrt{R_S{}^2-y^2}+R_T-R+\sqrt{R^2+R_T{}^2-y^2+2R\sqrt{R_T{}^2-y^2\sin^2\theta}}\right)\end{array}\right]\end{array}\right\}dyd\theta$$

$$+4\varepsilon_r\varepsilon_0\kappa\psi_{o1}\psi_{o2}\int_{R_T}^{R_S}\int_0^{\arcsin\left(\frac{R_T}{y}\right)}\frac{y\sqrt{\left(R_T{}^2-y^2\sin^2\theta\right)\left(R^2-2R\sqrt{R_T{}^2-y^2\sin^2\theta}+R_T{}^2-y^2\right)}}{R_T\left(R-\sqrt{R_T{}^2-y^2\sin^2\theta}\right)}$$

$$\times\left\{\begin{array}{l}\csc h\left[\kappa\left(D+R_S-\sqrt{R_S{}^2-y^2}+R_T-R+\sqrt{R^2+R_T{}^2-y^2-2R\sqrt{R_T{}^2-y^2\sin^2\theta}}\right)\right]\\-\csc h\left[\kappa\left(D+R_S+\sqrt{R_S{}^2-y^2}+R_T-R+\sqrt{R^2+R_T{}^2-y^2-2R\sqrt{R_T{}^2-y^2\sin^2\theta}}\right)\right]\\-\csc h\left[\kappa\left(D+R_S-\sqrt{R_S{}^2-y^2}+R_T-R+\sqrt{R^2+R_T{}^2-y^2+2R\sqrt{R_T{}^2-y^2\sin^2\theta}}\right)\right]\\+\csc h\left[\kappa\left(D+R_S+\sqrt{R_S{}^2-y^2}+R_T-R+\sqrt{R^2+R_T{}^2-y^2+2R\sqrt{R_T{}^2-y^2\sin^2\theta}}\right)\right]\\+\dfrac{\psi_{o1}{}^2+\psi_{o2}{}^2}{2\psi_{o1}\psi_{o2}}\left[\begin{array}{l}-\coth\kappa\left(D+R_S-\sqrt{R_S{}^2-y^2}+R_T-R+\sqrt{R^2+R_T{}^2-y^2-2R\sqrt{R_T{}^2-y^2\sin^2\theta}}\right)\\+\coth\kappa\left(D+R_S+\sqrt{R_S{}^2-y^2}+R_T-R+\sqrt{R^2+R_T{}^2-y^2-2R\sqrt{R_T{}^2-y^2\sin^2\theta}}\right)\\+\coth\kappa\left(D+R_S-\sqrt{R_S{}^2-y^2}+R_T-R+\sqrt{R^2+R_T{}^2-y^2+2R\sqrt{R_T{}^2-y^2\sin^2\theta}}\right)\\-\coth\kappa\left(D+R_S+\sqrt{R_S{}^2-y^2}+R_T-R+\sqrt{R^2+R_T{}^2-y^2+2R\sqrt{R_T{}^2-y^2\sin^2\theta}}\right)\end{array}\right]\end{array}\right\}d\theta dy \quad (9)$$

B.2. vdW energy between a sphere and a section of torus

The vdW energy between a sphere and a section of torus was derived with Hamaker's approach, as schemed in Figure B.2. This approach first evaluates the vdW interaction between a point and a sphere, and then integrates the point-sphere interaction over the torus section volume. The vdW interaction between a point and a sphere of radius R_S is given by [498, 499]:

$$V_{vdW,point-sphere}(r) = -\frac{4A}{3\pi}\frac{{R_S}^3}{\left(r^2 - {R_S}^2\right)^3} \qquad (10)$$

In torus coordinates, the element volume is $\rho d\delta d\rho\left(R-\rho\cos\delta\right)d\beta$.

$$r^2 = \rho^2\sin^2\delta + \left(R-\rho\cos\delta\right)^2\sin^2\beta + \left[\left(R-\rho\cos\delta\right)\cos\beta + R_C + R_S + D - R\right]^2 \qquad (11)$$

$$V_{vdW,sphere-torus}^{Hamaker}(D) = -\frac{4A{R_S}^3}{3\pi}\int_{V_t}\frac{dV_c}{\left(r^2-{R_S}^2\right)^3}$$

$$= -\frac{16A{R_S}^3}{3\pi}\cdot\int_0^u d\beta\int_0^{\pi} d\delta\int_0^{R_C} \qquad (12)$$

$$\frac{\rho\left(R-\rho\cos\delta\right)}{\left\{\rho^2\sin^2\delta + \left(R-\rho\cos\delta\right)^2\sin^2\beta + \left[\left(R-\rho\cos\delta\right)\cos\beta + R_C + R_S + D - R\right]^2 - {R_S}^2\right\}^3}d\rho$$

where u is the integration upper limit of β. Setting u as $\pi/4$ and $\pi/2$ gives almost identical results, indicating that choosing any value of u between $\pi/4$ and $\pi/2$ does not have a significant effect on the integration result. To save the execution time in computational integration, u is set as $\pi/4$. Moreover, although the above equation can be reduced to double integration form, we did not do that, as the double integration expression is too complicated.

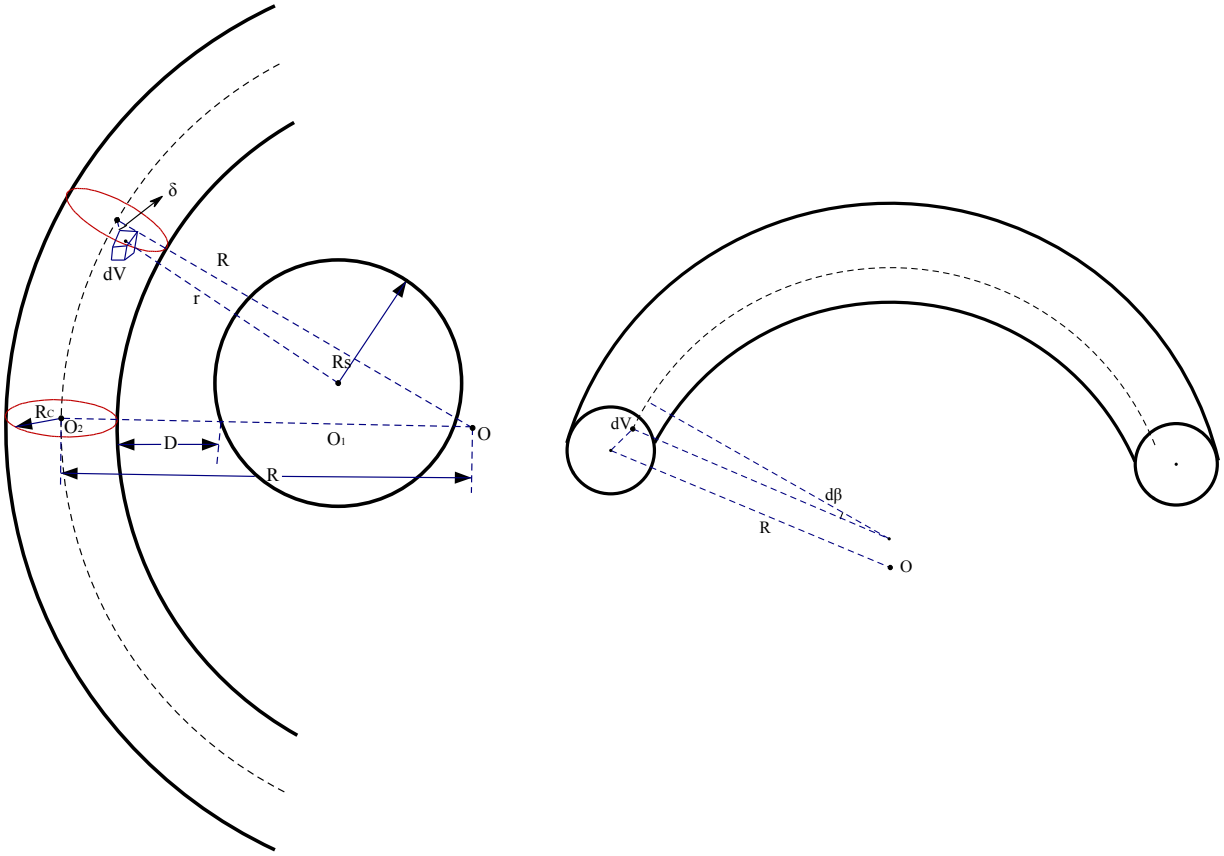

Figure B.2. Schematic representation of the vdW interaction between a sphere of radius R_S and a section of torus of major radius R and minor radius R_C. The sphere is separated from the torus with a distance D. The volume element in the cylinder is denoted as dV. The separation distance between the volume element and the center of the sphere is denoted as r. The geometry is described with cylindrical coordinates (ρ, r, δ, β). The radial distance ρ is the Euclidean distance from the center of the tube to the volume element. The azimuth δ is the angle between the reference direction and the line from the center of the tube to the volume element on the plane. The azimuth β is the angel between the reference direction and the line from the volume element to the center of the circle composed of points all with the same distance to the origin of torus.

REFERENCES

1. http://www.nano.gov/nanotech-101/nanotechnology-facts.
2. Donaldson, K.; Stone, V.; Tran, C. L.; Kreyling, W.; Borm, P. J., Nanotoxicology. *Occup Environ Med* **2004,** *61*, (9), 727-8.
3. Borm, P. J.; Robbins, D.; Haubold, S.; Kuhlbusch, T.; Fissan, H.; Donaldson, K.; Schins, R.; Stone, V.; Kreyling, W.; Lademann, J.; Krutmann, J.; Warheit, D.; Oberdorster, E., The potential risks of nanomaterials: a review carried out for ECETOC. *Part Fibre Toxicol* **2006,** *3*, 11.
4. Stebounova, L. V.; Morgan, H.; Grassian, V. H.; Brenner, S., Health and safety implications of occupational exposure to engineered nanomaterials. *Wiley Interdisciplinary Reviews-Nanomedicine and Nanobiotechnology* **2012,** *4*, (3), 310-321.
5. Sharifi, S.; Behzadi, S.; Laurent, S.; Forrest, M. L.; Stroeve, P.; Mahmoudi, M., Toxicity of nanomaterials. *Chem. Soc. Rev.* **2012,** *41*, (6), 2323-2343.
6. Maurer-Jones, M. A.; Gunsolus, I. L.; Murphy, C. J.; Haynes, C. L., Toxicity of Engineered Nanoparticles in the Environment. *Anal. Chem.* **2013,** *85*, (6), 3036-3049.
7. Wiesner, M. R.; Bottero, J.-Y., *Environmental nanotechnology : applications and impacts of nanomaterials*. McGraw-Hill: New York, 2007; p xii, 540 p.
8. Thomas, S. P.; Al-Mutairi, E. M.; De, S. K., Impact of Nanomaterials on Health and Environment. *Arabian Journal for Science and Engineering* **2013,** *38*, (3), 457-477.
9. Bakand, S.; Hayes, A.; Dechsakulthorn, F., Nanoparticles: a review of particle toxicology following inhalation exposure. *Inhalation Toxicol.* **2012,** *24*, (2), 125-135.
10. Proj. Emerg. Nanotechnol. 2013. Project on Emerging Nanotechnologies Consumer Product Inventory. Washington, DC: Woodrow Wilson Int. Cent. Sch. http://www.nanotechproject.org/inventories/.
11. NIOSH. Strategic Plan for NIOSH Nanotechnology Research and Guidance: Filling the Knowledge Gaps. Cincinnati, OH: Department of Health and Human Services (DHHS); 2009.
12. IEEE - USA -Eye on Washington. House Subcommittee Explores Economic Benefits of Federal Nanotechnology Initiative, 2011. Available at: http://www.ieeeusa.org/ policy/eyeonwashington/2011/06eow2011.asp.
13. Lux State of the market report, July 2008.Available at: https://portal.luxresearchinc.com/reporting/research/report_excerpt/3735.
14. Global Industry Analysts, 2011. Available at: http://www.prweb.com/releases/nanotechnology/nano_products/prweb4719764.htm.
15. Thompson, S. E.; Parthasarathy, S., Moore's law: the future of Si microelectronics. *Materials Today* **2006,** *9*, (6), 20-25.
16. Jacoby, M., Nanoscale electronics. *Chem. Eng. News* **2002,** *80*, (39), 38-43.
17. Buzea, C.; Robbie, K., Assembling the puzzle of superconducting elements: a review. *Supercond. Sci. Technol.* **2005,** *18*, (1), R1-R8.
18. Carey, J. D., Engineering the next generation of large-area displays: prospects and pitfalls. *Philosophical Transactions of the Royal Society of London Series a-Mathematical Physical and Engineering Sciences* **2003,** *361*, (1813), 2891-2907.

19. Liu, H. K.; Wang, G. X.; Guo, Z. P.; Wang, J. Z.; Konstantinov, K., Nanomaterials for lithium-ion rechargeable batteries. *J. Nanosci. Nanotechnol.* **2006,** *6*, (1), 1-15.
20. Nikolaou, K., Emissions reduction of high and low polluting new technology vehicles equipped with a CeO2 catalytic system. *Science of the Total Environment* **1999,** *235*, (1-3), 71-76.
21. Ozawa, M., Role of cerium-zirconium mixed oxides as catalysts for car pollution: A short review. *Journal of Alloys and Compounds* **1998,** *275*, 886-890.
22. Hafner, J. H.; Cheung, C. L.; Woolley, A. T.; Lieber, C. M., Structural and functional imaging with carbon nanotube AFM probes. *Prog. Biophys. Mol. Biol.* **2001,** *77*, (1), 73-110.
23. Wilson, N. R.; Macpherson, J. V., Carbon nanotube tips for atomic force microscopy. *Nat. Nanotechnol.* **2009,** *4*, (8), 483-491.
24. Ellis-Behnke, R. G.; Liang, Y. X.; You, S. W.; Tay, D. K. C.; Zhang, S. G.; So, K. F.; Schneider, G. E., Nano neuro knitting: Peptide nanofiber scaffold for brain repair and axon regeneration with functional return of vision (vol 103, pg 5054, 2006). *Proc. Natl. Acad. Sci. U. S. A.* **2006,** *103*, (19), 7530-7530.
25. Martin, C. R.; Kohli, P., The emerging field of nanotube biotechnology. *Nat. Rev. Drug Discovery* **2003,** *2*, (1), 29-37.
26. Harisinghani, M. G.; Barentsz, J.; Hahn, P. F.; Deserno, W. M.; Tabatabaei, S.; van de Kaa, C. H.; de la Rosette, J.; Weissleder, R., Noninvasive detection of clinically occult lymph-node metastases in prostate cancer. *N. Engl. J. Med.* **2003,** *348*, (25), 2491-U5.
27. Rosi, N. L.; Mirkin, C. A., Nanostructures in biodiagnostics. *Chem. Rev. (Washington, DC, U. S.)* **2005,** *105*, (4), 1547-1562.
28. Labhasetwar, V.; Leslie-Pelecky, D. L., *Biomedical applications of nanotechnology*. Wiley-Interscience: Hoboken, N.J., 2007; p x, 249 p.
29. Chaloupka, K.; Malam, Y.; Seifalian, A. M., Nanosilver as a new generation of nanoproduct in biomedical applications. *Trends Biotechnol.* **2010,** *28*, (11), 580-588.
30. He, F.; Zhao, D. Y., Preparation and characterization of a new class of starch-stabilized bimetallic nanoparticles for degradation of chlorinated hydrocarbons in water. *Environ. Sci. Technol.* **2005,** *39*, (9), 3314-3320.
31. Ariga, K.; Ishihara, S.; Abe, H.; Li, M.; Hill, J. P., Materials nanoarchitectonics for environmental remediation and sensing. *J. Mater. Chem.* **2012,** *22*, (6), 2369-2377.
32. Noubactep, C.; Care, S.; Crane, R., Nanoscale Metallic Iron for Environmental Remediation: Prospects and Limitations. *Water Air and Soil Pollution* **2012,** *223*, (3), 1363-1382.
33. Khin, M. M.; Nair, A. S.; Babu, V. J.; Murugan, R.; Ramakrishna, S., A review on nanomaterials for environmental remediation. *Energy & Environmental Science* **2012,** *5*, (8), 8075-8109.
34. Raj, S.; Jose, S.; Sumod, U. S.; Sabitha, M., Nanotechnology in cosmetics: Opportunities and challenges. *J Pharm Bioallied Sci* **2012,** *4*, (3), 186-93.
35. Tran, P. A.; Webster, T. J., Antimicrobial selenium nanoparticle coatings on polymeric medical devices. *Nanotechnology* **2013,** *24*, (15).

36. Yan, L. G.; Wang, J. B.; Han, X. H.; Ren, Y.; Liu, Q. F.; Li, F. S., Enhanced microwave absorption of Fe nanoflakes after coating with SiO2 nanoshell. *Nanotechnology* **2010,** *21*, (9).
37. Carbajal, G.; Martinez-Villafane, A.; Gonzalez-Rodriguez, J. G.; Castano, V. M., Corrosion-resistant coatings: a nanotechnology approach. *Anti-Corrosion Methods and Materials* **2001,** *48*, (4), 241-244.
38. Baer, D. R.; Burrows, P. E.; El-Azab, A. A., Enhancing coating functionality using nanoscience and nanotechnology. *Prog. Org. Coat.* **2003,** *47*, (3-4), 342-356.
39. Chen, J.; Gu, J. H.; Liu, Y., Perspective on Devolpment of Nanotechnology In Textiles. *Environment Materials and Environment Management Pts 1-3* **2010,** *113-116*, 670-673.
40. Hebeish, A.; El-Naggar, M. E.; Fouda, M. M. G.; Ramadan, M. A.; Al-Deyab, S. S.; El-Rafie, M. H., Highly effective antibacterial textiles containing green synthesized silver nanoparticles. *Carbohydr. Polym.* **2011,** *86*, (2), 936-940.
41. Hu, L. B.; Cui, Y., Energy and environmental nanotechnology in conductive paper and textiles. *Energy & Environmental Science* **2012,** *5*, (4), 6423-6435.
42. Gugliuzza, A.; Drioli, E., A review on membrane engineering for innovation in wearable fabrics and protective textiles. *J. Membr. Sci.* **2013,** *446*, 350-375.
43. Buzea, C.; Pacheco, I. I.; Robbie, K., Nanomaterials and nanoparticles: Sources and toxicity. *Biointerphases* **2007,** *2*, (4), Mr17-Mr71.
44. Hanus, M. J.; Harris, A. T., Nanotechnology innovations for the construction industry. *Progress in Materials Science* **2013,** *58*, (7), 1056-1102.
45. Kaiser, J. P.; Zuin, S.; Wick, P., Is nanotechnology revolutionizing the paint and lacquer industry? A critical opinion. *Sci. Total Environ.* **2013,** *442*, 282-289.
46. Helland, A.; Scheringer, M.; Siegrist, M.; Kastenholz, H. G.; Wiek, A.; Scholz, R. W., Risk assessment of engineered nanomaterials: A survey of industrial approaches. *Environ. Sci. Technol.* **2008,** *42*, (2), 640-646.
47. Love, S. A.; Maurer-Jones, M. A.; Thompson, J. W.; Lin, Y. S.; Haynes, C. L., Assessing Nanoparticle Toxicity. *Annual Review of Analytical Chemistry, Vol 5* **2012,** *5*, 181-205.
48. Joris, F.; Manshian, B. B.; Peynshaert, K.; De Smedt, S. C.; Braeckmans, K.; Soenen, S. J., Assessing nanoparticle toxicity in cell-based assays: influence of cell culture parameters and optimized models for bridging the in vitro-in vivo gap. *Chem. Soc. Rev.* **2013,** *42*, (21), 8339-8359.
49. Arora, S.; Rajwade, J. M.; Paknikar, K. M., Nanotoxicology and in vitro studies: The need of the hour. *Toxicol. Appl. Pharmacol.* **2012,** *258*, (2), 151-165.
50. Nel, A.; Xia, T.; Madler, L.; Li, N., Toxic potential of materials at the nanolevel. *Science* **2006,** *311*, (5761), 622-627.
51. Aillon, K. L.; Xie, Y. M.; El-Gendy, N.; Berkland, C. J.; Forrest, M. L., Effects of nanomaterial physicochemical properties on in vivo toxicity. *Adv. Drug Delivery Rev.* **2009,** *61*, (6), 457-466.
52. Fischer, H. C.; Chan, W. C. W., Nanotoxicity: the growing need for in vivo study. *Curr. Opin. Biotechnol.* **2007,** *18*, (6), 565-571.
53. Warheit, D. B., How meaningful are the results of nanotoxicity studies in the absence of adequate material characterization? *Toxicol. Sci.* **2008,** *101*, (2), 183-185.

54. Maynard, A. D.; Warheit, D. B.; Philbert, M. A., The New Toxicology of Sophisticated Materials: Nanotoxicology and Beyond. *Toxicol. Sci.* **2011,** *120*, S109-S129.
55. Pumera, M., Nanotoxicology: The Molecular Science Point of View. *Chemistry-an Asian Journal* **2011,** *6*, (2), 340-348.
56. Krug, H. F.; Wick, P., Nanotoxicology: An Interdisciplinary Challenge. *Angewandte Chemie-International Edition* **2011,** *50*, (6), 1260-1278.
57. Boczkowski, J.; Hoet, P., What's new in nanotoxicology? Implications for public health from a brief review of the 2008 literature. *Nanotoxicology* **2010,** *4*, (1), 1-14.
58. Stensberg, M. C.; Wei, Q. S.; McLamore, E. S.; Porterfield, D. M.; Wei, A.; Sepulveda, M. S., Toxicological studies on silver nanoparticles: challenges and opportunities in assessment, monitoring and imaging. *Nanomedicine* **2011,** *6*, (5), 879-898.
59. Robichaud, C. O.; Uyar, A. E.; Darby, M. R.; Zucker, L. G.; Wiesner, M. R., Estimates of Upper Bounds and Trends in Nano-TiO2 Production As a Basis for Exposure Assessment. *Environ. Sci. Technol.* **2009,** *43*, (12), 4227-4233.
60. Holbrook, R. D.; Murphy, K. E.; Morrow, J. B.; Cole, K. D., Trophic transfer of nanoparticles in a simplified invertebrate food web. *Nat. Nanotechnol.* **2008,** *3*, (6), 352-355.
61. Ferry, J. L.; Craig, P.; Hexel, C.; Sisco, P.; Frey, R.; Pennington, P. L.; Fulton, M. H.; Scott, I. G.; Decho, A. W.; Kashiwada, S.; Murphy, C. J.; Shaw, T. J., Transfer of gold nanoparticles from the water column to the estuarine food web. *Nat. Nanotechnol.* **2009,** *4*, (7), 441-444.
62. Zhu, X. S.; Wang, J. X.; Zhang, X. Z.; Chang, Y.; Chen, Y. S., Trophic transfer of TiO2 nanoparticles from daphnia to zebrafish in a simplified freshwater food chain. *Chemosphere* **2010,** *79*, (9), 928-933.
63. Judy, J. D.; Unrine, J. M.; Bertsch, P. M., Evidence for Biomagnification of Gold Nanoparticles within a Terrestrial Food Chain. *Environ. Sci. Technol.* **2011,** *45*, (2), 776-781.
64. Cedervall, T.; Hansson, L. A.; Lard, M.; Frohm, B.; Linse, S., Food Chain Transport of Nanoparticles Affects Behaviour and Fat Metabolism in Fish. *PLoS One* **2012,** *7*, (2).
65. Gottschalk, F.; Sonderer, T.; Scholz, R. W.; Nowack, B., Possibilities and Limitations of Modeling Environmental Exposure to Engineered Nanomaterials by Probabilistic Material Flow Analysis. *Environ. Toxicol. Chem.* **2010,** *29*, (5), 1036-1048.
66. Mueller, N. C.; Nowack, B., Exposure modeling of engineered nanoparticles in the environment. *Environ. Sci. Technol.* **2008,** *42*, (12), 4447-4453.
67. Elsaesser, A.; Howard, C. V., Toxicology of nanoparticles. *Adv. Drug Delivery Rev.* **2012,** *64*, (2), 129-137.
68. Westerhoff, P.; Song, G. X.; Hristovski, K.; Kiser, M. A., Occurrence and removal of titanium at full scale wastewater treatment plants: implications for TiO2 nanomaterials. *J. Environ. Monit.* **2011,** *13*, (5), 1195-1203.
69. Kiser, M. A.; Westerhoff, P.; Benn, T.; Wang, Y.; Perez-Rivera, J.; Hristovski, K., Titanium Nanomaterial Removal and Release from Wastewater Treatment Plants. *Environ. Sci. Technol.* **2009,** *43*, (17), 6757-6763.

70. Praetorius, A.; Scheringer, M.; Hungerbuhler, K., Development of Environmental Fate Models for Engineered Nanoparticles-A Case Study of TiO2 Nanoparticles in the Rhine River. *Environ. Sci. Technol.* **2012,** *46*, (12), 6705-6713.
71. Arvidsson, R.; Molander, S.; Sanden, B. A.; Hassellov, M., Challenges in Exposure Modeling of Nanoparticles in Aquatic Environments. *Human and Ecological Risk Assessment* **2011,** *17*, (1), 245-262.
72. Blaser, S. A.; Scheringer, M.; MacLeod, M.; Hungerbuhler, K., Estimation of cumulative aquatic exposure and risk due to silver: Contribution of nano-functionalized plastics and textiles. *Sci. Total Environ.* **2008,** *390*, (2-3), 396-409.
73. Gottschalk, F.; Scholz, R. W.; Nowack, B., Probabilistic material flow modeling for assessing the environmental exposure to compounds: Methodology and an application to engineered nano-TiO2 particles. *Environmental Modelling & Software* **2010,** *25*, (3), 320-332.
74. Gottschalk, F.; Nowack, B., The release of engineered nanomaterials to the environment. *J. Environ. Monit.* **2011,** *13*, (5), 1145-1155.
75. Gottschalk, F.; Sonderer, T.; Scholz, R. W.; Nowack, B., Modeled Environmental Concentrations of Engineered Nanomaterials (TiO2, ZnO, Ag, CNT, Fullerenes) for Different Regions. *Environ. Sci. Technol.* **2009,** *43*, (24), 9216-9222.
76. Klaine, S. J.; Alvarez, P. J. J.; Batley, G. E.; Fernandes, T. F.; Handy, R. D.; Lyon, D. Y.; Mahendra, S.; McLaughlin, M. J.; Lead, J. R., Nanomaterials in the environment: Behavior, fate, bioavailability, and effects. *Environ. Toxicol. Chem.* **2008,** *27*, (9), 1825-1851.
77. Blaise, C.; Gagne, F.; Ferard, J. F.; Eullaffroy, P., Ecotoxicity of selected nano-materials to aquatic organisms. *Environ. Toxicol.* **2008,** *23*, (5), 591-598.
78. Farre, M.; Gajda-Schrantz, K.; Kantiani, L.; Barcelo, D., Ecotoxicity and analysis of nanomaterials in the aquatic environment. *Anal. Bioanal. Chem.* **2009,** *393*, (1), 81-95.
79. Ma, H. B.; Williams, P. L.; Diamond, S. A., Ecotoxicity of manufactured ZnO nanoparticles - A review. *Environ. Pollut.* **2013,** *172*, 76-85.
80. Lebkowska, M.; Zateska-Radziwill, M., Nanoparticles: Mode of Occurrence and Ecotoxicity. *Ochrona Srodowiska* **2011,** *33*, (4), 23-26.
81. Barrena, R.; Casals, E.; Colon, J.; Font, X.; Sanchez, A.; Puntes, V., Evaluation of the ecotoxicity of model nanoparticles. *Chemosphere* **2009,** *75*, (7), 850-857.
82. Navarro, E.; Baun, A.; Behra, R.; Hartmann, N. B.; Filser, J.; Miao, A. J.; Quigg, A.; Santschi, P. H.; Sigg, L., Environmental behavior and ecotoxicity of engineered nanoparticles to algae, plants, and fungi. *Ecotoxicology* **2008,** *17*, (5), 372-386.
83. Baun, A.; Hartmann, N. B.; Grieger, K.; Kusk, K. O., Ecotoxicity of engineered nanoparticles to aquatic invertebrates: a brief review and recommendations for future toxicity testing. *Ecotoxicology* **2008,** *17*, (5), 387-395.
84. Bernhardt, E. S.; Colman, B. P.; Hochella, M. F.; Cardinale, B. J.; Nisbet, R. M.; Richardson, C. J.; Yin, L. Y., An Ecological Perspective on Nanomaterial Impacts in the Environment. *Journal of Environmental Quality* **2010,** *39*, (6), 1954-1965.
85. Holden, P. A.; Nisbet, R. M.; Lenihan, H. S.; Miller, R. J.; Cherr, G. N.; Schimel, J. P.; Gardea-Torresdey, J. L., Ecological Nanotoxicology: Integrating Nanomaterial Hazard Considerations Across the Subcellular, Population, Community, and Ecosystems Levels. *Accounts of Chemical Research* **2013**, in press.

86. Ge, Y. G.; Schimel, J. P.; Holden, P. A., Evidence for Negative Effects of TiO2 and ZnO Nanoparticles on Soil Bacterial Communities. *Environmental Science & Technology* **2011,** *45*, (4), 1659-1664.
87. Priester, J. H.; Ge, Y.; Mielke, R. E.; Horst, A. M.; Moritz, S. C.; Espinosa, K.; Gelb, J.; Walker, S. L.; Nisbet, R. M.; An, Y. J.; Schimel, J. P.; Palmer, R. G.; Hernandez-Viezcas, J. A.; Zhao, L. J.; Gardea-Torresdey, J. L.; Holden, P. A., Soybean susceptibility to manufactured nanomaterials with evidence for food quality and soil fertility interruption. *Proceedings of the National Academy of Sciences of the United States of America* **2012,** *109*, (37), E2451-E2456.
88. Xia, T.; Kovochich, M.; Liong, M.; Madler, L.; Gilbert, B.; Shi, H. B.; Yeh, J. I.; Zink, J. I.; Nel, A. E., Comparison of the Mechanism of Toxicity of Zinc Oxide and Cerium Oxide Nanoparticles Based on Dissolution and Oxidative Stress Properties. *ACS Nano* **2008,** *2*, (10), 2121-2134.
89. Li, J. J.; Hartono, D.; Ong, C. N.; Bay, B. H.; Yung, L. Y. L., Autophagy and oxidative stress associated with gold nanoparticles. *Biomaterials* **2010,** *31*, (23), 5996-6003.
90. Xia, T.; Kovochich, M.; Brant, J.; Hotze, M.; Sempf, J.; Oberley, T.; Sioutas, C.; Yeh, J. I.; Wiesner, M. R.; Nel, A. E., Comparison of the abilities of ambient and manufactured nanoparticles to induce cellular toxicity according to an oxidative stress paradigm. *Nano Lett.* **2006,** *6*, (8), 1794-1807.
91. Chen, J. M.; Hessler, J. A.; Putchakayala, K.; Panama, B. K.; Khan, D. P.; Hong, S.; Mullen, D. G.; DiMaggio, S. C.; Som, A.; Tew, G. N.; Lopatin, A. N.; Baker, J. R.; Holl, M. M. B.; Orr, B. G., Cationic Nanoparticles Induce Nanoscale Disruption in Living Cell Plasma Membranes. *J. Phys. Chem. B* **2009,** *113*, (32), 11179-11185.
92. Leroueil, P. R.; Hong, S. Y.; Mecke, A.; Baker, J. R.; Orr, B. G.; Holl, M. M. B., Nanoparticle interaction with biological membranes: Does nanotechnology present a janus face? *Acc. Chem. Res.* **2007,** *40*, (5), 335-342.
93. Leroueil, P. R.; Berry, S. A.; Duthie, K.; Han, G.; Rotello, V. M.; McNerny, D. Q.; Baker, J. R.; Orr, B. G.; Holl, M. M. B., Wide varieties of cationic nanoparticles induce defects in supported lipid bilayers. *Nano Lett.* **2008,** *8*, (2), 420-424.
94. Xia, T.; Kovochich, M.; Liong, M.; Zink, J. I.; Nel, A. E., Cationic polystyrene nanosphere toxicity depends on cell-specific endocytic and mitochondrial injury pathways. *ACS Nano* **2008,** *2*, (1), 85-96.
95. Lynch, I.; Salvati, A.; Dawson, K. A., Protein-Nanoparticle Interactions What Does the Cell See? *Nat. Nanotechnol.* **2009,** *4*, (9), 546-547.
96. Mahmoudi, M.; Lynch, I.; Ejtehadi, M. R.; Monopoli, M. P.; Bombelli, F. B.; Laurent, S., Protein-Nanoparticle Interactions: Opportunities and Challenges. *Chem. Rev. (Washington, DC, U. S.)* **2011,** *111*, (9), 5610-5637.
97. Lynch, I.; Dawson, K. A., Protein-nanoparticle interactions. *Nano Today* **2008,** *3*, (1-2), 40-47.
98. Cedervall, T.; Lynch, I.; Lindman, S.; Berggard, T.; Thulin, E.; Nilsson, H.; Dawson, K. A.; Linse, S., Understanding the nanoparticle-protein corona using methods to quantify exchange rates and affinities of proteins for nanoparticles. *Proc. Natl. Acad. Sci. U. S. A.* **2007,** *104*, (7), 2050-2055.

99. Kang, B.; Mackey, M. A.; El-Sayed, M. A., Nuclear Targeting of Gold Nanoparticles in Cancer Cells Induces DNA Damage, Causing Cytokinesis Arrest and Apoptosis. *J. Am. Chem. Soc.* **2010,** *132*, (5), 1517-+.
100. Shukla, R. K.; Kumar, A.; Gurbani, D.; Pandey, A. K.; Singh, S.; Dhawan, A., TiO2 nanoparticles induce oxidative DNA damage and apoptosis in human liver cells. *Nanotoxicology* **2013,** *7*, (1), 48-60.
101. Sood, A.; Salih, S.; Roh, D.; Lacharme-Lora, L.; Parry, M.; Hardiman, B.; Keehan, R.; Grummer, R.; Winterhager, E.; Gokhale, P. J.; Andrews, P. W.; Abbott, C.; Forbes, K.; Westwood, M.; Aplin, J. D.; Ingham, E.; Papageorgiou, I.; Berry, M.; Liu, J.; Dick, A. D.; Garland, R. J.; Williams, N.; Singh, R.; Simon, A. K.; Lewis, M.; Ham, J.; Roger, L.; Baird, D. M.; Crompton, L. A.; Caldwell, M. A.; Swalwell, H.; Birch-Machin, M.; Lopez-Castejon, G.; Randall, A.; Lin, H.; Suleiman, M. S.; Evans, W. H.; Newson, R.; Case, C. P., Signalling of DNA damage and cytokines across cell barriers exposed to nanoparticles depends on barrier thickness. *Nat. Nanotechnol.* **2011,** *6*, (12), 824-833.
102. AshaRani, P. V.; Mun, G. L. K.; Hande, M. P.; Valiyaveettil, S., Cytotoxicity and Genotoxicity of Silver Nanoparticles in Human Cells. *ACS Nano* **2009,** *3*, (2), 279-290.
103. Chen, W. H.; Chen, J. X.; Cheng, H.; Chen, C. S.; Yang, J.; Xu, X. D.; Wang, Y.; Zhuo, R. X.; Zhang, X. Z., A new anti-cancer strategy of damaging mitochondria by pro-apoptotic peptide functionalized gold nanoparticles. *Chem. Commun. (Cambridge, U. K.)* **2013,** *49*, (57), 6403-6405.
104. Jeng, H. A.; Swanson, J., Toxicity of metal oxide nanoparticles in mammalian cells. *Journal of Environmental Science and Health Part a-Toxic/Hazardous Substances & Environmental Engineering* **2006,** *41*, (12), 2699-2711.
105. Khan, M. I.; Mohammad, A.; Patil, G.; Naqvi, S. A. H.; Chauhan, L. K. S.; Ahmad, I., Induction of ROS, mitochondrial damage and autophagy in lung epithelial cancer cells by iron oxide nanoparticles. *Biomaterials* **2012,** *33*, (5), 1477-1488.
106. Pan, Y.; Leifert, A.; Ruau, D.; Neuss, S.; Bornemann, J.; Schmid, G.; Brandau, W.; Simon, U.; Jahnen-Dechent, W., Gold Nanoparticles of Diameter 1.4 nm Trigger Necrosis by Oxidative Stress and Mitochondrial Damage. *Small* **2009,** *5*, (18), 2067-2076.
107. Domenech, M.; Marrero-Berrios, I.; Torres-Lugo, M.; Rinaldi, C., Lysosomal Membrane Permeabilization by Targeted Magnetic Nanoparticles in Alternating Magnetic Fields. *ACS Nano* **2013,** *7*, (6), 5091-5101.
108. Cho, W. S.; Duffin, R.; Howie, S. E. M.; Scotton, C. J.; Wallace, W. A. H.; MacNee, W.; Bradley, M.; Megson, I. L.; Donaldson, K., Progressive severe lung injury by zinc oxide nanoparticles; the role of Zn2+ dissolution inside lysosomes. *Particle and Fibre Toxicology* **2011,** *8*.
109. Halamoda Kenzaoui, B.; Chapuis Bernasconi, C.; Guney-Ayra, S.; Juillerat-Jeanneret, L., Induction of oxidative stress, lysosome activation and autophagy by nanoparticles in human brain-derived endothelial cells. *Biochem. J.* **2012,** *441*, (3), 813-21.
110. Hussain, S.; Thomassen, L. C.; Ferecatu, I.; Borot, M. C.; Andreau, K.; Martens, J. A.; Fleury, J.; Baeza-Squiban, A.; Marano, F.; Boland, S., Carbon black and titanium dioxide nanoparticles elicit distinct apoptotic pathways in bronchial epithelial cells. *Part Fibre Toxicol* **2010,** *7*, 10.

111. Poland, C. A.; Duffin, R.; Kinloch, I.; Maynard, A.; Wallace, W. A. H.; Seaton, A.; Stone, V.; Brown, S.; MacNee, W.; Donaldson, K., Carbon nanotubes introduced into the abdominal cavity of mice show asbestos-like pathogenicity in a pilot study. *Nat. Nanotechnol.* **2008,** *3*, (7), 423-428.
112. Ambalavanan, N.; Stanishevsky, A.; Bulger, A.; Halloran, B.; Steele, C.; Vohra, Y.; Matalon, S., Titanium oxide nanoparticle instillation induces inflammation and inhibits lung development in mice. *American Journal of Physiology-Lung Cellular and Molecular Physiology* **2013,** *304*, (3), L152-L161.
113. Gojova, A.; Guo, B.; Kota, R. S.; Rutledge, J. C.; Kennedy, I. M.; Barakat, A. I., Induction of inflammation in vascular endothelial cells by metal oxide nanoparticles: Effect of particle composition. *Environ. Health Perspect.* **2007,** *115*, (3), 403-409.
114. Yazdi, A. S.; Guarda, G.; Riteau, N.; Drexler, S. K.; Tardivel, A.; Couillin, I.; Tschopp, J., Nanoparticles activate the NLR pyrin domain containing 3 (Nlrp3) inflammasome and cause pulmonary inflammation through release of IL-1 alpha and IL-1 beta. *Proc. Natl. Acad. Sci. U. S. A.* **2010,** *107*, (45), 19449-19454.
115. Deng, Z. J.; Liang, M. T.; Monteiro, M.; Toth, I.; Minchin, R. F., Nanoparticle-induced unfolding of fibrinogen promotes Mac-1 receptor activation and inflammation. *Nat. Nanotechnol.* **2011,** *6*, (1), 39-44.
116. Formiga, F. R.; Pelacho, B.; Garbayo, E.; Abizanda, G.; Gavira, J. J.; Simon-Yarza, T.; Mazo, M.; Tamayo, E.; Jauquicoa, C.; Ortiz-de-Solorzano, C.; Prosper, F.; Blanco-Prieto, M. J., Sustained release of VEGF through PLGA microparticles improves vasculogenesis and tissue remodeling in an acute myocardial ischemia-reperfusion model. *J. Controlled Release* **2010,** *147*, (1), 30-37.
117. Apopa, P. L.; Qian, Y.; Shao, R.; Guo, N. L.; Schwegler-Berry, D.; Pacurari, M.; Porter, D.; Shi, X. L.; Vallyathan, V.; Castranova, V.; Flynn, D. C., Iron oxide nanoparticles induce human microvascular endothelial cell permeability through reactive oxygen species production and microtubule remodeling. *Particle and Fibre Toxicology* **2009,** *6*.
118. Wang, L. Y.; Mercer, R. R.; Rojanasakul, Y.; Qiu, A. J.; Lu, Y. J.; Scabilloni, J. F.; Wu, N. Q.; Castranova, V., Direct Fibrogenic Effects of Dispersed Single-Walled Carbon Nanotubes on Human Lung Fibroblasts. *Journal of Toxicology and Environmental Health-Part a-Current Issues* **2010,** *73*, (5-6), 410-422.
119. Shvedova, A. A.; Kisin, E. R.; Mercer, R.; Murray, A. R.; Johnson, V. J.; Potapovich, A. I.; Tyurina, Y. Y.; Gorelik, O.; Arepalli, S.; Schwegler-Berry, D.; Hubbs, A. F.; Antonini, J.; Evans, D. E.; Ku, B. K.; Ramsey, D.; Maynard, A.; Kagan, V. E.; Castranova, V.; Baron, P., Unusual inflammatory and fibrogenic pulmonary responses to single-walled carbon nanotubes in mice. *American Journal of Physiology-Lung Cellular and Molecular Physiology* **2005,** *289*, (5), L698-L708.
120. Meng, H.; Xia, T.; George, S.; Nel, A. E., A Predictive Toxicological Paradigm for the Safety Assessment of Nanomaterials. *ACS Nano* **2009,** *3*, (7), 1620-1627.
121. Jones, C. F.; Campbell, R. A.; Brooks, A. E.; Assemi, S.; Tadjiki, S.; Thiagarajan, G.; Mulcock, C.; Weyrich, A. S.; Brooks, B. D.; Ghandehari, H.; Grainger, D. W., Cationic PAMAM Dendrimers Aggressively Initiate Blood Clot Formation. *ACS Nano* **2012,** *6*, (11), 9900-9910.

122. Oslakovic, C.; Cedervall, T.; Linse, S.; Dahlback, B., Polystyrene nanoparticles affecting blood coagulation. *Nanomedicine-Nanotechnology Biology and Medicine* **2012,** *8*, (6), 981-986.
123. Chen, Z.; Meng, H.; Xing, G. M.; Yuan, H.; Zhao, F.; Liu, R.; Chang, X. L.; Gao, X. Y.; Wang, T. C.; Jia, G.; Ye, C.; Chai, Z. F.; Zhao, Y. L., Age-Related Differences in Pulmonary and Cardiovascular Responses to SiO(2) Nanoparticle Inhalation: Nanotoxicity Has Susceptible Population. *Environ. Sci. Technol.* **2008,** *42*, (23), 8985-8992.
124. Sharma, V.; Shukla, R. K.; Saxena, N.; Parmar, D.; Das, M.; Dhawan, A., DNA damaging potential of zinc oxide nanoparticles in human epidermal cells. *Toxicol. Lett.* **2009,** *185*, (3), 211-218.
125. Sharma, V.; Anderson, D.; Dhawan, A., Zinc oxide nanoparticles induce oxidative DNA damage and ROS-triggered mitochondria mediated apoptosis in human liver cells (HepG2). *Apoptosis* **2012,** *17*, (8), 852-870.
126. Reeves, J. F.; Davies, S. J.; Dodd, N. J. F.; Jha, A. N., Hydroxyl radicals ((OH)-O-center dot) are associated with titanium dioxide (TiO2) nanoparticle-induced cytotoxicity and oxidative DNA damage in fish cells. *Mutation Research-Fundamental and Molecular Mechanisms of Mutagenesis* **2008,** *640*, (1-2), 113-122.
127. Soenen, S. J.; Rivera-Gil, P.; Montenegro, J. M.; Parak, W. J.; De Smedt, S. C.; Braeckmans, K., Cellular toxicity of inorganic nanoparticles: Common aspects and guidelines for improved nanotoxicity evaluation. *Nano Today* **2011,** *6*, (5), 446-465.
128. Eom, H. J.; Choi, J., Oxidative stress of silica nanoparticles in human bronchial epithelial cell, Beas-2B. *Toxicol. in Vitro* **2009,** *23*, (7), 1326-1332.
129. Kim, S.; Choi, J. E.; Choi, J.; Chung, K. H.; Park, K.; Yi, J.; Ryu, D. Y., Oxidative stress-dependent toxicity of silver nanoparticles in human hepatoma cells. *Toxicol. in Vitro* **2009,** *23*, (6), 1076-1084.
130. Chompoosor, A.; Saha, K.; Ghosh, P. S.; Macarthy, D. J.; Miranda, O. R.; Zhu, Z. J.; Arcaro, K. F.; Rotello, V. M., The Role of Surface Functionality on Acute Cytotoxicity, ROS Generation and DNA Damage by Cationic Gold Nanoparticles. *Small* **2010,** *6*, (20), 2246-2249.
131. Shukla, R. K.; Sharma, V.; Pandey, A. K.; Singh, S.; Sultana, S.; Dhawan, A., ROS-mediated genotoxicity induced by titanium dioxide nanoparticles in human epidermal cells. *Toxicol. in Vitro* **2011,** *25*, (1), 231-241.
132. Park, E. J.; Park, K., Oxidative stress and pro-inflammatory responses induced by silica nanoparticles in vivo and in vitro. *Toxicol. Lett.* **2009,** *184*, (1), 18-25.
133. Hillegass, J. M.; Shukla, A.; Lathrop, S. A.; MacPherson, M. B.; Fukagawa, N. K.; Mossman, B. T., Assessing nanotoxicity in cells in vitro. *Wiley Interdisciplinary Reviews-Nanomedicine and Nanobiotechnology* **2010,** *2*, (3), 219-231.
134. Sahu, S. C.; Casciano, D., *Nanotoxicity : from in vivo and in vitro models to health risks*. John Wiley: Chichester, West Sussex, UK, 2009; p xviii, 609 p., 4 p. of col. plates.
135. Arya, A.; Sethy, N. K.; Singh, S. K.; Das, M.; Bhargava, K., Cerium oxide nanoparticles protect rodent lungs from hypobaric hypoxia-induced oxidative stress and inflammation. *International Journal of Nanomedicine* **2013,** *8*, 4507-4519.

136. Pagliari, F.; Mandoli, C.; Forte, G.; Magnani, E.; Pagliari, S.; Nardone, G.; Licoccia, S.; Minieri, M.; Di Nardo, P.; Traversa, E., Cerium Oxide Nanoparticles Protect Cardiac Progenitor Cells from Oxidative Stress. *ACS Nano* **2012,** *6*, (5), 3767-3775.
137. Sondi, I.; Salopek-Sondi, B., Silver nanoparticles as antimicrobial agent: a case study on E-coli as a model for Gram-negative bacteria. *J. Colloid Interface Sci.* **2004,** *275*, (1), 177-182.
138. Klabunde, K. J.; Stark, J.; Koper, O.; Mohs, C.; Park, D. G.; Decker, S.; Jiang, Y.; Lagadic, I.; Zhang, D. J., Nanocrystals as stoichiometric reagents with unique surface chemistry. *J. Phys. Chem.* **1996,** *100*, (30), 12142-12153.
139. Feris, K.; Otto, C.; Tinker, J.; Wingett, D.; Punnoose, A.; Thurber, A.; Kongara, M.; Sabetian, M.; Quinn, B.; Hanna, C.; Pink, D., Electrostatic interactions affect nanoparticle-mediated toxicity to Gram-negative bacterium *Pseudomonas aeruginosa* PAO1. *Langmuir* **2010,** *26*, (6), 4429-4436.
140. Verma, A.; Stellacci, F., Effect of surface properties on nanoparticle-cell interactions. *Small* **2010,** *6*, (1), 12-21.
141. Arvizo, R. R.; Miranda, O. R.; Thompson, M. A.; Pabelick, C. M.; Bhattacharya, R.; Robertson, J. D.; Rotello, V. M.; Prakash, Y. S.; Mukherjee, P., Effect of Nanoparticle Surface Charge at the Plasma Membrane and Beyond. *Nano Lett.* **2010,** *10*, (7), 2543-2548.
142. Casals, E.; Pfaller, T.; Duschl, A.; Oostingh, G. J.; Puntes, V., Time Evolution of the Nanoparticle Protein Corona. *ACS Nano* **2010,** *4*, (7), 3623-3632.
143. Lundqvist, M.; Stigler, J.; Elia, G.; Lynch, I.; Cedervall, T.; Dawson, K. A., Nanoparticle size and surface properties determine the protein corona with possible implications for biological impacts. *Proc. Natl. Acad. Sci. U. S. A.* **2008,** *105*, (38), 14265-14270.
144. Walkey, C. D.; Chan, W. C. W., Understanding and controlling the interaction of nanomaterials with proteins in a physiological environment. *Chem. Soc. Rev.* **2012,** *41*, (7), 2780-2799.
145. Fei, L.; Perrett, S., Effect of Nanoparticles on Protein Folding and Fibrillogenesis. *International Journal of Molecular Sciences* **2009,** *10*, (2), 646-655.
146. Linse, S.; Cabaleiro-Lago, C.; Xue, W. F.; Lynch, I.; Lindman, S.; Thulin, E.; Radford, S. E.; Dawson, K. A., Nucleation of protein fibrillation by nanoparticles. *Proc. Natl. Acad. Sci. U. S. A.* **2007,** *104*, (21), 8691-8696.
147. Magdolenova, Z.; Collins, A.; Kumar, A.; Dhawan, A.; Stone, V.; Dusinska, M., Mechanisms of genotoxicity. A review of in vitro and in vivo studies with engineered nanoparticles. *Nanotoxicology* **2014,** *8*, (3), 233-278.
148. Kisin, E. R.; Murray, A. R.; Keane, M. J.; Shi, X. C.; Schwegler-Berry, D.; Gorelik, O.; Arepalli, S.; Castranova, V.; Wallace, W. E.; Kagan, V. E.; Shvedova, A. A., Single-walled carbon nanotubes: Geno- and cytotoxic effects in lung fibroblast V79 cells. *Journal of Toxicology and Environmental Health-Part a-Current Issues* **2007,** *70*, (24), 2071-2079.
149. Stone, V.; Johnston, H.; Schins, R. P. F., Development of in vitro systems for nanotoxicology: methodological considerations. *Critical Reviews in Toxicology* **2009,** *39*, (7), 613-626.

150. Gu, Y. J.; Cheng, J. P.; Lin, C. C.; Lam, Y. W.; Cheng, S. H.; Wong, W. T., Nuclear penetration of surface functionalized gold nanoparticles. *Toxicol. Appl. Pharmacol.* **2009,** *237*, (2), 196-204.
151. Barillet, S.; Jugan, M. L.; Laye, M.; Leconte, Y.; Herlin-Boime, N.; Reynaud, C.; Carriere, M., In vitro evaluation of SiC nanoparticles impact on A549 pulmonary cells: Cyto-, genotoxicity and oxidative stress. *Toxicol. Lett.* **2010,** *198*, (3), 324-330.
152. Singh, N.; Manshian, B.; Jenkins, G. J. S.; Griffiths, S. M.; Williams, P. M.; Maffeis, T. G. G.; Wright, C. J.; Doak, S. H., NanoGenotoxicology: The DNA damaging potential of engineered nanomaterials. *Biomaterials* **2009,** *30*, (23-24), 3891-3914.
153. Liang, X. J.; Chen, C. Y.; Zhao, Y. L.; Jia, L.; Wang, P. C., Biopharmaceutics and Therapeutic Potential of Engineered Nanomaterials. *Curr. Drug Metab.* **2008,** *9*, (8), 697-709.
154. Pisanic, T. R.; Blackwell, J. D.; Shubayev, V. I.; Finones, R. R.; Jin, S., Nanotoxicity of iron oxide nanoparticle internalization in growing neurons. *Biomaterials* **2007,** *28*, (16), 2572-2581.
155. Soenen, S. J. H.; Himmelreich, U.; Nuytten, N.; Pisanic, T. R.; Ferrari, A.; De Cuyper, M., Intracellular Nanoparticle Coating Stability Determines Nanoparticle Diagnostics Efficacy and Cell Functionality. *Small* **2010,** *6*, (19), 2136-2145.
156. Miller, I. S.; Lynch, I.; Dowling, D.; Dawson, K. A.; Gallagher, W. M., Surface-induced cell signaling events control actin rearrangements and motility. *Journal of Biomedical Materials Research Part A* **2010,** *93A*, (2), 493-504.
157. Kedziorek, D. A.; Muja, N.; Walczak, P.; Ruiz-Cabello, J.; Gilad, A. A.; Jie, C. F. C.; Bulte, J. W. M., Gene Expression Profiling Reveals Early Cellular Responses to Intracellular Magnetic Labeling with Superparamagnetic Iron Oxide Nanoparticles. *Magnetic Resonance in Medicine* **2010,** *63*, (4), 1031-1043.
158. Madigan, M. T., *Brock biology of microorganisms*. 13th ed.; Benjamin Cummings: San Francisco, 2012; p xxviii, 1043, 77 p.
159. Hansen, J. M.; Go, Y. M.; Jones, D. P., Nuclear and mitochondrial compartmentation of oxidative stress and redox signaling. *Annu. Rev. Pharmacol. Toxicol.* **2006,** *46*, 215-234.
160. Chan, W. C. W., *Bio-applications of nanoparticles*. Springer Science + Business Media ;
Landes Bioscience: New York
Austin, Tex., 2007; p xx, 207 p.
161. Lovric, J.; Cho, S. J.; Winnik, F. M.; Maysinger, D., Unmodified cadmium telluride quantum dots induce reactive oxygen species formation leading to multiple organelle damage and cell death. *Chem. Biol.* **2005,** *12*, (11), 1227-1234.
162. Li, N.; Sioutas, C.; Cho, A.; Schmitz, D.; Misra, C.; Sempf, J.; Wang, M. Y.; Oberley, T.; Froines, J.; Nel, A., Ultrafine particulate pollutants induce oxidative stress and mitochondrial damage. *Environ. Health Perspect.* **2003,** *111*, (4), 455-460.
163. Teodoro, J. S.; Simoes, A. M.; Duarte, F. V.; Rolo, A. P.; Murdoch, R. C.; Hussain, S. M.; Palmeira, C. M., Assessment of the toxicity of silver nanoparticles in vitro: A mitochondrial perspective. *Toxicol. in Vitro* **2011,** *25*, (3), 664-670.
164. Hiura, T. S.; Li, N.; Kaplan, R.; Horwitz, M.; Seagrave, J. C.; Nel, A. E., The role of a mitochondrial pathway in the induction of apoptosis by chemicals extracted from diesel exhaust particles. *J. Immunol.* **2000,** *165*, (5), 2703-2711.

165. Stearns, R. C.; Paulauskis, J. D.; Godleski, J. J., Endocytosis of ultrafine particles by A549 cells. *Am. J. Respir. Cell Mol. Biol.* **2001,** *24*, (2), 108-115.
166. Jaiswal, J. K.; Mattoussi, H.; Mauro, J. M.; Simon, S. M., Long-term multiple color imaging of live cells using quantum dot bioconjugates. *Nat. Biotechnol.* **2003,** *21*, (1), 47-51.
167. Chithrani, B. D.; Ghazani, A. A.; Chan, W. C. W., Determining the size and shape dependence of gold nanoparticle uptake into mammalian cells. *Nano Lett.* **2006,** *6*, (4), 662-668.
168. Frohlich, E.; Meindl, C.; Roblegg, E.; Ebner, B.; Absenger, M.; Pieber, T. R., Action of polystyrene nanoparticles of different sizes on lysosomal function and integrity. *Particle and Fibre Toxicology* **2012,** *9*.
169. Rivera-Gil, P.; De Aberasturi, D. J.; Wulf, V.; Pelaz, B.; Del Pino, P.; Zhao, Y. Y.; De La Fuente, J. M.; De Larramendi, I. R.; Rojo, T.; Liang, X. J.; Parak, W. J., The Challenge To Relate the Physicochemical Properties of Colloidal Nanoparticles to Their Cytotoxicity. *Acc. Chem. Res.* **2013,** *46*, (3), 743-749.
170. Zhu, M. T.; Nie, G. J.; Meng, H.; Xia, T.; Nel, A.; Zhao, Y. L., Physicochemical Properties Determine Nanomaterial Cellular Uptake, Transport, and Fate. *Acc. Chem. Res.* **2013,** *46*, (3), 622-631.
171. Stone, V.; Nowack, B.; Baun, A.; van den Brink, N.; von der Kammer, F.; Dusinska, M.; Handy, R.; Hankin, S.; Hassellov, M.; Joner, E.; Fernandes, T. F., Nanomaterials for environmental studies: Classification, reference material issues, and strategies for physico-chemical characterisation. *Sci. Total Environ.* **2010,** *408*, (7), 1745-1754.
172. He, C. B.; Hu, Y. P.; Yin, L. C.; Tang, C.; Yin, C. H., Effects of particle size and surface charge on cellular uptake and biodistribution of polymeric nanoparticles. *Biomaterials* **2010,** *31*, (13), 3657-3666.
173. Zhang, S. L.; Li, J.; Lykotrafitis, G.; Bao, G.; Suresh, S., Size-Dependent Endocytosis of Nanoparticles. *Adv. Mater. (Weinheim, Ger.)* **2009,** *21*, (4), 419-+.
174. Gao, H. J.; Shi, W. D.; Freund, L. B., Mechanics of receptor-mediated endocytosis. *Proc. Natl. Acad. Sci. U. S. A.* **2005,** *102*, (27), 9469-9474.
175. Jiang, W.; Kim, B. Y. S.; Rutka, J. T.; Chan, W. C. W., Nanoparticle-mediated cellular response is size-dependent. *Nat. Nanotechnol.* **2008,** *3*, (3), 145-150.
176. Schaeublin, N. M.; Braydich-Stolle, L. K.; Schrand, A. M.; Miller, J. M.; Hutchison, J.; Schlager, J. J.; Hussain, S. M., Surface charge of gold nanoparticles mediates mechanism of toxicity. *Nanoscale* **2011,** *3*, (2), 410-420.
177. El Badawy, A. M.; Silva, R. G.; Morris, B.; Scheckel, K. G.; Suidan, M. T.; Tolaymat, T. M., Surface Charge-Dependent Toxicity of Silver Nanoparticles. *Environ. Sci. Technol.* **2011,** *45*, (1), 283-287.
178. Hoshino, A.; Fujioka, K.; Oku, T.; Suga, M.; Sasaki, Y. F.; Ohta, T.; Yasuhara, M.; Suzuki, K.; Yamamoto, K., Physicochemical properties and cellular toxicity of nanocrystal quantum dots depend on their surface modification. *Nano Lett.* **2004,** *4*, (11), 2163-2169.
179. Champion, J. A.; Mitragotri, S., Role of target geometry in phagocytosis. *Proc. Natl. Acad. Sci. U. S. A.* **2006,** *103*, (13), 4930-4934.

180. Albanese, A.; Sykes, E. A.; Chan, W. C. W., Rough around the Edges: The Inflammatory Response of Microglial Cells to Spiky Nanoparticles. *ACS Nano* **2010,** *4*, (5), 2490-2493.
181. George, S.; Lin, S. J.; Jo, Z. X.; Thomas, C. R.; Li, L. J.; Mecklenburg, M.; Meng, H.; Wang, X.; Zhang, H. Y.; Xia, T.; Hohman, J. N.; Lin, S.; Zink, J. I.; Weiss, P. S.; Nel, A. E., Surface Defects on Plate-Shaped Silver Nanoparticles Contribute to Its Hazard Potential in a Fish Gill Cell Line and Zebrafish Embryos. *ACS Nano* **2012,** *6*, (5), 3745-3759.
182. Nguyen, K. C.; Seligy, V. L.; Massarsky, A.; Moon, T. W.; Rippstein, P.; Tan, J.; Tayabali, A. F., Comparison of toxicity of uncoated and coated silver nanoparticles. *Nanosafe 2012: International Conferences on Safe Production and Use of Nanomaterials* **2013,** *429*.
183. Kirchner, C.; Liedl, T.; Kudera, S.; Pellegrino, T.; Javier, A. M.; Gaub, H. E.; Stolzle, S.; Fertig, N.; Parak, W. J., Cytotoxicity of colloidal CdSe and CdSe/ZnS nanoparticles. *Nano Lett.* **2005,** *5*, (2), 331-338.
184. Wick, P.; Manser, P.; Limbach, L. K.; Dettlaff-Weglikowska, U.; Krumeich, F.; Roth, S.; Stark, W. J.; Bruinink, A., The degree and kind of agglomeration affect carbon nanotube cytotoxicity. *Toxicol. Lett.* **2007,** *168*, (2), 121-131.
185. Roebben, G.; Ramirez-Garcia, S.; Hackley, V. A.; Roesslein, M.; Klaessig, F.; Kestens, V.; Lynch, I.; Garner, C. M.; Rawle, A.; Elder, A.; Colvin, V. L.; Kreyling, W.; Krug, H. F.; Lewicka, Z. A.; McNeil, S.; Nel, A.; Patri, A.; Wick, P.; Wiesner, M.; Xia, T.; Oberdorster, G.; Dawson, K. A., Interlaboratory comparison of size and surface charge measurements on nanoparticles prior to biological impact assessment. *Journal of Nanoparticle Research* **2011,** *13*, (7), 2675-2687.
186. Limbach, L. K.; Li, Y. C.; Grass, R. N.; Brunner, T. J.; Hintermann, M. A.; Muller, M.; Gunther, D.; Stark, W. J., Oxide nanoparticle uptake in human lung fibroblasts: Effects of particle size, agglomeration, and diffusion at low concentrations. *Environ. Sci. Technol.* **2005,** *39*, (23), 9370-9376.
187. Brown, S. C.; Kamal, M.; Nasreen, N.; Baumuratov, A.; Sharma, P.; Antony, V. B.; Moudgil, B. M., Influence of shape, adhesion and simulated lung mechanics on amorphous silica nanoparticle toxicity. *Advanced Powder Technology* **2007,** *18*, (1), 69-79.
188. Allouni, Z. E.; Cimpan, M. R.; Hol, P. J.; Skodvin, T.; Gjerdet, N. R., Agglomeration and sedimentation of TiO2 nanoparticles in cell culture medium. *Colloids and Surfaces B-Biointerfaces* **2009,** *68*, (1), 83-87.
189. Stebounova, L. V.; Guio, E.; Grassian, V. H., Silver nanoparticles in simulated biological media: a study of aggregation, sedimentation, and dissolution. *Journal of Nanoparticle Research* **2011,** *13*, (1), 233-244.
190. Albanese, A.; Chan, W. C. W., Effect of Gold Nanoparticle Aggregation on Cell Uptake and Toxicity. *ACS Nano* **2011,** *5*, (7), 5478-5489.
191. Drescher, D.; Orts-Gil, G.; Laube, G.; Natte, K.; Veh, R. W.; Osterle, W.; Kneipp, J., Toxicity of amorphous silica nanoparticles on eukaryotic cell model is determined by particle agglomeration and serum protein adsorption effects. *Anal. Bioanal. Chem.* **2011,** *400*, (5), 1367-1373.

192. Okuda-Shimazaki, J.; Takaku, S.; Kanehira, K.; Sonezaki, S.; Taniguchi, A., Effects of Titanium Dioxide Nanoparticle Aggregate Size on Gene Expression. *International Journal of Molecular Sciences* **2010,** *11*, (6), 2383-2392.
193. Cui, W.; Li, J.; Zhang, Y.; Rong, H.; Lu, W.; Jiang, L., Effects of aggregation and the surface properties of gold nanoparticles on cytotoxicity and cell growth. *Nanomedicine* **2012,** *8*, (1), 46-53.
194. Judson, R. S.; Houck, K. A.; Kavlock, R. J.; Knudsen, T. B.; Martin, M. T.; Mortensen, H. M.; Reif, D. M.; Rotroff, D. M.; Shah, I.; Richard, A. M.; Dix, D. J., In Vitro Screening of Environmental Chemicals for Targeted Testing Prioritization: The ToxCast Project. *Environ. Health Perspect.* **2010,** *118*, (4), 485-492.
195. Choi, J. Y.; Ramachandran, G.; Kandlikar, M., The Impact of Toxicity Testing Costs on Nanomaterial Regulation. *Environ. Sci. Technol.* **2009,** *43*, (9), 3030-3034.
196. Li, K. G.; Chen, Y.; Zhang, W.; Pu, Z. C.; Jiang, L.; Chen, Y. S., Surface Interactions Affect the Toxicity of Engineered Metal Oxide Nanoparticles toward Paramecium. *Chem. Res. Toxicol.* **2012,** *25*, (8), 1675-1681.
197. Li, K. G.; Chen, Y. S., Effect of natural organic matter on the aggregation kinetics of CeO2 nanoparticles in KCl and CaCl2 solutions: Measurements and modeling. *J. Hazard. Mater.* **2012,** *209*, 264-270.
198. Puzyn, T.; Rasulev, B.; Gajewicz, A.; Hu, X. K.; Dasari, T. P.; Michalkova, A.; Hwang, H. M.; Toropov, A.; Leszczynska, D.; Leszczynski, J., Using nano-QSAR to predict the cytotoxicity of metal oxide nanoparticles. *Nat. Nanotechnol.* **2011,** *6*, (3), 175-178.
199. Sayes, C.; Ivanov, I., Comparative Study of Predictive Computational Models for Nanoparticle-Induced Cytotoxicity. *Risk Analysis* **2010,** *30*, (11), 1723-1734.
200. Chau, Y. T.; Yap, C. W., Quantitative Nanostructure-Activity Relationship modelling of nanoparticles. *Rsc Advances* **2012,** *2*, (22), 8489-8496.
201. Fourches, D.; Pu, D. Q. Y.; Tassa, C.; Weissleder, R.; Shaw, S. Y.; Mumper, R. J.; Tropsha, A., Quantitative Nanostructure-Activity Relationship Modeling. *ACS Nano* **2010,** *4*, (10), 5703-5712.
202. Gajewicz, A.; Rasulev, B.; Dinadayalane, T. C.; Urbaszek, P.; Puzyn, T.; Leszczynska, D.; Leszczynski, J., Advancing risk assessment of engineered nanomaterials: Application of computational approaches. *Adv. Drug Delivery Rev.* **2012,** *64*, (15), 1663-1693.
203. Xia, X. R.; Monteiro-Riviere, N. A.; Riviere, J. E., An index for characterization of nanomaterials in biological systems. *Nat. Nanotechnol.* **2010,** *5*, (9), 671-675.
204. Puzyn, T.; Leszczynska, D.; Leszczynski, J., Toward the Development of "Nano-QSARs": Advances and Challenges. *Small* **2009,** *5*, (22), 2494-2509.
205. Kubinyi, H., *QSAR : Hansch analysis and related approaches*. VCH: Weinheim ; New York, 1993; p xii, 240 p.
206. Karelson, M.; Lobanov, V. S.; Katritzky, A. R., Quantum-chemical descriptors in QSAR/QSPR studies. *Chem. Rev. (Washington, DC, U. S.)* **1996,** *96*, (3), 1027-1043.
207. Hansch, C.; Leo, A.; Hoekman, D. H., *Exploring QSAR*. American Chemical Society: Washington, DC, 1995.
208. Li, Y.; Zhang, W.; Niu, J.; Chen, Y., Mechanism of photogenerated reactive oxygen species and correlation with the antibacterial properties of engineered metal-oxide nanoparticles. *ACS Nano* **2012,** *6*, (6), 5164-73.

209. Somasundaran, P.; Fang, X.; Ponnurangam, S.; Li, B., Nanoparticles: Characteristics, Mechanisms and Modulation of Biotoxicity. *Kona Powder and Particle Journal* **2010**, (28), 38-49.
210. Nel, A. E.; Madler, L.; Velegol, D.; Xia, T.; Hoek, E. M. V.; Somasundaran, P.; Klaessig, F.; Castranova, V.; Thompson, M., Understanding biophysicochemical interactions at the nano-bio interface. *Nat. Mater.* **2009,** *8*, (7), 543-557.
211. Grasso, D.; Subramaniam, K.; Butkus, M.; Strevett, K.; Bergendahl, J., A review of non-DLVO interactions in environmental colloidal systems. *Reviews in Environmental Science and Biotechnology* **2002,** *1*, (1), 17-38.
212. B.V. Derjaguin, L. D. L., Theory of stability of highly charged lyophobic sols and adhesion of highly charged particles in solutions of electrolytes. *Acta Physicochim* **1941,** *14*, 633.
213. Verwey, E. J. W.; Overbeek, J. T. G.; Nes, K. v., *Theory of the stability of lyophobic colloids; the interaction of sol particles having an electric double layer*. Elsevier Pub. Co.: New York, 1948; p xi, 205 p.
214. Benos, P. V.; Bulyk, M. L.; Stormo, G. D., Additivity in protein-DNA interactions: how good an approximation is it? *Nucleic Acids Res.* **2002,** *30*, (20), 4442-4451.
215. Xia, T.; Li, N.; Nel, A. E., Potential health impact of nanoparticles. *Annu. Rev. Publ. Health* **2009,** *30*, 137-150.
216. Petosa, A. R.; Jaisi, D. P.; Quevedo, I. R.; Elimelech, M.; Tufenkji, N., Aggregation and deposition of engineered nanomaterials in aquatic environments: role of physicochemical interactions. *Environ. Sci. Technol.* **2010,** *44*, (17), 6532-6549.
217. Buettner, K. M.; Rinciog, C. I.; Mylon, S. E., Aggregation kinetics of cerium oxide nanoparticles in monovalent and divalent electrolytes. *Colloids and Surfaces a-Physicochemical and Engineering Aspects* **2010,** *366*, (1-3), 74-79.
218. Van Hoecke, K.; Quik, J. T. K.; Mankiewicz-Boczek, J.; De Schamphelaere, K. A. C.; Elsaesser, A.; Van der Meeren, P.; Barnes, C.; McKerr, G.; Howard, C. V.; Van De Meent, D.; Rydzynski, K.; Dawson, K. A.; Salvati, A.; Lesniak, A.; Lynch, I.; Silversmit, G.; De Samber, B.; Vincze, L.; Janssen, C. R., Fate and Effects of CeO2 Nanoparticles in Aquatic Ecotoxicity Tests. *Environ. Sci. Technol.* **2009,** *43*, (12), 4537-4546.
219. Saleh, N. B.; Pfefferle, L. D.; Elimelech, M., Aggregation kinetics of multiwalled carbon nanotubes in aquatic systems: measurements and environmental implications. *Environ. Sci. Technol.* **2008,** *42*, (21), 7963-7969.
220. Chen, K. L.; Elimelech, M., Aggregation and deposition kinetics of fullerene (C-60) nanoparticles. *Langmuir* **2006,** *22*, (26), 10994-11001.
221. Chen, K. L.; Elimelech, M., Influence of humic acid on the aggregation kinetics of fullerene (C-60) nanoparticles in monovalent and divalent electrolyte solutions. *J. Colloid Interface Sci.* **2007,** *309*, (1), 126-134.
222. Kim, T.; Lee, K.; Gong, M. S.; Joo, S. W., Control of gold nanoparticle aggregates by manipulation of interparticle interaction. *Langmuir* **2005,** *21*, (21), 9524-9528.
223. Behrens, S. H.; Christl, D. I.; Emmerzael, R.; Schurtenberger, P.; Borkovec, M., Charging and aggregation properties of carboxyl latex particles: Experiments versus DLVO theory. *Langmuir* **2000,** *16*, (6), 2566-2575.

224. Ohki, S.; Ohshima, H., Interaction and aggregation of lipid vesicles (DLVO theory versus modified DLVO theory). *Colloids and Surfaces B-Biointerfaces* **1999,** *14*, (1-4), 27-45.
225. Elimelech, M.; Omelia, C. R., Kinetics of Deposition of Colloidal Particles in Porous-Media. *Environ. Sci. Technol.* **1990,** *24*, (10), 1528-1536.
226. Tsuruta, L. R.; Lessa, M. M.; Carmonaribeiro, A. M., Effect of Particle-Size on Colloid Stability of Bilayer-Covered Polystyrene Microspheres. *J. Colloid Interface Sci.* **1995,** *175*, (2), 470-475.
227. Vanoss, C. J.; Giese, R. F.; Costanzo, P. M., Dlvo and Non-Dlvo Interactions in Hectorite. *Clays Clay Miner.* **1990,** *38*, (2), 151-159.
228. van Oss, C. J., Long-range and short-range mechanisms of hydrophobic attraction and hydrophilic repulsion in specific and aspecific interactions. *J. Mol. Recognit.* **2003,** *16*, (4), 177-190.
229. Vanoss, C. J., Acid-Base Interfacial Interactions in Aqueous-Media. *Colloids and Surfaces a-Physicochemical and Engineering Aspects* **1993,** *78*, 1-49.
230. Van Oss, C. J., *Interfacial forces in aqueous media*. 2nd ed.; Taylor & Francis: Boca Raton, Fl., 2006; p 438 p.
231. Vanoss, C. J.; Chaudhury, M. K.; Good, R. J., Interfacial Lifshitz-Vanderwaals and Polar Interactions in Macroscopic Systems. *Chem. Rev. (Washington, DC, U. S.)* **1988,** *88*, (6), 927-941.
232. Schwarzer, H. C.; Peukert, W., Prediction of aggregation kinetics based on surface properties of nanoparticles. *Chem. Eng. Sci.* **2005,** *60*, (1), 11-25.
233. Kusters, K. A.; Wijers, J. G.; Thoenes, D., Aggregation kinetics of small particles in agitated vessels. *Chem. Eng. Sci.* **1997,** *52*, (1), 107-121.
234. Kobayashi, M.; Juillerat, F.; Galletto, P.; Bowen, P.; Borkovec, M., Aggregation and charging of colloidal silica particles: Effect of particle size. *Langmuir* **2005,** *21*, (13), 5761-5769.
235. Lin, M. Y.; Lindsay, H. M.; Weitz, D. A.; Ball, R. C.; Klein, R.; Meakin, P., Universality in colloid aggregation. *Nature* **1989,** *339*, (6223), 360-362.
236. Lin, M. Y.; Lindsay, H. M.; Weitz, D. A.; Klein, R.; Ball, R. C.; Meakin, P., Universal diffusion-limited colloid aggregation. *Journal of Physics-Condensed Matter* **1990,** *2*, (13), 3093-3113.
237. Runkana, V.; Somasundaran, P.; Kapur, P. C., Reaction-limited aggregation in presence of short-range structural forces. *AIChE J.* **2005,** *51*, (4), 1233-1245.
238. **!!! INVALID CITATION !!!**
239. Aguila, G.; Gracia, F.; Araya, P., CuO and CeO2 catalysts supported on Al2O3, ZrO2, and SiO2 in the oxidation of CO at low temperature. *Appl Catal A-General* **2008,** *343*, (1-2), 16-24.
240. Bekyarova, E.; Fornasiero, P.; Kaspar, J.; Graziani, M., CO oxidation on Pd/CeO2-ZrO2 catalysts. *Catal. Today* **1998,** *45*, (1-4), 179-183.
241. Kaneko, K.; Inoke, K.; Freitag, B.; Hungria, A. B.; Midgley, P. A.; Hansen, T. W.; Zhang, J.; Ohara, S.; Adschiri, T., Structural and morphological characterization of cerium oxide nanocrystals prepared by hydrothermal synthesis. *Nano Lett.* **2007,** *7*, (2), 421-425.

242. Shiono, M.; Kobayashi, K.; Nguyen, T. L.; Hosoda, K.; Kato, T.; Ota, K.; Dokiya, M., Effect of CeO2 interlayer on ZrO2 electrolyte/La(Sr)CoO3 cathode for low-temperature SOFCs. *Solid State Ionics* **2004,** *170*, (1-2), 1-7.
243. Lee, D. S.; Kim, W. S.; Choi, S. H.; Kim, J.; Lee, H. W.; Lee, J. H., Characterization of ZrO2 co-doped with SC2O3 and CeO2 electrolyte for the application of intermediate temperature SOFCs. *Solid State Ionics* **2005,** *176*, (1-2), 33-39.
244. Organization for Economic Co-operation and Development (2010) List of manufactured nanomaterials and list of endpoints for phase one of the sponsorship programme for the testing of manufactured nanomaterials: revision. Series on the Safety of Manufactured Nanomaterials No. 27. http://www.oecd.org/officialdocuments/displaydocumentpdf?cote=env/jm/mono%282010%2946&doclanguage=en. Accessed 10 August 2011.
245. Smoluchowski, v., Versuch einer mathematischen Theorie der Koagulationskinetik kolloider Lösungen. *Z Phys Chem* **1917,** *92*, 40.
246. Elimelech, M., *Particle deposition and aggregation: measurement, modelling, and simulation*. Butterworth-Heinemann: Oxford, UK, 1995; p xv., 441 p.
247. Holthoff, H.; Egelhaaf, S. U.; Borkovec, M.; Schurtenberger, P.; Sticher, H., Coagulation rate measurements of colloidal particles by simultaneous static and dynamic light scattering. *Langmuir* **1996,** *12*, (23), 5541-5549.
248. Honig, E. P.; Roeberse.Gj; Wiersema, P. H., Effect of hydrodynamic interaction on coagulation rate of hydrophobic colloids. *J. Colloid Interface Sci.* **1971,** *36*, (1), 97-&.
249. Mcgown, D. N. L.; Parfitt, G. D., Improved theoretical calculation of stability ratio for colloidal systems. *J. Phys. Chem.* **1967,** *71*, (2), 449-&.
250. Abu-Lail, N. I.; Camesano, T. A., Role of ionic strength on the relationship of biopolymer conformation, DLVO contributions, and steric interactions to bioadhesion of Pseudomonas putida KT2442. *Biomacromolecules* **2003,** *4*, (4), 1000-1012.
251. Gregory, J., Interaction of Unequal Double-Layers at Constant Charge. *J. Colloid Interface Sci.* **1975,** *51*, (1), 44-51.
252. Karimian, H.; Babaluo, A. A., Halos mechanism in stabilizing of colloidal suspensions: Nanoparticle weight fraction and pH effects. *J. Eur. Ceram. Soc.* **2007,** *27*, (1), 19-25.
253. Grasso, D.; Subramaniam, K.; Butkus, M.; Strevett, K.; Bergendahl, J., A review of non-DLVO interactions in environmental colloidal systems. *Rev. Environ. Sci. Biotechnol.* **2002,** *1*, 17-38.
254. Ohshima, H., *Theory of colloid and interfacial electric phenomena*. Academic Press: Amsterdam ; London, 2006; p xvi, 473 p.
255. Ball, R. C.; Weitz, D. A.; Witten, T. A.; Leyvraz, F., Universal Kinetics in Reaction-Limited Aggregation. *Phys. Rev. Lett.* **1987,** *58*, (3), 274-277.
256. Barz, D. P. J.; Vogel, M. J.; Steen, P. H., Determination of the Zeta Potential of Porous Substrates by Droplet Deflection. I. The Influence of Ionic Strength and pH Value of an Aqueous Electrolyte in Contact with a Borosilicate Surface. *Langmuir* **2009,** *25*, (3), 1842-1850.
257. Kirby, B. J.; Hasselbrink, E. F., Zeta potential of microfluidic substrates: 1. Theory, experimental techniques, and effects on separations. *Electrophoresis* **2004,** *25*, (2), 187-202.

258. Revil, A.; Pezard, P. A.; Glover, P. W. J., Streaming potential in porous media 1. Theory of the zeta potential. *Journal of Geophysical Research-Solid Earth* **1999,** *104*, (B9), 20021-20031.
259. Chen, K. L.; Mylon, S. E.; Elimelech, M., Aggregation kinetics of alginate-coated hematite nanoparticles in monovalent and divalent electrolytes. *Environ. Sci. Technol.* **2006,** *40*, (5), 1516-1523.
260. French, R. A.; Jacobson, A. R.; Kim, B.; Isley, S. L.; Penn, R. L.; Baveye, P. C., Influence of Ionic Strength, pH, and Cation Valence on Aggregation Kinetics of Titanium Dioxide Nanoparticles. *Environ. Sci. Technol.* **2009,** *43*, (5), 1354-1359.
261. Santander-Ortega, M. J.; Lozano-Lopez, M. V.; Bastos-Gonzalez, D.; Peula-Garcia, J. M.; Ortega-Vinuesa, J. L., Novel core-shell lipid-chitosan and lipid-poloxamer nanocapsules: stability by hydration forces. *Colloid Polym. Sci.* **2010,** *288*, (2), 159-172.
262. Hoek, E. M. V.; Agarwal, G. K., Extended DLVO interactions between spherical particles and rough surfaces. *J. Colloid Interface Sci.* **2006,** *298*, (1), 50-58.
263. Rekveld, S. Ellipsometric Studies of Protein Adsorption onto Hard Surfaces in a Flow Cell. Dissertation, Twente, 1997.
264. Pashley, R. M., Dlvo and Hydration Forces between Mica Surfaces in Li+,Na+,K+,and Cs+ Electrolyte-Solutions - a Correlation of Double-Layer and Hydration Forces with Surface Cation-Exchange Properties. *J. Colloid Interface Sci.* **1981,** *83*, (2), 531-546.
265. Pashley, R. M.; Israelachvili, J. N., Dlvo and Hydration Forces between Mica Surfaces in Mg-2+, Ca-2+, Sr-2+, and Ba-2+ Chloride Solutions. *J. Colloid Interface Sci.* **1984,** *97*, (2), 446-455.
266. Israelachvili, J., *Intermolecular and surface forces*. 2nd ed.; Academic Press: London ; San Diego, 1991; p xxi, 450 p.
267. Cevc, G., Hydration Force and the Interfacial Structure of the Polar Surface. *Journal of the Chemical Society-Faraday Transactions* **1991,** *87*, (17), 2733-2739.
268. Berka, M.; Rice, J. A., Relation between aggregation kinetics and the structure of kaolinite aggregates. *Langmuir* **2005,** *21*, (4), 1223-1229.
269. Sandkuhler, P.; Sefcik, J.; Lattuada, M.; Wu, H.; Morbidelli, M., Modeling structure effects on aggregation kinetics in colloidal dispersions. *AIChE J.* **2003,** *49*, (6), 1542-1555.
270. Weitz, D. A.; Huang, J. S.; Lin, M. Y.; Sung, J., Limits of the Fractal Dimension for Irreversible Kinetic Aggregation of Gold Colloids. *Phys. Rev. Lett.* **1985,** *54*, (13), 1416-1419.
271. Keller, A. A.; Wang, H. T.; Zhou, D. X.; Lenihan, H. S.; Cherr, G.; Cardinale, B. J.; Miller, R.; Ji, Z. X., Stability and aggregation of metal oxide nanoparticles in natural aqueous matrices. *Environ. Sci. Technol.* **2010,** *44*, (6), 1962-1967.
272. Byrd, T. L.; Walz, J. Y., Interaction force profiles between Cryptosporidium parvum oocysts and silica surfaces. *Environ. Sci. Technol.* **2005,** *39*, (24), 9574-9582.
273. Runkana, V.; Somasundaran, P.; Kapur, P. C., A population balance model for flocculation of colloidal suspensions by polymer bridging. *Chem. Eng. Sci.* **2006,** *61*, (1), 182-191.
274. Hong, S. K.; Elimelech, M., Chemical and physical aspects of natural organic matter (NOM) fouling of nanofiltration membranes. *J. Membr. Sci.* **1997,** *132*, (2), 159-181.

275. Gregory, J., Approximate Expressions for Retarded Vanderwaals Interaction. *J. Colloid Interface Sci.* **1981,** *83*, (1), 138-145.
276. French, R. H., Origins and applications of London dispersion forces and Hamaker constants in ceramics. *J. Am. Ceram. Soc.* **2000,** *83*, (9), 2117-2146.
277. Zhao, Y.; Ng, H. T.; Hanson, E.; Dong, J. N.; Corti, D. S.; Franses, E. I., Computation of Nonretarded London Dispersion Coefficients and Hamaker Constants of Copper Phthalocyanine. *J. Chem. Theory Comput.* **2010,** *6*, (2), 491-498.
278. Huber, G.; Mantz, H.; Spolenak, R.; Mecke, K.; Jacobs, K.; Gorb, S. N.; Arzt, E., Evidence for capillarity contributions to gecko adhesion from single spatula nanomechanical measurements. *Proc. Natl. Acad. Sci. U. S. A.* **2005,** *102*, (45), 16293-16296.
279. Croucher, M. D.; Hair, M. L., Hamaker Constants and Principle of Corresponding States. *J. Phys. Chem.* **1977,** *81*, (17), 1631-1636.
280. Ohshima, H., Effective Surface-Potential and Double-Layer Interaction of Colloidal Particles. *J. Colloid Interface Sci.* **1995,** *174*, (1), 45-52.
281. Degennes, P. G., Polymer-Solutions near an Interface .1. Adsorption and Depletion Layers. *Macromolecules* **1981,** *14*, (6), 1637-1644.
282. Degennes, P. G., Polymer-Solutions near an Interface. 2. Interaction between two plates carrying adsorbed polymer layers. *Macromolecules* **1982,** *15*, 492-500.
283. Li, K. G.; Zhang, W.; Huang, Y.; Chen, Y. S., Aggregation kinetics of CeO2 nanoparticles in KCl and CaCl2 solutions: Measurements and modeling. *J. Nanopart. Res.* **2011**, in press. DOI: 10.1007/s11051-011-0548-z.
284. Zhang, F.; Chan, S. W.; Spanier, J. E.; Apak, E.; Jin, Q.; Robinson, R. D.; Herman, I. P., Cerium oxide nanoparticles: Size-selective formation and structure analysis. *Applied Physics Letters* **2002,** *80*, (1), 127-129.
285. Moller, L.; Karlsson, H. L.; Cronholm, P.; Gustafsson, J., Copper oxide nanoparticles are highly toxic: A comparison between metal oxide nanoparticles and carbon nanotubes. *Chem. Res. Toxicol.* **2008,** *21*, (9), 1726-1732.
286. Li, Q. L.; Elimelech, M., Organic fouling and chemical cleaning of nanofiltration membranes: Measurements and mechanisms. *Environ. Sci. Technol.* **2004,** *38*, (17), 4683-4693.
287. Liu, X. Y.; Wazne, M.; Christodoulatos, C.; Jasinkiewicz, K. L., Aggregation and deposition behavior of boron nanoparticles in porous media. *J. Colloid Interface Sci.* **2009,** *330*, (1), 90-96.
288. Pelley, A. J.; Tufenkji, N., Effect of particle size and natural organic matter on the migration of nano- and microscale latex particles in saturated porous media. *J. Colloid Interface Sci.* **2008,** *321*, (1), 74-83.
289. Elimelech, M.; Omelia, C. R., Effect of electrolyte type on the electrophoretic mobility of polystyrene latex colloids. *Colloids Surf.* **1990,** *44*, 165-178.
290. Kirby, B., *Micro- and nanoscale fluid bechanics: transport in microfluidic devices*. 1st ed.; Cambridge University Press: New York, USA, 2010; p 513 p.
291. Saleh, N. B.; Pfefferle, L. D.; Elimelech, M., Influence of biomacromolecules and humic acid on the aggregation kinetics of single-walled carbon nanotubes. *Environ. Sci. Technol.* **2010,** *44*, (7), 2412-2418.
292. Tipping, E.; Ohnstad, M., Colloid stability of Iron-oxide particles from a fresh-water lake. *Nature* **1984,** *308*, (5956), 266-268.

293. Liu, X. Y.; Wazne, M.; Chou, T. M.; Xiao, R.; Xu, S. Y., Influence of Ca2+ and Suwannee River Humic Acid on aggregation of silicon nanoparticles in aqueous media. *Water Res.* **2011,** *45*, (1), 105-112.
294. Phenrat, T.; Saleh, N.; Sirk, K.; Kim, H. J.; Tilton, R. D.; Lowry, G. V., Stabilization of aqueous nanoscale zerovalent iron dispersions by anionic polyelectrolytes: adsorbed anionic polyelectrolyte layer properties and their effect on aggregation and sedimentation. *Journal of Nanoparticle Research* **2008,** *10*, (5), 795-814.
295. Ohshima, H., Electrophoresis of soft particles. *Adv. Colloid Interface Sci.* **1995,** *62*, (2-3), 189-235.
296. Phenrat, T.; Song, J. E.; Cisneros, C. M.; Schoenfelder, D. P.; Tilton, R. D.; Lowry, G. V., Estimating attachment of nano- and submicrometer-particles coated with organic macromolecules in porous media: development of an empirical model. *Environ. Sci. Technol.* **2010,** *44*, (12), 4531-4538.
297. Ahmad, A. L.; Chong, M. F.; Bhatia, S., Population Balance Model (PBM) for flocculation process: Simulation and experimental studies of palm oil mill effluent (POME) pretreatment. *Chem. Eng. J. (Lausanne)* **2008,** *140*, (1-3), 86-100.
298. Cosgrove, T.; Crowley, T. L.; Ryan, K.; Webster, J. R. P., The effects of solvency on the structure of an adsorbed polymer layer and dispersion stability. *Colloids Surf.* **1990,** *51*, 255-269.
299. Klein, J.; Rossi, G., Analysis of the experimental implications of the scaling theory of polymer adsorption. *Macromolecules* **1998,** *31*, (6), 1979-1988.
300. Hao, Y. Q.; Wang, Y. F.; Weng, Y. X., Particle-size-dependent hydrophilicity of TiO2 nanoparticles characterized by Marcus reorganization energy of interfacial charge recombination. *J. Phys. Chem. C* **2008,** *112*, (24), 8995-9000.
301. Chithrani, B. D.; Chan, W. C. W., Elucidating the mechanism of cellular uptake and removal of protein-coated gold nanoparticles of different sizes and shapes. *Nano Lett.* **2007,** *7*, (6), 1542-1550.
302. Li, K. G.; Chen, Y. S., Effect of natural organic matter on the aggregation kinetics of CeO_2 nanoparticles in KCl and $CaCl_2$ solutions: measurements and modeling. *J. Hazard. Mater.* **2012**, in press. DOI: 10.1016/j.jhazmat.2012.01.013.
303. Li, K.; Zhang, W.; Huang, Y.; Chen, Y., Aggregation kinetics of CeO_2 nanoparticles in KCl and $CaCl_2$ solutions: measurements and modeling. *Journal of Nanoparticle Research* **2011,** *13*, (12), 6483-6491.
304. Valdivieso, A. L.; Bahena, J. L. R.; Song, S.; Urbina, R. H., Temperature effect on the zeta potential and fluoride adsorption at the alpha-Al2O3/aqueous solution interface. *J. Colloid Interface Sci.* **2006,** *298*, (1), 1-5.
305. Rodriguez, K.; Araujo, M., Temperature and pressure effects on zeta potential values of reservoir minerals. *J. Colloid Interface Sci.* **2006,** *300*, (2), 788-794.
306. Schrand, A. M.; Rahman, M. F.; Hussain, S. M.; Schlager, J. J.; Smith, D. A.; Syed, A. F., Metal-based nanoparticles and their toxicity assessment. *Wiley Interdiscip Rev Nanomed Nanobiotechnol* **2010,** *2*, (5), 544-568.
307. Zhu, X. S.; Chang, Y.; Chen, Y. S., Toxicity and bioaccumulation of TiO(2) nanoparticle aggregates in Daphnia magna. *Chemosphere* **2010,** *78*, (3), V-215.
308. Zhu, X. S.; Zhu, L.; Chen, Y. S.; Tian, S. Y., Acute toxicities of six manufactured nanomaterial suspensions to Daphnia magna. *J. Nanopart. Res* **2009,** *11*, (1), 67-75.

309. Chang, Y.; Zhu, X. S.; Wang, J. X.; Zhang, X. Z.; Chen, Y. S., Trophic transfer of TiO_2 nanoparticles from daphnia to zebrafish in a simplified freshwater food chain. *Chemosphere* **2010,** *79*, (9), 928-933.
310. Van Hoecke, K.; Quik, J. T. K.; Mankiewicz-Boczek, J.; De Schamphelaere, K. A. C.; Elsaesser, A.; Van der Meeren, P.; Barnes, C.; McKerr, G.; Howard, C. V.; Van De Meent, D.; Rydzynski, K.; Dawson, K. A.; Salvati, A.; Lesniak, A.; Lynch, I.; Silversmit, G.; De Samber, B.; Vincze, L.; Janssen, C. R., Fate and effects of CeO_2 nanoparticles in aquatic ecotoxicity tests. *Environ. Sci. Technol.* **2009,** *43*, (12), 4537-4546.
311. Chang, Y.; Zhu, X. S.; Wang, J. X.; Zhang, X. Z.; Chen, Y. S., The impact of ZnO nanoparticle aggregates on the embryonic development of zebrafish (Danio rerio). *Nanotechnology* **2009,** *20*, (19), 195103-195111.
312. Chen, Y. S.; Zhu, X. S.; Zhu, L.; Tian, S. Y., Acute toxicities of six manufactured nanomaterial suspensions to Daphnia magna. *J. Nanopart. Res.* **2009,** *11*, (1), 67-75.
313. Chang, Y.; Zhu, X. S.; Chen, Y. S., Toxicity and bioaccumulation of TiO_2 nanoparticle aggregates in Daphnia magna. *Chemosphere* **2010,** *78*, (3), V-215.
314. He, Y. L.; Tao, X. J.; Zhang, B.; Chen, Y. S.; Hughes, J. B., Effects of stable aqueous fullerene nanocrystal (nC_{60}) on Daphnia magna: Evaluation of hop frequency and accumulations under different conditions. *J Environ Sci-China* **2011,** *23*, (2), 322-329.
315. Chang, Y.; Wang, J. X.; Zhu, X. S.; Zhang, X. Z.; Zhao, Z.; Liu, H.; George, R.; Wilson-Rawls, J.; Chen, Y. S., Disruption of zebrafish (Danio rerio) reproduction upon chronic exposure to TiO_2 nanoparticles. *Chemosphere* **2011,** *83*, (4), 461-467.
316. Iwamoto, M.; Allen, R. D., Uptake and rapid transfer of fluorescent ceramide analogues to acidosomes (late enclosomes) in Paramecium. *J. Histochem. Cytochem.* **2004,** *52*, (5), 557-565.
317. Pagnout, C.; Jomini, S.; Dadhwal, M.; Caillet, C.; Thomas, F.; Bauda, P., Role of electrostatic interactions in the toxicity of titanium dioxide nanoparticles toward *Escherichia coli*. *Colloids and Surfaces B: Biointerfaces* **2012,** *92*, 315-321.
318. Wang, Y.; Aker, W.; Hwang, H. M.; Yedjou, C.; Yu, H.; Tchounwou, P. B., A study of the mechanism of in vitro cytotoxicity of metal oxide nanoparticles using catfish primary hepatocytes and human HepG2 cells. *Sci. Total Environ.* **2011,** *409*, 4753-4762.
319. Thill, A.; Zeyons, O.; Spalla, O.; Chauvat, F.; Rose, J.; Auffan, M.; Flank, A. M., Cytotoxicity of CeO2 nanoparticles for Escherichia coli. Physico-chemical insight of the cytotoxicity mechanism. *Environ. Sci. Technol.* **2006,** *40*, (19), 6151-6156.
320. Jiang, W.; Mashayekhi, H.; Xing, B. S., Bacterial toxicity comparison between nano- and micro-scaled oxide particles. *Environ. Pollut.* **2009,** *157*, (5), 1619-1625.
321. Stoimenov, P. K.; Klinger, R. L.; Marchin, G. L.; Klabunde, K. J., Metal oxide nanoparticles as bactericidal agents. *Langmuir* **2002,** *18*, (17), 6679-6686.
322. El Badawy, A. M.; Silva, R. G.; Morris, B.; Scheckel, K. G.; Suidan, M. T.; Tolaymat, T. M., Surface charge-dependent toxicity of silver nanoparticles. *Environ. Sci. Technol.* **2011,** *45*, (1), 283-287.
323. Goodman, C. M.; McCusker, C. D.; Yilmaz, T.; Rotello, V. M., Toxicity of gold nanoparticles functionalized with cationic and anionic side chains. *Bioconjugate Chem.* **2004,** *15*, (4), 897-900.

324. Zhang, W.; Hughes, J.; Chen, Y., Impacts of hematite nanoparticle exposure on biomechanical, adhesive, and surface electrical properties of *E. coli* cells. *Appl. Environ. Microbiol.* **2012**, *doi: 10.1128/AEM.00193-12*.
325. Zhang, W.; Kalive, M.; Capco, D. G.; Chen, Y. S., Adsorption of hematite nanoparticles onto Caco-2 cells and the cellular impairments: effect of particle size. *Nanotechnology* **2010,** *21*, (35).
326. Lin, J. Q.; Zhang, H. W.; Chen, Z.; Zheng, Y. G., Penetration of lipid membranes by gold nanoparticles: insights into cellular uptake, cytotoxicity, and their relationship. *ACS Nano* **2010,** *4*, (9), 5421-5429.
327. Green, M.; Howman, E., Semiconductor quantum dots and free radical induced DNA nicking. *Chem. Commun. (Cambridge, U. K.)* **2005**, (1), 121-123.
328. Bhabra, G.; Sood, A.; Fisher, B.; Cartwright, L.; Saunders, M.; Evans, W. H.; Surprenant, A.; Lopez-Castejon, G.; Mann, S.; Davis, S. A.; Hails, L. A.; Ingham, E.; Verkade, P.; Lane, J.; Heesom, K.; Newson, R.; Case, C. P., Nanoparticles can cause DNA damage across a cellular barrier. *Nat. Nanotechnol.* **2009,** *4*, (12), 876-883.
329. Zhang, W.; Stack, A. G.; Chen, Y. S., Interaction force measurement between E. coli cells and nanoparticles immobilized surfaces by using AFM. *Colloids and Surfaces B-Biointerfaces* **2011,** *82*, (2), 316-324.
330. Yu, T.; Malugin, A.; Ghandehari, H., Impact of silica nanoparticle design on cellular toxicity and hemolytic activity. *ACS Nano* **2011,** *5*, (7), 5717-5728.
331. Jiang, L.; Morin, P. J., Temperature-dependent interactions explain unexpected responses to environmental warming in communities of competitors. *J Anim Ecol* **2004,** *73*, (3), 569-576.
332. Zhang, W.; Yao, Y.; Sullivan, N.; Chen, Y. S., Modeling the primary size effects of citrate-coated silver nanoparticles on their ion release kinetics. *Environ. Sci. Technol.* **2011,** *45*, (10), 4422-4428.
333. Li, Y.; Zhang, W.; Li, K.; Yao, Y.; Niu, J.; Chen, Y., Oxidative dissolution of polymer-coated CdSe/ZnS quantum dots under UV irradiation: Mechanisms and kinetics. *Environ. Pollut.* **2012,** *164*, 259-266.
334. OECD 202 (2004) OECD guideline for the testing of chemicals. 'Daphnia sp., acute immobilisation test'.
335. Hu, X. K.; Cook, S.; Wang, P.; Hwang, H. M., In vitro evaluation of cytotoxicity of engineered metal oxide nanoparticles. *Sci. Total Environ.* **2009,** *407*, (8), 3070-3072.
336. Kahru, A.; Heinlaan, M.; Ivask, A.; Blinova, I.; Dubourguier, H. C., Toxicity of nanosized and bulk ZnO, CuO and TiO_2 to bacteria Vibrio fischeri and crustaceans Daphnia magna and Thamnocephalus platyurus. *Chemosphere* **2008,** *71*, (7), 1308-1316.
337. Feng, W. Y.; Wang, B.; Zhu, M. T.; Wang, Y.; Wang, M.; Gu, Y. Q.; Ouyang, H.; Wang, H. J.; Li, M.; Zhao, Y. L.; Chai, Z. F.; Wang, H. F., Neurotoxicity of low-dose repeatedly intranasal instillation of nano- and submicron-sized ferric oxide particles in mice. *J. Nanopart. Res.* **2009,** *11*, (1), 41-53.
338. Ding, W. J.; Wang, L. J.; Wang, L.; Zhang, F., Acute toxicity of ferricoxide and zinc oxide nanoparticles in rats. *J. Nanosci. Nanotechnol.* **2010,** *10*, (12), 8617-8624.
339. Sayes, C. M.; Berg, J. M.; Romoser, A.; Banerjee, N.; Zebda, R., The relationship between pH and zeta potential of similar to 30 nm metal oxide nanoparticle suspensions relevant to in vitro toxicological evaluations. *Nanotoxicology* **2009,** *3*, (4), 276-283.

340. Kim, I. S.; Baek, M.; Choi, S. J., Comparative cytotoxicity of Al_2O_3, CeO_2, TiO_2 and ZnO nanoparticles to human lung cells. *J. Nanosci. Nanotechnol.* **2010,** *10*, (5), 3453-3458.
341. Lovern, S. B.; Klaper, R., Daphnia magna mortality when exposed to titanium dioxide and fullerene (C-60) nanoparticles. *Environ. Toxicol. Chem.* **2006,** *25*, (4), 1132-1137.
342. Adams, L. K.; Lyon, D. Y.; McIntosh, A.; Alvarez, P. J. J., Comparative toxicity of nano-scale TiO_2, SiO_2 and ZnO water suspensions. *Water Sci. Technol.* **2006,** *54*, (11-12), 327-334.
343. Franklin, N. M.; Rogers, N. J.; Apte, S. C.; Batley, G. E.; Gadd, G. E.; Casey, P. S., Comparative toxicity of nanoparticulate ZnO, bulk ZnO, and ZnCl2 to a freshwater microalga (Pseudokirchneriella subcapitata): The importance of particle solubility. *Environ. Sci. Technol.* **2007,** *41*, (24), 8484-8490.
344. Byer, K.; Khan, S. R., Citrate provides protection against oxalate and calcium oxalate crystal induced oxidative damage to renal epithelium. *Journal of Urology* **2005,** *173*, (2), 640-646.
345. Sallam, K. I., Antimicrobial and antioxidant effects of sodium acetate, sodium lactate, and sodium citrate in refrigerated sliced salmon. *Food Control* **2007,** *18*, (5), 566-575.
346. Kawano, T.; Kadono, T.; Kosaka, T.; Hosoya, H., Green paramecia as an evolutionary winner of oxidative symbiosis: A hypothesis and supportive data. *Zeitschrift Fur Naturforschung C-a Journal of Biosciences* **2004,** *59*, (7-8), 538-542.
347. Derjaguin, B.; Landau, L., Theory of the stability of strongly charged lyophobic sols and of the adhesion of strongly charged particles in solutions of electrolytes. *Acta Physicochim (URSS)* **1941,** *14*, (6), 633-662.
348. Nguyen, A. V., Improved approximation of water dielectric permittivity for calculation of Hamaker constants. *J. Colloid Interface Sci.* **2000,** *229*, (2), 648-651.
349. van der Mei, H. C.; Bos, R.; Busscher, H. J., A reference guide to microbial cell surface hydrophobicity based on contact angles. *Colloids and Surfaces B-Biointerfaces* **1998,** *11*, (4), 213-221.
350. Bergstrom, L., Hamaker constants of inorganic materials. *Adv. Colloid Interface Sci.* **1997,** *70*, 125-169.
351. Amal, R.; Coury, J. R.; Raper, J. A.; Walsh, W. P.; Waite, T. D., Structure and kinetics of aggregating colloidal hematite. *Colloids Surf.* **1990,** *46*, (1), 1-19.
352. Rubio-Hernandez, F. J.; Gomez-Merino, A. L.; Velazquez-Navarro, J. F.; Galindo-Rosales, F. J.; Fortes-Quesada, P., The Hamaker constant of anatase aqueous suspensions. *J. Colloid Interface Sci.* **2007,** *316*, (2), 451-456.
353. Bouchard, D.; Ma, X.; Wigington, B., Fullerene C_{60}: surface energy and interfacial interactions in aqueous systems. *Langmuir* **2010,** *26*, (14), 11886-11893.
354. Zhang, W.; Rittmann, B.; Chen, Y. S., Size Effects on Adsorption of Hematite Nanoparticles on E. coli cells. *Environ. Sci. Technol.* **2011,** *45*, (6), 2172-2178.
355. Pan, Y.; Neuss, S.; Leifert, A.; Fischler, M.; Wen, F.; Simon, U.; Schmid, G.; Brandau, W.; Jahnen-Dechent, W., Size-dependent cytotoxicity of gold nanoparticles. *Small* **2007,** *3*, (11), 1941-1949.

356. Baek, M.; Kim, M. K.; Cho, H. J.; Lee, J. A.; Yu, J.; Chung, H. E.; Choi, S. J., Factors influencing the cytotoxicity of zinc oxide nanoparticles: particle size and surface charge. *Journal of Physics: Conferences Series* **2011,** *304*, 012044.
357. Chan, W. C. W.; Maxwell, D. J.; Gao, X. H.; Bailey, R. E.; Han, M. Y.; Nie, S. M., Luminescent quantum dots for multiplexed biological detection and imaging. *Curr. Opin. Biotechnol.* **2002,** *13*, (1), 40-46.
358. De, M.; Ghosh, P. S.; Rotello, V. M., Applications of Nanoparticles in Biology. *Adv. Mater. (Weinheim, Ger.)* **2008,** *20*, (22), 4225-4241.
359. Medintz, I. L.; Uyeda, H. T.; Goldman, E. R.; Mattoussi, H., Quantum dot bioconjugates for imaging, labelling and sensing. *Nat. Mater.* **2005,** *4*, (6), 435-446.
360. Aubin-Tam, M. E.; Hamad-Schifferli, K., Structure and function of nanoparticle-protein conjugates. *Biomedical Materials* **2008,** *3*, (3), 17.
361. Tom, R. T.; Samal, A. K.; Sreeprasad, T. S.; Pradeep, T., Hemoprotein bioconjugates of gold and silver nanoparticles and gold nanorods: Structure-function correlations. *Langmuir* **2007,** *23*, (3), 1320-1325.
362. Hardman, R., A toxicologic review of quantum dots: Toxicity depends on physicochemical and environmental factors. *Environ. Health Perspect.* **2006,** *114*, (2), 165-172.
363. Derfus, A. M.; Chan, W. C. W.; Bhatia, S. N., Probing the cytotoxicity of semiconductor quantum dots. *Nano Lett.* **2004,** *4*, (1), 11-18.
364. Zhang, L. W.; Monteiro-Riviere, N. A., Mechanisms of Quantum Dot Nanoparticle Cellular Uptake. *Toxicol. Sci.* **2009,** *110*, (1), 138-155.
365. Takenaka, S.; Yamashita, K.; Takagi, M.; Hatta, T.; Tanaka, A.; Tsuge, O., Study of the DNA interaction with water-soluble cationic fullerene derivatives. *Chem. Lett.* **1999**, (4), 319-320.
366. Zhao, X. C.; Striolo, A.; Cummings, P. T., C-60 binds to and deforms nucleotides. *Biophys. J.* **2005,** *89*, (6), 3856-3862.
367. Han, G.; Chari, N. S.; Verma, A.; Hong, R.; Martin, C. T.; Rotello, V. M., Controlled recovery of the transcription of nanoparticle-bound DNA by intracellular concentrations of glutathione. *Bioconjugate Chem.* **2005,** *16*, (6), 1356-1359.
368. McIntosh, C. M.; Esposito, E. A.; Boal, A. K.; Simard, J. M.; Martin, C. T.; Rotello, V. M., Inhibition of DNA transcription using cationic mixed monolayer protected gold clusters. *J. Am. Chem. Soc.* **2001,** *123*, (31), 7626-7629.
369. You, C. C.; Chompoosor, A.; Rotello, V. M., The biomacromolecule-nanoparticle interface. *Nano Today* **2007,** *2*, (3), 34-43.
370. Hansma, H. G., Surface biology of DNA by atomic force microscopy. *Annu. Rev. Phys. Chem.* **2001,** *52*, 71-92.
371. Lyubchenko, Y. L.; Shlyakhtenko, L. S., AFM for analysis of structure and dynamics of DNA and protein-DNA complexes. *Methods* **2009,** *47*, (3), 206-213.
372. Alonso-Sarduy, L.; Roduit, C.; Dietler, G.; Kasas, S., Human topoisomerase II-DNA interaction study by using atomic force microscopy. *FEBS Lett.* **2011,** *585*, (19), 3139-3145.
373. Pastre, D.; Hamon, L.; Sorel, I.; Le Cam, E.; Curmi, P. A.; Pietrement, O., Specific DNA-Protein Interactions on Mica Investigated by Atomic Force Microscopy. *Langmuir* **2010,** *26*, (4), 2618-2623.

374. Doktycz, M. J.; Allison, D. P.; Mortensen, N. P.; Sullivan, C. J., Atomic force microscopy of biological samples. *Wiley Interdisciplinary Reviews-Nanomedicine and Nanobiotechnology* **2010,** *2*, (6), 618-634.
375. Leung, C.; Maradan, D.; Kramer, A.; Howorka, S.; Mesquida, P.; Hoogenboom, B. W., Improved Kelvin probe force microscopy for imaging individual DNA molecules on insulating surfaces. *Appl. Phys. Lett.* **2010,** *97*, (20).
376. Guthold, M.; Zhu, X. S.; Rivetti, C.; Yang, G. L.; Thomson, N. H.; Kasas, S.; Hansma, H. G.; Smith, B.; Hansma, P. K.; Bustamante, C., Direct observation of one-dimensional diffusion and transcription by Escherichia coli RNA polymerase. *Biophys. J.* **1999,** *77*, (4), 2284-2294.
377. Lyubchenko, Y. L.; Shlyakhtenko, L. S., Visualization of supercoiled DNA with atomic force microscopy in situ. *Proc. Natl. Acad. Sci. U. S. A.* **1997,** *94*, (2), 496-501.
378. Allen, M. J.; Bradbury, E. M.; Balhorn, R., AFM analysis of DNA-protamine complexes bound to mica. *Nucleic Acids Res.* **1997,** *25*, (11), 2221-2226.
379. Tessmer, I.; Moore, T.; Lloyd, R. G.; Wilson, A.; Erie, D. A.; Allen, S.; Tendler, S. J. B., AFM studies on the role of the protein RdgC in bacterial DNA recombination. *J. Mol. Biol.* **2005,** *350*, (2), 254-262.
380. An, H. J.; Liu, Q. D.; Ji, Q. L.; Jin, B., DNA binding and aggregation by carbon nanoparticles. *Biochem. Biophys. Res. Commun.* **2010,** *393*, (4), 571-576.
381. Zhang, W.; Yao, Y.; Chen, Y. S., Imaging and Quantifying the Morphology and Nanoelectrical Properties of Quantum Dot Nanoparticles Interacting with DNA. *J. Phys. Chem. C* **2011,** *115*, (3), 599-606.
382. Gill, R.; Zayats, M.; Willner, I., Semiconductor quantum dots for bioanalysis. *Angewandte Chemie-International Edition* **2008,** *47*, (40), 7602-7625.
383. Michalet, X.; Pinaud, F. F.; Bentolila, L. A.; Tsay, J. M.; Doose, S.; Li, J. J.; Sundaresan, G.; Wu, A. M.; Gambhir, S. S.; Weiss, S., Quantum dots for live cells, in vivo imaging, and diagnostics. *Science* **2005,** *307*, (5709), 538-544.
384. Qi, L. F.; Gao, X. H., Emerging application of quantum dots for drug delivery and therapy. *Expert Opinion on Drug Delivery* **2008,** *5*, (3), 263-267.
385. Lohr, D.; Bash, R.; Wang, H.; Yodh, J.; Lindsay, S., Using atomic force microscopy to study chromatin structure and nucleosome remodeling. *Methods* **2007,** *41*, (3), 333-341.
386. Lyubchenko, Y.; Shlyakhtenko, L.; Harrington, R.; Oden, P.; Lindsay, S., Atomic Force Microscopy of Long DNA - Imaging in Air and under Water. *Proc. Natl. Acad. Sci. U. S. A.* **1993,** *90*, (6), 2137-2140.
387. Thundat, T.; Zheng, X. Y.; Sharp, S. L.; Allison, D. P.; Warmack, R. J.; Joy, D. C.; Ferrell, T. L., Calibration of Atomic Force Microscope Tips Using Biomolecules. *Scanning Microscopy* **1992,** *6*, (4), 903-910.
388. Allen, M. J.; Hud, N. V.; Balooch, M.; Tench, R. J.; Siekhaus, W. J.; Balhorn, R., Tip-Radius-Induced Artifacts in Afm Images of Protamine-Complexed DNA Fibers. *Ultramicroscopy* **1992,** *42*, 1095-1100.
389. Thundat, T.; Allison, D. P.; Warmack, R. J., Stretched DNA Structures Observed with Atomic-Force Microscopy. *Nucleic Acids Res.* **1994,** *22*, (20), 4224-4228.
390. Kasas, S.; Thomson, N. H.; Smith, B. L.; Hansma, H. G.; Zhu, X. S.; Guthold, M.; Bustamante, C.; Kool, E. T.; Kashlev, M.; Hansma, P. K., Escherichia coli RNA

polymerase activity observed using atomic force microscopy. *Biochemistry* **1997,** *36*, (3), 461-468.
391. Ono, M. Y.; Spain, E. M., Dynamics of DNA condensates at the solid-liquid interface by atomic force microscopy. *J. Am. Chem. Soc.* **1999,** *121*, (32), 7330-7334.
392. Argaman, M.; Golan, R.; Thomson, N. H.; Hansma, H. G., Phase imaging of moving DNA molecules and DNA molecules replicated in the atomic force microscope. *Nucleic Acids Res.* **1997,** *25*, (21), 4379-4384.
393. Liu, Z. G.; Li, Z.; Zhou, H. L.; Wei, G.; Song, Y. H.; Wang, L., Imaging DNA molecules on mica surface by atomic force microscopy in air and in liquid. *Microscopy Research and Technique* **2005,** *66*, (4), 179-185.
394. Jen-Jacobson, L.; Engler, L. E.; Ames, J. T.; Kurpiewski, M. R.; Grigorescu, A., Thermodynamic parameters of specific and nonspecific protein-DNA binding. *Supramol. Chem.* **2000,** *12*, (2), 143-+.
395. Yang, Y.; Sass, L. E.; Du, C. W.; Hsieh, P.; Erie, D. A., Determination of protein-DNA binding constants and specificities from statistical analyses of single molecules: MutS-DNA interactions. *Nucleic Acids Res.* **2005,** *33*, (13), 4322-4334.
396. Nagao, E.; Dvorak, J. A., Phase imaging by atomic force microscopy: Analysis of living homoiothermic vertebrate cells. *Biophys. J.* **1999,** *76*, (6), 3289-3297.
397. Stark, M.; Moller, C.; Muller, D. J.; Guckenberger, R., From images to interactions: High-resolution phase imaging in tapping-mode atomic force microscopy. *Biophys. J.* **2001,** *80*, (6), 3009-3018.
398. Bloomfield, V. A., DNA condensation. *Curr. Opin. Struct. Biol.* **1996,** *6*, (3), 334-341.
399. Saiz, L.; Vilar, J. M. G., DNA looping: the consequences and its control. *Curr. Opin. Struct. Biol.* **2006,** *16*, (3), 344-350.
400. Schleif, R., DNA Looping. *Annu. Rev. Biochem.* **1992,** *61*, 199-223.
401. Manning, G. S., The persistence length of DNA is reached from the persistence length of its null isomer through an internal electrostatic stretching force. *Biophys. J.* **2006,** *91*, (10), 3607-3616.
402. Harries, D., Solving the Poisson-Boltzmann equation for two parallel cylinders. *Langmuir* **1998,** *14*, (12), 3149-3152.
403. Rogers, B.; Adams, J.; Pennathur, S., Nanotechnology the whole story. In CRC ; Taylor & Francis distributor: Boca Raton, Fla.
London, 2013.
404. Webster, T. J., Safety of nanoparticles from manufacturing to medical applications. In *Nanostructure science and technology,*, Springer: New York, 2009.
405. Zhang, C. Y.; Yeh, H. C.; Kuroki, M. T.; Wang, T. H., Single-quantum-dot-based DNA nanosensor. *Nat. Mater.* **2005,** *4*, (11), 826-831.
406. Boeneman, K.; Deschamps, J. R.; Buckhout-White, S.; Prasuhn, D. E.; Blanco-Canosa, J. B.; Dawson, P. E.; Stewart, M. H.; Susumu, K.; Goldman, E. R.; Ancona, M.; Medintz, I. L., Quantum Dot DNA Bioconjugates: Attachment Chemistry Strongly Influences the Resulting Composite Architecture. *ACS Nano* **2010,** *4*, (12), 7253-7266.
407. Chan, W. C. W.; Nie, S. M., Quantum dot bioconjugates for ultrasensitive nonisotopic detection. *Science* **1998,** *281*, (5385), 2016-2018.
408. Farokhzad, O. C.; Langer, R., Impact of Nanotechnology on Drug Delivery. *ACS Nano* **2009,** *3*, (1), 16-20.

409. Wang, Z. X.; Ma, L. N., Gold nanoparticle probes. *Coord. Chem. Rev.* **2009,** *253*, (11-12), 1607-1618.
410. Dykman, L.; Khlebtsov, N., Gold nanoparticles in biomedical applications: recent advances and perspectives. *Chem. Soc. Rev.* **2012,** *41*, (6), 2256-2282.
411. De Jong, W. H.; Borm, P. J. A., Drug delivery and nanoparticles: Applications and hazards. *International Journal of Nanomedicine* **2008,** *3*, (2), 133-149.
412. Li, K.; Zhao, X.; B, K. H.; Du, S.; Chen, Y., Nanoparticles Inhibit DNA Replication by Binding to DNA: Modeling and Experimental Validation. *ACS Nano* **2013,** *7*, (11), 9664-74.
413. Li, K. G.; Zhang, W.; Chen, Y. S., Quantum dot binding to DNA: Single-molecule imaging with atomic force microscopy. *Biotechnol. J.* **2013,** *8*, (1).
414. Mahtab, R.; Harden, H. H.; Murphy, C. J., Temperature- and salt-dependent binding of long DNA to protein-sized quantum dots: Thermodynamics of "inorganic protein"-DNA interactions. *J. Am. Chem. Soc.* **2000,** *122*, (1), 14-17.
415. Mahtab, R.; Sealey, S. M.; Hunyadi, S. E.; Kinard, B.; Ray, T.; Murphy, C. J., Influence of the nature of quantum dot surface cations on interactions with DNA. *J. Inorg. Biochem.* **2007,** *101*, (4), 559-564.
416. Zhao, Y. D.; Xu, Q.; Wang, J. H.; Wang, Z.; Yin, Z. H.; Yang, Q., Interaction of CdTe quantum dots with DNA. *Electrochem. Commun.* **2008,** *10*, (9), 1337-1339.
417. Acton, F. S., *Numerical methods that work*. Mathematical Association of America: Washington, D.C., 1990; p xx, 549 p.
418. Blier, P. R.; Griffith, A. J.; Craft, J.; Hardin, J. A., Binding of Ku Protein to DNA - Measurement of Affinity for Ends and Demonstration of Binding to Nicks. *J. Biol. Chem.* **1993,** *268*, (10), 7594-7601.
419. Collins, T. J., ImageJ for microscopy. *BioTechniques* **2007,** *43*, (1), 25-+.
420. Winter, R. B.; Berg, O. G.; Vonhippel, P. H., Diffusion-Driven Mechanisms of Protein Translocation on Nucleic-Acids .3. The Escherichia-Coli-Lac Repressor-Operator Interaction - Kinetic Measurements and Conclusions. *Biochemistry* **1981,** *20*, (24), 6961-6977.
421. Schofield, M. J.; Brownewell, F. E.; Nayak, S.; Du, C. W.; Kool, E. T.; Hsieh, P., The Phe-X-Glu DNA binding motif of MutS - The role of hydrogen bonding in mismatch recognition. *J. Biol. Chem.* **2001,** *276*, (49), 45505-45508.
422. Hussain, S. M.; Braydich-Stolle, L. K.; Schrand, A. M.; Murdock, R. C.; Yu, K. O.; Mattie, D. M.; Schlager, J. J.; Terrones, M., Toxicity Evaluation for Safe Use of Nanomaterials: Recent Achievements and Technical Challenges. *Adv. Mater. (Weinheim, Ger.)* **2009,** *21*, (16), 1549-1559.
423. Pal, S.; Tak, Y. K.; Song, J. M., Does the antibacterial activity of silver nanoparticles depend on the shape of the nanoparticle? A study of the gram-negative bacterium Escherichia coli. *Appl. Environ. Microbiol.* **2007,** *73*, (6), 1712-1720.
424. Jiang, J. K.; Oberdorster, G.; Biswas, P., Characterization of size, surface charge, and agglomeration state of nanoparticle dispersions for toxicological studies. *Journal of Nanoparticle Research* **2009,** *11*, (1), 77-89.
425. Dhawan, A.; Sharma, V., Toxicity assessment of nanomaterials: methods and challenges. *Anal. Bioanal. Chem.* **2010,** *398*, (2), 589-605.

426. Bae, E.; Park, H. J.; Lee, J.; Kim, Y.; Yoon, J.; Park, K.; Choi, K.; Yi, J., Bacterial Cytotoxicity of the Silver Nanoparticle Related to Physicochemical Metrics and Agglomeration Properties. *Environ. Toxicol. Chem.* **2010,** *29*, (10), 2154-2160.
427. Keller, A. A.; Wang, H. T.; Zhou, D. X.; Lenihan, H. S.; Cherr, G.; Cardinale, B. J.; Miller, R.; Ji, Z. X., Stability and Aggregation of Metal Oxide Nanoparticles in Natural Aqueous Matrices. *Environ. Sci. Technol.* **2010,** *44*, (6), 1962-1967.
428. Petosa, A. R.; Jaisi, D. P.; Quevedo, I. R.; Elimelech, M.; Tufenkji, N., Aggregation and Deposition of Engineered Nanomaterials in Aquatic Environments: Role of Physicochemical Interactions. *Environ. Sci. Technol.* **2010,** *44*, (17), 6532-6549.
429. Hotze, E. M.; Phenrat, T.; Lowry, G. V., Nanoparticle Aggregation: Challenges to Understanding Transport and Reactivity in the Environment. *J. Environ. Qual.* **2010,** *39*, (6), 1909-1924.
430. Li, K. G.; Zhang, W.; Chen, Y. S., Quantum dot binding to DNA: Single-molecule imaging with atomic force microscopy. *Biotechnol. J.* **2012,** *in press*, DOI: 10.1002/biot.201200155.
431. Zhang, W.; Hughes, J.; Chen, Y. S., Impacts of Hematite Nanoparticle Exposure on Biomechanical, Adhesive, and Surface Electrical Properties of Escherichia coli Cells. *Appl. Environ. Microbiol.* **2012,** *78*, (11), 3905-3915.
432. Desai, M. P.; Labhasetwar, V.; Amidon, G. L.; Levy, R. J., Gastrointestinal uptake of biodegradable microparticles: Effect of particle size. *Pharm. Res.* **1996,** *13*, (12), 1838-1845.
433. Desai, M. P.; Labhasetwar, V.; Walter, E.; Levy, R. J.; Amidon, G. L., The mechanism of uptake of biodegradable microparticles in Caco-2 cells is size dependent. *Pharm. Res.* **1997,** *14*, (11), 1568-1573.
434. Gaiser, B. K.; Fernandes, T. F.; Jepson, M.; Lead, J. R.; Tyler, C. R.; Stone, V., Assessing exposure, uptake and toxicity of silver and cerium dioxide nanoparticles from contaminated environments. *Environmental Health* **2009,** *8*.
435. Moore, M. N., Do nanoparticles present ecotoxicological risks for the health of the aquatic environment? *Environment International* **2006,** *32*, (8), 967-976.
436. Kumar, A.; Pandey, A. K.; Singh, S. S.; Shanker, R.; Dhawan, A., Engineered ZnO and TiO2 nanoparticles induce oxidative stress and DNA damage leading to reduced viability of Escherichia coli. *Free Radical Biol. Med.* **2011,** *51*, (10), 1872-1881.
437. Sanvicens, N.; Marco, M. P., Multifunctional nanoparticles - properties and prospects for their use in human medicine. *Trends Biotechnol.* **2008,** *26*, (8), 425-433.
438. Li, J. J.; Zou, L.; Hartono, D.; Ong, C. N.; Bay, B. H.; Yung, L. Y. L., Gold nanoparticles induce oxidative damage in lung fibroblasts in vitro. *Adv. Mater. (Weinheim, Ger.)* **2008,** *20*, (1), 138-+.
439. Xu, A.; Chai, Y. F.; Nohmi, T.; Hei, T. K., Genotoxic responses to titanium dioxide nanoparticles and fullerene in gpt delta transgenic MEF cells. *Particle and Fibre Toxicology* **2009,** *6*.
440. Trouiller, B.; Reliene, R.; Westbrook, A.; Solaimani, P.; Schiestl, R. H., Titanium Dioxide Nanoparticles Induce DNA Damage and Genetic Instability In vivo in Mice. *Cancer Res.* **2009,** *69*, (22), 8784-8789.
441. Bhattacharya, K.; Davoren, M.; Boertz, J.; Schins, R. P. F.; Hoffmann, E.; Dopp, E., Titanium dioxide nanoparticles induce oxidative stress and DNA-adduct formation but not DNA-breakage in human lung cells. *Particle and Fibre Toxicology* **2009,** *6*.

442. Sharma, V.; Anderson, D.; Dhawan, A., Zinc Oxide Nanoparticles Induce Oxidative Stress and Genotoxicity in Human Liver Cells (HepG2). *J. Biomed. Nanotechnol.* **2011,** *7*, (1), 98-99.
443. Karlsson, H. L.; Cronholm, P.; Gustafsson, J.; Moller, L., Copper oxide nanoparticles are highly toxic: A comparison between metal oxide nanoparticles and carbon nanotubes. *Chem. Res. Toxicol.* **2008,** *21*, (9), 1726-1732.
444. Auffan, M.; Rose, J.; Orsiere, T.; De Meo, M.; Thill, A.; Zeyons, O.; Proux, O.; Masion, A.; Chaurand, P.; Spalla, O.; Botta, A.; Wiesner, M. R.; Bottero, J. Y., CeO2 nanoparticles induce DNA damage towards human dermal fibroblasts in vitro. *Nanotoxicology* **2009,** *3*, (2), 161-U115.
445. Yang, H.; Liu, C.; Yang, D. F.; Zhang, H. S.; Xi, Z. G., Comparative study of cytotoxicity, oxidative stress and genotoxicity induced by four typical nanomaterials: the role of particle size, shape and composition. *J. Appl. Toxicol.* **2009,** *29*, (1), 69-78.
446. Railsback, J. G.; Singh, A.; Pearce, R. C.; McKnight, T. E.; Collazo, R.; Sitar, Z.; Yingling, Y. G.; Melechko, A. V., Weakly Charged Cationic Nanoparticles Induce DNA Bending and Strand Separation. *Adv. Mater. (Weinheim, Ger.)* **2012,** *24*, (31), 4261-4265.
447. Johnston, H. J.; Hutchison, G.; Christensen, F. M.; Peters, S.; Hankin, S.; Stone, V., A review of the in vivo and in vitro toxicity of silver and gold particulates: Particle attributes and biological mechanisms responsible for the observed toxicity. *Critical Reviews in Toxicology* **2010,** *40*, (4), 328-346.
448. Turro, C., Binding manners. *Nature Chem.* **2012,** *4*, 591.
449. Cao, Q. Q.; Zuo, C. C.; Ma, Y. H.; Li, L. J.; Zhang, Z., Interaction of double-stranded DNA with a nanosphere: a coarse-grained molecular dynamics simulation study. *Soft Matter* **2011,** *7*, (2), 506-514.
450. Schellman, J. A.; Stigter, D., Electrical Double-Layer, Zeta Potential, and Electrophoretic Charge of Double-Stranded DNA. *Biopolymers* **1977,** *16*, (7), 1415-1434.
451. Stigter, D., Interactions of Highly Charged Colloidal Cylinders with Applications to Double-Stranded DNA. *Biopolymers* **1977,** *16*, (7), 1435-1448.
452. Sharp, K. A.; Honig, B., Electrostatic Interactions in Macromolecules - Theory and Applications. *Annual Review of Biophysics and Biophysical Chemistry* **1990,** *19*, 301-332.
453. Sushko, M. L.; Shluger, A. L., DLVO theory for like-charged polyelectrolyte and surface interactions. *Materials Science & Engineering C-Biomimetic and Supramolecular Systems* **2007,** *27*, (5-8), 1090-1095.
454. Penners, N. H. G.; Koopal, L. K., Preparation and Optical-Properties of Homodisperse Hematite Hydrosols. *Colloids Surf.* **1986,** *19*, (4), 337-349.
455. Li, Y.; Zhang, W.; Niu, J. F.; Chen, Y. S., Mechanism of Photogenerated Reactive Oxygen Species and Correlation with the Antibacterial Properties of Engineered Metal-Oxide Nanoparticles. *ACS Nano* **2012,** *6*, (6), 5164-5173.
456. Zhang, W.; Li, Y.; Niu, J. F.; Chen, Y. S., Photogeneration of Reactive Oxygen Species on Uncoated Silver, Gold, Nickel, and Silicon Nanoparticles and Their Antibacterial Effects. *Langmuir* **2013,** *29*, (15), 4647-4651.
457. Li, K. G.; Chen, Y. S., Evaluation of DLVO interaction between a sphere and a cylinder. *Colloids and Surfaces A: Physicochemical and Engineering Aspects* **2012**, in press. DOI:dx.doi.org/10.1016/j.colsurfa.2012.09.027.

458. Butt, H.-J.; Graf, K.; Kappl, M., *Physics and chemistry of interfaces*. 2nd., rev. and enl. ed.; Wiley-VCH: Weinheim, 2006; p x, 386 p.
459. Hubbard, A. T., *Encyclopedia of surface and colloid science*. Marcel Dekker: New York, 2002; p 4 v. (5667 p.).
460. Park, I. K.; Kim, T. H.; Park, Y. H.; Shin, B. A.; Choi, E. S.; Chowdhury, E. H.; Akaike, T.; Cho, C. S., Galactosylated chitosan-graft-poly(ethylene glycol) as hepatocyte-targeting DNA carrier. *J. Controlled Release* **2001,** *76*, (3), 349-362.
461. Kirby, B., Micro- and nanoscale fluid mechanics transport in microfluidic devices. In Cambridge University Press: New York, pp 1 online resource (xxiii, 512 p.).
462. Munoz, O.; Volten, H.; Hovenier, J. W.; Min, M.; Shkuratov, Y. G.; Jalava, J. P.; van der Zande, W. J.; Waters, L. B. F. M., Experimental and computational study of light scattering by irregular particles with extreme refractive indices: hematite and rutile. *Astron. Astrophys.* **2006,** *446*, (2), 525-535.
463. Bueno, R. M.; MartinezDuart, J. M.; HernandezVelez, M.; Vazquez, L., Optical and structural characterization of rf sputtered CeO2 thin films. *J. Mater. Sci.* **1997,** *32*, (7), 1861-1865.
464. Bass, M.; Optical Society of America., *Handbook of optics*. 2nd ed.; McGraw-Hill: New York, 1995.
465. Cha, H. G.; Song, J.; Kim, H. S.; Shin, W.; Yoon, K. B.; Kang, Y. S., Facile preparation of Fe2O3 thin film with photoelectrochemical properties. *Chem. Commun. (Cambridge, U. K.)* **2011,** *47*, (8), 2441-2443.
466. Yamamoto, T.; Momida, H.; Hamada, T.; Uda, T.; Ohno, T., First-principles study of dielectric properties of cerium oxide. *Thin Solid Films* **2005,** *486*, (1-2), 136-140.
467. Catlow, C. R. A.; French, S. A.; Sokol, A. A.; Al-Sunaidi, A. A.; Woodley, S. M., Zinc oxide: A case study in contemporary computational solid state chemistry. *J. Comput. Chem.* **2008,** *29*, (13), 2234-2249.
468. The Semiconductors-Information Website. Access Year 2012. http://www.semiconductors.co.uk/propiivi5410.htm
469. Paillusson, F.; Dahirel, V.; Jardat, M.; Victor, J. M.; Barbi, M., Effective interaction between charged nanoparticles and DNA. *Phys. Chem. Chem. Phys.* **2011,** *13*, (27), 12603-12613.
470. Erickson, H. P., Size and Shape of Protein Molecules at the Nanometer Level Determined by Sedimentation, Gel Filtration, and Electron Microscopy. *Biological Procedures Online* **2009,** *11*, (1), 32-51.
471. Tiwari, D. K.; Jin, T.; Behari, J., Bio-distribution and toxicity assessment of intravenously injected anti-HER2 antibody conjugated CdSe/ZnS quantum dots in Wistar rats. *International Journal of Nanomedicine* **2011,** *6*, 463-475.
472. Asare, N.; Instanes, C.; Sandberg, W. J.; Refsnes, M.; Schwarze, P.; Kruszewski, M.; Brunborg, G., Cytotoxic and genotoxic effects of silver nanoparticles in testicular cells. *Toxicology* **2012,** *291*, (1-3), 65-72.
473. de Lima, R.; Seabra, A. B.; Duran, N., Silver nanoparticles: a brief review of cytotoxicity and genotoxicity of chemically and biogenically synthesized nanoparticles. *J. Appl. Toxicol.* **2012,** *32*, (11), 867-879.
474. Bhattacharya, K.; Hoffmann, E.; Schins, R. F. P.; Boertz, J.; Prantl, E. M.; Alink, G. M.; Byrne, H. J.; Kuhlbusch, T. A. J.; Rahman, Q.; Wiggers, H.; Schulz, C.; Dopp, E.,

Comparison of Micro- and Nanoscale Fe+3-Containing (Hematite) Particles for Their Toxicological Properties in Human Lung Cells In Vitro. *Toxicol. Sci.* **2012,** *126*, (1), 173-182.
475. Khaliq, A.; Sonawane, P. J.; Sasi, B. K.; Sahu, B. S.; Pradeep, T.; Das, S. K.; Mahapatra, N. R., Enhancement in the efficiency of polymerase chain reaction by TiO2 nanoparticles: crucial role of enhanced thermal conductivity. *Nanotechnology* **2010,** *21*, (25).
476. Park, E. J.; Yi, J.; Kim, Y.; Choi, K.; Park, K., Silver nanoparticles induce cytotoxicity by a Trojan-horse type mechanism. *Toxicol. in Vitro* **2010,** *24*, (3), 872-878.
477. Marambio-Jones, C.; Hoek, E. M. V., A review of the antibacterial effects of silver nanomaterials and potential implications for human health and the environment. *Journal of Nanoparticle Research* **2010,** *12*, (5), 1531-1551.
478. Wiseman, H.; Halliwell, B., Damage to DNA by reactive oxygen and nitrogen species: Role in inflammatory disease and progression to cancer. *Biochem. J.* **1996,** *313*, 17-29.
479. Cooke, M. S.; Evans, M. D.; Dizdaroglu, M.; Lunec, J., Oxidative DNA damage: mechanisms, mutation, and disease. *FASEB J.* **2003,** *17*, (10), 1195-1214.
480. Zhang, W.; Crittenden, J.; Li, K. G.; Chen, Y. S., Attachment Efficiency of Nanoparticle Aggregation in Aqueous Dispersions: Modeling and Experimental Validation. *Environ. Sci. Technol.* **2012,** *46*, (13), 7054-7062.
481. Li, G.; Levitus, M.; Bustamante, C.; Widom, J., Rapid spontaneous accessibility of nucleosomal DNA. *Nat. Struct. Mol. Biol.* **2005,** *12*, (1), 46-53.
482. Li, G.; Widom, J., Nucleosomes facilitate their own invasion. *Nat. Struct. Mol. Biol.* **2004,** *11*, (8), 763-769.
483. Polach, K. J.; Widom, J., Mechanism of Protein Access to Specific DNA-Sequences in Chromatin - a Dynamic Equilibrium-Model for Gene-Regulation. *J. Mol. Biol.* **1995,** *254*, (2), 130-149.
484. Dell'Orco, D.; Lundqvist, M.; Oslakovic, C.; Cedervall, T.; Linse, S., Modeling the Time Evolution of the Nanoparticle-Protein Corona in a Body Fluid. *PLoS One* **2010,** *5*, (6).
485. Lesniak, A.; Fenaroli, F.; Monopoli, M. R.; Aberg, C.; Dawson, K. A.; Salvati, A., Effects of the Presence or Absence of a Protein Corona on Silica Nanoparticle Uptake and Impact on Cells. *ACS Nano* **2012,** *6*, (7), 5845-5857.
486. Vonhippel, P. H.; Berg, O. G., On the Specificity of DNA-Protein Interactions. *Proc. Natl. Acad. Sci. U. S. A.* **1986,** *83*, (6), 1608-1612.
487. Ohshima, H.; Furusawa, K., *Electrical phenomena at interfaces : fundamentals, measurements, and applications*. 2nd ed.; M. Dekker: New York, 1998; p xiii, 628 p.
488. Hogg, R.; Healy, T. W.; Fuersten.Dw, Mutual Coagulation of Colloidal Dispersions. *Transactions of the Faraday Society* **1966,** *62*, (522P), 1638-&.
489. Derjaguin, B., Analysis of friction and adhesion IV The theory of the adhesion of small particles. *Kolloid-Zeitschrift* **1934,** *69*, (2), 155-164.
490. Bhattacharjee, S.; Elimelech, M.; Borkovec, M., DLVO interaction between colloidal particles: Beyond Derjaguin's approximation. *Croat. Chem. Acta* **1998,** *71*, (4), 883-903.

491. Bhattacharjee, S.; Elimelech, M., Surface element integration: A novel technique for evaluation of DLVO interaction between a particle and a flat plate. *J. Colloid Interface Sci.* **1997,** *193*, (2), 273-285.
492. Lifshitz, E. M., The Theory of Molecular Attractive Forces between Solids. *Soviet Physics Jetp-Ussr* **1956,** *2*, (1), 73-83.
493. Hamaker, H. C., The London - Van Der Waals attraction between spherical particles. *Physica* **1937,** *4*, 1058-1072.
494. Bhattacharjee, S.; Sharma, A., Lifshitz-Van Der Waals Energy of Spherical-Particles in Cylindrical Pores. *J. Colloid Interface Sci.* **1995,** *171*, (2), 288-296.
495. Montgomery, S. W.; Franchek, M. A.; Goldschmidt, V. W., Analytical dispersion force calculations for nontraditional geometries. *J. Colloid Interface Sci.* **2000,** *227*, (2), 567-584.
496. Gu, Y. G., The electrical double-layer interaction between a spherical particle and a cylinder. *J. Colloid Interface Sci.* **2000,** *231*, (1), 199-203.
497. Gu, Y. G.; Li, D. Q., The van der Waals interaction between a spherical particle and a cylinder. *J. Colloid Interface Sci.* **1999,** *217*, (1), 60-69.
498. Kirsch, V. A., Calculation of the van der Waals force between a spherical particle and an infinite cylinder. *Adv. Colloid Interface Sci.* **2003,** *104*, 311-324.
499. Rosenfel.Ji; Wasan, D. T., London Force Contribution to Vanderwaals,Hg Der Waals Force between a Sphere and a Cylinder. *J. Colloid Interface Sci.* **1974,** *47*, (1), 27-31.
500. Ohshima, H., Electrostatic interaction between two parallel cylinders. *Colloid Polym. Sci.* **1996,** *274*, (12), 1176-1182.

VITA

KUNGANG LI

Kungang was born in China. He received a B.S. in Environmental Science from Nankai University, Tianjin, China in 2008 before coming to Georgia Tech to pursue a doctorate in Environmental Engineering. When he is not working on his research, he enjoys trading stocks/options and traveling short distances around Atlanta.